Dissertation
submitted to the
Combined Faculty for the Natural Sciences and for Mathematics
of the Ruperto Carola University Heidelberg, Germany
for the degree of
Doctor of Natural Sciences (Dr. rer. nat.)

presented by
M.Sc. Peter Johannes Manuel Eduard Kumberger
born in Regensburg, Germany

Oral examination: November 5th, 2018

Quantifying the Impact of Cell-to-Cell Transmission on Viral Spread

Referees: Prof. Dr. Ursula Kummer

Dr. Frederik Graw

M.Sc. Peter Johannes Manuel Eduard Kumberger
Quantifying the Impact of Cell-to-Cell Transmission on Viral Spread
Dissertation, Version 1.0

Ruperto Carola University Heidelberg, Germany
Combined Faculty of the Natural Sciences and for Mathematics
Faculty of Biosciences
Im Neuenheimer Feld 234
69120 Heidelberg

Abstract

Over time, viruses have evolved several strategies to infect host cells, which can be roughly categorized into two distinct modes of viral transmission, namely cell-free and cell-to-cell. Various studies have opted for the latter to play the dominant role in infections with human immunodeficiency virus (HIV) and hepatitis C virus (HCV). How to quantify the exact contribution of each transmission mode to the infection dynamics, without biasing results due to the experimental protocol, remains to be answered to allow for more efficient drug and vaccine development.

Previously, mathematical models based on mass-action kinetics were fitted to bulk measurements obtained from *in vitro* cell cultures cultivated in aqueous media. This combination of experiment and modeling is very specific and might not be appropriate to describe other situations such as *in vivo* studies. To allow generalization, the effect of modeling strategy and experimental protocol on the predicted contributions of cell-to-cell spread to the infection dynamics should be studied in more detail. In this thesis, I therefore analyzed possible consequences of varying extracellular microenvironments and types of target cells on the different transmission modes during an infection and how certain modeling strategies affect predictions.

In a first step, I studied the impact of varying extracellular microenvironments on *in vitro* spread of HIV. To this end, I developed a detailed mass-action kinetics model combining experiments and mathematical modeling to describe HIV infection dynamics in aqueous media and two types of collagen. My results show that for HIV infection of motile target cells the contribution of transmission modes varies dependent on the environment.

Next, I moved from motile to stationary cells analyzing cell-to-cell transmission of HCV among immobile hepatocytes. To account for the local nature of cell-to-cell spread in stationary target cells, I developed an agent-based model, which combines deterministic intracellular viral processes with stochastic intercellular infection events. This model was applied to spatially-resolved data, describing HCV infection dynamics obtained from an *in vitro* experiment conducted on hepatocytes in a monolayer. I found that the contribution of cell-to-cell transmission to the infection dynamics is dominant in the early stages of the experiment. However, depending on the composition of the used serum, the contribution can shift towards a stronger role of cell-free spread during the experiment.

Moreover, I investigated how to reconcile bulk measurement data with mass-action kinetics models in the context of viral cell-to-cell transmission among stationary target cells. Fitting complex models to describe various aspects of viral infections such as cell-to-cell transmission usually requires sufficiently resolved data. Nonetheless, experimental protocols often only allow bulk measurements, which are generally combined with mass-action kinetics models

that assume a well-mixed system. In the context of locally confined movement of target cells infected by viruses, which are capable of infecting via cell-to-cell transmission, this assumption is likely violated. Therefore, I developed an extension of a previously published model, incorporating the decreasing proportion of cells contributing to cell-to-cell transmission with progression of infection. The extended model then allowed correct quantification of the infection dynamics.

In summary, I developed different modeling approaches to analyze the contribution of cell-to-cell transmission to the infection dynamics of HIV and HCV under varying conditions. Furthermore, I provide an extension to a mass-action kinetics model to allow correct description of cell-to-cell transmission in the context of stationary cells while still keeping a simple structure, which can be fitted to population-level data. All approaches can be adapted to other viruses to allow quantification of transmission modes, which will help to guide drug and vaccine development more efficiently.

Zusammenfassung

Viren haben im Laufe der Zeit verschiedene Strategien entwickelt um Wirtszellen zu infizieren. Dabei können grob zwei Übertragungswege unterschieden werden, nämlich zellfreie und Zell-Zell-Übertragungen. Mehrere Studien kamen zu dem Ergebnis, dass sowohl bei dem Humanen Immundefizienz-Virus (HIV) als auch dem Hepatitis C Virus (HCV) Wirtszellen hauptsächlich durch Zell-Zell-Übertragungen infiziert werden. Es stellt sich jedoch die Frage, wie stark die Resultate durch das verwendete experimentelle Protokoll beeinflusst wurden. Um die Entwicklung neuer Medikamente und Impfungen effizienter zu gestalten, ist eine korrekte Quantifizierung der Transmissionsmechanismen von großer Bedeutung.

Bisher wurden Modelle, die auf dem Massenwirkungsgesetz basierten, an Konzentrationsmessungen angepasst, welche von Experimenten mit *in vitro* Zellkulturen in Suspension stammten. Diese Kombination aus *in vitro* Experimenten mit einfachen Modellen ist jedoch sehr spezifisch und lässt in der Regel keine Verallgemeinerung zu. Um eine allgemeingültige Aussage zu ermöglichen, muss sowohl der Effekt der Modellierungsstrategie als auch des experimentellen Protokolls auf das Verhältnis zwischen zellfreien und Zell-Zell-Übertragungen berücksichtigt werden.

In dieser Arbeit untersuchte ich deshalb den Einfluss sowohl der extrazellulären Umgebung als auch verschiedener Zelltypen auf die beiden Transmissionsmechanismen und analysierte, wie verschiedene Modellierungsstrategien die Vorhersagen beeinflussen.

In einem ersten Schritt betrachtete ich den Einfluss verschiedener extrazellulärer Umgebungen auf die *in vitro* Ausbreitung von HIV. Mithilfe einer Kombination aus Experimenten und mathematischen Analysen entwickelte ich ein detailliertes, auf dem Massenwirkungsgesetz basierendes Modell, um HIV Infektionsdynamiken in Suspension und zwei verschiedenen Kollagentypen zu beschreiben. Meine Resultate zeigen, dass bei HIV Infektionen von beweglichen T-Zellen der Beitrag der verschiedenen Transmissionsmechanismen von der extrazellulären Umgebung abhängt.

Als Nächstes analysierte ich Zell-Zell Transmissionen von HCV zwischen unbeweglichen Hepatozyten, also stationären statt beweglichen Zellen. Um dabei auch die räumliche Struktur zu berücksichtigen, entwickelte ich ein Agenten-basiertes Modell, welches deterministische intrazelluläre Virusprozesse mit stochastischen interzellulären Infektionsereignissen kombinierte. Dieses Modell wendete ich dann auf räumlich aufgelöste Daten an. Diese Daten resultierten aus einem *in vitro* Experiment bei dem in einer flachen Schicht angeordnete Hepatozyten von HCV infiziert wurden. Dabei zeigte sich, dass Zell-Zell-Übertragungen anfangs die Infektionsdynamik dominierten. In Abhängigkeit vom verwendeten Serum kam es jedoch im Laufe des Experiments zu einer steigenden Anzahl zellfreier Übertragungen.

Ausgehend von diesen Beobachtungen untersuchte ich die Möglichkeit einfache Modelle zu erweitern, um die Analyse von Konzentrationsmessungen einer experimentellen Virusinfektion stationärer Zellen basierend auf Zell-Zell Übertragungen zu verbessern. Um verschiedene Aspekte viraler Infektionen wie z.B. Zell-Zell Transmissionen zu beschreiben, benötigen komplexe Modelle in der Regel hoch aufgelöste Daten. Oft erlauben die eingesetzten experimentellen Protokolle jedoch nur Konzentrationsmessungen. Unter der Annahme eines gut gemischten Systems werden diese Daten häufig mit einfachen mathematischen Modellen analysiert. Falls die Bewegung von Zellen eingeschränkt ist, führt dies jedoch zu einer Verletzung dieser Annahme. Deswegen erweiterte ich ein bereits publiziertes Modell, um den Verlust an Zellen, welche zu Zell-Zell Infektionen beitragen können, zu berücksichtigen. Die Erweiterung des Modells erlaubte damit eine korrekte Quantifizierung der Infektionsdynamik.

Zusammenfassend entwickelte ich verschiedene Modellierungsansätze, um den Beitrag von Zell-Zell Transmissionen zu den Infektionsdynamiken von HIV und HCV bezüglich verschiedener Bedingungen zu untersuchen. Des Weiteren resultiert meine Arbeit in einer Erweiterung eines Modelles basierend auf dem Massenwirkungsgesetz, welches die korrekte Beschreibung von Zell-Zell Transmissionen zwischen unbeweglichen Zellen erlaubt. Dabei behält das Modell seine einfache Struktur bei und ermöglicht so eine Anpassung an Konzentrationsmessungen. Alle Ansätze können außerdem auf andere Viren angewendet werden, um auch für diese die jeweiligen Übertragungsmechanismen zu quantifizieren. Dies sollte zu einem erweiterten Verständnis der untersuchten Viren führen. Die gewonnenen Erkenntnisse und entwickelten Methoden könnten in Zukunft dabei helfen, die Entwicklung von Medikamenten und Impfungen für verschiedene Viren effizienter zu gestalten.

Acknowledgments

First of all I want to to thank my supervisor Dr. Frederik Graw, without whom this work would not have been possible. He was always there if input was needed and, more importantly, he helped me in the transition from a theoretician to somebody actually applying his work to data.

I am also grateful to Prof. Dr. Ursula Kummer, who really believes in the concept of interdisciplinary and gave me the opportunity to focus more on the biological side of my work. Furthermore, I want to thank Prof. Dr. Oliver Fackler and Prof. Dr. Thomas Höfer for their interest in my work and their valuable input. Without all the people who did experiments my goals could have never been reached. Here, special thanks goes to Karina Durso-Cain for living in the lab for days to get me time-resolved data any modeler can dream of and also her supervisor Prof. Susan L. Uprichard for all the advice she put into the HCV modeling. For the HIV part, I really want to thank Prof. Dr. Oliver Fackler and Dr. Andrea Imle for designing this great study. Furthermore, without experiments, all statements relating to biological questions are less impressive. This means that I have to give a special thanks to Dr. Andrea Imle, who besides doing a ton of experiments always knew exactly what kind of data I would need (sometimes even without my own knowledge). In this context, I also have to thank Dr. Nikolas Schnellbächer, Dr. Paola Carrillo-Bustamante and Jana Fehr, who were part of our weekly meetings, really making this a close collaboration. I gained tons of new perspectives and I wouldn't want to miss it.

Colleagues are an important asset in generating a great working environment resulting in presentable output. In my case this were all the people of the mathematical immunology group, who always played along Eco-Pete's annoying habits, e.g., turning off screens. First, I want to mention Michael Gabel from this group, our lunch and coffee break guy. Without you, I'm sure I would have starved. Other than that I also want to thank you for all the discussions we had, really improving my work. Furthermore special thanks goes to Neha Thakre, who had the great idea that I could use a hexagonal grid, allowing me to create awesome figures. Michael and Neha, I have to say our puzzle solving times were great. Next, I want to thank Sam Wilks, who tried to teach me the fine nuances of the English language. Paola Carrillo-Bustamante needs to be mentioned here as well for introducing me into the world of Inkscape and ggplot and never giving up on trying to explain to me how to properly write, despite my continuous incompetence. Lastly, I want to thank all the people, who came and went during my thesis, namely Sarah Kaspar, Verena Körber, Arne Schoch, Martin Zauser, Priyata Kalra, Jan Jongmanns, Jana Fehr, Sophia Eijkman and all others that I might have missed. Without you my daily routine would have been boring and dull. Finally, from a

work-related perspective, I am grateful to all the people who read parts of my thesis and gave me advice on how to improve it, and to Benjamin Busam for allowing me to use his awesome template for my thesis layout.

Of course, I need to mention and want to thank my parents for their never ending support, be it financially, psychologically or whatever else parents do. I really appreciate all the trouble you went through to get me to this point!

Last, but obviously not least, I am deeply grateful to my wife and son, who were there to cheer me up and make me laugh when needed, always got my back and challenged me to do my best. Without your help this would have been basically impossible. THANKS!!

Contents

Part I

Introduction

1 Introduction

1.1 Viruses

We are under attack!

Every day viruses try to intrude into our bodies and, by this process, challenge our immune system. The viral invaders are minimal working examples of a life form with the most elementary ones only consisting of a capsid and ribonucleic acid (RNA) or deoxyribonucleic acid (DNA) acting as genetic material. Some have a few additional proteins all directed at ensuring survival of the virus [1]. Without the possibility to replicate genetic material or synthesize proteins themselves, viruses have always depended on the cellular machinery of other organisms to multiply [2]. Therefore, the entry of viruses into and subsequent infection of formerly uninfected cells is an essential part of the viral life cycle to ensure survival [1]. This leads to a constant struggle between the immune system trying to fight off the virus and viral attempts to establish infection.

Viruses have evolved several evasion mechanisms to escape the immune response shifting disease progression from acute to latent or persistent infections. A virus leading to an acute infection is for example Influenza virus [3], which is in most cases cleared by the immune response in healthy individuals within a couple of weeks. Others, like herpes simplex virus [4], can persist in the body at low levels with sporadic outbursts during times of a weakened immune response in latent infections. Similarly, in persistent infections the virus remains in the body after an acute period. However, without treatment the viral life cycle continues as the virus cannot be controlled by the immune system and constant occurrence of new infections is observed, e.g., majority of cases in human immunodeficiency virus (HIV) [5] as well as hepatitis C virus (HCV) [6]. Although we have learned a great deal about viral infections in the past and even found cures or preventive vaccines for certain viruses, an essential part, i.e., the exact processes governing viral entry into host cells, generally remains unknown [7]. As viral entry is the first step in establishing an infection, it is a likely candidate to target in antiviral therapy. Therefore, deciphering its key aspects will help to guide efficient drug and vaccine development as it allows identification of potential pharmaceutical targets.

1.1.1 Viral transmission modes

Albeit the varying shapes and structures of viruses, viral transmission between host cells can be generally categorized into two distinct transmission modes [7].

Cell-free transmission

Viral entry was first assumed to be solely transmitted by cell-free diffusing viral particles. In brief, upon encountering uninfected target cells, viruses can recruit internalization or entry

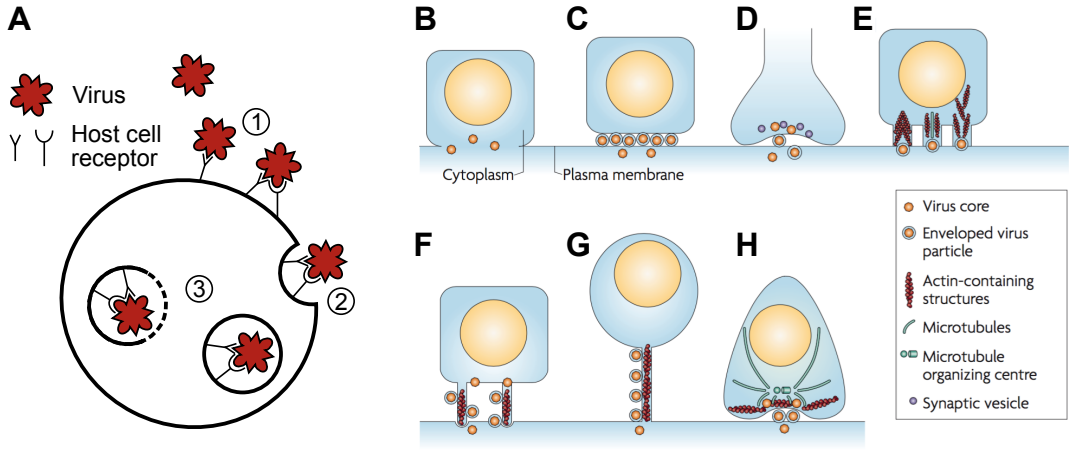

Fig. 1.1. **Sketch of viral transmission mechanisms.** **(A)** A virion diffuses freely across the host cell's membrane. After attaching to virus specific receptors (1), the virus enters the cell via endocytosis (2) or membrane fusion (not shown). After digestion of the endosome's membrane and viral envelope, viral material is released into the cytoplasm (3). **(B-H)** Several mechanisms of viral cell-to-cell transmission are known. Passive viral transport processes involve plasma membrane fusion (**B**), tight junctions (**C**) and neural synapses formation (**D**). Active processes include induction of actin- or tubulin-containing structure (**E**), subversion of actin-containing structures such as filopodia (**F**) and membrane nanotubes (**G**). Last but not least the virus can also polarize the infected cell towards a neighboring cell, budding the virus in direction of a virological synapse (**G**). **(B-H)** Reprinted by permission from Springer Nature: Nature Reviews Microbiology [7] © (2008).

receptors and subsequently infect the host cell via membrane fusion or endocytosis (Fig. 1.1A). For many viruses, various elements such as the duration and receptors involved remain to be elucidated [8]. This transmission mode has been termed cell-free (CF) transmission [7].

In general, cell-free transmission allows far-range spread. For example, virus surfing in the blood stream can disseminate to distant uninfected tissue regions. In addition, cell-free viruses in saliva droplets can spread from host-to-host [7, 9]. Within a host, cell-free transmission is independent of cellular interactions as successful infections require only uninfected host cells and cell-free virus. However, extracellular virions permanently risk of being neutralized by antibodies or patrolling immune cells leading to constant immune pressure exerted by the host's immune response on cell-free virus [10].

Cell-to-cell transmission

Since experimental procedures have evolved, several other possibilities for the virus to enter cells have been identified, which can be categorized into a second transmission mode known as cell-to-cell (CC) transmission. In this process virus replicating cells can directly infect adjoining cells through different passive or active transport processes of virions [7]. While passive transport includes plasma membrane fusion, tight junctions and neural synapses, active transport processes involve viral induction/subversion of actin- or tubulin-containing structures, the formation of actin-containing nanotubes and virological synapses (Fig. 1.1). Which process is exploited for the infection of cells depends on the virus and several other environmental factors [7].

Sometimes, cell-to-cell transmission is also observed in the context of host-to-host infections. For example, T cells are assumed to be the carrier from host-to-host of human T-lymphotropic

virus type 1 [11]. To allow transfer of infected cells from host-to-host, a close interaction between infected and uninfected host is generally needed. Within a host, local confinement of infection in stationary cells due to the short-range nature of cell-to-cell transmission resulting in large foci of infected cells, provides a barrier for fast infection dynamics [12]. This can be explained by the decreasing proportion of infected cells contributing to the infection with growing focus sizes as uninfected neighbors are required for successful cell-to-cell transmissions [12]. Nonetheless, cell-to-cell transmission is believed to be highly efficient on a per cell basis as it can avoid patrolling immune cells [7] or extracellular antibodies [13] through the direct transfer of viral material from infected to uninfected cells, thus, shielding the virus from the immune response. Since cell-to-cell transmission can effectively circumvent the immune response, it is thought to play an important role in the establishment of persistent infections [14–16]. Still, the immune system is able to enforce pressure on cell-to-cell transmission through paracrine signaling, which can lead to protected neighbors, limiting possible targets for cell-to-cell infections [17].

Considering the advantages and disadvantages of the two modes of viral transmission, it is difficult to determine the main route of infection *a priori*. However, cell-to-cell transmission is believed to be orders of magnitude more efficient than cell-free [9, 18–21] due to transfer of large numbers of viral particles during cell-to-cell spread of various pathogens [22–24]. Nonetheless, the contributions of the different transmission modes might not only vary between viruses, but also depend on the target cells and their behavior. As cell-to-cell transmission relies on cellular interactions, it is shaped by communication between and motility of target cells, where the latter is defined by a combination of the inherent cellular motility as well as the cellular environment. Depending on the environment, changing cell densities and cells interacting with the environment influence cellular motility.

The importance of getting reliable estimates goes beyond sheer scientific curiosity as in-depth knowledge of the contributions to infection dynamics can help to identify targets to efficiently fight viral pathogens [15]. While cell-free virus can be cleared by extracellular components such as antibodies, cell-to-cell transmission is more difficult to prevent [24]. Here, blocking early steps in the viral life cycle hindering the maturation into fully infectious virions, can be an effective strategy to assist the host in fighting the pathogen [24].

1.1.2 Hepatitis C virus

Hepatitis C virus (HCV), the predominant causing agent of non-A, non-B hepatitis (nowadays known as hepatitis C), an enveloped, positive-sense, single-stranded RNA virus, was discovered in 1989 and classified as part of the family flaviviridae [25, 26]. A large number of viral variants is known, rendering it a quasispecies rather than a conventional virus species with subtypes 1a and 1b being the major cause of the approximately 120 million infections worldwide [27, 28]. Despite the major health burden and excessive research still no preventive vaccine exists. Early treatments of HCV consisted of a combination therapy with pegylated interferon and ribavarin. Unfortunately, this treatment had strong side effects and a sustained viral response (SVR) was only observed in about 50% of HCV genotype 1 cases [29, 30]. With the development of direct acting agents such as sofosbuvir and daclatasvir, SVR rose to over 90%, finally providing clinicians with an effective drug to treat infected patients [31].

The primary target cells of HCV are hepatocytes. However, there are also reports of rare infections of peripheral blood mononuclear cells [32]. Within the host, the virus first needs to enter a hepatocyte. This process is governed by complex interactions with several receptors, e.g. low density lipoprotein receptor, CD81, claudin 1 and occludin [33, 34]. Once inside its target, the viral genome is translated - using host ribosomes - into a single polyprotein, which is subsequently cleaved and processed into structural and non-structural proteins [33]. Allowing the virus to escape humoral and cellular immune pressure [6, 35], negative-stranded RNA is transcribed from its positive counterpart using an error-prone viral RNA polymerase in the membranous web, which is induced by the viral protein NS4B. In a next step the negative-stranded RNA acts as a template for the synthesis of new positive-stranded RNA [33]. The exact processes within and the role of the membranous web, also known as viral replication complex, are not yet fully characterized. So far, the membranous web is thought to be the site of viral replication and assembly [36, 37]. Finally, assembled virions are released into the extracellular space. How budding of HCV from the host cell exactly works is still unknown and subject to ongoing research [38]. Whereas cell-free virions are capable of infecting hepatocytes through a cascade of interactions with several host receptors, HCV can additionally infect host cells through cell-to-cell transmission [16]. In contrast to other viruses, e.g., HIV-1 and herpes simplex virus, the exact mechanism of infection establishment through cell-to-cell transmission regarding HCV still needs to be elucidated [7]. Additionally, at which step in the viral replication cell-to-cell transmission occurs remains unknown, where the most important question is whether a viral envelope is necessary for successful cell-to-cell spread. Despite this lack of knowledge, cell-to-cell transmission is considered the major cause for viral persistence in the body due to viral escape from neutralizing antibodies [16, 39] or during therapy [40].

Deciphering the various steps in the viral life cycle has been a challenging task in HCV research. Missing small-animal models and, early on, a replication competent *in vitro* system made it difficult to discover the processes governing infection. Knowledge of the hepatitis C virus increased tremendously with the development of a replicon system in Huh-7 cells, a human hepatoma cell line [41], and the discovery of JFH-1, a virus isolated from a patient with Japanese fulminant hepatitis, which is capable of going through the full viral life cycle and is infectious for naive Huh-7 cells [42, 43].

Despite identifying the viral structure and understanding most parts of its life cycle, the contribution of each transmission mode to HCV infection dynamics remains an open question.

1.1.3 Human immunodeficiency virus

First described in 1983 by Barré-Sinoussi *et al.* [44], the human immunodeficiency virus (HIV) is a positive-sense, single-stranded, enveloped RNA virus of the genus lentivirus, a subgroup of retroviruses [45], which are known for their slow disease progression. It can be divided into two groups, namely HIV-1 and HIV-2, where the former is more virulent and infective and, thus, the main cause of the approximately 40 million HIV infections worldwide [46, 47]. Despite tremendous efforts, to this date pharmaceutical research has been unable to develop a vaccine or complete cure for HIV. Current antiretroviral therapies are not able to clear the virus from the patient, but increase life expectancy of infected people to the same level as observed for uninfected individuals [48].

The main target cells for HIV are activated CD4+ T lymphocytes [49, 50] and rarely dendritic cells, where the latter cell type is believed to play an important role in the early establishment of the virus in humans [51]. At the beginning of the infection, small foci comprised of infected cells can be observed at the location of viral entry in the body. These foci form due to recruitment and activation of T cells in the proximity of already infected cells [52–54]. Upon interaction with CD4 and co-receptors C-C chemokine receptor type 5 (CCR5) or C-X-C chemokine receptor type 4 (CXCR4) and subsequent entry [55], HIV follows the characteristic path of retroviruses. First, viral RNA is transcribed into double-stranded DNA by reverse transcriptase and then integrated into the host cell genome by the enzyme integrase [56, 57]. In this step depending on the activation state of the infected cell, the virus genome, integrated into the host cell's DNA at this point, can enter latency, a state of non-productive infection with low gene expression levels. At later stages translated viral proteins and genomic RNA are exported to the cytoplasm, where new particles are assembled at the plasma membrane [58, 59].

HIV has several strategies to evade the immune response. For example, reverse transcription is an error-prone process, which leads to high mutation rates and subsequently viral escape from immune pressure. Another mechanism is the down-regulation of surface markers on infected cells, which limits their ability to present viral material to patrolling immune cells [60]. In addition, latently infected cells provide the dormant virus with protection against the immune response over long periods, thus, probably playing a key role in viral rebound after therapy completion [61].

Similar to HCV, new infections can occur either via cell-free virions or cell-to-cell transmission, which is assumed to predominantly occur through formation of viral synapses [22]. For HIV, the latter mode of transmission is believed to be orders of magnitude more efficient than cell-free spread [18–20]. However, experimental limitations (see below) may have biased these results and the exact contributions still remain unresolved.

1.1.4 Experimental procedures

To experimentally investigate different aspects of viruses under controlled conditions, several techniques have been developed to collect data [62]. These techniques range from case-control studies on humans or animal models over *ex vivo* to *in vitro* experiments.

While case-control studies on humans or animal-models resemble realistic conditions, they often struggle with low sample sizes, high variability within groups as well as difficulties in assessing individual steps of the infection process. To address the latter, experiments are usually conducted with cells submerged in aqueous media, allowing for easy manipulation of processes and access to virus and cells. In this approach cells nourish on the supplemented nutrients of the media and sediment to the bottom of the well forming a dense monolayer (Fig. 1.2A) [63]. This technique is useful in the context of infection dynamics among tissue-forming cells, e.g. hepatitis C or B virus infecting hepatocytes. Here, cells are stationary and a dense layer resembles realistic conditions for hepatocytes.

However, this generally applied technique falls short, when studying viruses infecting motile target cells, such as HIV or human T-lymphotropic virus, as high cell densities can affect

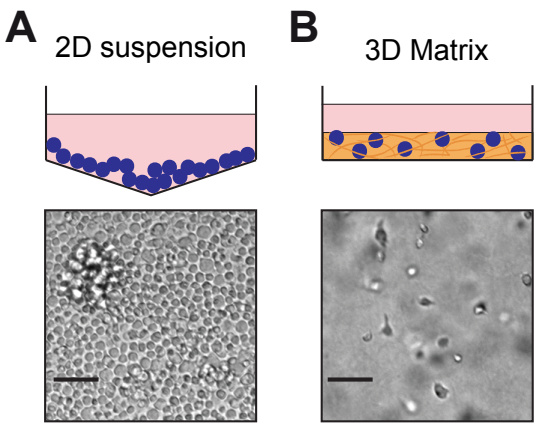

Fig. 1.2. **Different experimental environments.** **(A)** Shortly after addition of cells to aqueous media, cells sediment to the bottom of the well essentially forming a dense monolayer. **(B)** In contrast, collagen provides a scaffold for the cells, decreasing cell density and allowing for movement in all directions. Scale bar: $40\ \mu m$. Adapted by permission from Springer Nature: Nature Reviews Microbiology [63] © (2014).

cell motilities potentially biasing the results [63]. This shows the necessity of extending the experimental technique of culturing cells in aqueous media to a more realistic setting. Studying HIV for example in human tonsil explants, which provide the cells with a scaffold structure, achieves a closer resemblance of the human lymph node. Although this allows for more realistic cell densities, it is difficult to follow cells in real-time with live cell imaging as microscopy beyond a few hundred microns in solid tissue is not yet possible [64]. Additionally, manipulation of explants with regard to changes in the cellular environment such as the cellular composition and activation state of lymphocytes is difficult to accomplish and, thus, studying the effects of these changes on the infection dynamics cannot be conducted with this technique [63]. To overcome these problems in the context of migrating cells with the advantage of providing a scaffold structure allowing for reasonable cell densities and cellular migration patterns, 3D collagen structures are an optimal solution (Fig. 1.2B) [63, 65]. For these structures, Collagen I, obtained from bovine cartilage or rat tails [65], is favored over natural occurring collagen as it allows retrieval of viable cells through the administration of Collagenase, which digests the collagen matrix [66]. Without retrieval of viable cells, fluorescence-activated cell sorting (FACS), an important experimental technique for the sorting of cells, can lead to wrong results as dead cells can take up antibodies non-specifically and are also often auto-fluorescent.

After determining a reasonable cell culture system for a particular virus, the contribution of the different transmission modes to the infection dynamics still needs to be disentangled. To this end, several *in vitro* approaches have been developed. Spatially separating infected and uninfected cells with a transwell allows virus but not cells to diffuse between chambers [67], thus, blocking cell-to-cell transmission. Using this technique generally leads to a bias in favor of efficient cell-to-cell spread. Large distances as featured in transwells automatically cause increased loss of viral infectivity [68] because diffusion of virions usually is too slow to cover large distances [69]. A different experimental approach is to harvest infected cells or virus from infected cultures and co-culture them with uninfected cells [68]. However, this technique presents the scientist with another problem as it tries to link different entities, i.e., amount of cell-free virus and number of infected cells, which are not comparable. For example,

infected cells can act as production sites for new virions over long time intervals. Despite their shortcomings, both approaches were applied to measure the efficiency of transmission modes during HIV infection [19, 20]. Using these experimental techniques indicated that cell-to-cell is considerably more efficient than cell-free transmission.

Additionally, there have been efforts to infer relative contributions of the respective transmission modes for particular viruses such as HIV and HCV by blocking one transmission mode without affecting the other. To achieve this in the context of HIV, cultures were shaken to prevent cell-to-cell transmission [20, 70]. However, the authors came to conflicting results [18, 20, 67], showing that this method is not yet applicable for HIV. In the case of HCV administration of anti-E2, an antibody against a viral envelope protein, successfully blocked cell-free transmission [16, 71, 72]. Interpretation of the obtained results was difficult, as only differences between transmission modes were considered, neglecting possible synergistic effects [70]. To my knowledge, no experimental approach has been developed, which can block each transmission mode separately for a particular pathogen in the same experimental set-up. However, developing such a technique would still not provide the opportunity of disentangling the contribution of the respective transmission modes to the infection dynamics experimentally as the simultaneous occurrence cannot be described as the sum of both transmission modes individually due to synergistic effects.

Altogether, it is important to use an adequate system when studying a particular virus, also having in mind the goals of the experiment as well as experimental limitations and implications of the utilized environment on viral spread. When trying to quantify the efficacy of transmission modes, experimental techniques are still limited with respect to interpreting the obtained results. Here, mathematical modeling helps to fill this gap and disentangle the contribution of each transmission mode to the overall dynamics.

1.2 Mathematical modeling of viral infections

Experimental techniques often suffer several limitations when addressing certain aspects of viral kinetics, for example, to infer particular steps in the viral life cycle or to disentangle the contribution of each transmission mode to the infection. Here, mathematical modeling has been an important tool when studying viral infections. Several approaches, stretching over multiple scales and including various steps in the infection dynamics, have been developed to complement experimental procedures, providing valuable insights into processes that cannot be measured directly. The following overview partly addresses aspects introduced in [73]. Further reading on this topic can be found in [74–76].

1.2.1 Standard model of viral dynamics

A general model, often used to describe viral dynamics, is an adaptation of a model developed by Kermack and McKendrick in the field of epidemiology, namely the susceptible-infected-recovered (SIR) model [77–79]. The model is comprised of a set of ordinary differential

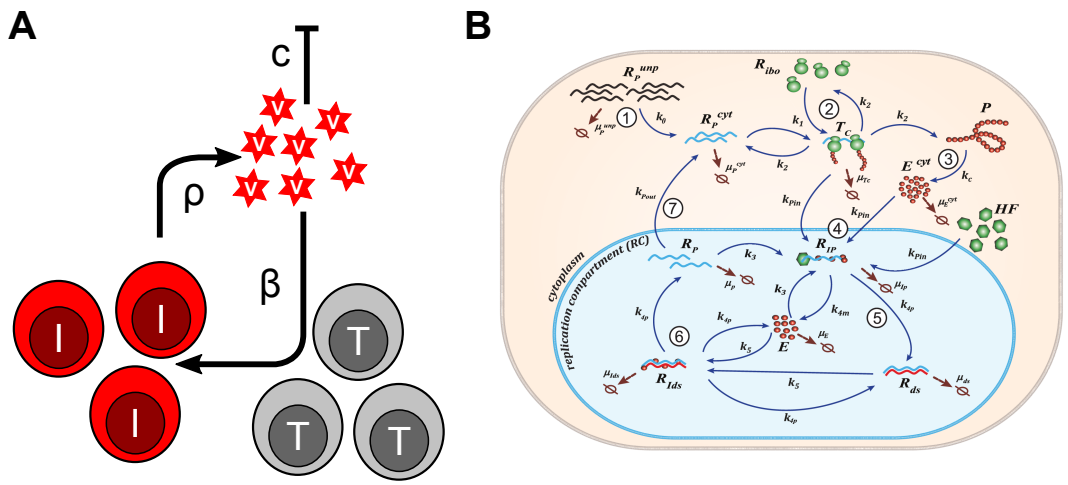

Fig. 1.3. **Increasing complexity of developed models to determine virus dynamics.** **(A)** Sketch of the standard model of virus dynamics. Virus production and export are merged into a single process occurring at rate ρ proportional to the density of infected cells. Intracellular processes are not modeled explicitly. **(B)** Sketch of a detailed model of the viral life-cycle of HCV in Huh7 cells, which follows a total of eleven variables, ranging from processes in the cytoplasm to the formation of replication complexes and synthesis of new viral RNA (adapted from [82], `https://doi.org/10.1371/journal.ppat.1003561`).

equations (ODE). It was first applied to viral spread of HIV *in vivo* [80] and is now known as the standard model of viral dynamics (SMV) (Fig. 1.3A) [81]:

$$\begin{aligned} \frac{dT}{dt} &= \lambda - dT - \beta VT \\ \frac{dI}{dt} &= \beta VT - \delta I \\ \frac{dV}{dt} &= \rho I - cV \end{aligned} \tag{1.1}$$

Here, virus concentration, V, densities of susceptible target, T, and infected cells, I, are followed. Target cells have an average lifetime of $1/d$ and constantly enter the system with influx rate λ. Cell-free virions infect target cells proportional to the viral concentration and target cell density with rate β and are produced by infected cells at constant rate ρ. Lastly, infected cells have a half-life of $\log(2)/\delta$ and virus is cleared with rate c.

This model merged several processes into individual constant rates, e.g., intracellular transport, transcription, assembly of the virus and subsequent export were combined in the viral production rate ρ. Still, these approximations provided first estimations of the viral life cycle at that time not accessible through experimental procedures [83].

1.2.2 Viral dynamics modeling with clinical data

Various simple modifications and extensions of this model have been published to account for additional processes, such as intracellular delays [84, 85], multiple infections of target cells [86] and viral mutations [87–89], increasing our knowledge of several viruses such as HIV and HCV. For instance, using viral load data from infected patients during therapy, Perelson *et al.* [90] and Wei *et al.* [91] were able to show that HIV-1 replicates rapidly during chronic infection, contradicting the former hypothesis of a slow viral turnover. A similar result was

obtained for HCV [92]. Additionally, with these models identification of drug regimes under which resistant mutants can arise [85, 87, 93] and appropriate targets for drug treatment [85] were possible. Moreover, mathematical models could also propose the mode of action of drugs in use and their efficacy [94].

1.2.3 Modeling of viral replication using *in vitro* data

Around the same time as Perelson *et al.* [90] and Wei *et al.* [91], other researchers used *in vitro* data to get a deeper understanding of the intracellular processes governing viral infections by developing in-depth models [95, 96]. Although the infection kinetics were described well, they struggled with the limited amount of data and the complexity of their models, and accordingly the confidence into their estimated rates was limited. With the development of an HCV replicon system *in vitro* [41], the study of HCV replication progressed considerably. Dahari *et al.* developed a first model of intracellular replication accounting for the subgenomic processes involved [97]. Building on their model, Binder *et al.* extended it to additionally capture early kinetics after infecting Huh-7 cells through electroporation (Fig. 1.3) [82]. Using their model, they could show that replication compartments act as a protection to ensure sustained RNA replication. Furthermore, applying a sensitivity analysis they learned that the system can be disturbed best shortly after infection. In addition, they determined key steps in the viral life cycle such as polyprotein translation and RNA polymerization rate of NS5B, which should help to clear the virus when targeted by drugs [82]. In fact, this finding nicely agreed with the proposed targets of newly developed direct acting antiviral drugs against HCV, which were found to be highly effective with sustained viral responses of over 90% [31].

1.2.4 Infection dynamics in spatially heterogeneous environments

Models incorporating the viral life cycle and the turnover of infected cells gave already valuable quantitative insights into viral dynamics [81]. However, the whole infection process in these models was built on the assumption of cell-free transmission. For viruses able to exploit both transmission routes, this meant that cell-to-cell spread had been neglected. As each mode of transmission differs in the proposed infection patterns, which in turn have an effect on the overall infection kinetics, results might have been biased.

With this in mind, Zhang *et al.* [98] developed a variation of the standard model of virus dynamics to additionally account for cell-to-cell spread including a simple mass-action kinetics term $\beta_c IT$, i.e., cells could get infected through cell-to-cell transmission with rate β_c proportional to the available density of target and infected cells. Based on this approach, Komarova *et al.* [99] and Iwami *et al.* [70] developed a model to predict the proportion of Jurkat cells, an immortalized human T cell line, infected through cell-free transmission in an experiment, where they followed the experimental protocol as introduced in [20]. To get more information on the individual modes of transmission, Iwami *et al.* investigated two scenarios [70]. While they allowed the simultaneous occurrence of both transmission modes in some cultures, cell-to-cell spread was blocked in others through constant shaking of the well-plate, preventing the formation of cellular bonds necessary for successful cell-to-cell infection. Simultaneously fitting a model with both transmission modes or only cell-free transmission to the static and shaking culture, respectively, they concluded that cell-free transmission accounted

for approximately 40% of infections in this experimental setup. This gave a first estimate of the contribution of each transmission mode to the infection kinetics for HIV-1. However, various elements of their experimental procedure and modeling approach might have biased their results, making it difficult to generalize their findings. From an experimental point of view, they performed their experiments in a cancerous cell line in suspension as compared to infecting peripheral mononuclear cells in collagen. Additionally, their model lacked an eclipse phase accounting for the duration until cells become virus-producing cells and did not explicitly account for the experimental change of media after each measurement. As movement of Jurkat cells in a densely packed environment characteristic for aqueous media is not yet characterized, the validity of assuming a well-mixed system, i.e., considering a spatially homogeneous model, and its implications for their predictions will need further investigation.

To address some of the shortcomings on the modeling side, several other approaches have been developed. For example Kandathil *et al.* [100] and Graw *et al.* [101] used statistical processes describing focus formation to analyze liver biopsy samples of HCV-positive patients for spatial patterns of infected cells. They found that foci contained between 4 and 50 infected cells. This wide range convinced them that both transmission modes were exploited by HCV *in vivo*. A different approach was used to include the time since a cell was infected and to explicitly account for spatial effects. To this end, age-structured [84, 102, 103] and models including spatial derivatives [104], both partial differential equation models, were developed. However, applying these models to data is generally not feasible as they are difficult to fit due to their complexity while also being limited to deterministic processes, thus, not able to account for stochasticity. For example, a reaction diffusion equation model, which is described by a set of partial differential equations, cannot explain the formation of new foci through cell-free transmission in static cells at more or less random locations.

Deterministic mass-action kinetic models generally cannot capture stochastic processes such as extinction of an infection due to low numbers of infected cells. Thus, a completely different type of model was sought out to describe stochastic processes, which are often a key element in viral infections. In this process infectious disease modelers made use of cellular automata and cellular Potts models (CPM) [105, 106], rule-based and spatially explicit discrete computational models that can describe a large variety of phenomena, used in a wide range of fields. They are known to generate complex patterns despite their behavior being governed by few and simple rules [107]. A famous example is the glider in John Conway's game of life [108]. An extension of cellular automata is also known as agent-based models (ABM), where each cell is an individual agent following simple rules based on stochastic processes. Their rule-based structure makes description of various mechanisms including stochastic and spatial processes relatively easy compared to incorporating them into conventional mass-action kinetics models. An overview of the success agent-based models have provided in host-pathogen systems can be found in [109]. However, these models were generally used to analyze the dependence of specific parameters [110] and mechanisms [111] on the qualitative behavior of viral spread due to their high computational costs and large number of unknown parameters, which in addition were often difficult to interpret. Furthermore, the data obtained from experiments are often based on bulk measurements, which usually provide too little information to allow discrimination of the various processes

in an agent-based model. Therefore, despite their obvious advantages, these models were seldom used for data fitting.

Making complex stochastic models accessible to quantitatively use with experimental data has been a field of recent research. For example, approximate Bayesian computation allows likelihood-free fitting of complex models in computationally reasonable time [112]. Implementations of these algorithms such as pyABC [113] nowadays become more important to allow parameter estimation for agent-based models, thus, allowing prediction of processes, which are difficult to model with conventional mass-action kinetics models and cannot be measured directly.

1.3 Overview of the thesis

In this thesis I address the question how to quantify the impact of cell-to-cell transmission on viral spread. To this end, I use several modeling approaches, which allow me to quantify the infection dynamics of HIV and HCV *in vitro*. Furthermore, using estimated parameters I predict the contribution of the individual transmission modes to the progression of infection for the studied viruses in different experimental environments. Lastly, I analyze the effect of modeling cell-to-cell transmission in stationary cells with the standard model of virus dynamics and extend this model to correctly describe infection dynamics. A graphical overview of the different topics treated in this thesis is shown in Fig. 1.4.

This thesis is structured as follows.

2. Material and Methods. Here, I explain the experimental procedures followed by my collaborators to collect data. These data are used to parameterize my models and to answer the raised question of the contribution of the different transmission modes to viral spread. Furthermore, I introduce some mathematical basics, which are needed in the subsequent chapters.

3. Different environments shape the contribution of cell-to-cell transmission to HIV spread *in vitro*. In this chapter I analyze the implications of experiments studying HIV spread conducted in aqueous media, where abnormal high cell densities are often observed. With the help of an extensive data set based on bulk measurements comprised of experiments conducted in aqueous media as well as two types of collagen matrices, I build a model able to describe the dynamics in the different environments as observed in the data. This model allows me to predict the proportion of cells infected by each mode of transmission dependent on the experimental condition.

4. Dissecting the contribution of cell-to-cell transmission to HCV spread in stationary cells *in vitro*. After treating motile target cells, which are inherent to HIV in different environments, I investigate stationary target cells, where spatial limitations of cell-to-cell transmission might violate the assumption of homogeneous distributions, in the context of viral infections. To this end, spatially-resolved data collected by my collaborators allow me to develop an agent-based model, which describes the infection of hepatocytes in a monolayer with HCV. To parameterize the model correctly, I use data that characterize intracellular replication of HCV in Huh7 cells

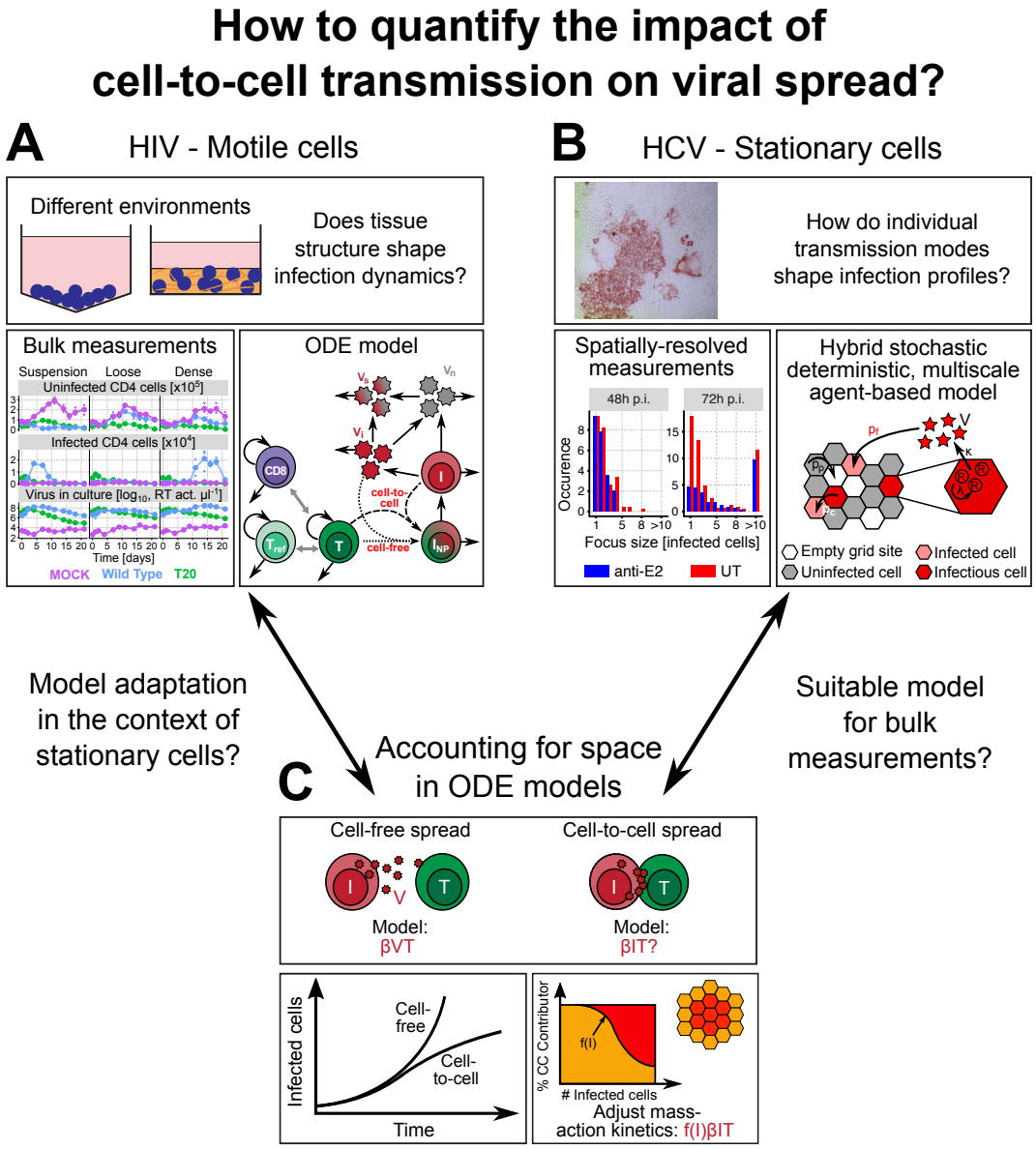

Fig. 1.4. **Graphical overview of the thesis.** **(A)** In Chapter 3 I analyze the spread of HIV in motile T cells cultured in different environments based on bulk measurements . **(B)** In Chapter 4 I use spatially-resolved data to investigate the contribution of cell-to-cell transmission during the progression of HCV infection in stationary hepatocytes. **(C)** In Chapter 5 I show that the standard model of virus dynamics falls short in the context of cell-to-cell transmission, when the assumption of a well-mixed system is breached, and introduce an extension, which allows to describe the infection dynamics correctly.

and export of infective virions and the focus size distribution of infected cells in experiments where cell-to-cell transmission is either blocked or not. The model is then able to predict the proportion of cells infected by either transmission mode and the synergistic effect by the combination of cell-to-cell and cell-free transmission.

5. Accounting for Space - How to Improve Quantification of Cell-to-Cell Transmission Using Virus Dynamics Models. In contrast to the previous chapters, where either infection dynamics in motile cells are studied or spatially-resolved data are available, experiments are often performed with slow moving or immobile cells while only retrieving bulk measurements. As pointed out previously, cell-to-cell transmission is a local process, showing spatial patterns in the absence of motile cells. In general, spatially structured processes should be described with appropriate models such as agent-based models. However, bulk measurements generally do not provide sufficient information to fit an agent-based model with its large amount of parameters. Additionally, fitting complex models is usually time-inefficient and computationally-expensive. Hence, spatially homogeneous virus-dynamics models using simple mass-action kinetics are often used. To address this issue, when studying stationary target cells, without loss of the simple ODE structure of the standard model of virus dynamics, I develop an extension that accounts for the decrease of cells contributing to cell-to-cell transmission with progression of infection. Finally, I test this model on previously published data [70].

In summary, I introduce different modeling approaches to describe the infection dynamics of HCV and HIV *in vitro*. These approaches subsequently allow prediction of the proportion of cells infected by either transmission mode for the respective virus and environment. Considering the provided data and motility of target cells, these approaches can be generalized to various viruses, thus, allowing disentanglement of the contribution of each transmission mode to the infection dynamics. Subsequently, enabling the identification of potential targets, these findings can be used for more efficient strategies in drug and vaccine development.

Part II

Materials and Methods

2 Materials and Methods

2.1 Experimental protocols

In this part, I explain the experimental protocols as followed by my collaborators from the University Hospital Heidelberg and Loyola University Medical Center to collect data that were analyzed in this thesis.

2.1.1 *In vitro* spread assays of HIV-1 in different environments

Experiments on HIV-1 were performed by the Fackler lab, Center for Integrative Infectious Disease Research (CIID), Integrative Virology, University Hospital Heidelberg. A rough sketch of the experimental procedure followed to analyze HIV infection kinetics in different environments is shown in Fig. 2.1. Details of the applied procedures were published in [69].

To produce a stock of replication-competent HIV-1, it was harvested from a cell line derived from human embryonic kidney cells (HEK 293) two to three days after transient transfection, filtered and concentrated via ultracentrifugation through a sucrose cushion. Experiments were conducted in HIV-non-specific human peripheral blood mononuclear cells (PBMC), which were obtained from healthy individuals, thus, resulting in HIV-non-specific CD8 cells not partaking in the infection process. PBMCs were stimulated for 72 hours with phytohemagglutinin (PHA) and surface-immobilized anti-CD3 monoclonal antibody in Roswell Park Memorial Institute medium (RPMI 1640) supplemented with FCS, penicillin/streptomycin (PenStrep) and interleukin-2 (IL-2). This procedure yielded PBMCs containing around 95% CD3-positive T lymphocytes with approximately 80% CD4-positive and 20% CD8-positive T cells. Afterwards activated cells were subjected to spin-infection with HIV-1 in high IL-2 medium and then cultured for 72 hours in media with IL-2. To prepare dense and loose collagen gels for the experiments concentrated rat tail and bovine collagen I, respectively, were mixed with bicarbonate-buffered minimal essential medium. Buffered collagen was then combined with uninfected and spin-infected cells in 96 well-plates, such that approximately 1% to 1.7% infected cells were present at the start of the experiment in each well, and allowed to polymerize within half an hour. Cells were added to collagen at a density of 10^5 cells/$100\ \mu l$ gel. Finally, polymerized gels were overlain with media, consisting of RPMI 1640, FCS, PenStrep and IL-2. For the aqueous media environment (suspension) the same number of uninfected and spin-infected cells as in the collagen were combined with media containing RPMI 1640, FCS, PenStrep and IL-2. To ensure comparability, all cultures were treated with collagenase I on the day of harvest, resulting in cell suspensions, which allowed analysis of infection kinetics. Cells were then washed and stained with anti-CD8-PE Vio770 and anti-CD3-PE to detect CD8 and CD4 T cells, where the latter were identified as CD3 positive/CD8 negative cells. To detect intracellular p24, cells were permeabilized and stained with anti-p24-FITC. As my modeling

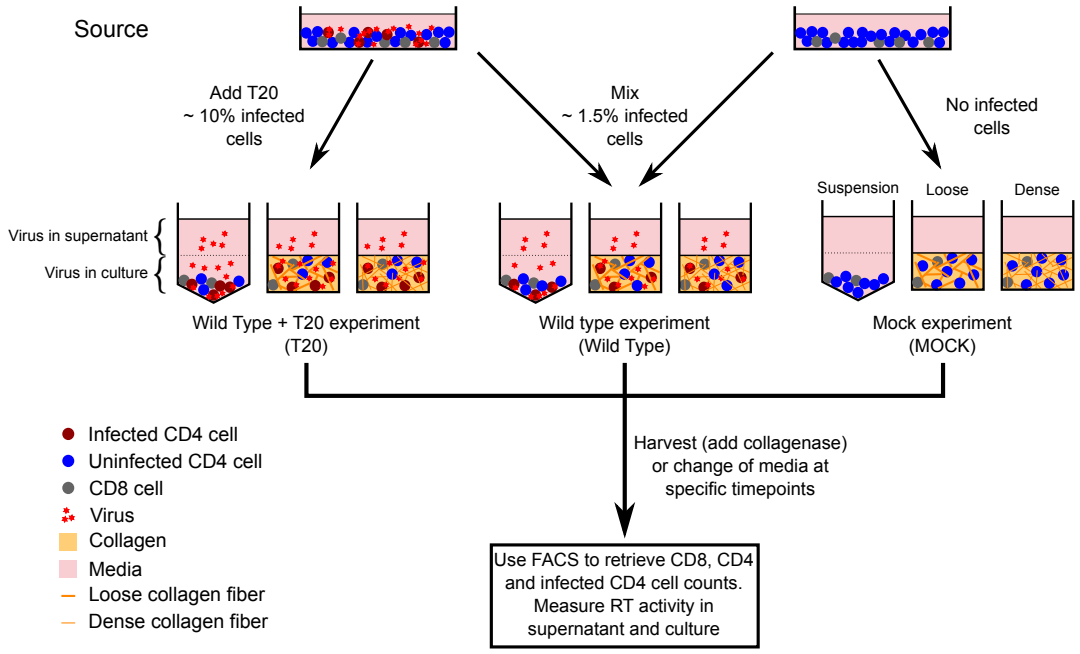

Fig. 2.1. **Sketch of experimental protocol for HIV-1 spread assays.** Cells were drawn from a batch of T cells without infection (mock), a batch containing cells, which underwent spin-infection 72 hours before the start of the experiment (T20x2) or a mixture of the two (wt) and transferred into media containing well-plates (suspension) additionally mixed with bovine collagen I (loose) or rat tail collagen I (dense). At several time points, virus titer from the supernatant was collected from the different environments. After removal of the supernatant, collagenase was added and the virus titer in culture was measured. Furthermore, counts of CD8, CD4 and infected CD4 cells from the resulting cell suspensions were measured. For the remaining wells, i.e., wells that were not harvested, the supernatant was removed and new media was added. Experiments were performed by the Fackler lab, Center for Integrative Infectious Disease Research (CIID), Integrative Virology, University Hospital Heidelberg.

approaches depended on absolute rather than relative counts, counting beads were added prior to the analysis with a FACSVerse and FlowJo software.

Additionally, different experimental conditions including control cell cultures without infection (MOCK) and cultures with high percentages of 8% to 10% infected cells supplemented with fusion inhibitor T20 (T20), which is known to block HIV-1 infections, were followed.

Furthermore, a one step PCR-enhanced reverse transcriptase assay (SG-PERT) was performed to measure viral concentrations in terms of reverse transcriptase activity as described in [114, 115]. Here, virus samples were lysed, RT-PCR reactions were performed and finally read out using a Real-Time PCR detector. To obtain absolute values of RT activity, a standard curve of replication-competent HIV-1 containing supernatant with known RT activity level was run in parallel during quantification of the different experimental samples [115]. Absolute RT activity levels were extrapolated from the Cq values of the standard curve.

2.1.2 *In vitro* experiments on HCV infection in Huh7 cells

Experiments on HCV were performed by the lab of Susan Uprichard, Department of Microbiology and Immunology, Loyola University Medical Center, Maywood, Illinois, USA.

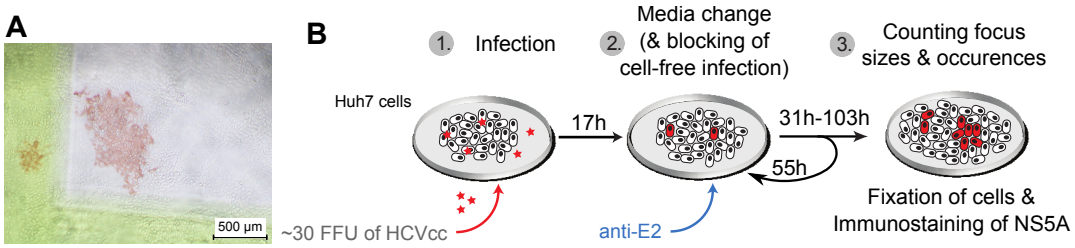

Fig. 2.2. **Photograph and sketch of experimental protocol for HCV spread assays. (A)** Representative photograph of a well-section showing foci of HCV-infected hepatocytes in red and uninfected hepatocytes in transparent. Green lines were drawn for orientation. **(B)** Experimental protocol sketch of the spread assays (Adapted from [117]). After Huh7 cells were plated and grown to a confluent monolayer, they were co-cultured with approximately 30 FFU/well hepatitis C virus for 17 hours. Then, the inoculum was removed, media was changed and in case cell-free transmission was blocked, anti-E2 was additionally administered. The same procedure was repeated 72 hours post infection. At several time points the cells were fixed, stained for NS5A or anti-E2 and the sizes of occurring foci were manually counted. Experiments were performed by the lab of Susan Uprichard, Department of Microbiology and Immunology, Loyola University Medical Center, Maywood, Illinois, USA.

Spread assays

Details of the procedure were published in [116]. Huh7 cells were plated at high densities, resulting in approximately 2.4×10^4 (Exp. 29D) and 1×10^4 (Exp. 29J) cells at time of infection, in $100\ \mu l/well$ with complete Dulbecco's modified Eagle's medium (cDMEM) including fetal bovine serum (FBS) on a 96-well plate and incubated until confluence was reached. To initiate infection genotype 2a cell culture-propagated hepatitis C virus from a Japanese Fulminant Hepatitis patient (JFH-1 HCVcc, referred to as HCV in the following) was diluted to approximately 35 (Exp. 29D) or 25 (Exp. 29J) focus forming units (FFU) per well and added to each cell culture, which were incubated together for 17 hours. Afterwards viral inoculum was removed and cells were rinsed with phosphate-buffered saline (PBS). Media containing cDMEM and dimethyl sulfoxide (DMSO) was added to the culture. When blocking cell-free spread, $10\ \mu g/ml$ HCV E2 antibody MAb AR3A (anti-E2) was added to the media. Cells were incubated and different wells were fixed at 48, 72, 96 and 120 hours post infection. To visualize infected cells several steps were necessary. In a first step, cells were fixed by adding paraformaldehyde (PFA), incubated 20 min at room temperature (RT), rinsed with PBS and permeabilized with a cold methanol-acetone solution for 10 min at RT. Next, cells were incubated with cold PBS containing hydrogen peroxide for 5 min to block endogenous peroxidases, decanted and rinsed with PBS. Following this, a blocking solution was administered for 1 h with PBS containing Triton X-100, bovine serum albumin (BSA) and FBS to reduce nonspecific binding of antibodies. The blocking solution was aspirated off and immediately mouse polyclonal serum anti-HCV NS5A 9E10 (Exp. 29D) or AR3A anti-E2 (Exp. 29J) was added. In a next step, antibodies were decanted and cells rinsed with PBS. Then cells were incubated with a 1:500 dilution of horseradish peroxidase conjugated anti-mouse. Cells were rinsed and incubated with aminoethyl carbazole detection substrate for 10 min at RT and washed with dH_2O, add dH_2O:glycerol (1:1) solution for storage. Lastly, foci were photographed using an appropriate microscope and cells per focus counted. A schematic overview of the procedure is shown in Fig. 2.2.

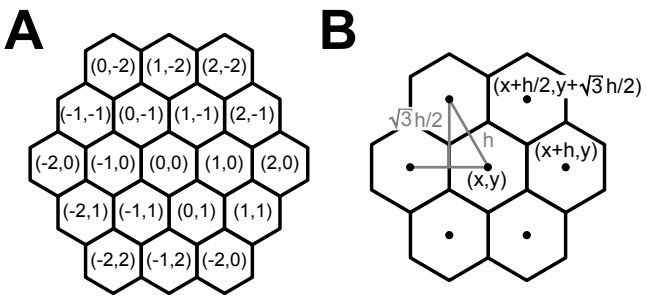

Fig. 2.3. **Sketch of hexagonal grid for simulating viral spread. (A)** Axial hexagonal coordinates as used in the agent-based model of Chapter 4. **(B)** Coordinates and length units necessary to calculate the 7-point finite difference approximation of the Laplacian.

Intracellular replication

Huh-7 cells were plated on a 96-well plate, with 4000 cells per well and infected with serum-free cell-culture propagated HCV at a multiplicity of infection (MOI) of six in $50\ \mu l$ serum-free cDMEM. Three hours post infection, virus was removed from all wells and after rinsing with cDMEM containing FBS, the wells were supplemented with $200\mu l$ cDMEM containing FBS. At various later time points between 3 and 96 hours post infection supernatant and cell lysates were harvested from three wells at each time point to quantify intra- and extracellular RNA. Quantification was achieved by processing RNA, applying reverse transcriptase and, in a last step, using quantitative polymerase chain reaction in relation to a serially diluted standard JFH-1 plasmid curve and normalized to GAPDH. To retrieve cell numbers, parallel plates were counted at 0, 36, 72 and 96 hours p.i. The percentage of infected cells was measured in duplicates by fixing cells at 21, 30 and 72 hours. Extracellular RNA was measured in duplicates.

2.2 Mathematical Methods

The mathematical basics used in this thesis to achieve the presented results are introduced in this part.

2.2.1 Hexagonal grid structure for simulating viral spread

The underlying hexagonal grid of the agent-based model describing the spread of hepatitis C virus in a monolayer of hepatocytes was implemented following the description in [118]. In the model, agents, i.e., hepatocytes, were distributed on a hexagonal grid with axial coordinates describing the location (Fig. 2.3A). Neighbors were calculated assuming that a cell with coordinates (i^*, j^*) is neighboring cell (i, j), if $i^* \in \{i-1, i, i+1\}$, $j^* \in \{j-1, j, j+1\}$ and $i^* \neq j^*$.

Stencil method for discretization

Assume the distance between neighboring nodes is h (Fig. 2.3B). Using a Taylor series expansion of a function $u : \mathbb{R}^2 \to \mathbb{R}$ for nodes $(x \pm h, y)$ around (x, y), gives

$$u(x \pm h, y) = u(x, y) \pm h\partial_x u(x, y) + \frac{h^2}{2}\partial_{xx} u(x, y) + \mathcal{O}(h^3) \tag{2.1}$$

Similarly, for nodes $(x \pm h/2, y \pm \sqrt{3}h/2)$ the Taylor series is as follows

$$\begin{aligned} u(x \pm \frac{h}{2}, y \pm \frac{\sqrt{3}h}{2}) =& u(x, y) \pm \frac{h}{2}\partial_x u(x, y) \pm \frac{\sqrt{3}h}{2}\partial_y u(x, y) \\ &+ \frac{1}{2}\left(\frac{h^2}{4}\partial_{xx} u(x, y) + \frac{3h^2}{4}\partial_{yy} u(x, y)\right) + \mathcal{O}(h^3) \end{aligned} \tag{2.2}$$

Adding Eqs. (2.1) and (2.2) gives the 7-point finite difference approximation of the two-dimensional Laplacian [119, 120]:

$$\begin{aligned} \Delta u(x, y) = \frac{2}{3h^2}\,&(u(x-1, y) + u(x+1, y) + u(x, y-1) \\ &+ u(x, y+1) + u(x-1, y+1) + u(x+1, y-1) - 6u(x, y)) \end{aligned} \tag{2.3}$$

2.2.2 Parameter estimation

Maximum Likelihood Estimator

In this thesis, ODE models of Chapter 3 and Chapter 5 were fitted using the optimizing function `optim` in the statistical language `R` [121], which, in my case, minimized the negative log-likelihood function [122]

$$\begin{aligned} l(\theta) :=& \frac{1}{2}\sum_{t=t_0}^{t_m}\left(\frac{\bar{x}(t) - f(\theta, t)}{\sigma}\right)^2 + \frac{n}{2}\ln\sigma^2 \\ \text{with } \sigma :=& \frac{\sigma_t^2}{n} + \sigma_{\text{me}}^2 \text{ and } \bar{x}(t) := \frac{1}{n}\sum_{j=1}^{n} x_j(t). \end{aligned} \tag{2.4}$$

This results in the maximum likelihood estimator (MLE). Here, n is the number of independent experiments, t the measured time points, and $x_j(t)$ the concentration or density of the different measured variables at time t from experiment j. The empirical variation within the data is denoted with σ_t and $f(\theta, t)$ the corresponding model prediction, where θ is defined as the set of fitted parameters. Furthermore, a measurement error, σ_{me}, was estimated, which was assumed to be either constant (homoscedastic) or relative (heteroscedastic). A homoscedastic error was assumed in Chapter 5 for fits solely to the infected cells and a heteroscedastic error in Chapters 3 and 5 when fitting to infected cells and extracellular virus. For all *in vitro* data, empirical variation was neglected due to low sample sizes, i.e., $\sigma_t = 0$, and only the measurement error was estimated. This log-likelihood function assumed normally distributed errors within the data.

Profile Likelihood

To construct pointwise 95%-confidence intervals for the parameters, a profile likelihood approach was adopted [123]. The confidence intervals were calculated using likelihood-based confidence intervals (CI) [124]

$$\{\theta | l(\theta) - l(\hat{\theta}) < \Delta_{0.05}\} \text{ with } \Delta_{0.05} = \chi^2(0.05, 1), \tag{2.5}$$

where $l(\hat{\theta})$ is twice the negative log-likelihood of the best fitting parameter set $\hat{\theta}$ and $\chi^2(0.05, 1)$ is the χ^2-distribution with one degree of freedom to a significance level of 0.05. Hence, all parameter sets θ differing less than $\chi^2(0.05, 1)$ from $l(\hat{\theta})$ are within the 95%-confidence interval.

Akaike Information Criterion

Comparison of the performance of models can be achieved with the Akaike Information Criterion (AICc), which compares models by their likelihoods as well as the number of fitted parameters within those models. To account for small sample sizes, I evaluated performances with the corrected Akaike Information Criterion [125]

$$\text{AICc} = l(\theta) + 2K + \frac{2K(K+1)}{n - K - 1} \tag{2.6}$$

Here, $l(\theta)$ is the likelihood as defined above, K the number of fitted parameters and n the sample size. Hence, inclusion of more parameters leads to higher AICc-values assuming constant likelihoods. The AICc is typically used for comparison of a set of models, $\mathcal{M}$, where the absolute AICc-value of model $m \in \mathcal{M}$ is not of importance, but the absolute difference to the best performing model [125]

$$\Delta_{\text{AICc}}(m) = \text{AICc}(m) - \min_{m \in \mathcal{M}} \{\text{AICc(m)}\}. \tag{2.7}$$

Distributed, likelihood-free inference method to fit a complex stochastic model

I used an approximate Bayesian computation approach based on sequential Monte Carlo (ABC SMC) [112] to fit the agent-based model from Chapter 4 to experimental data such as focus size distributions at different time points. This likelihood-free method is implemented in pyABC [113], which uses dynamic scheduling as a parallelization strategy to minimize runtime. The algorithm subsequently follows these steps to find the best fitting parameter set:

1. Sample parameters from predefined prior distribution
2. Run simulation with sampled parameters
3. Calculate distance between simulation output and experimental data using a predefined distance measure
4. If lower than ϵ, accept parameter set
5. If 100 parameter sets are accepted, calculate new distribution of parameters and repeat steps 1-5 with $\epsilon := median(\epsilon)$ of accepted parameter sets and the calculated distribution

Part III

Results

3 Different environments shape the contribution of cell-to-cell transmission to HIV spread *in vitro*

3.1 Introduction

Human immunodeficiency virus infects mainly motile cells of the immune system, thus, allowing it to spread through the body without the need of movement on its own accord. How the environment shapes the motility of T cells and subsequently the infection dynamics of HIV-1 (termed HIV in the following) has not yet been studied in detail as most published studies limited their work to cells cultured in aqueous media. Culturing cells in aqueous media leads to 2D cell culture systems as cells sink to the bottom of wells, creating non-physiologically high cell densities [63]. An additional caveat of previously designed studies was the use of immortalized cell lines, which allowed for better reproducibility of experiments. However, this might have changed the infection dynamics compared to healthy target cells such as PBMCs due to changed viral replication, behavior and permissivity of target cells. Altogether, this might have biased obtained results and impedes transfer of these studies to within-host dynamics because different tissue architectures and cell types presumably shape the infection kinetics. To address these points, an experiment was conducted following infection of human peripheral blood mononuclear cells (PBMC) with HIV in different environments, namely aqueous media, loose and dense collagen, resembling different tissue structures in the body. Comparing parameters, which were obtained from fitting the data collected from this experiment, across environments could give insights into differences regarding the infection kinetics in a particular tissue structure, resulting in a deeper understanding of the virus. From a clinical point of view investigating varying infection strategies with regard to the transmission mode exploited by the virus can be helpful for efficient drug screenings.

In this chapter ordinary differential equation (ODE) models are used to parameterize viral replication and spread following a stepwise approach. In a first step I quantify cell proliferation and turnover using a data set without infection (MOCK). Next, with the parameters of cellular turnover in hand, I parameterize viral kinetics by fitting a model following the decline of infected cells and viral kinetics to a data set obtained from culturing infected cells in different environments with fusion inhibitor T20, which blocks new infections. Lastly, I incorporate the previously estimated parameters in a model describing the full infection kinetics in all environments simultaneously. With this model, I predict the contribution of each transmission mode to the infection process and the time course of cell-free and cell-to-cell transmission separately. Additionally, I study the effect of different target cell densities on the infection dynamics. In a last part of this chapter, I identify important processes necessary to describe the data and compare my modeling results to a previously published model [70].

In summary, in this chapter I develop a model able to describe the infection kinetics in various environments. This analysis shows that cell-to-cell transmission is more important in collagen environments than suspension, supporting the necessity of carefully choosing experimental conditions. In addition, low target cell densities limit the infection in loose collagen. However, this limitation could be overcome with high contact frequencies between infected and uninfected cells.

3.2 Experimental data of HIV infection and T cell dynamics

All experiments in this chapter were performed by the Fackler lab, Center for Integrative Infectious Disease Research (CIID), Integrative Virology, University Hospital Heidelberg. The experimental protocol is explained in Section 2.1.1.

The data set is comprised of several quantities, measured in aqueous media (suspension), loose and dense collagen (Fig. 3.1). While three different cell types were measured, namely CD8+ and CD4+ T cells, with the latter being divided into uninfected and infected subpopulations, viral RT activity was measured in the culture and the supernatant. In suspension this implied measuring viral RT activity in the lower and upper half of the supernatant. To parameterize T cell dynamics, experiments were performed only with uninfected PBMCs (MOCK). Co-culturing uninfected and infected cells supplemented with fusion inhibitor T20 (termed T20 from here on) allowed parameterization of infected cell turnover and viral kinetics. Lastly, to characterize the infection dynamics, uninfected and infected cells were co-cultured without administration of T20 (Wild Type). To get stable measurements of the decline of infected cells in the T20 scenario, higher amounts of initially infected cells were used (Fig. 2.1).

Recovery of T cells in collagen compared to suspension was diminished to about 55 percent of original cells, presumably due to cells sticking to the collagen (personal communication Dr. Andrea Imle). However, as all cells were initially drawn from the same batch, the initial T cell counts should have been similar irrespective the environment. To compensate for this experimental bias, I multiplied all cell counts in collagen environments with a factor of 1.8 to obtain approximately the same T cell counts at start of the experiment assuming full recovery of cells in suspension.

In the early phase, i.e., within the first two days, of the experiment a decrease across all T cell subpopulations was observed in the data. This effect was least prominent in suspension. Transfer of cells into new environments might have been the cause as the increase of cells was lower at early (0-2 days) than intermediate (4-11 days) time points in the experiment. Additionally, at the beginning of the experiment cells decreased more in collagen than suspension, which could be linked to cells sensing less growth factors form surrounding cells in low cell densities as inherent to collagen environments (see Section 1.1.4). Nonetheless, T cell capacities of each well were approximately the same across all environments (comparison of combined CD8 and CD4 cells in MOCK between environments, Fig. 3.1). After reaching the highest T cell concentrations around 11 days after start of the experiment, T cell numbers showed oscillatory behavior. This observation was presumably a combination of measurement

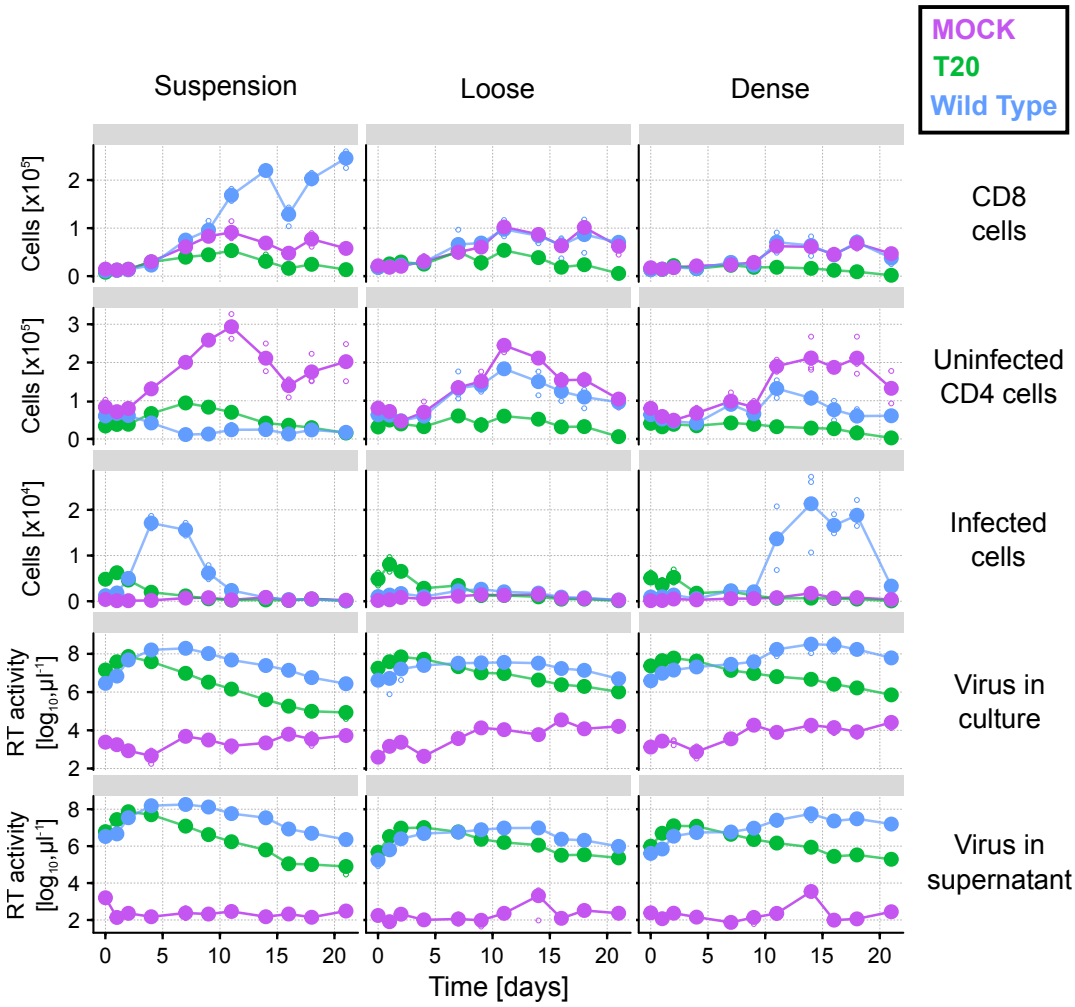

Fig. 3.1. **Experimental data used to evaluate HIV infection dynamics.** Shown are the mean values (large solid dots) of three independent experiments per scenario (small open dots) of CD8 (1^{st} row), uninfected (2^{nd} row) and infected CD4 cell counts (3^{rd} row), virus in culture (4^{th} row) and in supernatant (5^{th} row) in suspension (left column), loose (middle column), and dense collagen (right column). Experiments were conducted with no infection (MOCK, purple), administration of T20 at the beginning of the experiment to block new infections (T20, green) or infection without T20 (Wild Type, blue). To compensate for diminished recovery of T cells in collagen, all cell counts in collagen environments were multiplied with a factor of 1.8. Experiments were conducted by the Fackler lab, Center for Integrative Infectious Disease Research (CIID), Integrative Virology, University Hospital Heidelberg

errors and loss of cell viability in the course of the experiment. Thus, these oscillations seemed rather an experimental artifact than biologically meaningful.

Apparently, infection progressed faster in suspension than in collagen, with loose collagen showing almost no infected cells (Fig. 3.1). The fast infection process in suspension lead to a depletion of target cells, resulting in low residual numbers of uninfected CD4 cells. The depletion of CD4 cells in turn lead to a prolonged proliferation of CD8 cells, which overgrew CD4 cells substantially in this environment. A slower infection as observed in dense collagen allowed CD4 cells an extended proliferation period. Subsequently, depletion was not as pronounced in dense collagen even though the total number of infected cells over the complete course of the experiment was higher compared to suspension. Comparison of RT activity in collagen showed lower amounts in the supernatant than in culture, presumably due to slow viral diffusion from culture to supernatant [69]. This difference was not observed in suspension, also hinting towards viral diffusion being the key factor for the variation between viral concentrations in supernatant and culture.

In case of T20 administration infected cells increased (suspension and loose collagen) or stayed stable (dense collagen) at the first measured time points. As T20 was supposed to block new infections, there seemed to be a time lag between the infection event and detection of infected cells with FACS. Although total T cell counts in this scenario were surprisingly low, this feature of the data did not skew my results as T cell turnover was of no importance. After 9 days infected cells dropped to background levels as indicated by measurements obtained from the MOCK experiment.

3.3 A stepwise approach to parameterize HIV infection in different environments

Several processes governed the infection dynamics in this experiment. Those ranged from T cell turnover of the various subsets, over virus kinetics in culture and supernatant to infection dynamics including change of media. Describing these processes with a biologically reasonable model in all environments simultaneously required a large number of parameters (more than 20). To reduce the number of free parameters, I applied a stepwise approach with the help of additional experimental data obtained by my collaborators. First, parameters governing T cell dynamics were fixed by fitting a model describing T cell dynamics to the MOCK data. Subsequently, I fitted a model describing viral dynamics to experimental data retrieved by administering T20 after spin infection of CD4 cells with HIV. Finally, the previously estimated parameters were included in a model describing the full infection dynamics across all environments simultaneously. If not mentioned otherwise, I took the initial conditions for all variables from the experimental measurements. For all fitting procedures, I fitted the models to the mean of three independent experiments, while neglecting the experimental standard deviation due to the low sample size. To account for measurement and experimental errors, I fitted a relative, i.e., heteroscedastic, standard deviation error as described in Section 2.2.2 for cells and virus, respectively. In the following, data used for fitting are indicated with solid black dots and neglected/not used data with solid gray dots.

3.3.1 Formulation of a T cell dynamics model

To describe T cell dynamics in the different environments, I used a competition model without infection, in which CD8 and CD4 cells compete for resources and space during proliferation after a given time of adaptation has passed

$$\begin{aligned} \frac{dT_{\mathrm{CD8}}}{dt} &= \lambda_{\mathrm{CD8}} T_{\mathrm{CD8}} \left(1 - \frac{T_{\mathrm{CD8}} + T_{\mathrm{CD4}}}{T_c}\right) - \delta_{\mathrm{CD8}} T_{\mathrm{CD8}} \\ \frac{dT_{\mathrm{CD4}}}{dt} &= \lambda_{\mathrm{CD4}} T_{\mathrm{CD4}} \left(1 - \frac{T_{\mathrm{CD8}} + T_{\mathrm{CD4}}}{T_c}\right) - \delta_{\mathrm{CD4}} T_{\mathrm{CD4}} \end{aligned} \tag{3.1}$$

$$\text{with } T_{\mathrm{CD8}}(0) = T_{\mathrm{CD8},0},\ T_{\mathrm{CD4}}(0) = T_{\mathrm{CD4},0} \text{ and } \lambda_{\mathrm{CD8}} = \lambda_{\mathrm{CD4}} = 0 \ \text{ for } t < \tau \quad .$$

Here, T cells, namely CD8, T_{CD8}, and CD4 T cells, T_{CD4}, proliferate with different rates λ_{CD8} and λ_{CD4} after an adaptation phase τ, competing for resources such that a carrying capacity, T_c, is reached in the absence of virus and cell death. T cell subpopulations, i.e., CD8 and CD4 cells, die with rate δ_{CD8} and δ_{CD4}, respectively. For simplification and to ensure parameter identifiability, I assumed constant proliferation and death rates of T cells.

3.3.2 Parametrization of T cell dynamics in different environments

As already mentioned in the *Introduction*, cells in aqueous media settle on the bottom of wells leading to high cell densities (Fig. 1.2). Therefore, in this media space is a limiting resource restricting proliferation of T cells. In collagen low cell densities give rise to low concentrations of growth factors in the surroundings of cells. These points predict disadvantages in both types of environment in the context of proliferation, thus, obstructing *a priori* assumptions on T cell proliferation and death with respect to different environments. Therefore, I allowed proliferation and death rates as well as the carrying capacity to vary across environments, implying separate fits of model (3.1) to the data collected from the different environments. From the data it seemed that T cell counts decreased until day 2 and recovered afterwards. I fixed the adaptation phase to 2.5 days, because trying several adaptation phases considerably longer lead to high - biologically implausible - proliferation rates. While the initial decline of cell counts was captured by my model, it could not entirely explain the oscillations present in the experiment at late times (Fig. 3.2). I obtained the best fitting parameters and their respective 95%-confidence intervals (Fig. A.1 and Table 3.1) by performing a profile likelihood approach as described in Section 2.2.2.

While proliferation of CD8 cells occurred at a faster rate in suspension than in collagen ($\lambda_{\mathrm{CD8}} = 1.13\ [0.74, 1.74]$ vs. $0.58\ [0.24, 1.01]$ and $0.29\ [0.12, 0.56]$ day^{-1}), CD4 cells proliferated at similar rates as implied by overlapping confidence intervals ($\lambda_{\mathrm{CD4}} = 0.6\ [0.36, 1.02]$ vs. $0.78\ [0.36, 1.29]$ and $0.59\ [0.32, 0.89]$ day^{-1}). The capacity of total T cells per well were comparable between environments again exhibiting overlapping confidence intervals (see Table 3.1 and Fig. A.1). As the death rate during the adaptation phase was only a net rate, differentiation between proliferation and death rate was not possible. However, I found evidence that cells proliferated slower or died faster during adaptation phase in collagen compared to suspension. This was indicated by lower death rates for CD8 and CD4 cells in suspension, presumably due to cells being more adapted to this environment as cells were kept in aqueous media before transfer at the start of the experiment (see Fig. 2.1). However,

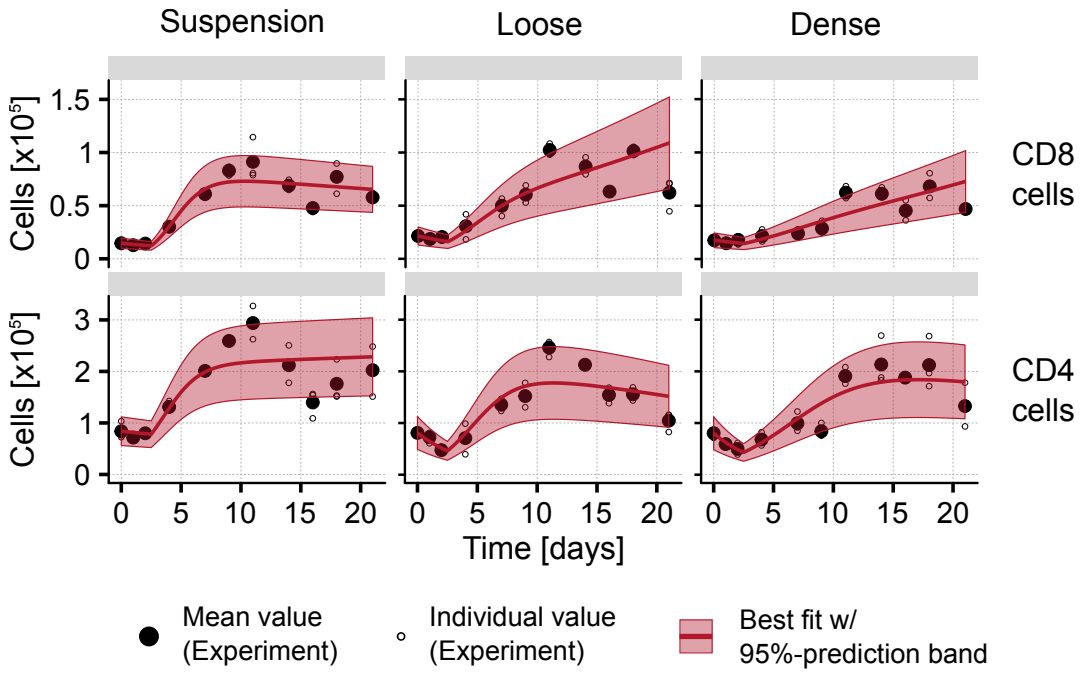

Fig. 3.2. **Estimation of T cell dynamics.** Shown are mean counts (solid black dots) from three independent experiments (open black dots) of proliferating CD8 (top row) and CD4 (bottom row) cells in suspension (left column), loose (middle column), and dense collagen (right column). Best fit of model (3.1) (thick red line) with estimated 95%-prediction band (shaded red area) describing MOCK data. Corresponding parameter estimates are shown in Table 3.1. Duration of the adaptation phase was fixed to 2.5 days.

Tab. 3.1. **Estimated parameter values governing T cell dynamics.** Best fitting parameters of the T cell dynamics model (3.1) in the absence of infection across different environments. The 95%-confidence intervals in brackets were obtained by performing a profile likelihood approach. To ensure parameter identifiability, the adaptation phase was fixed to 2.5 days. I conducted no profile likelihood approach for the fitted relative standard deviation. Thus, only the best estimate is given in this table. Graphical representation of the profiles is shown in Fig. A.1.

Parameter	Description	Unit	Suspension	Loose	Dense
λ_{CD8}	Proliferation of CD8 cells after adaptation phase	day^{-1}	1.13 [0.74, 1.74]	0.58 [0.24, 1.01]	0.29 [0.12, 0.56]
λ_{CD4}	Proliferation of CD4 cells after adaptation phase	day^{-1}	0.60 [0.36, 1.02]	0.78 [0.36, 1.29]	0.59 [0.32, 0.89]
T_c	Capacity of T cells	$\times 10^5$ cells $well^{-1}$	3.11 [2.72, 3.56]	3.53 [2.80, 4.52]	4.28 [3.15, 6.37]
δ_{CD8}	Net death rate of CD8 cells during adaptation phase	day^{-1}	0.07 (0, 0.19]	0.11 (0, 0.23]	0.08 (0, 0.19]
δ_{CD4}	Net death rate of CD4 cells during adaptation phase	day^{-1}	0.03 (0, 0.11]	0.23 [0.05, 0.39]	0.25 [0.09, 0.38]
σ_c	Relative standard deviation for cells	1	0.17	0.20	0.20

these differences were not significant as confidence intervals overlapped (see Fig. A.1 and Table 3.1). Comparing T cell subsets, one should note that in collagen CD4 cells proliferated faster than CD8 cells, in contrast to suspension, where the opposite was observed. The same held true for net death rates of cells during adaptation phase. If these differences between environments stemmed from variations in the data or were in fact governed by biological processes needs further investigation.

3.3.3 Formulation of a virus dynamics model

To describe infected cell turnover and viral kinetics a model following non-productively infected, J, and infectious cells, I, as well as virus in culture, V_c, and in the supernatant V_s was used to fit the T20 data

$$\begin{aligned}
\frac{dJ}{dt} =& -\kappa_I J - \delta_{\text{CD4}} J \\
\frac{dI}{dt} =& \kappa_I J - \delta_I I \\
\frac{dV_c}{dt} =& \rho I - c_v V_c - \kappa_v V_c \\
\frac{dV_s}{dt} =& \kappa_v V_c - c_v V_s \\
\text{with } J(0) =& J_0,\ I(0) = I_0,\ V_c(0) = V_{c,0},\ V_s(0) = V_{s,0}, \\
\text{and } V_c(t) =& \begin{cases} V_c(t) & \text{for } t \in t_m \text{ in collagen} \\ 0.5 \times V_c(t) & \text{for } t \in t_m \text{ in suspension} \end{cases} \\
V_s(t) =& \begin{cases} 0 & \text{for } t \in t_m \text{ in collagen} \\ 0.5 \times V_c(t) & \text{for } t \in t_m \text{ in suspension} \end{cases}.
\end{aligned} \tag{3.2}$$

Here, non-productively infected cells need on average $1/\kappa_I$ until they become infectious cells and die at the same rate δ_{CD4} as uninfected CD4 cells. Infectious cells have a half-life of $\log(2)/\delta_I$ and produce virus in culture with rate ρ. Virus irrespective its location is cleared from the media with c_v. Additionally, virus diffuses from culture to supernatant with rate κ_v. In contrast to previously published models, I accounted for the change of media at days $t_m \in \{2, 4, 7, 9, 11, 14, 16, 18\}$ by setting V_s in collagen at the specified time points to zero. In suspension after removal of the supernatant and subsequent addition of new media, mixing of the viral titer in the complete well occurred and, hence, the previous viral concentration in culture was equally distributed between culture and supernatant. Furthermore, as fusion inhibitor T20 blocked new infections I did not follow uninfected cells assuming that they had no impact on viral dynamics.

3.3.4 Parametrization of HIV virus kinetics in different environments

Using model (3.2) to describe data from an experiment without new infections (T20, Fig. 2.1), I fitted all environments simultaneously. Here, I assumed the same initial proportion of non-productively infected cells, f_J, with respect to the target cell count measured in the respective environments. This seemed like a reasonable assumption as cells before transfer into the different environments originated from the same batch (Fig. 2.1). Death rates for

Tab. 3.2. **Estimated parameter values governing infected cell turnover and viral kinetics.** Parameters best describing the T20 experiment. The 95%-confidence intervals in brackets were obtained by performing a profile likelihood approach. Average eclipse phase for non-productively infected cells, i.e., $1/\kappa_I$, was set to 17.3 hours and half-life of RT activity, c_v, was fixed to 38 hours. I conducted no profile likelihood approach for the relative standard deviations. Thus, only the best estimates are given in this table. Graphical representation of the profiles is shown in Fig. A.2.

Parameter	Description	Unit	Suspension	Loose	Dense
f_J	Initial fraction of non-productively infected cells in T20 experiment	1		0.17 [0.10, 0.23]	
ρ	Viral production rate	$\times 10^4$ RT act. $(\text{cell} \times \text{day})^{-1}$	1.02 [0.80, 1.38]	0.48 [0.37, 0.66]	0.43 [0.32, 0.61]
δ_I	Death of infected cells	day^{-1}	0.42 [0.40, 0.44]	0.48 [0.46, 0.50]	0.53 [0.51, 0.56]
κ_v	Viral diffusion rate from culture to supernatant	day^{-1}	0.72 [0.55, 0.95]	0.13 [0.10, 0.17]	0.15 [0.11, 0.19]
σ_c	Relative standard deviation for cells	1		0.35	
σ_v	Relative standard deviation for RT activity	1		0.34	

non-productively infected cells were taken from estimates obtained by fitting the MOCK experiment (see previous section). As infected cell counts after day 9 dropped to background levels of the MOCK experiment, those measurements were neglected in the fitting procedure (not fitted points are indicated in gray in Fig. 3.3). In contrast, viral titers from all time points were used for fitting as SG-PERT is a more sensitive assay than FACS with respect to measuring absolute numbers. In suspension and loose collagen my model captured the increase of infected cells between day 0 and 1 well assuming non-productively infected cells appear on average within 17.3 hours, i.e., a half-life of 12 hours, after being transmitted into their respective environments (Fig. 3.3). In dense collagen the early decline and later increase in infected cell counts between day 0 and 2 could not be explained, but was presumably due to measurement errors also indicated by the estimated 95%-prediction bands. Additionally, I set the half-life of RT activity to 38 hours [69]. As cellular behavior might have been shaped by its environment, death rates of infected cells and viral production rates were allowed to vary across environments. Furthermore, different viral diffusion rates were fitted with respect to the respective culture systems as viral diffusion was assumed to highly depend on the density of the media. While the model captured all measured quantities well, it performed better concerning RT activity than cell counts. Considering the higher sensitivity of the SG-PERT assay compared to detection of absolute numbers of infected cells using a FACS, this was not surprising.

Again, I obtained the best fitting parameters and their respective 95%-confidence intervals (Fig. A.2 and Table 3.2) by performing a profile likelihood approach as described in Section 2.2.2. At the start of the experiment a large proportion of target cells, almost 20%, were estimated to be non-productively infected. Accordingly, only approximately 40% of infected cells were detectable by FACS at the beginning. However, due to death some non-productively infected cells did not become infectious in the course of the experiment as they were lost before this transition. Across the different environments half-life of infected cells was comparable, between 31 and 40 hours. Interestingly, viral production was around two-fold

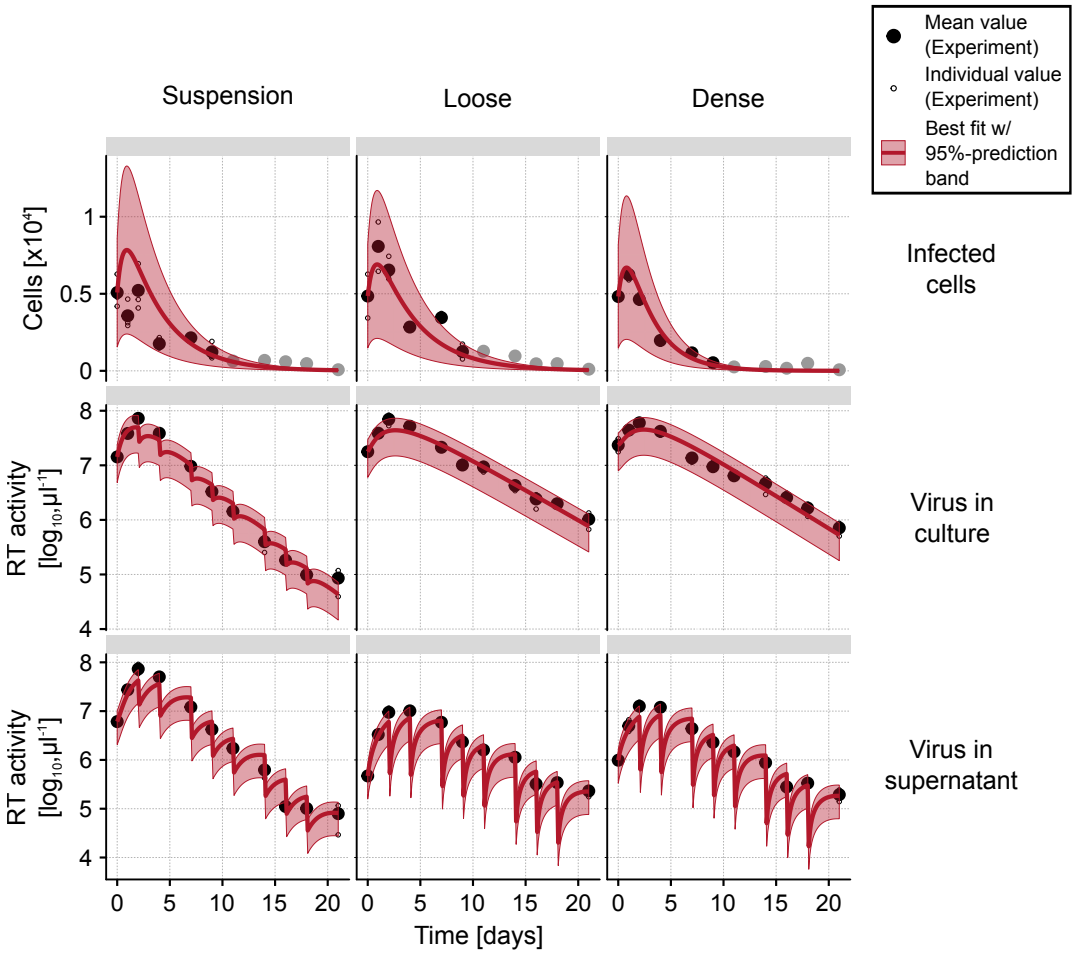

Fig. 3.3. **Estimation of infected cell turnover and viral kinetics.** Shown are mean counts (solid black dots) from three independent experiments (open black dots) of infected cells (top row), virus in culture (middle row) and virus in supernatant (bottom row) in suspension (left column), loose (middle column), and dense collagen (right column). Best fit of model (3.2) (thick red line) with estimated 95%-prediction band (shaded red area) describing the T20 data. All environments were fitted simultaneously with the same initial fraction of non-productively infected cells. Corresponding parameter estimates are shown in Table 3.2. Gray dots were not fitted (see main text for details). I set the average eclipse phase for non-productively infected cells, i.e., $1/\kappa_I$, to 17.3 hours and fixed the half-life of RT activity, c_v, to 38 hours.

enhanced in suspension compared to collagen ($\rho = 1.02\ [0.80, 1.38] \times 10^4$ (suspension) vs. $0.48\ [0.37, 0.66] \times 10^4$ (loose collagen) and $0.43\ [0.32, 0.61] \times 10^4$ (dense collagen) RT act. per day and cell). This has also been observed experimentally [69]. The exact mechanisms responsible for different viral production rates dependent on the environment still remain to be elucidated.

3.3.5 Formulation of a model describing HIV infection kinetics

Following my stepwise approach, all parameters estimated in the previous sections were fixed to the values obtained from the respective best fit. To describe HIV infection dynamics in different environments, I developed a model that follows various T cell and virus subsets. The former included CD8 cells, T_{CD8}, CD4 cells refractory to infection, T_r, target, T, non-

productively infected, J, and infectious cells, I. Refractory cells, a subset of CD4 cells, were assumed to be either not fully activated cells or cells that did not encounter an infected cell or cell-free virus in the course of the experiment. While virus in culture was split into infective, V_i, and non-infective, V_n, populations, this discrimination was not necessary for virus in supernatant, V_s, as it did not participate in the infection process. A sketch of the full model is shown in Fig. 3.4 and reads as follows

$$
\begin{aligned}
\frac{dT_{\mathrm{CD8}}}{dt} &= \lambda_{\mathrm{CD8}} T_{\mathrm{CD8}} \left(1 - \frac{T_{\mathrm{CD8}} + T + T_r + J + I}{T_c}\right) - \delta_{\mathrm{CD8}} T_{\mathrm{CD8}} \\
\frac{dT_r}{dt} &= \lambda_r T_r \left(1 - \frac{T_{\mathrm{CD8}} + T + T_r + J + I}{T_c}\right) - \delta_{\mathrm{CD4}} T_r \\
\frac{dT}{dt} &= (\lambda_{\mathrm{CD4}} T + (\lambda_{\mathrm{CD4}} - \lambda_r) T_r) \left(1 - \frac{T_{\mathrm{CD8}} + T + T_r + J + I}{T_c}\right) - \beta_f T V_i - \beta_c T I - \delta_{\mathrm{CD4}} T \\
\frac{dJ}{dt} &= \beta_f T V_i + (1 - f_b)\beta_c T I - \kappa_I J - \delta_{\mathrm{CD4}} J \\
\frac{dI}{dt} &= \kappa_I J - \delta_I I \\
\frac{dV_i}{dt} &= f_i \rho I - c_i V_i - c_v V_i - \kappa_v V_i \\
\frac{dV_n}{dt} &= (1 - f_i)\rho I + c_i V_i - c_v V_n - \kappa_v V_n \\
\frac{dV_s}{dt} &= \kappa_v (V_i + V_n) - c_v V_s, \\
\text{with } T_{\mathrm{CD8}}(0) &= T_{\mathrm{CD8},0},\ T_r(0) = f_R T_0,\ T(0) = (1 - f_R - f_J) T_0,\ J(0) = f_J T_0,\ I(0) = I_0, \\
V_i(0) &= f_V V_{c,0},\ V_n(0) = (1 - f_V) V_{c,0},\ V_s(0) = V_{s,0} \\
\text{and } V_i(t) &= \begin{cases} V_i(t) & \text{for } t \in t_m \text{ in collagen} \\ 0.5 \times V_i(t) & \text{for } t \in t_m \text{ in suspension} \end{cases}, \\
V_n(t) &= \begin{cases} V_n(t) & \text{for } t \in t_m \text{ in collagen} \\ 0.5 \times V_n(t) & \text{for } t \in t_m \text{ in suspension} \end{cases}, \\
V_s(t) &= \begin{cases} 0 & \text{for } t \in t_m \text{ in collagen} \\ 0.5 \times (V_i(t) + V_n(t)) & \text{for } t \in t_m \text{ in suspension} \end{cases}.
\end{aligned}
\tag{3.3}
$$

Here, $t_m := \{2, 4, 7, 9, 11, 14, 16, 18\}$ denotes the days of media change. In the model CD8 cells and refractory CD4 cells cannot be infected, but compete for resources and space with target cells such that each well can only reach a carrying capacity of total T cells, T_c, depending on the environment. The proliferation rate of target cells, λ_t, is defined such that $\lambda_{\mathrm{CD4}} T_{\mathrm{CD4}} = \lambda_t T + \lambda_r T_r$ holds true with λ_r being the proliferation rate of cells refractory to infection. Target and refractory cells die with the same rate δ_{CD4}. Depending on the available number of target cells, activated CD4 cells become non-productively infected cells by infection through cell-free transmission with rate β_f proportional to the infectious virus in culture. Furthermore, cell-to-cell transmission is also part of the model occurring with rate β_c proportional to the number of infectious cells. Whereas all target cells infected through cell-free (CF) transmission become non-productively infected cells, a fraction, f_b, of those infected through cell-to-cell (CC) transmission is killed instantly due to abortive infections [22, 126, 127]. The average time non-productively infected cells stay in eclipse phase is $1/\kappa_I$ and their half-life is $\log(2)/\delta_{\mathrm{CD4}}$. Infected and infectious cells are not allowed to proliferate in this model. Whereas in culture, infectious and non-infectious virus, V_n, is followed over time,

there is no discrimination in the supernatant as infection events are supposed to solely occur in culture. Only a fraction, f_i, of virus produced by infectious cells with rate ρ is infective, i.e., can infect uninfected target cells upon encounter. Virus is degraded at rate c_v independent of its location. Additionally, infectious virus looses infectivity with rate c_i and is subsequently considered non-infective virus. Viral diffusion from the culture to the supernatant is assumed to take place with rate κ_v due to concentration gradients and regular diffusion of viral particles. Finally, parameters f_R and f_J represent the initial fraction of refractory and non-productively infected cells in the population of target cells and f_V is the fraction of infectious virus in the culture at the beginning of the experiment with respect to the measurements from the data.

3.3.6 Parametrization of HIV infection dynamics in different environments

To parameterize HIV infection dynamics in suspension and collagen, I first fitted model (3.3) without abortive cell-to-cell infection ($\mathrm{R_p}$-model), i.e., $f_b = 0$, to data from the WT experiment (Fig. 2.1). At a later stage, when different models were compared, the process of pyroptosis, i.e., abortive infection in the context of cell-to-cell transmission, was included.

Except the initial fraction of non-productively infected cells, f_J, the best fitting or fixed parameters from the previous sections were inherited. In the experiment no discrimination between infective and non-infective virus was possible. Therefore, to ensure parameter identifiability some rates had to be fixed, namely the half-life of viral infectivity, c_i, to 17.9 hours [128] and the fraction of infective virus, f_I, with respect to the produced virus to 10^{-3}. The following equations show that the dynamics of viral RT activity in culture is independent of f_i and different values thereof can be compensated by β_f:

$$\begin{aligned} \frac{dV_c}{dt} &= \frac{d(V_i + V_n)}{dt} = \rho I - c_v(V_i + V_n) - \kappa_v(V_i + V_n) = \rho I - c_v V_c - \kappa_v V_c \\ &\text{and} \\ \frac{dJ}{dt} &= \beta_f T V_i \ldots = \beta_f^* T V_i^* \ldots \end{aligned} \quad , \tag{3.4}$$

where $V_i^* := V_i / f_i$ and $\beta_f^* := \beta_f f_i$ are. In the fitting procedure I limited the initial fraction of infective virus to values lower than 10^{-3} as loss of infectivity was assumed to occur at a faster rate than loss of RT activity. Furthermore, in collagen the efficacy of cell-free transmission was fixed to 14% its value in suspension, i.e., $\beta_f^{\mathrm{coll}} = 0.14 \times \beta_f^{\mathrm{susp}}$ based on additional experimental observations [69]. Therefore, only one cell-free transmission rate was fitted across all environments. Last but not least, I modeled the assumption that refractory cells are not fully activated CD4 cells by limiting proliferation of T_r, enforcing the following relation $\lambda_r < \lambda_{\mathrm{CD4}}$ [129]. However, the refractory cell population also included uninfected cells, which in principal could have been infected but did not encounter virus or infected cells during the course of the experiment. This spatial process was not explicitly captured in my model as it is based on the assumption of a well-mixed system. In loose collagen numbers of infected cells were too low to explain measured RT activity in the well and, hence, were not fitted (Fig. 3.5, indicated in gray). Interestingly, the model prediction for the true number of infected cells in loose collagen (red line in center panel of Fig. 3.5) deviated only slightly

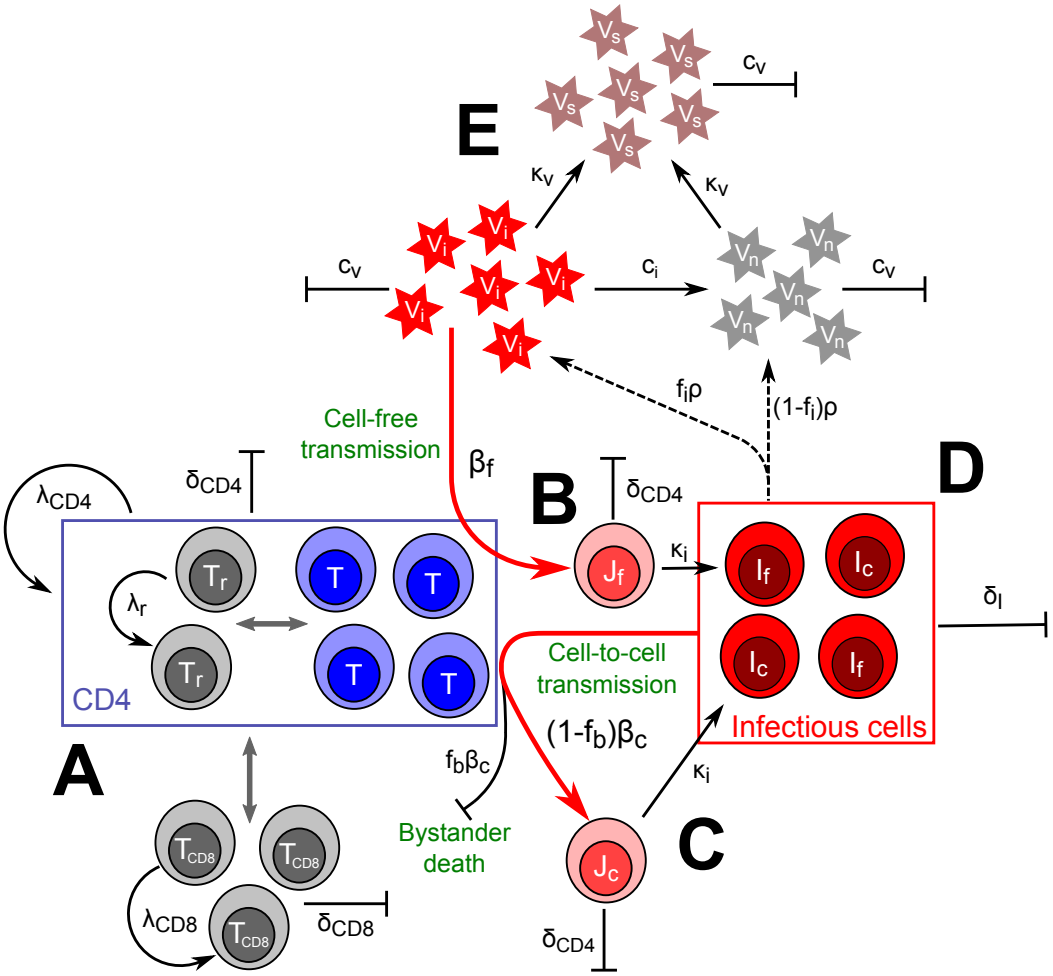

Fig. 3.4. **Sketch of the infection dynamics model.** Model (3.3) describes HIV infection dynamics in different environments. **(A)** Refractory CD4, $\mathrm{T_r}$, and CD8, $\mathrm{T_{CD8}}$ cannot get infected, both indicated in gray. They proliferate with rates λ_r and λ_{CD8}, respectively. While CD8 cells have an average lifespan of $1/\delta_{\mathrm{CD8}}$, the half-life of CD4 cells is $log(2)/\delta_{\mathrm{CD4}}$. In the absence of refractory cells, target cells, T (blue), proliferate with rate λ_{CD4} (for more information see main text). CD8 cells proliferate with rate λ_{CD8}. All T cells compete for nutrients and space (indicated with gray double arrows) until a carrying capacity of total T cells, T_c (not shown), is reached. **(B)** Target cells become non-productively infected cells, $\mathrm{J_f}$ (light red) by cell-free infection of infective virus in culture, $\mathrm{V_i}$ (red stars), with rate β_f. **(C)** Cell-to-cell infection of target cells occurs with rate β_c proportional to the concentration of infectious cells, $\mathrm{I_c}$ and $\mathrm{I_f}$ (both dark red). While a fraction, f_b, of newly CC-infected target cells dies due to abortive infection, $(1-f_b)$ of cell-to-cell infected cells proceeds to a non-productively infected state, $\mathrm{J_c}$ (light red). The half-life of non-productively infected cells not subject to abortive infection is $\log(2)/\delta_{\mathrm{CD4}}$ and they transit to an infectious state with rate κ_I. **(D)** Infectious cells have an average lifetime of $1/\delta_I$ and produce virus in culture at rate ρ. A fraction, $1-f_i$, of the produced virus is not infective, $\mathrm{V_n}$ (gray stars). **(E)** Virus diffuses from culture to supernatant, $\mathrm{V_s}$ (red-gray stars), with diffusion rate κ_v, where infective and non-infective virus is not longer discriminated. All virus is lost with rate c_v and additionally, infective virus looses infectivity with rate c_i.

Tab. 3.3. **Estimated parameter values governing infection dynamics.** Proliferation of refractory cells was restricted to be slower compared to activated CD4 cells, i.e., target cells. Additionally, I fixed the fraction of newly produced infectious virus to $f_i = 10^{-3}$ and limited the initial fraction f_V to be smaller than f_i due to faster degradation of infectious than non-infectious virus. Following experimental analysis, cell-free transmission in collagen was decreased to 14% its efficacy in suspension, i.e., $\beta_f^{\text{coll}} = 0.14 \times \beta_f^{\text{susp}}$. I conducted no profile likelihood approach for relative standard deviations. Thus, only the best estimates are given in this table. When a parameter was still within the confidence region at its predefined limit as explained above, this is indicated below with the parameter-name of this limit rather than its value. Graphical representation of the profiles is shown in Fig. A.3.

Parameter	Description	Unit	Suspension	Loose	Dense
f_J	Initial fraction of non-productively infected cells in WT experiment	$\times 10^{-2}$	$3.3\ [1.7, 4.8]$		
f_V	Initial fraction of infectious virus in WT experiment	1	$4.4 \times 10^{-8}\ [0, f_i]$		
f_R	Initial fraction of refractory cells in WT experiment	1	$0.10\ [0.074, 0.12]$		
β_f	Cell-free transmission rate	$\times 10^{-5}$ day^{-1} $\times$RT act.$^{-1}$	$2.3\ (0, 3.0]$		
β_c	Cell-to-cell transmission rate	$\times 10^{-5}$ $(\text{cell} \times \text{day})^{-1}$	1×10^{-6} $(0, 7.0]$	4.3 $[3.6, 5.4]$	1.7 $[1.4, 2.6]$
λ_r	Proliferation rate of refractory cells	day^{-1}	0.22 $[0.16, 0.29]$ and $[0.56, 0.58]$	0.78 $[0.77, \lambda_{\text{CD4}}]$	0.49 $[0.45, 0.52]$
σ_c	Relative standard deviation for cells	1	0.41		
σ_v	Relative standard deviation for RT activity	1	0.36		

from the observed values. While the introduction of refractory cells allowed the model to describe uninfected CD4 cell counts in suspension, it overestimated the number of CD8 cells (top left panel in Fig. 3.5). However, as the latter did not partake in the infection process, this was not considered a relevant shortcoming. Furthermore, the model was able to describe and capture viral RT activity in culture and supernatant across all environments (lower two rows in Fig. 3.5). Again, changes of media were clearly visible in the supernatant. In suspension this was also observed for virus in culture due to the assumption of fast mixing in suspension.

The best fitting parameters and their respective 95%-confidence intervals (Fig. A.3 and Table 3.3) were obtained performing a profile likelihood approach as described in Section 2.2.2. Here, around 3.4% of target cells were initially non-productively infected cells, which were counted as target cells as they presumably had too little viral material to be sorted into the compartment of infected cells using FACS. This proportion corresponded to about 20% of total infected cells. Interestingly, the estimated fraction was higher in the T20 experiment, which could not be explained except by experimental uncertainties (see Section 3.3.3). While estimates predicted that initially about 10% of uninfected CD4 cells were refractory to infection, this fraction changed over the course of the experiment due to different proliferation rates and cells being infected. Proliferation of refractory cells was fastest in loose ($\lambda_r = 0.78\ [0.77, \lambda_{\text{CD4}}]$

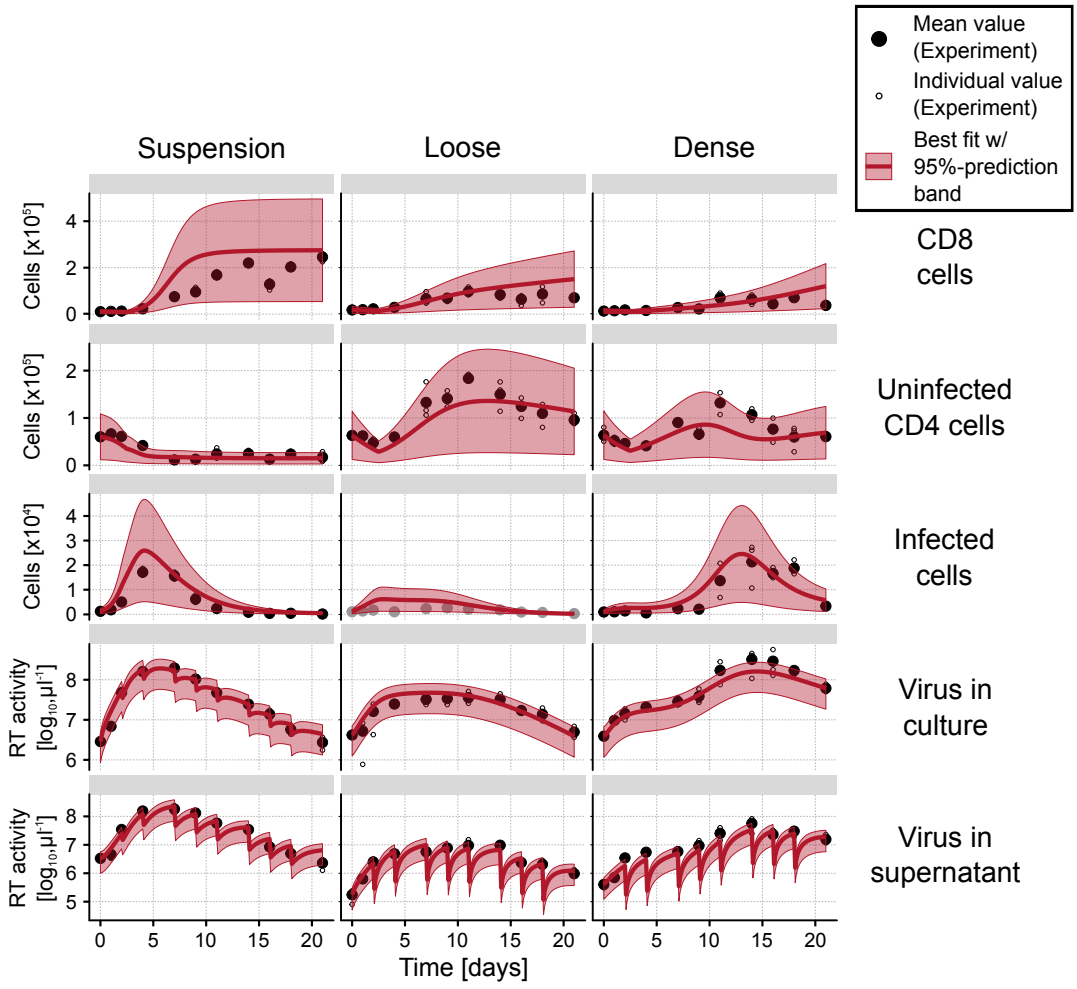

Fig. 3.5. **Infection dynamics of HIV in PBMCs.** Shown are mean counts (solid black dots) from three independent experiments (open black dots) of CD8 (1^{st} row), uninfected (2^{nd} row) and infected CD4 cell counts (3^{rd} row), virus in culture (4^{th} row) and virus in supernatant (5^{th} row) in suspension (left column), loose (middle column), and dense collagen (right column). Best fit of the Rp-model (model (3.3) without abortive infection, thick red line) with estimated 95%-prediction band (shaded red area) describing the WT experiment. All environments were fitted simultaneously with the same initial fraction of non-productively infected cells, f_J, of infective virus, f_V, and of refractory cells, f_R. Infected cells in loose collagen were not fitted (indicated in gray, see main text for more information). Corresponding parameter estimates are shown in Table 3.3. Parameters already estimated or fixed in the previous sections (except f_J) were adopted here. Additionally, I set the half-life of viral infectivity to 17.9 hours [128] and the fraction of infective virus with respect to newly produced virus in culture to 10^{-3}. Efficacy of cell-free transmission was assumed to decrease in collagen to 14% of its efficacy in suspension, i.e., $\beta_f^{\text{coll}} = 0.14 \times \beta_f^{\text{susp}}$.

day^{-1}), intermediate in dense collagen ($\lambda_r = 0.48\ [0.45, 0.52]$ day^{-1}) and slowest in suspension ($\lambda_r = 0.22\ [0.16, 0.29]$ and $[0.56, 0.58]$ day^{-1}). In the latter environment, the split into two distinct confidence intervals for the proliferation rate of refractory cells stem from difficulties in simultaneously describing CD4 and CD8 cell dynamics. However, the interval with larger proliferation rates could not capture the dynamics of CD4 cells, which were evidently more important to the overall infection dynamics than CD8 cells. This was also illustrated by a higher maximum likelihood estimator for large proliferation rates of refractory cells. The T cell subset of refractory cells was made up of target cells not encountering virus or infected cells during the experiment, and cells not fully activated, which could not get infected. Therefore, a high proliferation rate of this subset, as seen in loose collagen, could be linked to a large fraction of susceptible cells within the refractory population that were not infected due to spatial issues rather than a low level of activation. The initial fraction of infective virus was low indicating towards a negligible role of cell-free transmission early on. Even though cell-free transmission occurred at the same rate in both collagen environments and the cell-to-cell infection rate was estimated to be higher in loose than dense collagen ($\beta_c^{\text{loose}} = 4.3\ [3.6, 5.4] \times 10^{-5}\ (\text{cell} \times \text{day})^{-1}$ vs. $\beta_c^{\text{dense}} = 1.7\ [1.4, 2.6] \times 10^{-5}\ (\text{cell} \times \text{day})^{-1}$), more cells got infected in the latter. At a first glance this seemed counterintuitive, but could be explained by refractory cells overtaking the population of CD4 cells in loose collagen, thus, limiting target cell availability. Furthermore, the infection stayed at low levels in dense collagen for a longer time after initiation of the experiment compared to the other environments allowing target cell numbers to increase and, thus, for a larger pool of susceptible cells.

Being able to describe the data with well-defined parameters, my model was used to infer the proportion of cells infected through either transmission mode, thus, adding to current knowledge of the virus. To predict the contribution of each transmission mode to the infection dynamics, the governing equations of non-productively infected and infectious cells as described in model (3.3) had to be split as follows

$$
\begin{aligned}
\frac{dJ_{\text{init}}}{dt} &= -\kappa_I J_{\text{init}} - \delta_{\text{CD4}} J_{\text{init}} \\
\frac{dJ_f}{dt} &= \beta_f T V_i - \kappa_I J_f - \delta_{\text{CD4}} J_f \\
\frac{dJ_c}{dt} &= (1 - f_b)\beta_c T I - \kappa_I J_c - \delta_{\text{CD4}} J_c \\
\frac{dI_{\text{init}}}{dt} &= \kappa_I I_{\text{init}} - \delta_I I_{\text{init}} \\
\frac{dI_f}{dt} &= \kappa_I I_f - \delta_I I_f \\
\frac{dI_c}{dt} &= \kappa_I I_c - \delta_I I_c \\
J_{\text{init}}(0) = J_0,\ I_{\text{init}}(0) &= I_0,\ J_f(0) = J_c(0) = I_f(0) = I_c(0) = 0, \\
\text{with } J := J_{\text{init}} + J_f + J_c \text{ and } I &:= I_{\text{init}} + I_f + I_c \qquad ,
\end{aligned}
\tag{3.5}
$$

where f_b was set to zero as death by abortive infections was neglected here. Non-productively infected cells were split into initially, J_{init}, cell-free, J_f, and cell-to-cell, J_c, infected subsets. The same was done for infectious cells. All meanings of parameters were the same as described for model (3.3). To study the effect of different environments on the contribution of each transmission mode to the infection dynamics, only cells infected during the course of the

experiment that became infectious were of importance. Thus, the proportion of cells infected through cell-free transmission was defined as $f_{cf} := I_f/(I_c + I_f)$.

Considering only the best fitting parameter set for the Rp-model (Tab. 3.3), cell-free transmission seemed to be the predominant route of infection in suspension. A different picture, however, was painted in collagen environments, where the fraction of cells infected through cell-free transmission after establishment of the infection was decreased to approximately 40% and 25% in dense and loose collagen, respectively (Fig. 3.6A). However, the flexibility of the model lead to wide confidence intervals with respect to the proportion of cells infected through either transmission mode in the different environments (Fig. 3.6B). Nonetheless, the odds of getting infected through cell-free transmission in a specific environment, $f_{cf}/(1-f_{cf})$, after 21 days followed, on log-scales, an almost linear relationship between the respective environments (Fig. 3.6C). The likelihood of getting infected through cell-to-cell spread were approximately 7- and 4-fold higher in loose and dense collagen, respectively, than in suspension.

3.3.7 HIV infection kinetics for each transmission mode separately

In a next step the model was used to predict the infection dynamics with one transmission mode blocked. Again, modeling played a crucial role in deepening the understanding of HIV as blocking a particular transmission mode experimentally is difficult (refer to *Introduction* for more information). Fig. 3.6A hints towards cell-free being the predominant mode of transmission in suspension. Thus, blocking cell-to-cell spread had no visible impact on the time course of infection (Fig. 3.7, left column). In turn, when blocking cell-free transmission no new infections occurred and the dynamics followed in principle that of the T20 experiment. However, the contribution of cell-to-cell transmission in suspension may have been masked due to the dominant role of cell-free spread and ongoing infection in the absence of cell-free transmission could not be ruled out completely. This was also indicated by the large confidence intervals with respect to the contribution of each transmission mode. Surprisingly, in dense collagen blocking cell-free spread actually increased infected cell counts at the peak as it presumably allowed the virus to be more “patient” and, thus, for higher target cell availability (Fig. 3.7, center row and right column). To a smaller extent, the same could be observed in loose collagen.

3.3.8 HIV infection kinetics for different initial cell densities

After quantifying the contribution of the different transmission modes, I additionally analyzed the effect of target cell availability on the infection dynamics. To this end, an *in silico* experiment was simulated with higher initial densities of CD8 and uninfected CD4 cells than observed in the previously described experiments. Assuming that T cells *in vitro* divide only a certain number of times until exhaustion and that nutrients are a limiting resource for high cell densities, the capacity, $T_c(x)$, needed to be adapted for varying initial conditions. Here, I assumed that the capacity follows a saturated function dependent on the initial conditions, x, leading to

$$T_c(x) = T_{c,\max}\left(1 - e^{-\lambda x}\right), \tag{3.6}$$

where $T_{c,\max}$ describes the maximal capacity per well reachable, which is restricted due to nutrient limitations. Furthermore, x is a factor, which gives the relative deviation from the

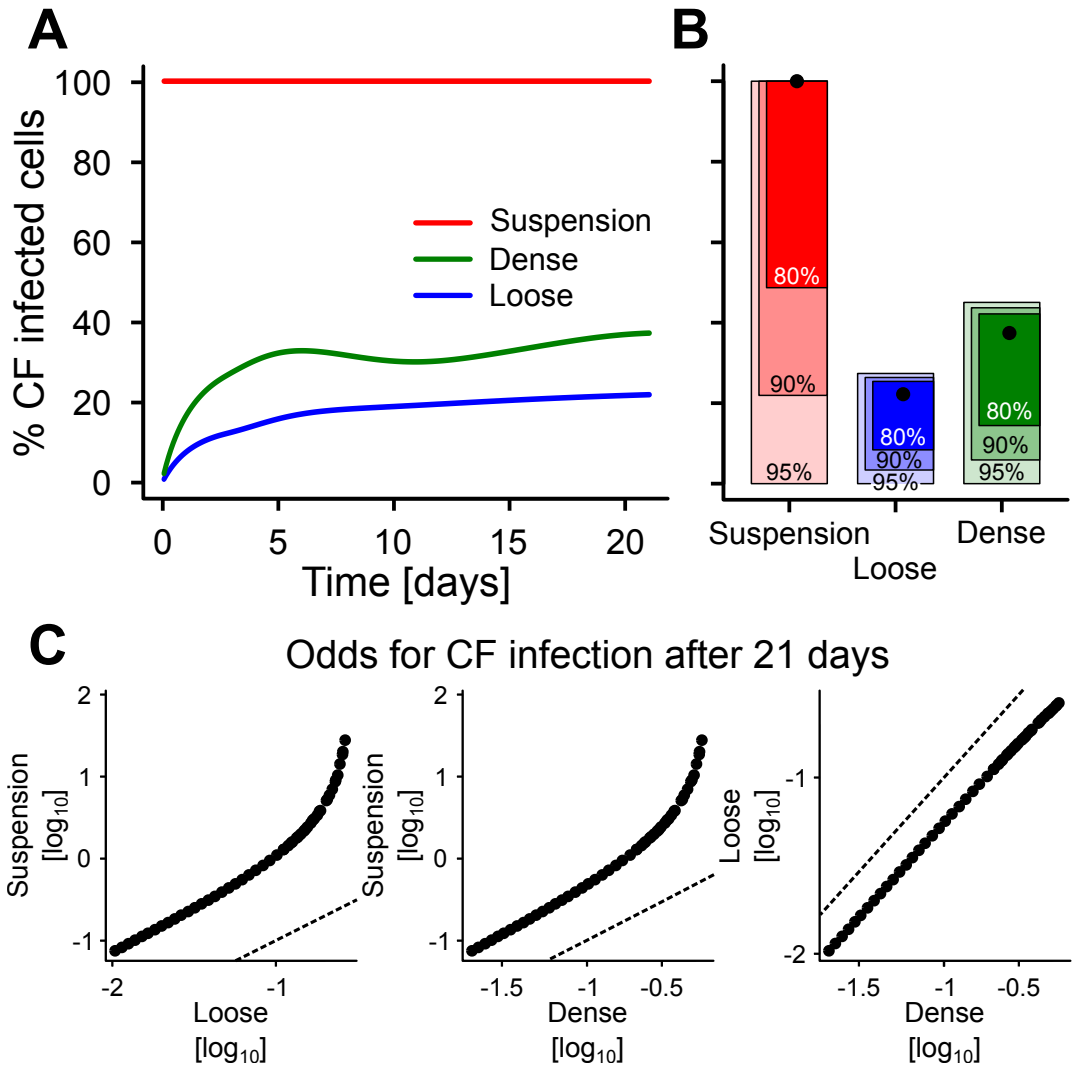

Fig. 3.6. **Contribution of cell-free transmission to the infection dynamics.** **(A)** Predicted percentage of cells infected through cell-free transmission in suspension (red), dense (green) and loose (blue) collagen using the best fitting parameters for the Rp-model (Tab. 3.3). **(B)** 80%-, 90%- and 95%-confidence intervals of the predicted percentage of CF-infected cells after day 21 in suspension (red), loose (blue) and dense (green) collagen (best fit is shown with solid black dots). **(C)** Odds for a cell to get infected through cell-free transmission after 21 days of the experiment in loose collagen vs. suspension (left), dense collagen vs. suspension (middle) and dense vs. loose collagen (right). In each panel the dashed line marks equal odds for both environments.

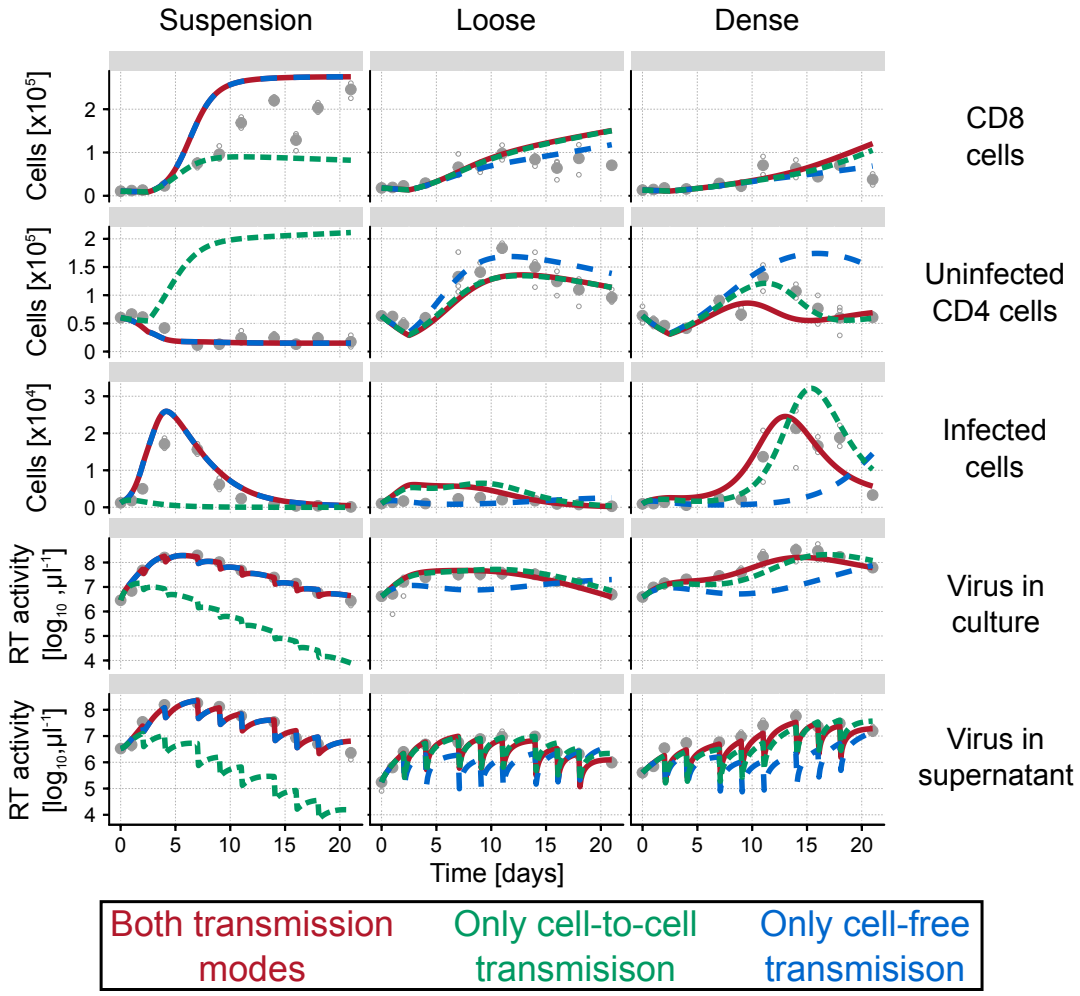

Fig. 3.7. **Infection kinetics for individual transmission modes separately.** Shown are mean counts (solid gray dots) from three independent experiments (open gray dots) of CD8 (1^{st} row), uninfected (2^{nd} row) and infected CD4 cell counts (3^{rd} row), virus in culture (4^{th} row) and virus in supernatant (5^{th} row) in suspension (left column), loose (middle column), and dense collagen (right column). Here, no separate fit was conducted, but rather best fitting parameter values from previous sections were used. Best fit of the Rp-model (red) as shown in the previous section describing the WT experiment. The estimated parameters were then used to predict the infection dynamics without cell-free (green) or cell-to-cell transmission (blue).

experiment, that is 1 for an initial cell density as observed in the experiment. Parameter λ represents the decline of the capacity per well as combination of a maximal number of divisions per cell and nutrient availability. Here, I assumed that for the initial density as observed in the experiment, nutrient limitation was not a factor due to frequent media changes. Therefore, the same should also hold for half the initial T cell density. Lastly, increasing the initial T cell density by ten-fold resulted in an assumed increase in the capacity compared to the experimental initial conditions of 10/3 (refer to Table 3.1 for estimated values of experimental capacity). Using these assumptions and fitting to Eq. (3.6), the capacity for two-fold and five-fold initial conditions was supposed to increase by 1.684 and 2.806 compared to the experimental initial conditions, respectively.

Comparing the proportion of infected cells among total CD4 cells between the experimental data and the predictions obtained from simulating the Rp-model with the best fitting parameters showed a slight deviation over the course of the infection (Fig. 3.8A, solid gray dots and blue lines). While varying initial T cell counts in suspension exhibited only minor effects on the proportion of infected CD4 cells, the increase in the average infected proportion was most notable in loose collagen (1x: 0.05, 2x: 0.05, 5x: 0.07 and 10x: 0.11) without changes in the time of the peak (Fig. 3.8B). However, the average proportion was already overestimated for the best fit (1x initial condition) in loose collagen, which was expected as the retrieval of infected cells in this environment was impaired. Interestingly, while the average infected proportion of CD4 cells stayed relatively constant in dense collagen (1x: 0.132, 2x: 0.127, 5x: 0.137 and 10x: 0.161) irrespective the initial number of T cells, the peak in infected proportions occurred earlier for high initial cell densities.

As proportions sometimes can occlude various processes occurring, I additionally analyzed the cumulative number of infected cells to gain more information. To allow for comparison of different initial cell densities, the cumulative number was normalized by the corresponding maximal value. While this revealed that in suspension the relative infection dynamics were almost independent of the initial cell density, they were drastically changed in loose and dense collagen due to their dependence on cell-to-cell transmission (Fig. 3.9A). In general, high initial cell densities in collagen shifted the steepest increase of infected cells towards earlier time points. Furthermore, comparing the increase in total infected cells for ten-fold initial cell densities, it became evident that loose collagen benefited most from high initial cell densities (10x/1x for suspension: 8.0, loose: 9.7 and dense: 3.4), reaching similar levels as observed in dense collagen (1x loose/dense: 0.32 vs. 10x loose/dense: 0.92) (Fig.3.9B).

3.3.9 Identification of processes necessary to describe the data

Iwami *et al.* previously published a model to infer the proportion of cells infected with HIV through either of the transmission modes [70]. Although their experimental setup was different to the one adopted here and their model neglected several processes, which were incorporated into my model, I compared their modeling approach to mine. To allow a fair comparison, I followed the same step-wise approach as described in the previous sections with an adaptation of their model, termed $Standard$-model in the following (for more information refer to Section A.4). I also fitted adaptations of model (3.3) to the experimental data, to gain more confidence in the predictions of the Rp-model. An overview of the compared models with additional assumptions and their respective AICc values is shown in Table 3.4.

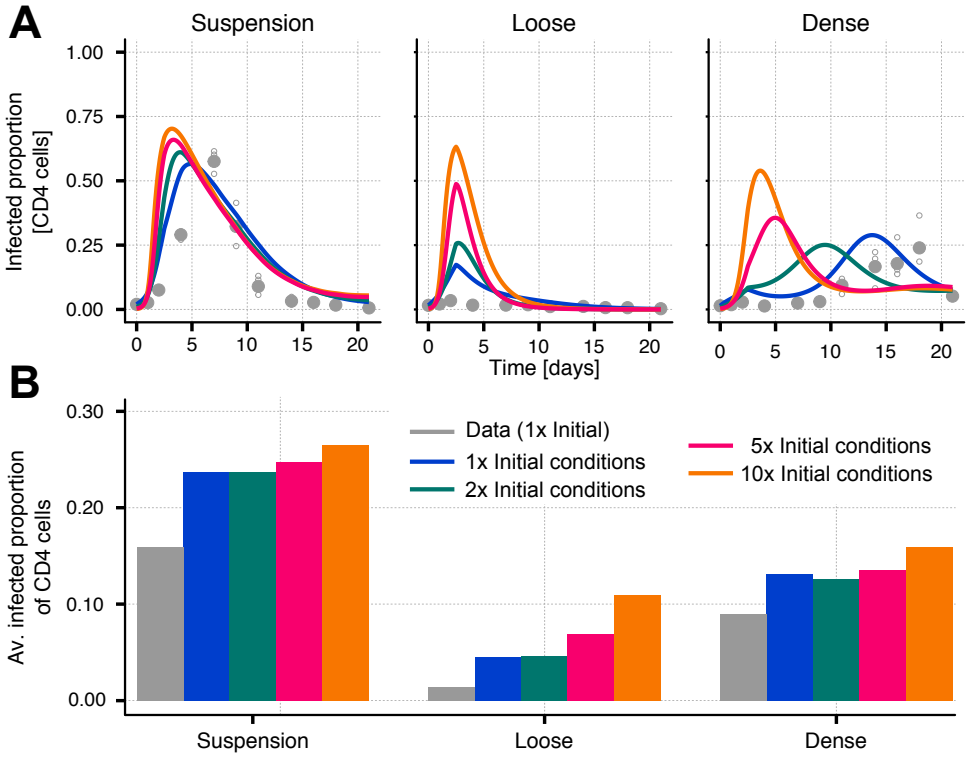

Fig. 3.8. Proportion of infected cells among total CD4 cells for different initial CD8 and uninfected CD4 cell densities in collagen and suspension. Model predictions were generated with the best fitting parameter set for the Rp-model (Fig. 3.5 and Tables 3.1, 3.2 and 3.3). **(A)** Time course of the mean infected proportion among CD4 cells (solid gray dots) calculated from three individual experiments (open gray dots) in suspension (left), loose (center) and dense (right) collagen. Lines represent predictions with the same (blue), 2-fold (green), 5-fold (pink) and 10-fold (orange) initial conditions of CD8 and uninfected CD4 cells compared to the experiment. **(B)** Infected proportion of CD4 cells averaged over the course of the experiment for different initial conditions and environments as described above.

From Table 3.4 it is evident that the $Standard$-model has the biggest difficulties in describing the data (see also Fig. A.5). Adaptations of model (3.3) could be divided into three categories. Models that did not incorporate refractory cells, i.e., S, $\mathrm{A_s}$ and A, performed worst. The category providing intermediate fits consisted of models including refractory cells, which proliferated with the same rate as CD4 cells (R, R-$\mathrm{A_s}$ and R-A). The best fitting models ($\mathrm{R_p}$, $\mathrm{R_p}$-$\mathrm{A_s}$, $\mathrm{R_p}$-A) allowed refractory cells to proliferate at different rates depending on the environment with $\mathrm{R_p}$ and $\mathrm{R_p}$-$\mathrm{A_s}$ being essentially the same models as death by abortive infection was estimated to be zero ($f_b = 0$) in the latter. Unfortunately, despite resulting in the lowest AICc value overall, no conclusions could be drawn from model $\mathrm{R_p}$-A concerning the contribution of each transmission mode. The high flexibility of this model allowed compensating varying rates of abortive infection with changing transmission rates. Thus, these parameters were non-identifiable and contributions of the respective transmission modes could vary between 0% and 100% without impairment of the fit. In summary, the $\mathrm{R_p}$-model was the only model able to capture the dynamics while still ensuring identifiability of parameters and was therefore the most informative among all tested models.

To demonstrate the shortcomings of each category mentioned above, the best fit of representative models is shown in Fig. 3.10. While the S-model (green lines) as part of the worst fitting category could not capture the dynamics - except CD8 cell dynamics - observed in suspension

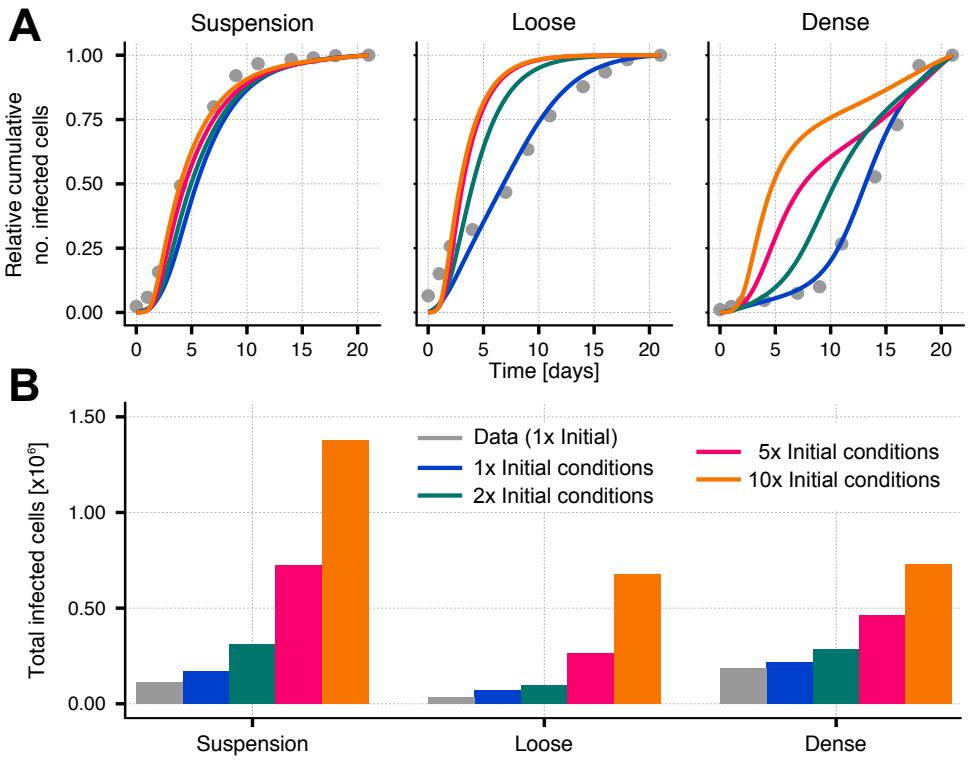

Fig. 3.9. Cumulative and total number of infected cells for different initial CD8 and uninfected CD4 cell densities in collagen and suspension. Model predictions were generated with the best fitting parameter set for the Rp-model (Fig. 3.5 and Tables 3.1, 3.2 and 3.3). **(A)** Time course of the mean cumulative number of infected cells (solid gray dots) relative to the maximal value calculated from three individual experiments in suspension (left), loose (center) and dense (right) collagen. Lines represent predictions with the same (blue), 2-fold (green), 5-fold (pink) and 10-fold (orange) initial conditions of CD8 and uninfected CD4 cells compared to the experiment. **(B)** Total number of infected cells during the infection calculated by the area under the curve representing the number of infected cells for different initial conditions and environments as described above.

due to missing refractory cells, the R-model (blue lines) had difficulties describing virus and infected cells in loose collagen (Fig. 3.10). Differences between models R_p and R_p-A (red and orange lines) were only minor indicated also by similar AICc values (Fig. 3.10 and Table 3.4).

3.4 Discussion

In this chapter I followed a step-wise approach, which resulted in a model able to describe infection kinetics in suspension, loose and dense collagen simultaneously, while still ensuring parameter identifiability. This model features several processes neglected in previously published models. The step-wise approach was based on models describing T cell and virus dynamics.

In a first step I parameterized T cell dynamics with the assumption of constant proliferation and death rates of T cells in the experiments. Albeit this being a simplification, as these processes most likely also depend on the number of divisions each cell has undergone ([130] and reviewed in [131]) and, hence, would change during the life of a cell, it was a necessary

Tab. 3.4. **Description and AICc comparison of different models.** Models (A.1) and (A.2) describing T cell and virus dynamics, respectively, underly model *Standard* (for more information see Section A.4). Except the *Standard*-model, all models are adaptations of model (3.3). For those models T cell dynamics were parameterized using model (3.1) and parameters governing infected cell turnover as well as viral kinetics were estimated using model (3.2). Here, S stands for simple model without refractory cells, R, and no death through abortive infection, A. Subscripts p and s represent different proliferation rates for refractory cells compared to CD4 cells and estimation of only a single rate describing death trough abortive infection across all environments, respectively. The difference of AICc-value for a given model to the lowest AICc is denoted with Δ_{AICc}. Best fitting ($\mathrm{R_p}$-A) and most informative ($\mathrm{R_p}$) models are marked with bold letters.

Name	Basic equation	Additional Assumptions	# Parameters	AICc	Δ_{AICc}
Standard	(A.3)	-	9	4263.1	386.3
S	(3.3)	$\lambda_r = f_b = 0$	8	4118.9	242.1
$\mathrm{A_s}$	(3.3)	$\lambda_r = 0$, only one f_b	9	4121.2	244.4
A	(3.3)	$\lambda_r = 0$	11	4041.8	165.0
R	(3.3)	$\lambda_r = \lambda_{\mathrm{CD4}}$, $f_b = 0$	9	3920.0	43.2
R-$\mathrm{A_s}$	(3.3)	$\lambda_r = \lambda_{\mathrm{CD4}}$, only one f_b	10	3923.0	46.2
R-A	(3.3)	$\lambda_r = \lambda_{\mathrm{CD4}}$	12	3922.5	45.7
$\mathbf{R_p}$	(3.3)	$f_b = 0$	**12**	**3888.4**	**11.6**
$\mathrm{R_p}$-$\mathrm{A_s}$	(3.3)	only one f_b	13	3891.8	15
$\mathbf{R_p}$-A	(3.3)	-	**15**	**3876.8**	**0**

assumption to ensure parameter identifiability. Furthermore, I only considered death rates during the adaptation phase. This assumed that death rates were higher than proliferation rates of T cells during this time leading to a net death of T cells concealing possible proliferation events. Following the observed drop of T cell counts in the first days of the experiment, this seemed a reasonable assumption (Fig. 3.1). A different approach could consider a net proliferation rate, i.e., no explicit cell death, for the time after adaptation while allowing death and proliferation events to take place during the adaptation phase. However, when trying to explain the T20 data, this approach was problematic as infected cells could not compensate high death rates with proliferation. This lead to a steep decrease of infected cells in this experimental setup, which was not observed in the data. Another possibility to model T cell dynamics would be to neglect the adaptation phase. This seemed unfeasible, because models not incorporating an adaptation phase tend to underestimate the first measurements (Fig. A.4A) and, additionally, lead to lower proliferation rates compared to a model incorporating the biologically reasonable adaptation. Indeed, comparison between estimated rates from model (3.1) and (A.1) revealed that all proliferation rates were higher in the model with adaptation phase (compare Table A.1). In a publication by Yates *et al.* the estimated net proliferation rate of activated CD8 cells was approximately 0 as proliferation and death rates canceled each other out [130]. With the knowledge of an adaptation phase at hand, this is not surprising as their experiment only lasted for 4 days, which was close to the time cells needed to adapt to their new environment in the experiments presented here. This shows, how disregarding the adaptation phase can bias results. A different publication by De Boer and Perelson gave estimates for *in vivo* CD4 and CD8 cell life spans and proliferation rates of CD8 cells in mice [131]. However, comparison across species and between environments

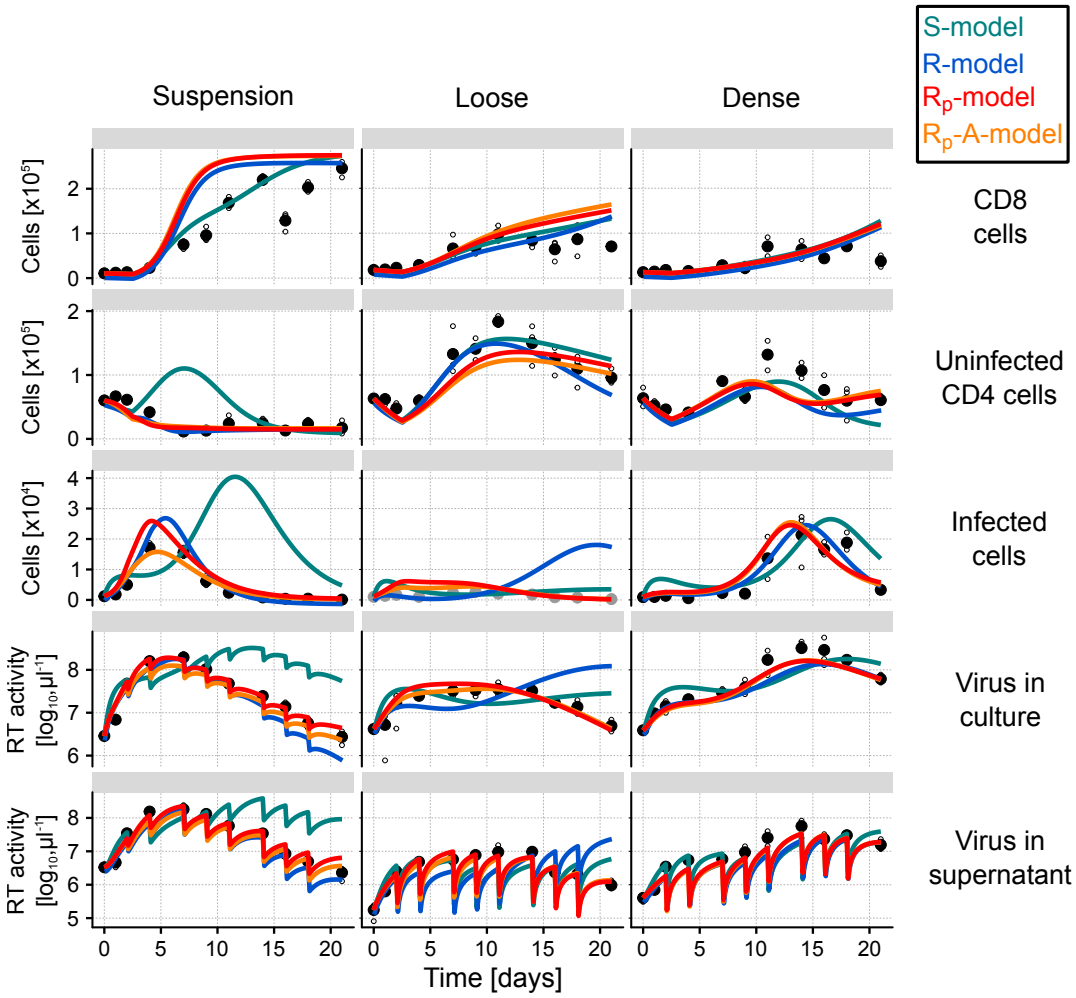

Fig. 3.10. **Comparison of different models describing HIV infection dynamics.** Shown are mean counts (solid black dots) calculated from three independent experiments (open black dots) of CD8 (1^{st} row), uninfected (2^{nd} row) and infected CD4 cell counts (3^{rd} row), virus in culture (4^{th} row) and virus in supernatant (5^{th} row) in suspension (left column), loose (middle column), and dense collagen (right column). The S- (blue-green), R- (blue), R_p- (red) and R_p-A-model (orange) were compared to visually show their capability of explaining the data (for a description of the fitted models refer to Table 3.4) indicated.

was difficult as already the *in vitro* situation presented here, yielded varying proliferation and death rates.

Following the characteristics of the data, I presented - to my knowledge - the first model that accounted for a period during which cells adapt to their new environment. It should be noted, though, that the experimental data was not sufficient enough to completely disentangle proliferation and death of T cells. It only allowed to estimate net death and proliferation rates during and after the adaptation phase, respectively. Nonetheless, from my analysis it showed that the adaptation of cells to a new environment at the beginning of an experiment should be taken into account to correctly describe T cell dynamics. However, new experimental designs would have to be employed to tackle the question of cell proliferation *in vitro* and *in vivo* in more detail. Another limitation of the model was its inability to capture the oscillations observed in the T cell measurements at late time points. Nonetheless, these could reflect

measurement uncertainties and were most likely biologically irrelevant processes (see also Section 3.2)

In a next step I introduced a model describing virus dynamics and infected cell turnover in the presence of fusion inhibitor T20. Here, I used an exponentially distributed eclipse phase until newly infected cells transit into an infectious state. Although modeling the eclipse phase with an exponential distribution has been challenged previously [132, 133], in this context the assumption seemed reasonable as cells had heterogeneous infection ages at the start of the experiment due to being spin-infected 72 hours earlier. Thus, one could safely assume that several rounds of infection occurred before transfer of cells into the different cultures at the start of the experiment. Furthermore, I incorporated the change of media into the model. Neglecting this would have given wrong predictions of the viral titers after media change and thereby bias the predicted contribution of cell-free transmission to the infection dynamics, which depended directly on the viral concentration in culture at any given time.

Interestingly, viral production was two-fold increased in suspension compared to collagen. This again highlighted the necessity of performing *in vitro* experiments in physiologically plausible environments, when trying to transfer the so-gained knowledge to *in vivo* situations. Why viral production of HIV was increased in suspension as compared to collagen environments remains unknown and still needs to be elucidated.

Using particle tracking of the virus, members of the Rohr lab, Heidelberg University, obtained the mean squared displacement in each environment. With this in hand, Dr. Nikolas Schnellbächer from the Schwarz lab, Heidelberg University, calculated the average first passage time, $\bar{\tau}$ for virus produced in collagen to reach the supernatant. Inverting $\bar{\tau}$ yielded a first order diffusion rate constant, κ_v^{exp}, which I subsequently compared to the estimated rates from model (3.2) in the different collagen environments (dense: $\kappa_v^{\mathrm{exp}} = 0.108$ vs. $\kappa_v = 0.15$ and loose: $\kappa_v^{\mathrm{exp}} = 0.105$ vs. $\kappa_v = 0.13$). Contrary to intuition, viral diffusion from culture to supernatant seemed slightly faster in dense than loose collagen. Besides raising confidence in the estimated rates, it also indicated that diffusion as described in my model did not only capture Brownian motion but also implicitly incorporated diffusion due to concentration gradients. To enhance robustness of infected cell measurements and, thus, estimated rates, the experimental setup was changed from the WT experiment to the T20 experiment, where the latter included more initially infected cells (cf. Fig. 3.4). This difference in the experimental protocols was nicely captured by the estimated initial proportion of non-productively infected cells ($f_J^{\mathrm{T20}} = 0.17\ [0.10, 0.23]$ vs. $f_J^{\mathrm{WT}} = 3.3\ [1.7, 4.8] \times 10^{-2}$).

Following this, I developed a model able to describe the infection dynamics of HIV in three different environments simultaneously. This model featured the discrimination of infective and non-infective virus to account for faster loss of viral infectivity compared to degradation of viral particles. Additionally, viral titers were followed in culture and supernatant. This was especially necessary in collagen as concentrations could vary between compartments due to slow viral diffusion. While virus in culture drove the infection dynamics caused by cell-free transmission, virus in supernatant was not partaking in the infection process. To compare my modeling approach to an already published model [70], I adapted their model to allow for a fair comparison. Although the S-model (model (3.3) without refractory cells or death by abortive infections) had fewer parameters than the adapted model (Eq. (A.3)), it yielded better results, emphasizing the necessity of the adaptation phase (see Table 3.4, Figures 3.5 and

A.5). Comparing different sub-models of Model (3.3) showed that incorporating refractory cells (model names including R) was essential to allow for a reasonable description of the data (Fig. 3.10 and Table 3.4). Assuming refractory cells to be in a state of low activation and, thus, allowing their proliferation rate to differ from that of target cells, i.e., activated CD4 cells, improved the fits even further (model names including $\mathrm{R_p}$). However, due to the assumption of spatial homogeneity in the ODE model, it could not distinguish between cells not getting infected due to their activation state or because they encountered neither infective virus nor infected cells during the course of the experiment. While the proliferation of refractory cells was slowest in suspension, my model estimated the same proliferation rate for target and refractory cells in loose collagen. This could be linked to a high proportion of target cells, which encountered neither infective virus nor infected cells during the course of the infection, within the subset of refractory cells. The best model ($\mathrm{R_p}$-A-model), including death by abortive infection, however, over-fitted part of the data as indicated by a correlation of the rates governing death by abortive infection and the two transmission rates (not shown). This also limited the predictive power with respect to the contribution of each transmission mode to the infection dynamics. Additionally, the process of pyroptosis, i.e., abortive infection, has been reported only for kidney cells [127] and its occurrence in PBMCs is still debated in the field. In summary, the $\mathrm{R_p}$-model, i.e., a model with varying proliferation rates of refractory cells without death by pyroptosis, was the most informative model despite a slightly higher AICc-value than the $\mathrm{R_p}$-A-model.

An important aspect of modeling is to predict certain elements of the infection process that could not be observed experimentally. From simulating the infection with the most informative model, I was able to predict the proportion of cells infected by either transmission mode over the course of the experiment (Fig. 3.6A), which was not possible from an experimental point of view. While cell-free transmission was the dominant mode in suspension, cell-to-cell spread played an important role in collagen environments. However, estimates ranged widely indicated by large confidence bounds (Fig. 3.6B). Nonetheless, a relationship between environments with respect to the contribution of cell-free spread to infection was observed. Following an almost linear relationship on a log-log scale, the odds of getting infected by cell-free transmission were always highest in suspension (Fig. 3.6C). Between the two collagen environments, cell-to-cell spread contributed more to the infection dynamics in loose than dense collagen. After 21 days approximately 21% and 38% of infected cells were infected through cell-to-cell transmission in loose and dense collagen, respectively. This could be explained by low numbers of infected cells in loose collagen and subsequently low viral titers, thus, not allowing for cell-free transmission to occur. Surprisingly, blocking cell-free spread in collagen enhanced the infection in terms of maximal numbers of infected cells at peak of infection (Fig. 3.7). This could be explained by the delayed onset of infection, which in turn allowed for higher target cell densities. From an evolutionary point of view, this could suggest the shift of HIV towards more cell-to-cell transmission as this allows for higher viral loads in collagen. Furthermore, I performed an *in silico* experiment with high initial T cell densities. Here, high target cell counts at the start of the experiment benefited the spread of virus in loose collagen more than in the other environments (Fig. 3.8 and Fig. 3.9). A biological explanation of this could be the formation of more stable cell-cell contacts in loose collagen, thus, overcoming the disadvantage of fast moving cells in this environment. While high initial cell densities shifted the peak of infection towards early time points in dense collagen, the other environments showed no relevant change.

In summary, one needs to be careful when drawing conclusions concerning the contribution of each transmission mode from a single experiment as it seems to vary across different environments. Additionally, the infection dynamics are probably also shaped by the specific cell types used in an experiment. Comparing my result to that of Iwami *et al.*, who predicted around 40% of cells infected through cell-free spread in an experiment performed with Jurkat cells, an immortalized cell line [70], indicated a difference between the contributions of each transmission mode in aqueous media. However, both confidence intervals overlapped. Although, at first glance both predictions contradicted the findings that cell-to-cell is orders of magnitude more efficient than cell-free transmission [18–20], this could be reconciled when recalling the experimental limitations explained above. Independent of the exact contribution, a shift towards cell-to-cell transmission was observed in collagen environments compared to aqueous media. As most HIV infections of target cells in the body occur in the lymph node, which is fairly similar to the collagen structure, this might reflect the *in vivo* situation.

Summarizing this chapter, I developed a model that allowed the simultaneous prediction of the proportion of cells infected through cell-free transmission of HIV *in vitro* in suspension, loose and dense collagen at any given time.

4 Dissecting the contribution of cell-to-cell transmission to HCV spread in stationary cells *in vitro*

4.1 Introduction

In the previous chapter, I used population-level measurements to analyze how different environments shape the contribution of each transmission mode to HIV infections of motile T cells. In this case, the motility of target cells allowed the virus to spread to distant regions without the need of extracellular diffusion. In principal, the main contribution of transmission modes in HIV infection could be shifted towards cell-to-cell spread as motility of cells circumvents the local confinement inherent to cell-to-cell infections. However, movement of cells impedes cellular interactions, making cell-to-cell transmission more difficult. In stationary cells a different picture is painted. Although immobile cells enforce the need of cell-free transmission for far range spread, the immobility of target cells ensures long-lasting and stable cell-cell contacts hinting towards increased cell-to-cell spread. With regard to modeling of infection dynamics in stationary cells the assumption of a well-mixed system is violated due to local confinement of infection in the context of cell-to-cell transmission, making application of mass-action kinetics models difficult.

In this chapter, I present my studies on infections of stationary cells, namely hepatocytes, with the hepatitis C virus. It is known that HCV utilizes both modes of viral transmission [7]. However, the exact contribution of each mode to viral dissemination remains unknown. I analyzed how the immobility of target cells favors or impedes cell-to-cell spread. To account for the local process of cell-to-cell transmission among stationary cells, my collaborators conducted a spread assay experiment which resulted in spatially-resolved data, i.e., the focus size distribution of infected cells. In theory, a freely diffusing virus, which utilizes only cell-free transmission, should have more small foci than one depending solely on cell-to-cell transmission. Considering the spatially-resolved data, I developed a multi-scale, hybrid deterministic stochastic agent-based model, which describes HCV-infection of hepatocytes in a monolayer, resembling the experimental procedure with great detail. While viral intracellular replication in infected cells and the extracellular diffusion of the virus were modeled with discretized sets of differential equations, the infection processes occurred stochastically depending on the intra- and extracellular RNA counts.

To parameterize the intracellular replication occurring within infected cells, a mass-action kinetics model developed for the agent-based model was adapted and fitted to an additional experiment conducted by the Uprichard lab. Assuming that nearly all cells were initially infected, this experiment resulted in population-level measurements describing the intra- and extracellular RNA counts per infected cell over time. Next, using the agent-based model (ABM)

I generated *in silico* data, resembling the *in vitro* experiment. These data were used to fit the agent-based model allowing to compare estimated and true parameters. Furthermore, the predicted contribution of cell-free spread to the infection dynamics was analyzed with respect to the true contribution. Having the parameters governing intracellular replication and the knowledge of pyABC's ability to recover parameters at hand, the unknown parameters, e.g., transmission rates, governing the infection dynamics were fitted to the focus size distributions and the number of infected cells at various time points of two separate spread assays, namely Exp. 29D and Exp. 29J.

4.2 Experimental data of *in vitro* HCV infection dynamics

All *in vitro* experiments in this chapter were performed by the Uprichard lab, Department of Microbiology and Immunology, Loyola University Medical Center, Maywood, Illinois, USA. The experimental protocol is explained in Section 2.1.2.

4.2.1 Experiment 29D

In this data set focus sizes of infected cells at 48h, 72h, 96h and 120h after the start of the experiment were counted by my collaborators. This allowed to plot the focus size distributions as well as the number of foci, infected cell counts and the average focus sizes at indicated time points post infection (Fig. 4.1). The experiment was conducted in duplicates with (AntiE2, blue in Fig. 4.1) and without (UT, red in Fig. 4.1) the administration of anti-E2, which blocks cell-free transmission in HCV spread.

After 48 hours mainly small foci were observed in both scenarios and the focus size distributions were comparable. As time progressed, a discrepancy with respect to small foci developed between anti-E2-treated and untreated wells. As administration of anti-E2 blocked cell-free spread, the number of small foci was higher in the untreated cultures. This was also reflected in the lower total focus counts and larger average focus sizes for AntiE2 after 120 hours p.i. Counter intuition, the number of infected cells after 72 hours was higher when administering anti-E2. This might have been due to experimental variation as in one well a focus of size 100, more than 1.5 fold larger than the next largest focus, was observed (not shown). The administration of anti-E2 seemed to not completely block cell-free spread, indicated by the appearance of small foci of infected cells at all times in the treated wells. Judging from the data approximately 35 foci were initiated, assuming that all initially infected cells were positive after 72 hrs and, at that time, anti-E2 was still efficiently blocking the formation of new foci (Fig. 4.1B). Cell counts increased approximately 2.5-fold during the course of the experiment with no difference between untreated and anti-E2-treated cultures (Fig. 4.1C).

4.2.2 Experiment 29J

In this data set focus sizes of infected cells at 48h, 53h, 72h, 83h, and 96h after start of the experiment were counted. Again, this allowed to plot the focus size distributions as well as the

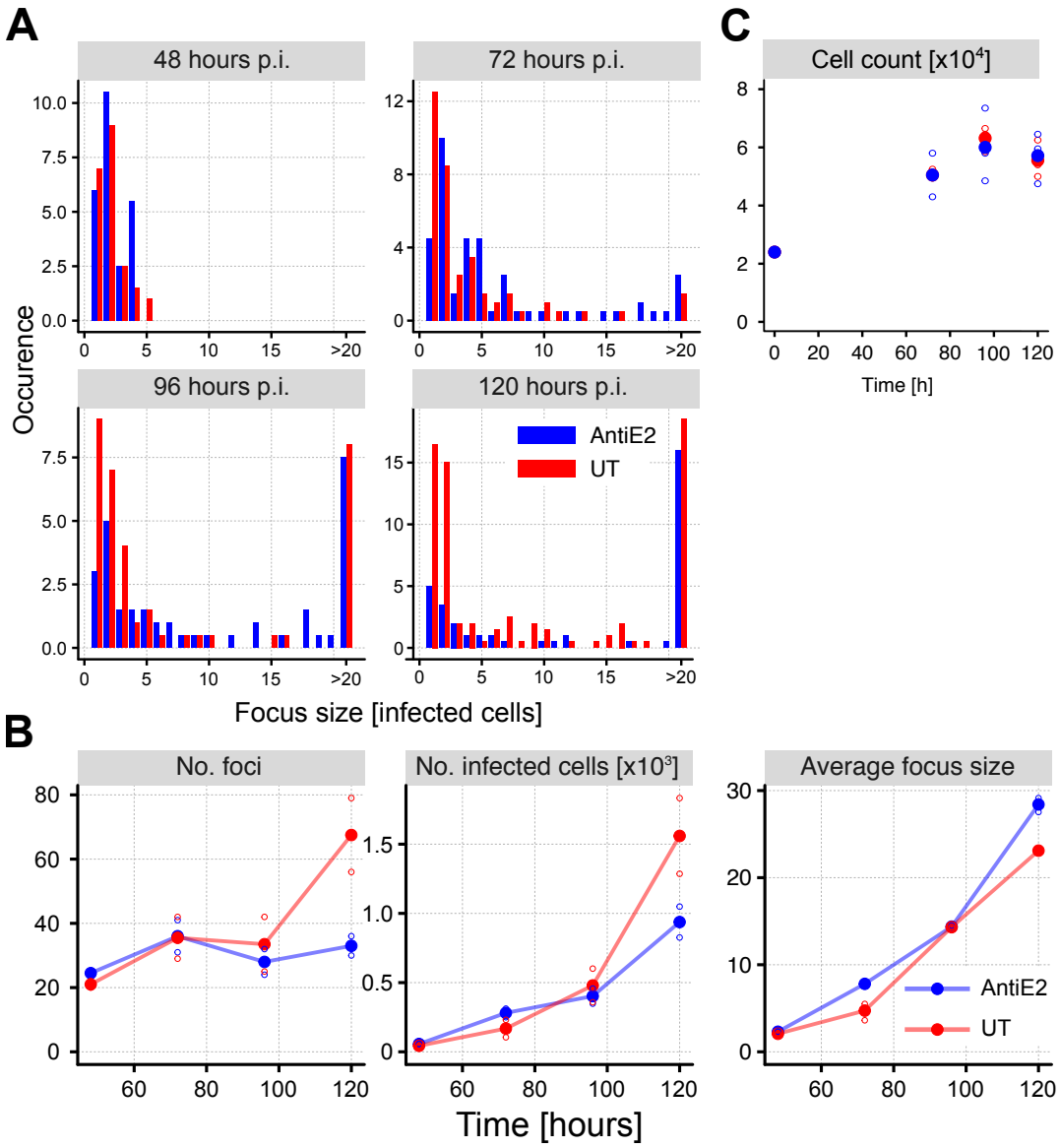

Fig. 4.1. **Experimental data of HCV spread *in vitro* as observed in Exp. 29D. (A)** Mean focus size distribution with (blue, AntiE2) and without (red, UT) anti-E2 calculated from two individual experiments at 48h (top left), 72h (top right), 96h (bottom left), and 120h (bottom right) post infection. For illustration purposes foci larger than 20 cells were combined to a single bin. In the data set this bin was resolved to account for all infected cells within a focus. **(B)** Mean (solid dots) number of foci (left), mean infected cell counts (middle) and mean average focus sizes (right) of AntiE2 (blue) and UT (red) calculated from two individual experiments (open dots). **(C)** Mean cell count (solid dots) calculated from three individual experiments (open circles) of cultures with (blue) and without (red) administration of anti-E2. Experiments were performed by the Uprichard lab, Department of Microbiology and Immunology, Loyola University Medical Center, Maywood, Illinois, USA.

number of foci, infected cell counts and the average focus sizes (Fig. 4.2). With the exception of AntiE2 at 83h p.i. (five replicates), the experiment was conducted using six replicates with (AntiE2, blue in Fig. 4.2) and without (UT, red in Fig. 4.2) the administration of anti-E2.

As in the previous data set, focus size distributions 48 hours p.i. were comparable between treated and untreated wells. In Exp. 29J, the difference between scenarios was already observable after 59 hours p.i., which reached its maximum 83 hours p.i. With regard to small foci, the anti-E2-treated cultures started to catch up with the untreated cultures after 96 hours p.i. Surprisingly, when administering anti-E2, the infected cell counts 96 hours p.i. were higher than in untreated cultures. This could not be explained and might have been due to experimental variation. Starting with lower initial cell counts compared to Exp. 29D, the proliferation of hepatocytes in untreated cultures was faster in this experiment, doubling every 24 hours and increasing approximately 10-fold. Following previously obtained results (personal communication Prof. Susan Uprichard), it was assumed that anti-E2-treated cultures would proliferate with the same rate as untreated cultures. Again, following the data, approximately 25 foci were initiated at the start of the experiment assuming that all initially infected cells were positive after 72 hrs and, at that time, anti-E2 was still efficiently blocking the formation of new foci through cell-free transmission (Fig. 4.1B).

4.2.3 Comparison of HCV spread data from two individual experiments

Even though the experiments followed the same experimental protocol, some differences could be observed between Exp. 29D and Exp. 29J. For example a doubling time of approximately 24 hours and a 10-fold increase of cells in Exp. 29J stood in contrast to a 32 hours doubling time and a 2.5-fold increase in Exp. 29D (Fig. 4.3C). This lead to final hepatocyte counts of 1.3×10^5 and 0.6×10^5 in Exp. 29J and Exp. 29D, respectively. Furthermore, the maximal number of infected cells observed in Exp. 29J was around four to six times higher than in Exp. 29D (Fig. 4.3B). The most striking difference between the experiments was observed when comparing the cumulative densities of focus size distributions (Fig. 4.3A). Here, the densities assumed completely distinct shapes indicating different infection kinetics underlying the two experiments.

4.3 Agent-based model of HCV infection dynamics

To make use of the spatially-resolved data sets provided by my collaborators, I developed an agent-based model, which described the infection of hepatocytes in a monolayer with HCV. It is an extension of a previously published model by Graw *et al.* [101]. In short, their ABM was a two-dimensional cellular automaton with a regular quadratic grid of 100×100 stationary hepatocytes, which could be uninfected, infected or infectious. On average, an infectious cell produced α viral RNAs per day and could infect uninfected neighbors by cell-to-cell transmission with a probability dependent on the scaling parameter β_c and the intracellular HCV RNA content. They assumed a Moore neighborhood, i.e., the number of neighbors per cell was eight. To resemble a well, the authors used closed boundary conditions meaning that no substances or cells could leave the domain.

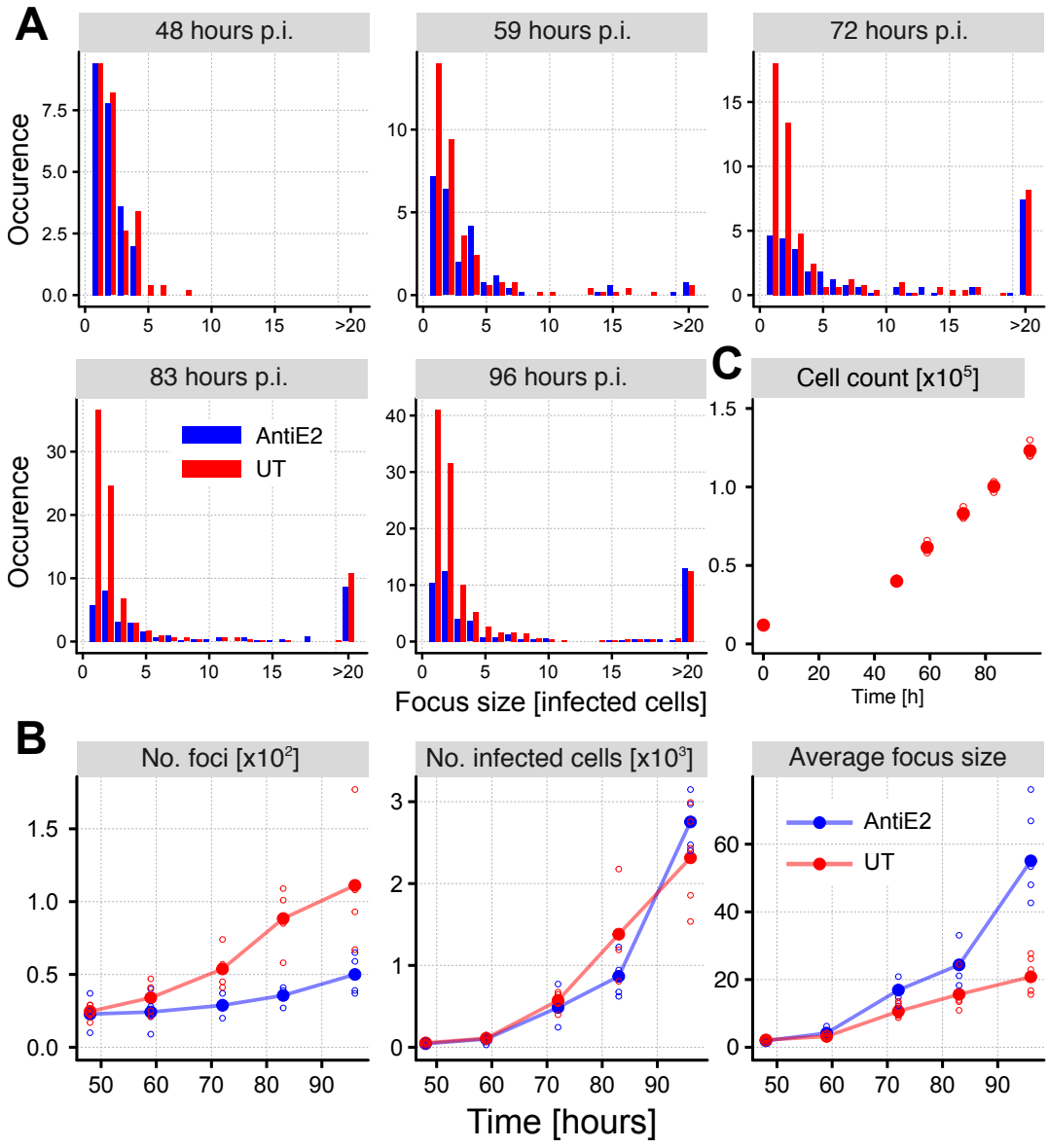

Fig. 4.2. **Experimental data of HCV spread *in vitro* as observed in Exp. 29J. (A)** Mean focus size distribution with (blue, AntiE2) and without (red, UT) anti-E2 calculated from five (83h, AntiE2) or six (all other measurements) individual experiments at 48h (top left), 59h (top center), 72h (top right), 83h (bottom left), and 96h (bottom right) post infection. For illustration purposes foci larger than 20 cells were combined to a single bin. In the data set this bin was resolved to account for all infected cells within a focus. **(B)** Mean (solid dots) number of foci (left), mean infected cell counts (middle) and mean average focus sizes (right) of AntiE2 (blue) and UT (red) calculated from five or six individual experiments (open dots). **(C)** Mean cell count (solid dots) calculated from three individual experiments (open circles) of untreated cultures. Experiments were performed by the Uprichard lab, Department of Microbiology and Immunology, Loyola University Medical Center, Maywood, Illinois, USA.

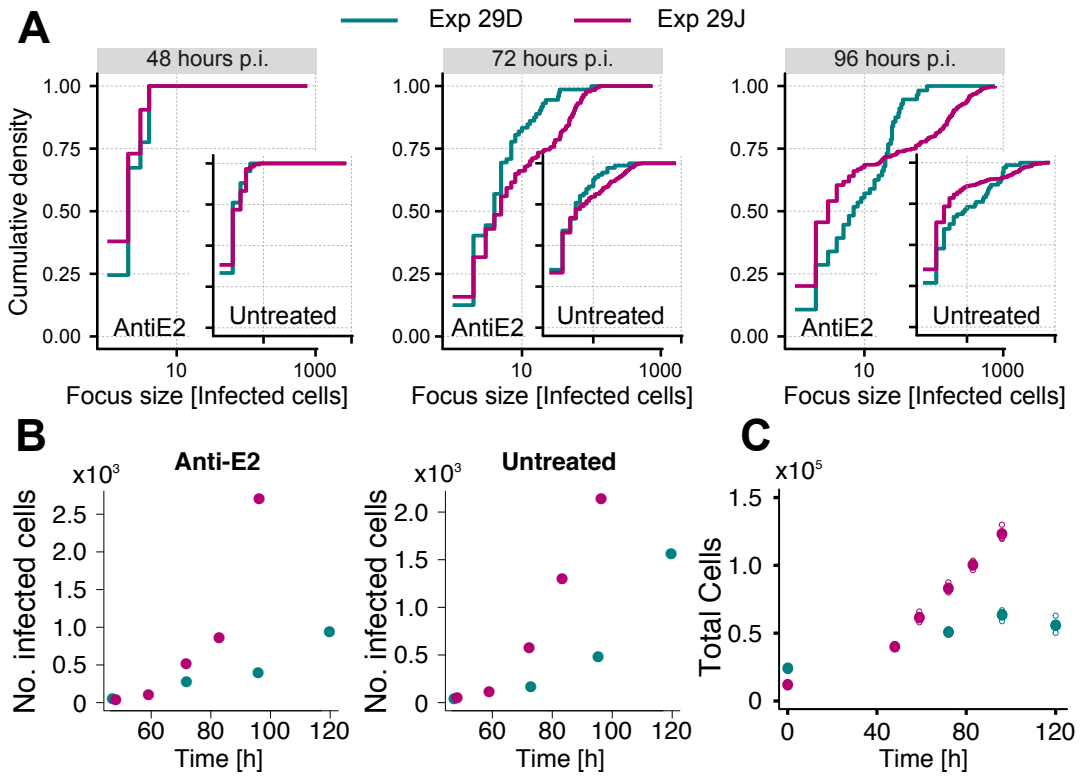

Fig. 4.3. **Comparison of two individual *in vitro* experiments of HCV spread.** **(A)** Large panels show the cumulative densities of focus size distributions obtained from Exp. 29D (blue-green) and Exp. 29J (purple) of anti-E2-treated (large panels) and untreated (inlays) wells after 48 hrs (top left), 72 hrs (top center) and 96 hrs (top right) on a logarithmic scale. Axis breaks are the same for large figures and the respective inlays. **(B)** Number of infected cells as measured in Exp. 29D (blue-green) and Exp. 29J (purple) with administration of anti-E2 (left) and without (right). **(C)** Total cells measured in untreated wells obtained from Exp. 29D (blue-green) and Exp. 29J (purple). Experiments were performed by the Uprichard lab, Department of Microbiology and Immunology, Loyola University Medical Center, Maywood, Illinois, USA.

I adapted their model to resemble the experiments performed by my collaborators with more detail. To account for the shape of hepatocytes, I used a hexagonal rather than a quadratic grid resulting in six neighbors per cell. In the simulations, the complete grid could hold 24031 cells with the outer edges being comprised of 90 cells similar to the numbers observed in the experiments. In a hexagonal grid, the total number of cells can be calculated depending on the number of cells on the outer edge, c:

$$\text{Total cells} = 3c^2 - 3c + 1 \tag{4.1}$$

In addition, I included proliferation of uninfected hepatocytes, which could proliferate into an empty adjacent grid site with probability $p \sim \mathcal{N}(\mu, (0.1\mu)^2)$ On average, cells were assumed to divide every 32 (*in silico* data and Exp. 29D) or 24 hours (Exp. 29J). In addition to Graw *et al.* [101] I introduced the possibility of a second mode of viral entry into uninfected hepatocytes, namely cell-free transmission. To this end, a second grid containing the extracellular viral concentration was included, overlaying and interacting with the cell-grid. Cell-free infection of uninfected hepatocytes occurred with a probability dependent on the virus concentration at the specific site and a cell-free scaling parameter, β_f. The extracellular virus was capable of diffusing through the extracellular space. This was modeled such that in each time-step a

fixed amount of HCV was able to diffuse to neighboring nodes, which was incorporated into the model as introduced in [134]

$$V_{i_0,j_0}(t_{n+1}) = V_{i_0,j_0}(t_n) - \frac{m}{k} \sum_{(i,j)\in\Omega} \left(V_{i_0,j_0}(t_n) - V_{i,j}(t_n)\right). \tag{4.2}$$

Here, $V_{i_0,j_0}(t_{n+1})$ is the extracellular HCV concentration at node (i_0, j_0) at time-step t_{n+1}. Parameter m describes the fraction of diffusing HCV particles and Ω is defined as the neighborhood of (i_0, j_0). The fraction of diffusing HCV particles is divided by the number of neighbors per cell, i.e., $k = 6$.

To compare the diffusion rate as implemented in the ABM with the theoretical diffusion coefficient of HCV in aqueous media, I needed to discretize the Laplacian (see Section 2.2.1). Discretization allowed me to re-write the diffusion equation as a difference equation, i.e.,

$$\partial_t x = D\Delta x \Leftrightarrow x(t+1) = x(t) - \frac{2\Delta t}{3\Delta h^2} D \sum_{i\in\Omega} \left(x(t) - x_i(t)\right), \tag{4.3}$$

where, h is the distance between two adjacent nodes and Δt is a time step in the simulation, i.e., one minute. Combining Eq. (4.2) and (4.3), the relation between diffusion coefficient and the coupling parameter on a hexagonal grid becomes apparent, i.e.,

$$m = \frac{4\Delta t}{\Delta h^2} D. \tag{4.4}$$

The diffusion coefficient of a spherical particle can be calculated using the Stokes-Einstein equation, $D = \frac{k_B T}{6\pi\eta r}$ [135], where k_B is Boltzmann's constant, T the absolute temperature, η the dynamic viscosity of the media, and r the radius of the spherical particle. The experiments were conducted at 310K in media with an approximate dynamic viscosity of $0.94 \times 10^{-3} \frac{\text{kg}}{\text{ms}}$ (at 298K, [136]). The radius of HCV was assumed to be approximately $30\ nm$ [137]. The diameter of a hepatocyte was taken as $20\ \mu m$, which resulted from personally evaluating photographs from the experiments, revealing diameters between 20 and $50\ \mu m$. With the Stokes-Einstein equation, the theoretical diffusion coefficient of HCV in the presented experiment was $D = 8.05 \times 10^{-12} \frac{m^2}{s} = 8.05 \times 10^{-2} \frac{\mu m^2}{s}$. Finally, this gave a coupling between lattice sites of $m = 4.83 \times 10^{-2}$. For the *in silico* data a higher coupling parameter was assumed, i.e., $m = 0.117$.

Adding to the approach chosen by Graw *et al.*, I explicitly modeled intracellular viral replication in infectious cells. The concentration of positive-sense single-stranded RNA ((+)ssRNA, in short positive-sense RNA), R, in an infectious cell at node (i, j) and its export is described with the following set of ODEs:

$$\begin{aligned} \frac{dR_{(i,j)}}{dt} &= \lambda R_{(i,j)} \left(1 - \frac{R_{(i,j)}}{R_c}\right) - \kappa R_{(i,j)} \\ \frac{dV_{(i,j)}}{dt} &= \kappa R_{(i,j)} - cV_{(i,j)}. \end{aligned} \tag{4.5}$$

In the simulation those ordinary differential equations were discretized to allow description with a set of difference equations:

$$R_{(i,j)}(t_{n+1}) = R_{(i,j)}(t_n) + \Delta t \left(\lambda R_{(i,j)}(t_n) \left(1 - \frac{R_{(i,j)}(t_n)}{R_c} \right) - \kappa R_{(i,j)}(t_n) \right)$$
$$V_{(i,j)}(t_{n+1}) = V_{(i,j)}(t_n) + \Delta t \left(\kappa R_{(i,j)}(t_n) - c V_{(i,j)}(t_n) \right).$$

Here, $R_{(i,j)}(t_n)$ and $V_{(i,j)}(t_n)$ are the intra- and extracellular RNA concentrations at node (i,j) and time t_n after initialization. In the simulation, I used time steps, Δt, of one minute. Intracellular HCV RNA, R, is produced with a maximal production rate λ, exported with rate κ, and able to reach a carrying capacity of R_c per infectious cell assuming no export. Extracellular virus looses infectivity with rate c. Administration of anti-E2, $E2$, was modeled such that it neutralized extracellular virus dependent on the initial anti-E2 concentration, $E2_0$

$$V_{(i,j)}(t_{n+1}) = \Delta t \kappa R_{(i,j)}(t_n) + V_{(i,j)}(t_n) \left(1 - \frac{E2(t_n)}{E2_0} \right) (1 - \Delta t c). \tag{4.6}$$

Furthermore, anti-E2 was assumed to be depleted/consumed at rate c_{E2} due to neutralization of extracellular virus as follows:

$$E2(t_{n+1}) = E2(t_n) - \sum_{(i,j)\in\Omega} c_{\mathrm{E2}} \frac{E2(t_n)}{E2_0} V_{(i,j)}(t_n), \tag{4.7}$$

where Ω is the set of all grid sites.

Whenever a cell was newly infected, it entered a re-orientation phase during which it could not contribute to cell-to-cell spread but was still producing virus. While the exact mechanism used by HCV during cell-to-cell transmission is unknown [7], all of the possible processes likely need time between successful transfer of virions from cell to cell. Therefore, I incorporated a re-orientation phase, which essentially provided a delay between successful cell-to-cell transmissions originating from the same infected cell. In the agent-based model I assumed the re-orientation phase lasted on average τ hours, following an exponential distribution.

As already mentioned above, HCV uses two different strategies to infect hepatocytes, namely cell-to-cell transmission and infection by cell-free virions, which were considered in the ABM as follows.

Cell-to-cell transmission

To model new infections by cell-to-cell transmission, a list of infected hepatocytes was used. For each infected cell existed the possibility of a cell-to-cell transmission. Assuming a Bernoulli trial with probability $p^c_{(i,j)}(t_n)$ gave a positive result for an infected cell at node (i,j) and there was at least one uninfected neighbor, an infection at time-step t_n took place, where $p^c_{(i,j)}(t_n)$ is defined as follows

$$p^c_{(i,j)}(t_n) := \beta_c \cdot R_{(i,j)}(t_n). \tag{4.8}$$

Here, β_c is the cell-to-cell scaling factor. The probability was capped at one. If cell-to-cell transmission was successful, intracellular viral RNA equivalent to R_0 from the cell at node (i,j) was subtracted assuming that R_0 viral RNA particles were needed to initiate infection. The cell originating the successful cell-to-cell transmission entered the same re-orientation phase as described for newly infected cells.

Cell-free transmission

The infection of hepatocytes by free diffusing, i.e., cell-free, virions is modeled using a probability $p^f_{(i,j)}(t_n)$ to infect a hepatocyte (uninfected or infected in the same time-step by CC) at node (i,j) at time t_n, which is calculated by the following equation:

$$p^f_{(i,j)}(t_n) = \beta_f \cdot V_{(i,j)}(t_n), \tag{4.9}$$

where β_f is the cell-free scaling factor. Again, the probability was capped at one. If infection of an uninfected hepatocyte at node (i,j) by cell-free virus was successful and the viral concentration at this site was higher than the concentration needed to initiate infection, R_0 was subtracted. In case it was smaller, the virus load of the surrounding nodes was also taken into account. One neighboring node was chosen at random and the viral concentration was subtracted. More nodes were chosen until in total R_0 viral particles were subtracted. Upon infection by either transmission mode, the initial intracellular RNA was R_0.

Simulation

Finally, the complete agent-based model was implemented in the C++ programming language and simulated for a fixed time (up to ten days) with discrete time steps of one per minute. For the first 17 hours of the simulation, a randomly chosen hepatocyte could get infected with the following probability at time t_n [117]:

$$p^{init}(t_n) := \frac{\alpha e^{-\alpha t_n}}{1 - e^{-17\alpha}}, \tag{4.10}$$

with $\alpha = c \times FFU$ describing the loss of viral infectivity multiplied by the focus forming units considered in the respective experiments to initiate infection.

After intracellular positive-sense RNA was produced in infected cells and exported, the described transmission modes were executed for each time-step. In a last step the extracellular virus was allowed to diffuse using the above explained mechanism.

4.4 Parameterizing the agent-based model

To predict the proportion of cells infected through either one of the transmission modes, correct description of the experimentally observed infection dynamics with the agent-based model is of paramount importance. The first step to achieve this, was fitting an ODE model, which described the intracellular viral replication and its export to the extracellular space, to experimental data obtained by infecting hepatocytes with a high initial inoculum. Next, this model and its best fitting parameters were incorporated into the ABM, which was subsequently fitted to focus size distributions and number of infected cells observed in two separate spread assay experiments (Section 4.2). To fit the agent-based model, I defined a measure describing the distance between experimental measurements and model predictions with respect to the relative difference of infected cell numbers and the relative area between cumulative density distributions of focus sizes dependent on the average focus size.

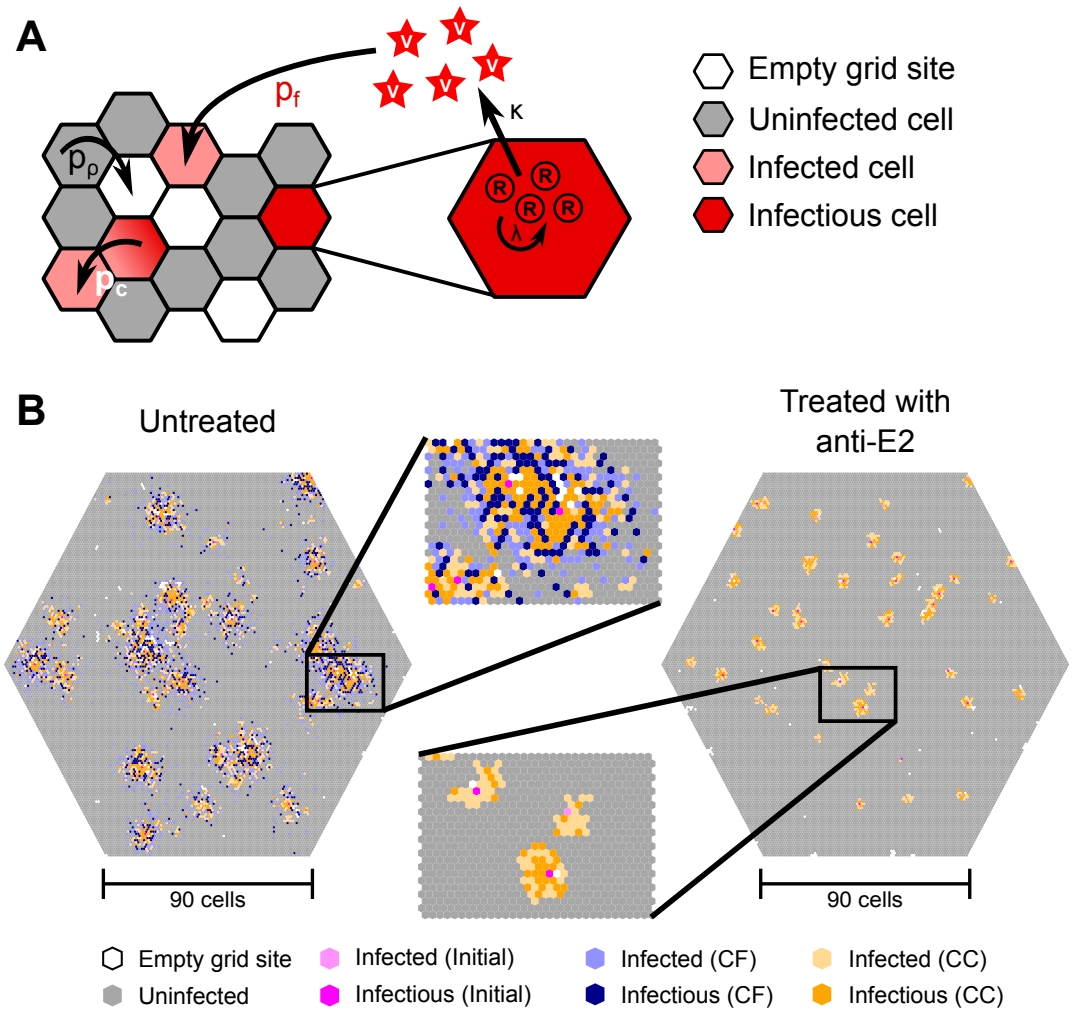

Fig. 4.4. **Sketch and realization of the agent-based model. (A)** Uninfected cells (gray) proliferate into empty grid sites (white) with probability p_ρ following a normal distribution with mean ρ and standard deviation 0.1ρ. Newly infected cells (light red) are in a latent phase during which they cannot infect neighboring cells via CC transmission. After a re-orientation phase in which infected cells spent on average τ hours following an exponential distribution, they become infectious (dark red), allowing them to contribute to CC transmission. Intracellular virus, R, is replicated within infected and infectious cells with rate λ up to an intracellular capacity of R_c and exported into the extracellular space at rate κ, where the virus, V (red stars), can diffuse freely. Viral cell-to-cell transmission from an infectious to a neighboring uninfected cell occurs with probability p_c, depending on the intracellular viral concentration and cell-to-cell scaling factor β_c. Upon successful CC transmission, the infectious cell becomes infected, thus, not contributing to CC transmission until re-transitioning into the infectious state. Cell-free infection of an uninfected hepatocyte depends on the extracellular viral concentration at the respective grid site and the cell-free scaling factor β_f. **(B)** Simulation of an individual ABM run after 4 days without (left) and with (right) the administration of anti-E2. Here, initially infected cells are marked in magenta, CF-infected cells in blue and CC-infected in orange. Light colors mark cells, which are currently in the re-orientation phase.

4.4.1 Intracellular replication and export of HCV

Experimental data describing intracellular viral replication and export

In order to retrieve the parameters governing intracellular replication of the virus and its export to the extracellular space, the Uprichard lab, Loyola University Medical Center, performed an additional experiment. The description of the followed experimental protocol can be found in Section 2.1.2.

In this experiment, viral intracellular replication was measured by infecting hepatocytes at a high multiplicity of infection (MOI=6) ensuring synchronous infection. Three hours p.i. the viral inoculum was removed. Despite removal of media, some viral particles adhered to hepatocytes resulting in high initial intracellular RNA counts as indicated by a drop between three and six hours p.i. (Fig. B.1A). Removal of viral inoculum seemed only partially successful as a decrease in extracellular HCV RNA levels was observed until 18 hours p.i. Afterwards counts increased, suggesting newly exported HCV RNAs (Fig. B.1B).

Estimating parameters governing intracellular HCV replication and export

I used a model that incorporated intracellular HCV RNA, R, residual, V_r and newly produced, V, extracellular HCV RNA, to parameterize intracellular replication in the agent-based model as described in Section 4.3. The parameter values resulted from fitting the model to experimental data obtained by infecting hepatocytes with high viral loads. The model is formulated as follows

$$\begin{aligned} \frac{dR}{dt} &= \lambda R\left(1-\frac{R}{R_C}\right)-\kappa R \\ \frac{dV_r}{dt} &= -c_r V_r \\ \frac{dV}{dt} &= \kappa R - cV \\ \text{with } R(0) &= R_0,\ V_r(0) = V_{r,0} \text{ and } V(0) = V_0 \end{aligned} \tag{4.11}$$

Here, each infected cell has a carrying capacity of positive-strand HCV RNA R_c, produces new RNA with maximal production rate λ and is exported with rate ρ. While exported extracellular RNA is subject to degradation at rate c, residual inoculum is degraded in the extracellular space at rate c_r.

To ensure parameter identifiability, degradation of intracellular RNA was neglected in model (4.11). Therefore, λ described a net proliferation already including degradation of RNA within infected cells. Additionally, I assumed loss of infectivity to occur at the same rate as degradation of extracellular RNA and fixed $c = c_r$ in the fitting routine. At three and six hours p.i. viral particles from the inoculum still adhered to cells skewing the measurements at these time points. Hence, these data were neglected in the fitting procedure (Fig. 4.5, gray dots).

The dynamics of intracellular viral replication and export were captured well (Fig. 4.5). To ensure validity of estimated parameter values, I performed a profile likelihood approach, which showed good identifiability of all parameters (Fig. B.2 and Table 4.1). Even though a reasonable description of the virus dynamics data, as presented in this section, could only be achieved when including the initial inoculum, V_r, into the model (not shown), it was not followed in the agent-based model. The excess amount of initial viral inoculum was not observed in the context of spread assay experiments, because infection was started with low initial viral titers.

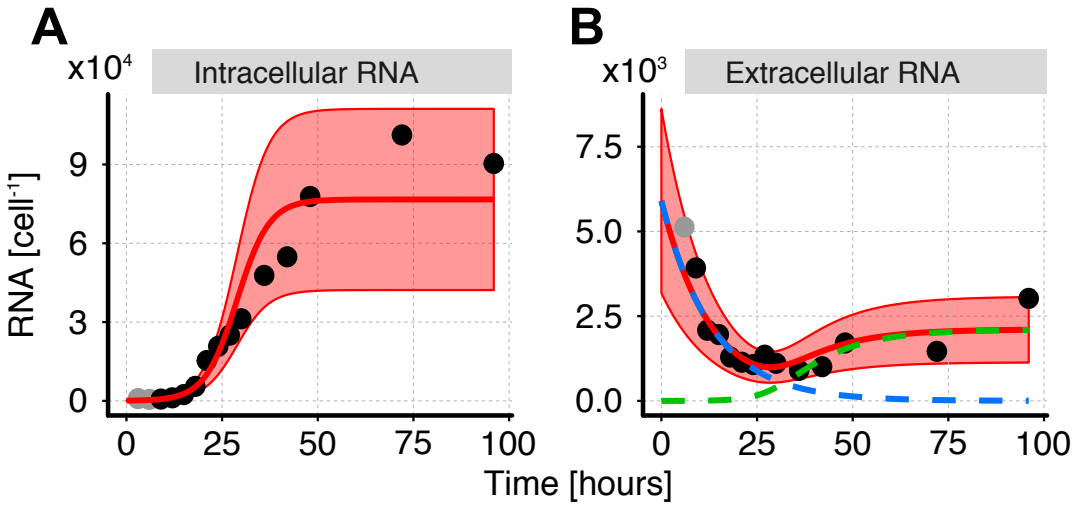

Fig. 4.5. **Estimation of intracellular HCV dynamics.** Mean values (black dots) of intracellular HCV RNA **(A)** and extracellular HCV RNA **(B)** calculated from three (intracellular) and two (extracellular) independent experiments. Best fit of model (4.11) (thick red line) with fitted 95% prediction band (shaded red area) to the experimental data. Newly exported extracellular RNA and residual inoculum are shown in dashed green and blue lines, respectively. Time points 3h and 6h p.i. were not considered in the fitting procedure (gray, see main text for more information). Extracellular RNA levels 3h p.i. are not shown for illustration purposes. Corresponding parameter estimates can be seen in Table 4.1.

Tab. 4.1. **Estimated parameter values governing viral kinetics.** Shown are the best fitting parameters with respective 95%-confidence intervals (CI) in brackets resulting from a profile likelihood approach.

Parameter	Description	Unit	Value [95%-CI]
R_0	Initial intracellular HCV RNA	RNA cell^{-1}	80.07 [42.2, 192]
V_0	Initial residual extracellular HCV RNA	$\times 10^3$ RNA cell^{-1}	5.91 [3.66, 10.5]
λ	Intracellular RNA production rate	h^{-1}	0.240 [0.194, 0.278]
κ_V	Export rate of intracellular RNA	$\times 10^{-3}$h^{-1}	2.10 [1.24, 3.47]
R_C	Carrying capacity of intracellular HCV RNA	$\times 10^4$RNA cell^{-1}	7.73 [6.30, 9.76]
c_r	Viral degradation and loss of infectivity	$\times 10^{-2}$h^{-1}	7.58 [4.88, 11.0]

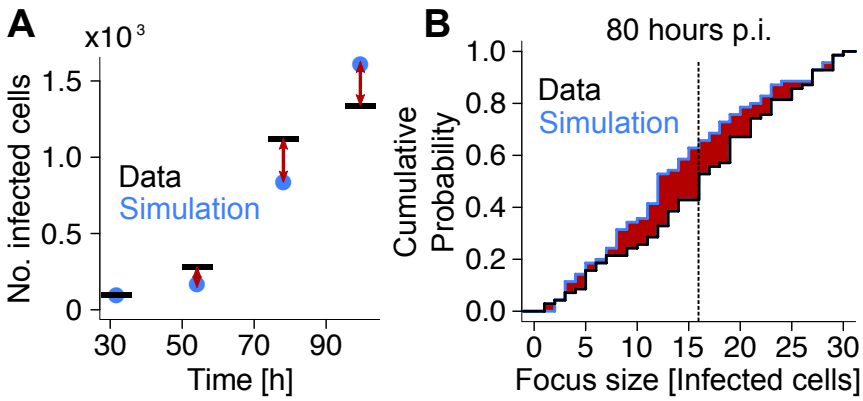

Fig. 4.6. **Sketch of distance measure used for fitting ABM to *in silico* or *in vitro* data.** **(A)** Shown is the absolute distance (red arrows) between hypothetical experiment (black lines) and prediction (blue dots). **(B)** The enclosed area of the hypothetical measured (black) and predicted (blue) cumulative density functions of the focus size distribution after 80 hours is indicated with the red shaded area. The dashed line indicates the measured average focus size.

4.4.2 Infection dynamics of HCV

With the parameters governing intracellular viral replication and export at hand, I parameterized the infection dynamics observed in spread assay experiments using a distributed, likelihood-free inference method, namely pyABC (for more information see Section 2.2.2). In a first step, I formulated a distance measure to describe the difference between data and model that was minimized with the help of pyABC. To ensure that this was a reasonable measure and that pyABC converged to the correct solution, I generated *in silico* data which were subsequently fitted. The estimates and predictions were then compared to the true parameters and the percentage of cell-free infected cells. Finally, I applied the fitting procedure to two sets of *in vitro* data to predict the contribution of each transmission mode to the infection dynamics.

Distance measure

Judging from the data, I wanted to capture the changing focus size distributions as well as the number of infected cells over the course of the experiment. To this end, I defined a relative distance between the predicted, I_{pred}, and measured, I_{exp}, total number of infected cells as follows

$$d_I = \frac{|I_{\mathrm{exp}} - I_{\mathrm{pred}}|}{I_{\mathrm{exp}}}. \tag{4.12}$$

To describe the focus size distribution (fsd), I calculated the predicted, f_{pred}, and measured, f_{exp}, cumulative density function for the occurrence of a focus with a specific size I and divided the resulting enclosed area between prediction and experiment by the average focus size

$$d_{\mathrm{fsd}} = \frac{\sum_I |f_{\mathrm{exp}}(I) - f_{\mathrm{pred}}(I)|}{\sum_I I n_{i,\mathrm{exp}}}. \tag{4.13}$$

In this equation the relative frequency of each focus size in the experiment is denoted with $n_{i,\mathrm{exp}}$. Dividing by the average focus size allowed comparable distances between early and late time points as the occurrence of large foci at late times would otherwise bias the calculated distance. A sketch of the individual distances is shown in Fig. 4.6.

The sum of both distances formed the total distance of the prediction from the experiment, i.e., $d_{\text{total}} = d_I + d_{\text{fsd}}$. This distance was calculated for each scenario, i.e., with and without administration of anti-E2. Finally, the complete distance was minimized using a likelihood-free method implemented in pyABC (see Section 2.2.2 for more information).

Recovery of parameters and predicted contribution of transmission modes using *in silico* data

Generation of *in silico* data. To test the ability of pyABC (see Section 2.2.2) with regard to recovery of the true parameters and, additionally, correct prediction of the contribution of each transmission mode, I generated *in silico* data. This yielded the knowledge of the true parameters and also allowed to neglect measurement uncertainties. The data were generated by simulating HCV spread in a monolayer of hepatocytes with help of the agent-based model as described in Section 4.3. In the experiments, it took some time until infected cells were detectable by NS5A- (Exp. 29D) or MAb AR3A-staining (Exp. 29J). To account for this, I assumed a time delay of 18 hours between time point of infection and detection with the applied visualization technique (personal communication Prof. Susan Uprichard). To mimic the experimental situation, the same time delay was also applied to the *in silico* data. Generating the *in silico* data, I assumed that infected cells halted their intracellular viral replication and degradation during the re-orientation phase following a successful cell-to-cell transmission and consequently keeping constant levels of intracellular RNA. When fitting to the experimental data, this was not the case. For each scenario, i.e., with and without administration of anti-E2, I ran the agent-based model five times. The parameters used to generate the data are shown in Table B.2, the focus size distributions as well as the number of infected cells, foci numbers and average focus sizes in Fig. B.4. In these data, approximately 20 percent of cells were infected with cell-free transmission after 120 hours (Fig. B.4C).

Fitting the agent-based model to *in silico* data. In the fitting procedure, I estimated the same parameters that were fitted with the *in vitro* data, i.e., the cell-to-cell, s_c, and cell-free, s_f, transmission rate scaling factors, the average re-orientation time after a successful cell-to-cell transmission, τ, and the amount of antibody necessary to neutralize extracellular RNA, c_{E2}. I ran the fitting procedure for 15 generations where each generation needed at least 100 individual simulations with a lower distance than the median distance of the previous generation. This accumulated in 35078 model evaluations with each evaluation using a different set of parameters. The median and lowest distance of the last generation were 1.67 and 1.31, respectively. A summary of the pyABC run is shown in Table B.1. An exemplary fit of a particle with distance 1.31 (ID 1) can be seen in Fig. B.5, which shows close resemblance of the prediction to the data for the focus size distributions as well as the number of infected cells. However, as indicated by the varying parameter values of the best fitting model realizations (Fig. B.6), stochasticity had a strong impact on the individual realizations and, accordingly, the distance between model output and data. Thus, ensembles of parameters should be considered rather than parameters from individual runs. This was achieved with the estimated kernel density of pyABC, which was calculated using the accepted particles within one generation. The estimated densities of the final generation are shown in Fig. B.6. Analyzing the estimated kernel densities revealed recovery of the re-orientation phase and the cell-free transmission scaling factor within small bounds. While the estimated amount of anti-E2 necessary to neutralize extracellular RNA was still reasonably confined, varying across 1.5 orders of magnitude, the cell-to-cell transmission scaling factor s_c spanned three orders

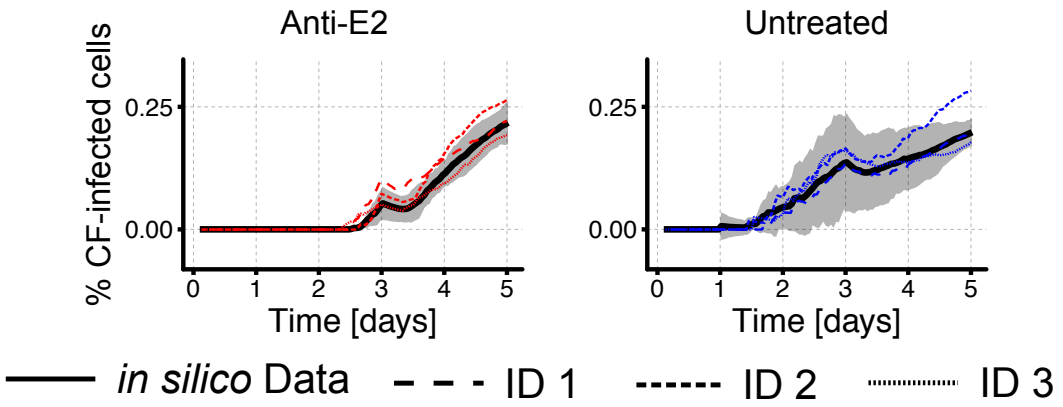

Fig. 4.7. **Proportion of cells infected through cell-free transmission.** The average percentage of cell-free infected cells with 95%-confidence intervals calculated from the *in silico* data are shown for anti-E2-treated (left) and untreated (right) cultures. Colored lines indicate the predicted proportions of three exemplary particles with distances below 1.34 obtained from the pyABC fitting routine. Parameters of these evaluations are shown in Fig. B.6 and as an example the fit of ID 1 in Fig. B.5.

of magnitude. However, this was not surprising as the probability for a successful cell-to-cell transmission was proportional to the intracellular RNA level, which was approximately 7×10^4 after 2 days. Taking the true parameter of $10^{-2.5}$ in the *in silico* data into account implied that a successful cell-to-cell transmission took place in case an infected cell was not in re-orientation phase two days after its initial time of infection with an uninfected cell in its neighborhood. Even for scaling factors as small as 1.5×10^{-5} $(\text{min} \times \text{intra RNA})^{-1}$ this held true.

Independent of the actual parameters, more importantly, all particles with a low distance predicted the contribution of cell-free spread to the infection dynamics correctly (Fig. 4.7). This gave confidence to apply my model with the help of pyABC also to experimental data and, using the obtained results, to infer the contribution of each transmission mode to the infection dynamics over the course of an experiment.

Inferred contribution of transmission modes to *in vitro* HCV infection dynamics

Even though recovery of the correct parameters was difficult due to the stochasticity of the model and experiments, my model predicted the correct contribution of each transmission mode to the infection dynamics. With this at hand, the model was fitted to two different experiments, namely Exp. 29D and Exp. 29J. In this process, all data were shifted by 18 hours to account for the delay between infection time point of a cell and detection with the applied visualization technique.

Fitting Experiment 29D. The data of this experiment are shown in Fig. 4.1. Here, I assumed an average doubling time of uninfected hepatocytes of 32 hours [16] and allowed for a 2.5-fold increase of cells as observed in the data (Fig. 4.1C), i.e., 60% of the grid was empty at the start of the experiment. Even though cell numbers in the agent-based model were approximately 2.5-fold lower than observed in the experiment, this had no effect on the infection dynamics due to low proportions of infected cells (maximal 4% at any time in the experiment, i.e., maximal 7.5% in the ABM.).

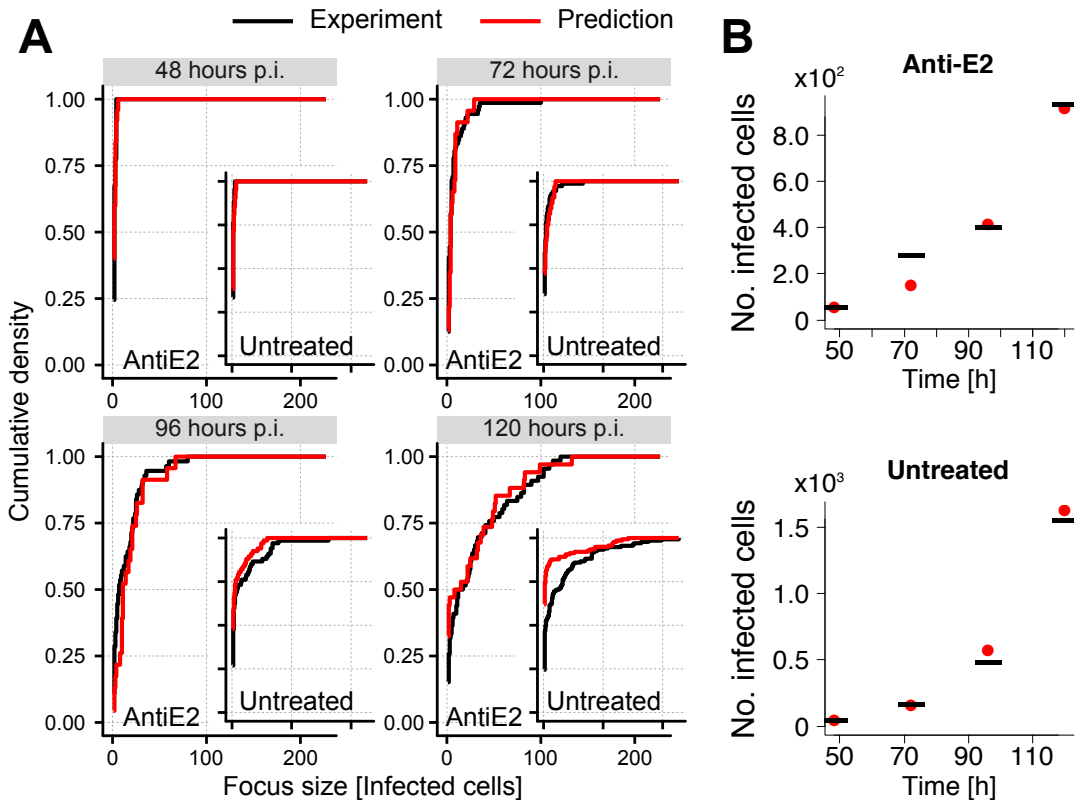

Fig. 4.8. **Fit of ABM to *in vitro* data of HCV spread as measured in Exp. 29D. (A)** Large panels show the predicted (red) and measured (black) cumulative densities of focus size distributions with (large panels) and without (inlays) administration of anti-E2 after 48 hrs (top left), 72 hrs (top right), 96 hrs (bottom left) and 120 hrs (bottom right). Average measured cumulative densities were calculated from two replicates. The predicted values stem from the best fitting run obtained from pyABC after 15 generations (termed ID 1 in Figures 4.9 and Fig. 4.10). Axis breaks are the same for large figures and the respective inlays. **(B)** Mean number of infected cells, calculated from two replicates, (black lines) and the prediction (red dots) in untreated (top) and anti-E2-treated (bottom) wells.

While the cumulative densities of the focus size distributions at most time points were captured well, the model had difficulties explaining the last time point in the untreated wells predicting too many small foci (Fig. 4.8A). This shortcoming of the model could be linked to the beforehand fixed diffusion rate of extracellular virus. Besides this, the number of infected cells was fitted well for the anti-E2-treated and untreated wells, except the 72h time point in the anti-E2-treated wells (Fig. 4.8B). However, the number of infected cells at this time point was unexpectedly high due to an outlier in focus sizes of infected cells in one of the wells (1.5-fold larger than any other focus) and a small sample size of only two replicates.

Within the last generation of pyABC, some parameter values varied less than others, indicating strong influence on the infection dynamics of those parameters estimated within small bounds (Fig. 4.9). For example, the re-orientation phase after a successful cell-to-cell transmission was estimated within small bounds varying between 17 and 24 hours. While the cell-free scaling factor varied about one order of magnitude, the cell-to-cell factor assumed values across almost three order of magnitude. However, this was to be expected as the re-orientation phase should have a stronger influence on the infection dynamics when the cell-to-cell transmission factor is larger than $1.5 \times 10^{-5}\ \mathrm{min} \times \mathrm{intra\ RNA}^{-1}$ (see the previous paragraph for more information). Although, the estimated amount of antibody necessary to neutralize

extracellular virus ranged over several orders of magnitude, the bulk of estimates predicted rather similar values with only some outliers. Running pyABC for more generations could resolve the problem of parameter identifiability in this case. A negative correlation between the re-orientation phase and cell-to-cell scaling factor was observed because decreasing the former could be compensated by also decreasing the latter. A similar trend emerged from the fitting routine between the neutralization rate of anti-E2 and the cell-free scaling factor. Comparing the best fitting parameter sets (colored dots in Fig. 4.9) showed large variations for some parameters, illustrating, besides the influence of certain parameters on the infection dynamics, also the stochasticity of the agent-based model.

Judging from the best fitting particles obtained by running pyABC for 15 generations, cell-to-cell transmission was initially the only source of infection in Exp. 29D (Fig. 4.10). Approximately one day p.i. enough extracellular virus was produced leading to the first cell-free infected cells (Fig. 4.10). As expected from Fig. 4.9, the proportion of cell-free infected cells over the course of the experiment was differed between ID 2 and the other particles. Especially an early increase of cells infected by cell-free virions in anti-E2-treated wells was observed for this particle. However, despite the differences between parameter sets with respect to the proportion of cell-free infected cells, the percentage was always below 25%. This indicated a dominant role of cell-to-cell transmission in the infection dynamics of HCV in Exp. 29D (Fig. 4.10). While the appearance of cell-free infected cells was slightly delayed in anti-E2-treated compared to untreated wells, the proportion of cell-free infected cells was approximately the same at the end of the experiment regardless their treatment for most particles with low distances to the data (2/4 in Fig. 4.10). The decrease observed in the proportion of cells infected through cell-free transmission after 72 hours p.i. was due to the media change removing all extracellular virus from the supernatant.

To investigate the influence of stochasticity and the stability of certain parameter sets, I ran ten replicates for eight parameter sets fitting best as obtained from pyABC and calculated the distance of each replicate to the data (Fig. 4.11). I also used the replicates to calculate average dynamics and compared it to the data. This showed that the best fitting particle exhibited large distances. In contrast, distances of the individual replicates with parameter sets of IDs 4 and 5 were closer to the distance obtained from pyABC and varied less than replicates of ID 1, indicating that the latter parameter set was chosen by pyABC as good fitting due to an outlier in the infection dynamics.

Fitting Experiment 29J. To evaluate the predictions using the previous data, my collaborators repeated the experiment (Exp. 29J). The data of this experiment are shown in Fig. 4.2.

In this experiment a doubling time of approximately 24 hours and a 10-fold increase of cells was observed (Fig. 4.2). Because cells in my agent-based model kept their size, empty space needed to be introduced to allow cell-proliferation. This lead to changing numbers of neighbors per cells as only cells on adjoining grid sites were considered neighbors. A ten-fold increase as observed in the data would result in 90% empty space in the simulations at the beginning leading to few neighbors per cell. To test if this was necessary, the neighbor distribution in the experiments from 48 hours onwards was analyzed by my collaborators. This revealed that the number of neighbors per cell stayed approximately constant as cells decreased in size during the course of the experiment. To keep the two *in vitro* experiments comparable, I allowed a 2.5-fold increase from initial cell counts in the ABM, which implied a

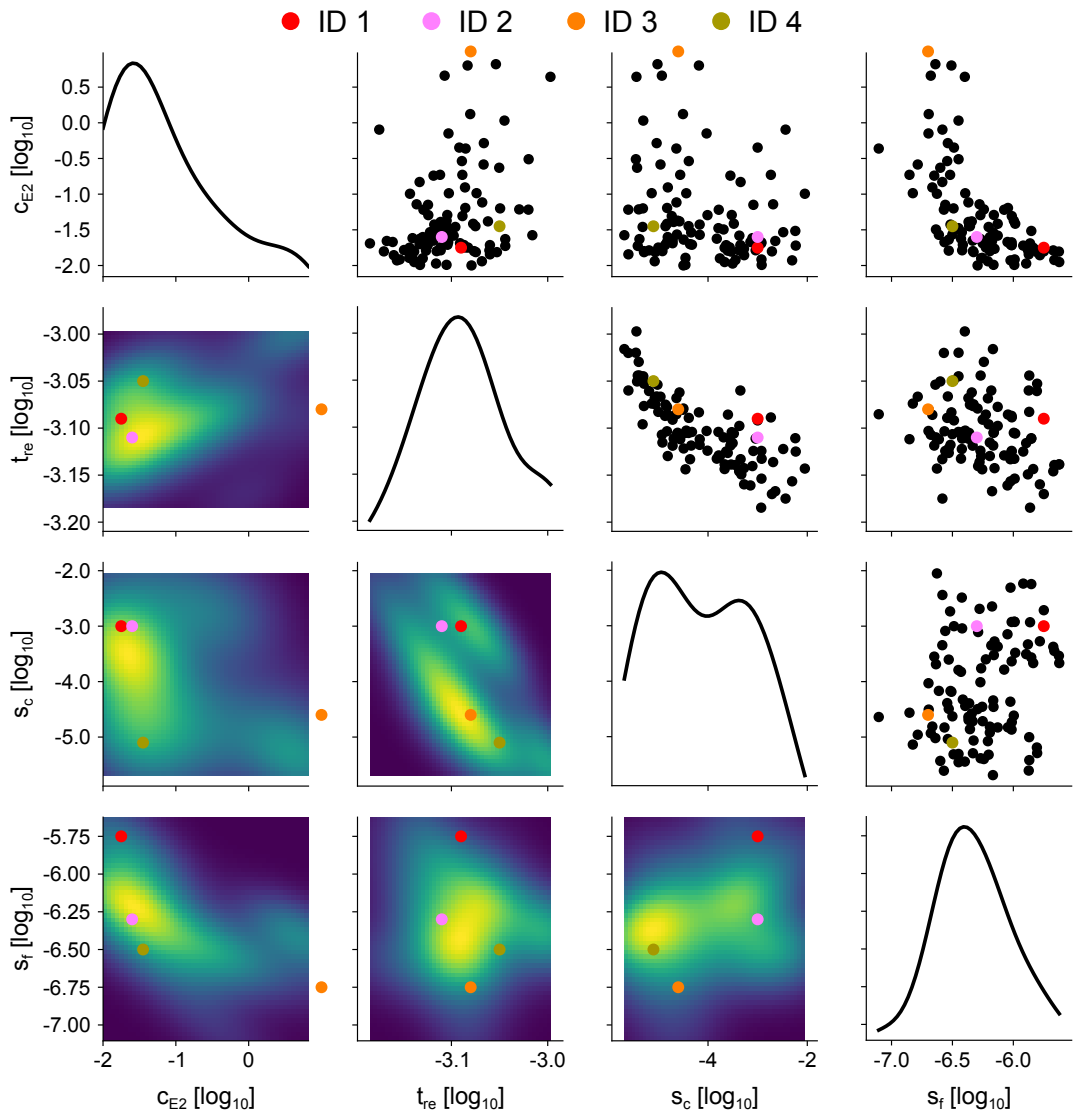

Fig. 4.9. **Estimated kernel densities after 15 pyABC generations of parameters fitted to *in vitro* data as measured in Exp. 29D.** 1^{st} row and column show the amount of anti-E2 necessary to neutralize one extracellular RNA in arbitrary units. 2^{nd} row and column display the rate of re-orientation after a successful cell-to-cell transmission per minute. 3^{rd} and 4^{th} row and column show the cell-to-cell and cell-free scaling factor, respectively. Panels above the diagonal present 100 individual parameter combinations (black), which had a distance smaller than 4.46 and below the diagonal the corresponding estimated two-dimensional kernel densities. The kernel density estimates of each parameter are shown on the diagonal. The parameters of the four best fitting realizations after 15 generations run with pyABC are indicated with red (ID 1), rose (ID 2), orange (ID 3) and olive green (ID 4).

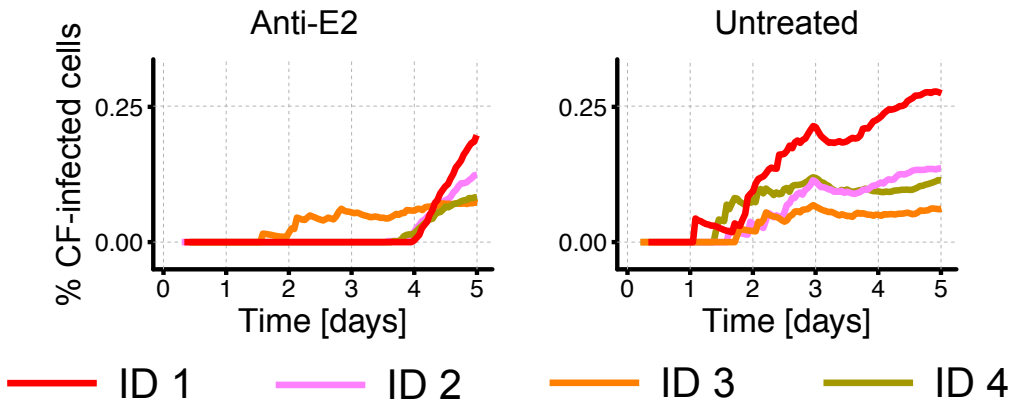

Fig. 4.10. **Predicted proportion of CF-infected cells in Exp. 29D.** The predicted percentage of cell-free infected cells over the course of the experiment of the four best particles as obtained from the pyABC fitting routine, i.e., ID 1 (red), ID 2 (rose), ID 3 (orange) and ID 4 (olive green). Left panel shows anti-E2-treated and right panel untreated wells. Parameters of these evaluations are shown in Fig. 4.9 and as an example the fit of ID 1 in Fig. 4.8.

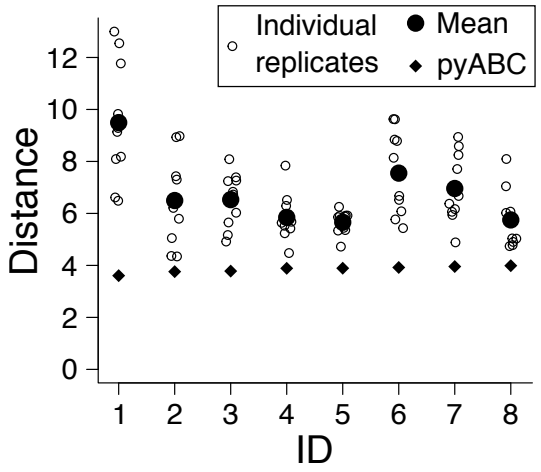

Fig. 4.11. **Distances of ten replicates using the best parameter sets obtained from pyABC fitting to Exp. 29D.** Diamonds indicate the distance as returned from pyABC. Using the parameters obtained from pyABC solid dots show the distance of the average dynamics calculated from individual replicates (open circles).

full grid after approximately 48 hours with the assumed doubling time of 24 hours, leading to six neighbors per cell. The maximal number of infected cells observed in the data of Exp. 29J was around 3×10^3 cells. With the previously used grid structure this accounted for approximately 12.5% infected cells in the model. The low percentage ensured that target cell limitation was not an issue and allowed me to use the smaller and computationally cheaper grid even though total cell numbers observed in the experiment reached up to 1.3×10^5, around 5-fold higher than the maximal number of total hepatocytes in the ABM.

Several approaches to describe the data with my agent-based model were undertaken. In a first step, all data were used for fitting. This showed that the agent-based model was not able to capture the number of infected cells in either scenario at 96 hours p.i. due to the surprisingly fast increase in the anti-E2-treated and the slow increase in untreated wells between 83 and 96 hours p.i. (see Fig. B.7). However, the last time point had some technical issues and was, thus, not considered in the following analysis (personal communication Prof. Susan Uprichard).

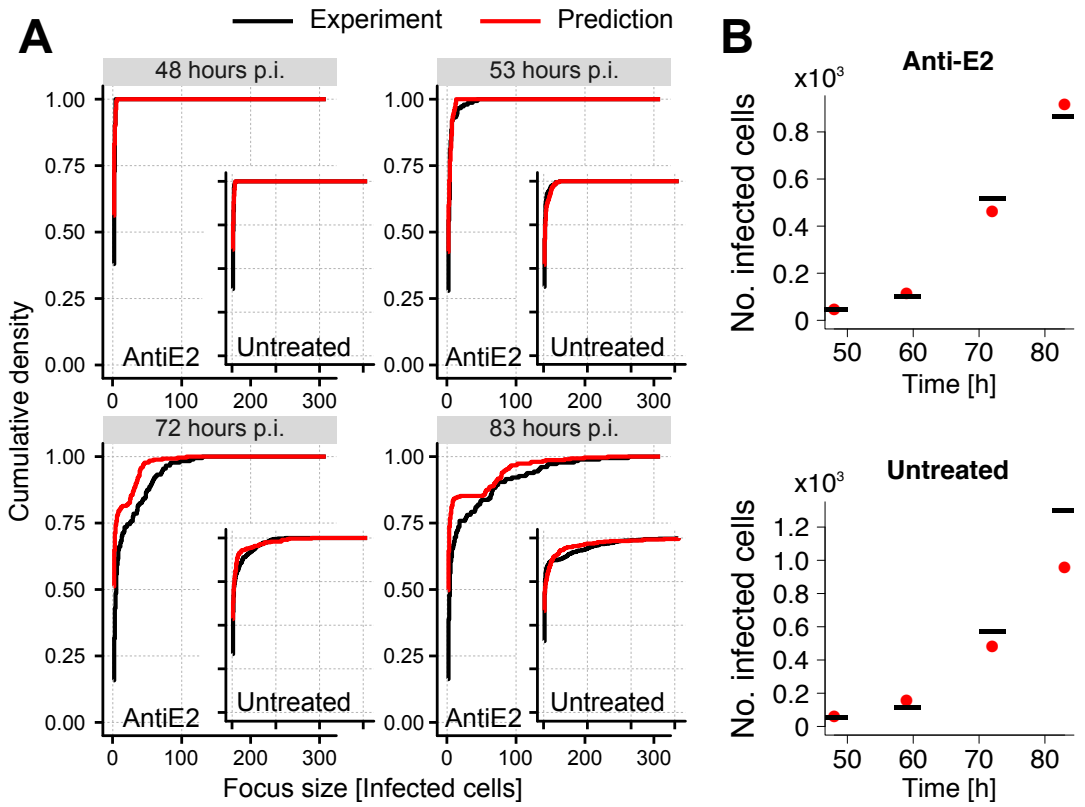

Fig. 4.12. **Average measured and predicted HCV infection dynamics of Exp. 29J.** In the fitting procedure the last time point of the experiment was neglected (see main text for more information) and each particle of pyABC used five individual ABM-simulations to calculate average infection dynamics. **(A)** Measured (black) and predicted (red) cumulative densities of focus size distributions with (large panels) and without (inlays) administration of anti-E2 after 48 hrs (top left), 59 hrs (top right), 72 hrs (bottom left) and 83 hrs (bottom right) calculated from 5-6 replicates. Axis breaks are the same for large figures and the respective inlays. **(B)** Predicted (red dots) and measured (black lines) average number of infected cells in untreated (top) and anti-E2-treated (bottom) wells calculated from 5-6 replicates. Predictions stem from the third best fit (ID 3, parameters shown in Fig. 4.13) obtained by running pyABC for 13 generations fitting average cumulative densities and mean number of infected cells, which were both calculated from five to six replicates, obtained from Exp. 29J neglecting data from 96h p.i.

Because my model was overestimating the number of small foci at late times (not shown), I reconsidered the theoretically derived diffusion rate used when fitting Exp. 29D. Virions released from an infected cell might not diffuse freely, but rather infect adjacent cells. Therefore, the theoretically derived diffusion rate of extracellular virions could be too high as it was calculated for freely diffusing particles. To account for this, I also fitted the diffusion rate in the following. Despite this approach, comparison of predicted and measured focus size distributions after 72 hours p.i. showed that my model was not able to capture the large variety of different focus sizes observed in the data (Fig. B.8). This could be linked to fitting individual simulations to data averaged over five to six independent replicates. In a last step, I therefore used averages of five agent-based simulations with the same parameter set to describe the averaged dynamics obtained from the experiment. Judging from the lowest distance reached (Averaged: 3.66 vs. Individual: 4.23, see Table B.1), this approach described the data better. Furthermore, visually comparing predicted and measured focus size distributions showed less deviation in the latter fitting approach (Fig. 4.12).

Studying the distribution of estimated parameter values of the 13^{th} pyABC generation indicated that more generations could improve the fit further as some outliers with respect to parameter values were found in this generation while the best fitting particles assumed similar values (Fig. 4.13). Presumably due to stopping pyABC early, all parameters varied largely except the extracellular viral diffusion rate. Interestingly, the estimated values of the diffusion rate were all smaller than the theoretically derived rate, following the above reasoning, while still in the same order of magnitude. Considering only the parameters with the smallest distances, the re-orientation phase varied between 33 and 42 hours. As pointed out previously, cell-to-cell scaling factors below 1.5×10^{-5} could not be identified. Taken together, this implied comparable values for the particles shown in Fig. 4.13 across all parameters.

With the particles obtained from running pyABC for 13 generations, I predicted the contribution of each transmission mode to the infection dynamics. After an initial phase during which only cell-to-cell transmission occurred, enough virus was produced and exported, leading to the first appearances of cell-free infected cells after approximately one day p.i. in the untreated wells (Fig. 4.14). Although the appearance of cell-free infected cells in the anti-E2-treated wells was delayed, these wells caught up to the untreated ones with respect to the proportions of cells infected through cell-free transmission, resulting in approximately 75% at the end of the experiment (Fig. 4.14). In Exp. 29J the media change after 72 hours was not observed as incorporating a time shift of 18 hours into the data meant that the last measurement was compared to the simulation output after 65 h.

To evaluate the influence of stochasticity on the estimated parameter values, I ran ten replicates for the five best fitting parameter sets. Keeping the same structure as previously, I used 5 individual ABM-simulations to calculate average dynamics per replicate. This showed that the distances obtained with pyABC were reasonably close to the ones from the individual replicates, indicating little stochasticity between replicates of a given parameter set (Fig. 4.15). Surprisingly, one replicate even resulted in a lower distance than accomplished with pyABC.

Long-term predictions and synergistic effects of transmission modes

Being able to describe the data reasonably well with my agent-based model, I made use of the ABM to predict the long-term HCV infection dynamics for both experiments over the course of ten days post infection. Furthermore, I studied possible synergistic effects between the transmission modes.

Long-term HCV infection dynamics For both experiments, I used ten replicates of the best fitting IDs as obtained from pyABC. In Exp. 29D however, this parameter set presumably fitted the data well only due to stochastic effects. To account for this, I also looked at the fourth best fit, which showed little variation between individual replicates and each was rather close to the distance obtained from pyABC. Indeed, the number of infected cells for ID 1 was too high compared to the data (not shown). Because ID 1 was rather stable in Exp. 29J, I chose a parameter set exhibiting more variation, i.e., ID 3. Despite differences between the different parameter sets and experiments, a trend was observed. The proportion of cell-free infected cells approached a constant value irrespective of treatment between four to eight days p.i., while the numbers of infected cells still increased (Fig. 4.16). In Exp. 29D a larger difference between anti-E2-treated and untreated wells was observed than in Exp. 29J.

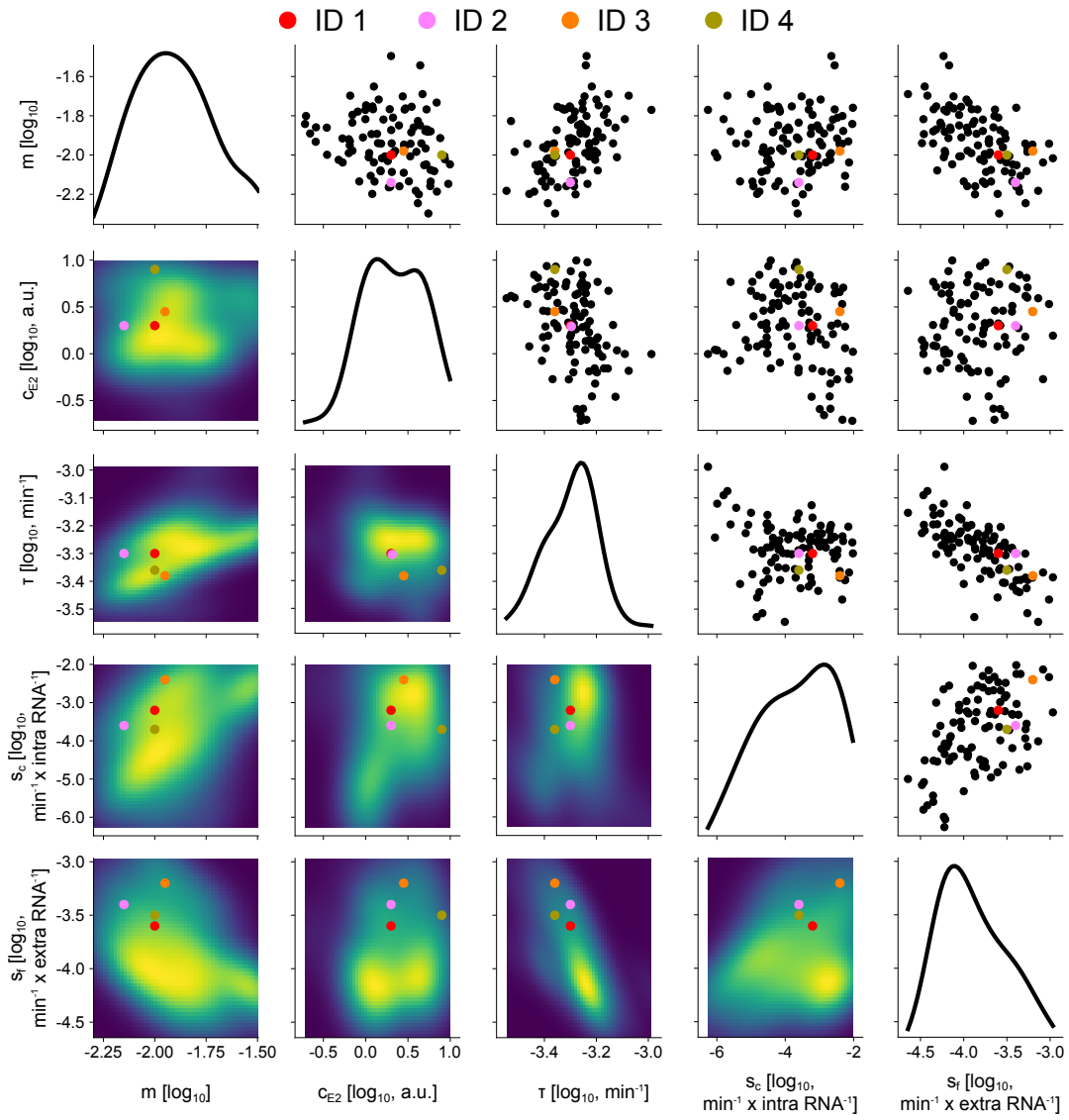

Fig. 4.13. **Estimated kernel densities of fitted parameters to *in vitro* data obtained from Exp. 29J.** In the fitting procedure, the last time point was neglected (see main text for more information) and each particle within pyABC used 5 individual ABM-simulations to calculate average infection dynamics. Results shown were obtained after 13 pyABC generations. 1^{st} row and column represent the diffusion rate for extracellular virus. 2^{nd} row and column show the amount of anti-E2 necessary to neutralize one extracellular RNA in arbitrary units. 3^{rd} row and column display the rate of re-orientation after a successful cell-to-cell transmission per minute. 4^{th} and 5^{th} row and column show the cell-to-cell and cell-free scaling factor, respectively. Panels above the diagonal present 100 individual parameter combinations (black), which had a distance smaller than 4.64 and below the diagonal the corresponding estimated two-dimensional kernel densities. The kernel density estimates of each parameter are shown on the diagonal. The parameters of the four best fitting particles after 13 generations run with pyABC are indicated with red (ID 1), rose (ID 2), orange (ID 3) and olive green (ID 4).

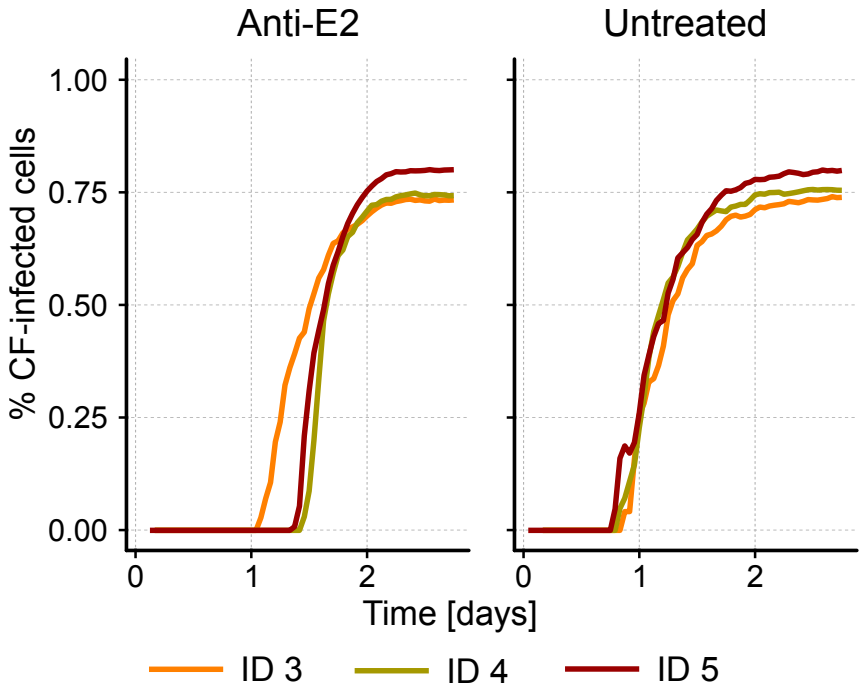

Fig. 4.14. **Predicted proportion of CF-infected cells in Exp. 29J.** The various lines indicate the predicted percentage of cell-free infected cells over the course of the experiment of three exemplary particles obtained from the pyABC fitting routine with distances below 3.74, i.e., ID 3 (orange), ID 4 (olive green) and ID 5 (dark red). Left panel shows Anti-E2-treated and right panel untreated wells. Parameters of these particles are shown in Fig. 4.13 (except ID 5) and as an example the fit of ID 3 in Fig. 4.12.

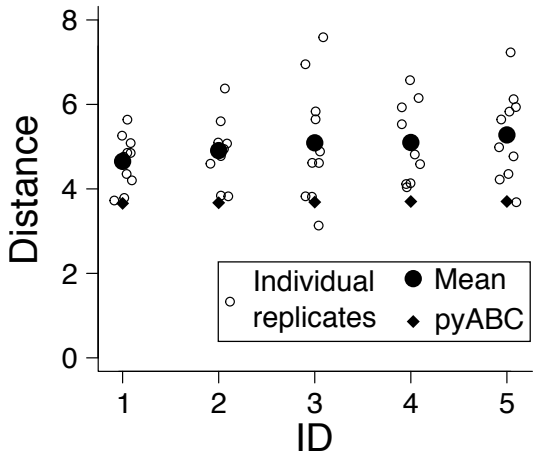

Fig. 4.15. **Distances of ten replicates using the best parameter sets obtained from pyABC fitting to Exp. 29J.** Diamonds indicate the distance as returned from pyABC. Using the parameters obtained from pyABC solid dots show the distance of the average dynamics calculated from individual replicates (open circles), where each replicate already consists of 5 ABM-simulations.

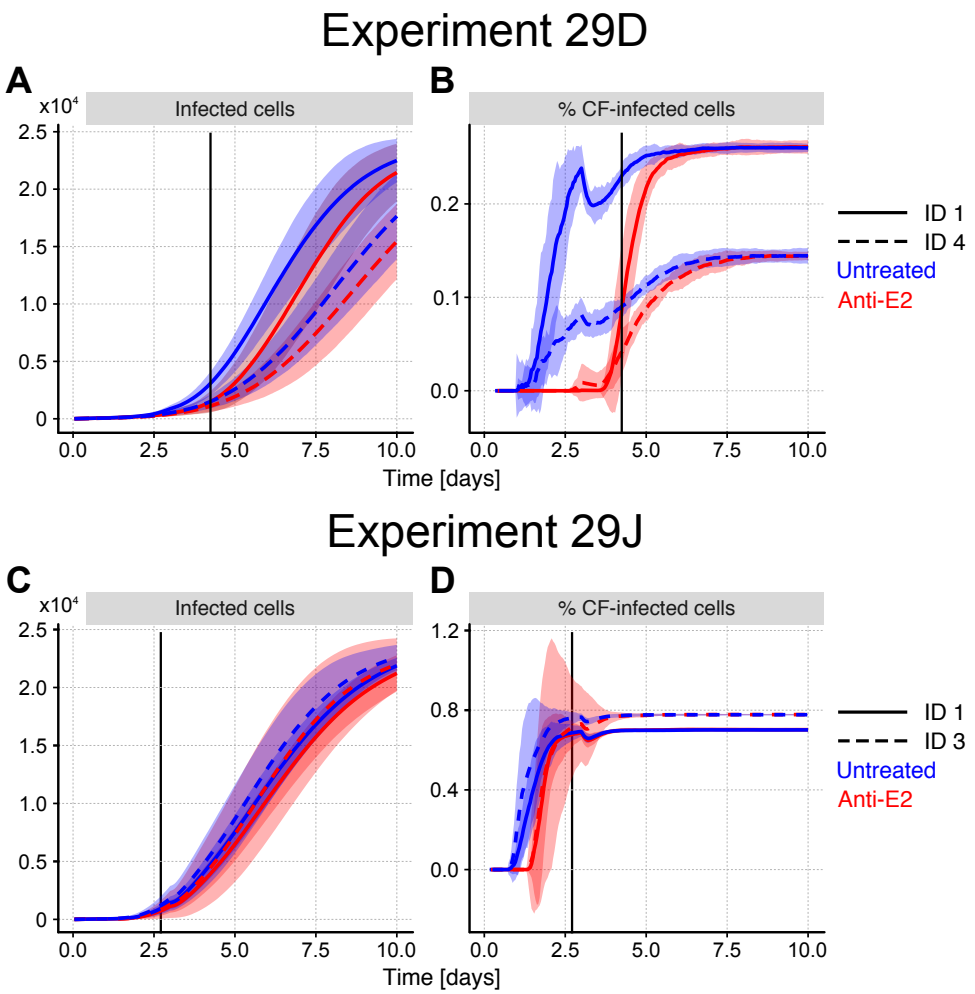

Fig. 4.16. **Long-term predictions of Exp. 29D and Exp. 29J from two parameter sets each obtained from pyABC.** Vertical line shows the end of the respective experiment including the 18 hour time shift (see Section 4.2 for more information). Average number of infected cells **(A+C)** and percentage of CF-infected cells **(B+D)** in Exp. 29D and Exp. 29J, respectively, with 95%-CI calculated from 10 individual ABM-simulations of untreated (blue) and anti-E2-treated wells (red). Parameter values of the two IDs are found in Fig. 4.9 and 4.13 for Exp. 29D and Exp. 29J, respectively.

Simultaneous occurrence of both transmission modes exhibits synergistic effects A trait of my agent-based model is the possibility of completely blocking one transmission mode while not affecting the other. This allowed me to study possible synergistic effects between the two transmission modes in terms of total infected cells. To this end, I ran the parameter sets of IDs 1 and 4 obtained from fitting to Exp. 29D and IDs 1 and 3 for Exp. 29J without cell-free or cell-to-cell transmission. Simultaneous occurrence of both transmission modes without treatment was compared to the combined number of infected cells with either cell-free or cell-to-cell blocked. I achieved comparability between combined individual and simultaneous occurrence of the transmission modes by infecting only half the number of infected cells during the initiation period in the former scenario compared to the latter. Ten replicates were run for all scenarios, where the average dynamics in Exp. 29J were calculated as previously. This showed that in both experiments the average number of infected cells was consistently higher during simultaneous occurrence than the combined individual dynamics would have predicted (Fig. 4.17). However, the synergistic effect was more prominent in Exp. 29D. Cell-free spread

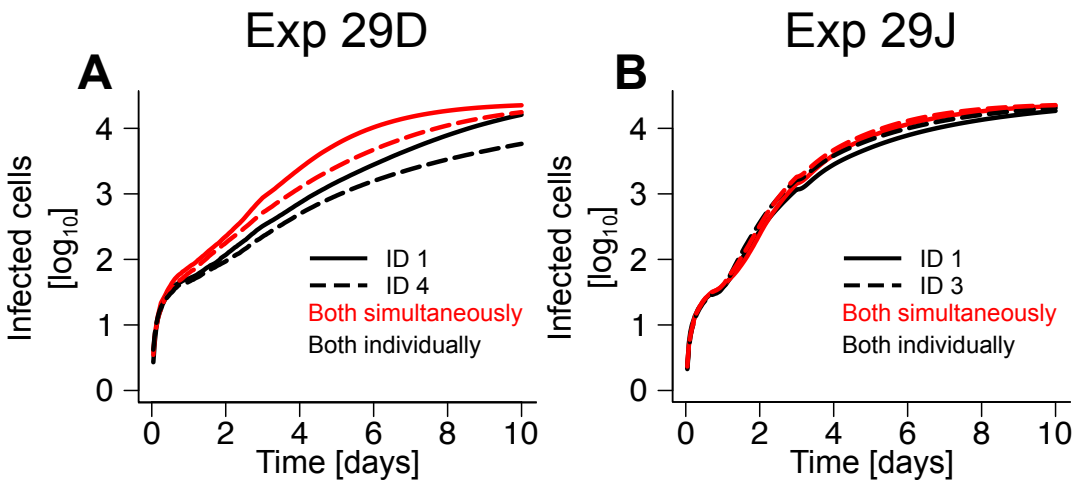

Fig. 4.17. Synergistic effect of simultaneous occurrence of both transmission modes predicted for Exp. 29D and 29J. Parameter sets were obtained from pyABC. Black lines show the number of infected cells when adding one simulation run without cell-free and one without cell-to-cell transmission to avoid synergistic effects. Red lines represent the simultaneous occurrence of both transmission modes with respect to the number of infected cells averaged over 10 simulations. While for Exp. 29D **(A)** parameter sets of ID 1 (solid lines) and ID 4 (dashed lines) were used, ID 1 (solid lines) and ID 3 (dashed lines) were taken to represent Exp. 29J **(B)**.

allowed to overcome the spatial limitations of cell-to-cell transmission through the formation of new foci, thus, increasing the synergistic effect observed in Exp. 29D compared to Exp. 29J, where this effect could not be exploited as much because cell-free spread was estimated to be more efficient.

4.5 Discussion

In this chapter, I studied the infection dynamics of HCV among stationary hepatocytes in a monolayer. The spatially-resolved data, provided by my collaborators, allowed fitting a newly developed extension of a previously published agent-based model. My extended model incorporated intracellular viral replication and extracellular diffusion of virions deterministically and infection processes stochastically while capable of utilizing two different transmission modes.

To reduce the number of free parameters in the complex agent-based model, I first estimated the parameters governing intracellular viral replication and export based on data from an additional experiment, which provided time-resolved bulk measurements of the average intra- and extracellular RNA content per infected cell. A simple mass-action kinetics model was able to capture the viral kinetics (Fig. 4.5). This model was incorporated into the agent-based model with minor modifications due to the changed experimental protocol for the performed spread assays. All parameters governing the viral kinetics in the agent-based model were identifiable and the best fitting estimates were adopted for the purpose of describing HCV spread in a monolayer of Huh7 cells (Table 4.1). The estimated value for the initial intracellular RNA was considerably larger than 1, hinting towards possible superinfections of cells when providing an excess of viral inoculum initially. Furthermore, the capacity of intracellular viral RNA was estimated to be approximately 10-30 times larger than previously reported [82, 138]. This was

presumably due to differences in the applied detection assays, especially with regard to the sensitivity. These results however should not bias any conclusions drawn from the agent-based model as the total number of viral RNA was always scaled with transmission factors, which were estimated in the fitting procedures. The loss rate of extracellular viral infectivity as estimated in my approach ($c_r = 0.076\ [0.049, 0.110]\ h^{-1}$) was comparable to the one stated in [117] ($c_r = 0.065\ h^{-1}$). Comparing my estimates for the export rate of virions and viral production rate to values published by Guedj *et al.* [94] revealed that their estimates were approximately 15-times higher and 4-times lower, respectively. However, besides choosing a different modeling approach, they also intertwined *in vitro* and *in vivo* measurements making comparison to my rates unfeasible.

In order to describe the infection dynamics observed in the data with reasonable accuracy, some assumptions, which were not backed by data, had to be made. For example, even though proliferation of infected hepatocytes cannot be ruled out completely, I did not account for this process in my agent-based model as this would have rendered identifiability of parameters impossible. In case infected cells could proliferate, this would mimic cell-to-cell transmission, thus, leading to biased results towards more cell-to-cell infected cells. I also included a re-orientation phase in my model, i.e., a delay between two successful cell-to-cell transmissions originating from the same cell. To this date, the exact mechanisms behind cell-to-cell transmission in the case of HCV are not known [7], giving rise to various interpretations of the re-orientation phase. For example, it could stand for the time a cell needs to form a virological synapse, as observed in the case of HIV [139], or to build tunneling nanotubes used for transfer of viral material from an infectious to an uninfected cell, a process possibly also exploited by HIV [140]. Another explanation could also be a multitude of unsuccessful cell-to-cell transmissions between successful ones due to a low percentage of infectious virus within infected cells.

The estimated parameters governing intracellular viral replication and export were incorporated into my agent-based model. With these parameters at hand, I used an approximate Bayesian computation approach based on sequential Monte Carlo, which was implemented in pyABC [113], to fit the agent-based model to two separate experiments, namely Exp. 29D and Exp. 29J. These experiments provided focus size distributions, which could be considered as spatially-resolved data, at several time points post infection. The experimental protocol was set up such that cell-free transmission was blocked in half of the wells in each experiment by administering anti-E2, an antibody against an envelope protein of HCV. Fitting my agent-based model to data, required the definition of a distance measure that would allow a reasonable description of the infection dynamics. As distance measure, I chose a relative deviation of the number of infected cells and of the cumulative densities of focus size distributions at the various times measurements were taken (Fig. 4.6). To validate the appropriateness of the ABM to describe the data and correctly predict the contribution of each transmission mode to the infection dynamics, I generated *in silico* data. In order to generate the *in silico* data, my agent-based model was set up to mimic the experimental protocol. Subsequently, I fitted my model to the *in silico* data set using pyABC. This showed, that the fitting method was able to recover the true parameters reasonably well and, more importantly, predict the proportion of cell-free infected cells correctly (Fig. B.5 and 4.7).

With confidence in my modeling approach and fitting method, I fitted the two separately conducted experiments. To this end, I first compared the experiments to reveal any discrep-

ancies *a priori*. This revealed faster proliferation and higher counts of Huh7 cells in Exp. 29J than in Exp. 29D (Fig. 4.3). Furthermore, the number of infected cells varied largely between experiments, with approximately 5-fold more infected cells in Exp. 29J than in Exp. 29D after 96 hours, despite viral inoculum equivalents of about 25 and 35 FFU, respectively (Fig. 4.3B). Additionally, the cumulative densities of the focus size distributions varied strongly in shape and form (Fig. 4.3B). Although stochastic variations in Exp. 29D could have had a large impact on the infection dynamics as a result of only two replicates per time point, the observed differences seemed too large to be explained solely by stochasticity. Instead, the change of fetal bovine serum (FBS) between experiments could be linked to the different cell counts due to varying compositions between applied sera. The high discrepancy between predicted contributions of cell-free transmission to the infection dynamics inferred by fits to the experiments could also be explained by this change of sera, because a connection between lipids and HCV entry, which can be associated with cell-free infections, has been reported previously [141–143]. For example, HCV is known to exploit the very low density lipoprotein pathway and needs lipid droplets for viral assembly [142, 144].

In my fitting routine, I assumed a re-orientation phase, i.e., a delay between time point of infection and experimental detection of infected cells, of 18 hours. Even though this delay varied between cells even within individual experiments (not shown), it could be considered as a lower bound. When fitting to the data, this meant that at any time probably more cells were already infected, but could not be detected yet. However, this proportion should be more or less constant over the course of the experiments, rendering the effect on the dynamics negligible. Besides this, my model had difficulties explaining some features of the data observed in the experiments. For instance, the agent-based model predicted too many small foci in the untreated wells after 120 hours p.i. compared to the measurements obtained from Exp. 29D (Fig. 4.8). Upon leaving an infected cell, HCV virions might attach directly to an adjoining cell. This would result in more cell-free infections close to already existing foci of infected cells than anticipated with the theoretically obtained diffusion rate of extracellular virions. Therefore, using a fixed diffusion rate could bias results towards more small foci in the model than observed in the data. Fitting the extracellular viral diffusion rate could potentially improve fits in Exp. 29D with regard to this aspect. It could also confirm the above reasoning if the estimated value was lower than the theoretical diffusion rate. The possibility of infected cells being infected by defective virus, thus, not partaking in the infection, while still being detectable, was not considered here. Although this could potentially lead to small foci even at late times for the anti-E2-treated wells, the high fraction of small foci could not fully explain the high absolute numbers of small foci as this number exceeded the initially infected cell counts. Furthermore, the number of infected cells in the anti-E2-treated wells was underestimated at 72hrs p.i. (Fig. 4.8). A closer look at the data revealed one single large focus increasing the average number of infected cells at this time point disproportionately. Fitting my model to Exp. 29J, too many small foci were predicted across all time points with and without anti-E2 treatment (Fig. 4.12). Additionally fitting the diffusion rate could not resolve this discrepancy. In terms of infected cell numbers, the sudden increase between 59 and 72 hours p.i. was recovered only to some extent. What lead to the observed dynamics, remains an open question.

Comparing the estimated parameter values on the basis of the exemplary parameter sets, showed various differences between the two experiments with all of them favoring cell-free

transmission in Exp. 29J compared to Exp. 29D (Figs. 4.9 and 4.13). The most striking disparity was the cell-free scaling factor, which was estimated three orders of magnitude larger in Exp. 29J. Furthermore, the re-orientation phase was almost twice as long and larger amounts of anti-E2 were estimated to be necessary to neutralize extracellular virus in Exp. 29J. As expected, favoring cell-free transmission with respect to the parameters also increased the proportion of cell-free infected cells in Exp. 29J, reaching almost 80% at its peak. This stood in stark contrast to the inferred cell-free proportion in Exp. 29D, where it did not exceed 25%. As already pointed out, this could be explained by the change of FBS between experiments, leading to higher amounts of supplied lipids in Exp. 29J [141]. To validate the above reasoning, I compared four different experimental data sets from Exp. 29C (cultured in serum of Exp. 29D), Exp. 29D, Exp. 29I (cultured in serum of Exp. 29J) and Exp. 29J. This showed a striking similarity in the cumulative densities of focus size distributions in the untreated wells within groups of experiments, which used the same serum (Fig. B.3A). With this knowledge at hand, I also fitted my model to another experiment, Exp. 29I, which was conducted after changing the FBS compared to Exp. 29D (Fig. B.3). The proportion inferred from this experiment coincided nicely with Exp. 29J (not shown), hinting towards an important role of the supplied FBS with respect to the infection dynamics and the contribution of each transmission mode over the course of the experiment.

The parameter values obtained from running pyABC in combination with my model allowed me to make several predictions besides the contribution of each transmission mode to the infection dynamics. Running my simulations for up to ten days p.i. showed that a constant proportion cell-free infected cells was established after 3 (Exp. 29J) and 8 (Exp. 29D) days p.i. while infected cell counts still increased (Fig. 4.16). It also revealed that upon exhaustion of anti-E2, treated wells were able to catch up to untreated wells with respect to the proportion of cell-free infected cells. However, long-term dynamics should be taken with care as for later time points differences in total hepatocyte counts between experiments and model could bias results due to target cell limitations occurring at different cell numbers.

Finally, the question of why HCV evolved and kept two different transmission modes remained open. To address this, I ran simulations blocking either cell-free or cell-to-cell spread and compared their combined number of infected cells with a simulation, where both transmission modes occurred simultaneously (Fig. 4.17). This showed a synergistic effect of both transmission modes during simultaneous occurrence. Here, the synergistic effect was more prominent in Exp. 29D. Judging from the high proportion of cell-free infected cells in Exp. 29J, cell-free transmission was more efficient in this experiment than cell-to-cell. When combining efficient short-range cell-to-cell spread with far-range less efficient cell-free transmissions, local restrictions of cell-to-cell transmission can be circumvented and therefore lead to a strong synergistic effect. Another reason that could explain the need of two transmission modes for HCV is the discrepancy between predicted contributions of cell-free infected cells in the experiments. As the conducted experiments differed only in the utilized FBS, which could stand for lipid-rich and -poor environments in the body, the difference in cell-free proportions hinted towards the necessity of HCV to adapt to changing environments.

In summary, I developed an agent-based model able to describe complex spatially-resolved data allowing predictions of the contribution of transmission modes to HCV infection dynamics *in vitro*. This revealed a possible impact of the supplied lipids on the infection dynamics and also on the proportion of cell-free infected cells during the course of the experiment.

5 Quantification of cell-to-cell transmission among stationary cells using virus dynamics models

5.1 Introduction

The results of this chapter have been mainly published in a study by Kumberger *et al.* [12].

Many viruses are able to exploit two different transmission modes, namely cell-free (CF) and cell-to-cell (CC) [7]. How a virus spreads in tissue strongly depends on the contribution of each transmission mode. To allow efficient drug and vaccine development, this needs to be taken into account in the future. In this thesis I have presented two approaches how to quantify cell-to-cell transmission in viral infections. However, transfer of these modeling approaches to all viral infections also depends on the availability of data. In the following, I introduce a new extended version of the standard model of virus dynamics to allow quantification of cell-to-cell transmission among immobile or slow moving cells also in the context of sparse data.

In Chapter 3, I inferred the contribution of cell-to-cell transmission in different extracellular microenvironments to HIV infection dynamics among motile CD4 T cells from *in vitro* bulk measurements. This was achieved with a detailed mass-action kinetics model, which was developed with a data-driven modeling approach. Although an adaptation of this model could in principal be applied to stationary cells, the local nature of cell-to-cell transmission might violate assumptions necessary to build the most informative model from Chapter 3. Next, I built an agent-based model to predict the proportion of Huh7 cells infected with HCV by cell-free spread *in vitro* from spatially-resolved data (Chapter 4). Even though this method could be applied to other viruses, mass-action kinetics models are often preferred to more complex models when describing infection dynamics due to their easy application in data fitting. Furthermore, population-based measurements as obtained from a variety of experimental protocols are often not sufficiently resolved to allow fitting of more complex models. However, the assumption of a well-mixed system, necessary for mass-action kinetics models, is in general violated in the context of stationary cells. To still permit application of mass-action kinetics models, they should be improved to correctly predict cell-to-cell spread among immobile cells while containing a simple structure necessary for fitting bulk measurements.

In this chapter, I show that the standard model of virus dynamics (see Section 1.2.1 for further information), which assumes a well-mixed system, is not able to capture the dynamics of cell-to-cell transmission in the context of stationary cells. Non-motile target cells can be found for example in the context of Influenza and Hepatitis C virus infecting epithelial cells and

hepatocytes, respectively. To rigorously test various models and their capability describing the infection dynamics of cell-to-cell transmission among immobile cells, I used a slight variation of the previously described agent-based model (see Section 4.3) to generate *in silico* data, to which models were subsequently fitted. Here, the usage of *in silico* data proofed to be advantageous over experimental data as it allowed to reveal model shortcomings without the confounding factors of experimental bias and measurement errors (see also Section 4.4.2). Additionally, every process in the agent-based model was known, thus, avoiding unwanted behavior of the system. After establishing shortcomings of the standard model when trying to describe infection dynamics by cell-to-cell spread among non-moving cells, I developed a simple extension of the standard model of virus dynamics incorporating an adjustment term. This allowed the model to capture the decreasing proportion of infected cells contributing to cell-to-cell transmission among stationary cells in the course of an infection. In contrast to previous models, the extended model is able to correctly quantify the infection dynamics of cell-to-cell spread without loss of the overall simple structure.

In a next step, the model was tested for its ability to disentangle the simultaneous occurrence of cell-free and cell-to-cell transmission dynamics, while also predicting the correct contribution of each transmission mode to viral dissemination. For all models tested, the latter was difficult to achieve. However, my extended model gave more appropriate predictions. Finally, I fitted my model to previously published data of HIV-1 infection dynamics revealing that the contribution of each transmission mode might be more variable during progression of infection than suggested by the authors [70]. Even though Jurkat cells, an immortalized T cell line, are supposed to be motile [145], thus, violating the assumption of stationary cells necessary to develop the adjustment term, my novel approach gave a better description of the data. This hints towards locally confined cellular movements or the formation of syncytia in this environment resulting in large foci of infected cells.

5.2 Data generation

The agent-based model as described in the previous chapter was simplified to generate *in silico* data (Fig. 5.1A and Table C.1). Here, to limit the number of confounding factors, I neglected proliferation of target cells, the re-orientation phase was set to zero, and no media change after 72 hours was simulated. Furthermore, I added sufficient amounts of anti-E2 *in silico* to prevent cell-free transmission in treated scenarios and used a different parameterization for the intracellular replication. A representation of the intracellular viral RNA and extracellular infective virus produced by one infected cell over the course of 100 hours is shown in Fig. 5.1B. To generate the data, the ABM was run for 10 days, while sampling the number of infected cells and the extracellular viral concentration every 24 hours mimicking realistic experimental conditions. Realizations of the model after approximately three days are shown in Fig. 5.1C, where both transmission modes or only cell-to-cell transmission occurred. The probability of cell-free and cell-to-cell infection were defined by $p_f := s_f V$ and $p_c := s_c f_{\text{inf}} R$, respectively. Here, the intracellular RNA content per infected cell is denoted by R and the extracellular viral concentration above each cell by V. Only a fraction f_{inf} of intracellular RNA was assumed to be infective virus. Furthermore, intra- and extracellular viral concentrations were scaled with scaling factors s_c and s_f, respectively. As before, cells were distributed on a hexagonal grid, i.e., each cell had six different neighbors, in the agent-based model. Furthermore, the ABM

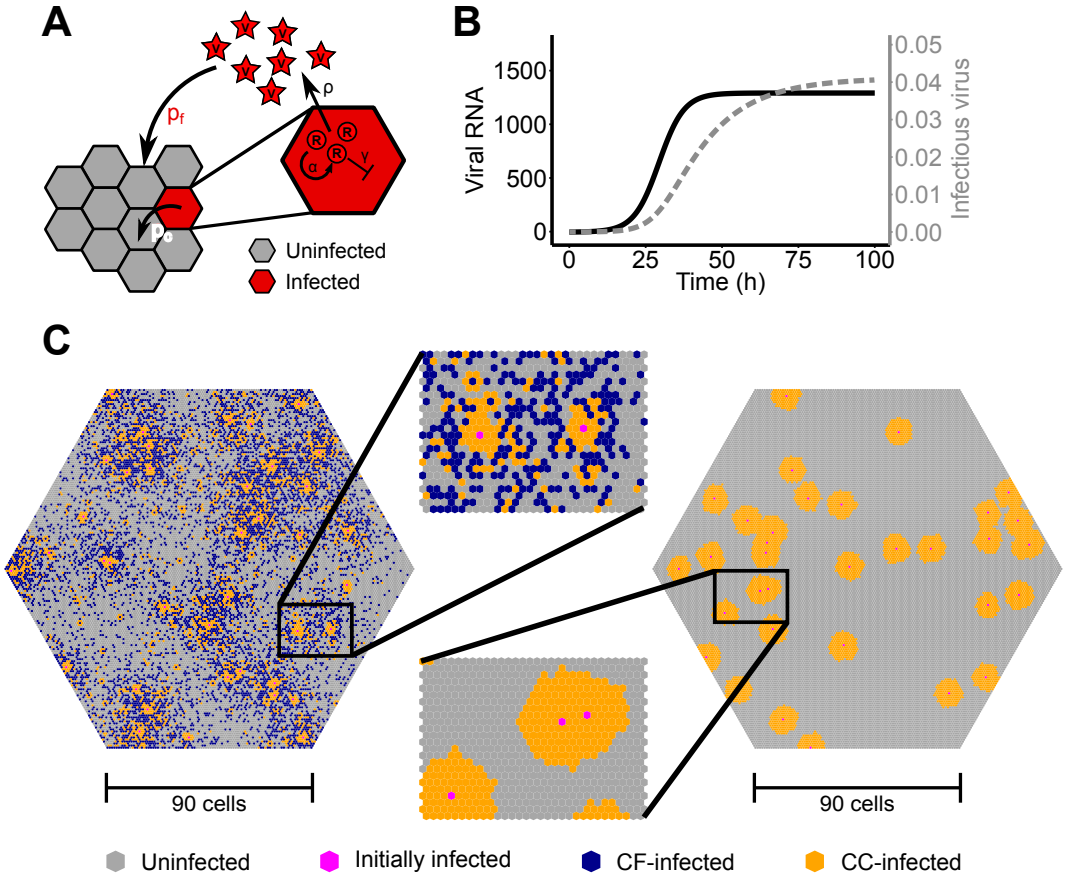

Fig. 5.1. **Agent-based model of infection dynamics among stationary cells in a monolayer.** **(A)** Schematic view of the agent-based model simulating intracellular viral replication and spread by cell-free and cell-to-cell transmission among stationary cells. Cells were assumed to be hexagonally shaped and could be either uninfected (gray) or infected (red). The parameters p_c and p_f define the probability of infection by cell-to-cell and cell-free transmission, respectively. They depend on the intra- (CC transmission) and extracellular (CF transmission) viral load at the corresponding grid sites. **(B)** Time course of intracellular viral load (black line) and produced extracellular virus (gray line) for one infected cell in the ABM. **(C)** Realization of simulation outcomes after approximately three days post infection assuming simultaneous occurrence of cell-free and cell-to-cell transmission (left) or only CC-transmission (right). Cells infected by CF- or CC-transmission are shown in blue and orange, respectively. Figure as published in [12]

accounted for intracellular viral replication and intercellular viral spread (see Section 4.3 for a detailed explanation). All other processes were taken from the agent-based model described in the previous chapter, e.g. no proliferation or death of hepatocytes.

5.3 Standard models of virus dynamics fail to describe cell-to-cell transmission among stationary cells

The standard model of virus dynamics has been used extensively to analyze time course data of various infections. It describes the coupled dynamics of the concentration of target cells, T, infected cells, I, and the extracellular viral load, V (see *Introduction* for more information) [81]. To also account for cell-to-cell transmission, previous model extensions of the standard model of virus dynamics introduced an additional infection term. Here, target cells can get

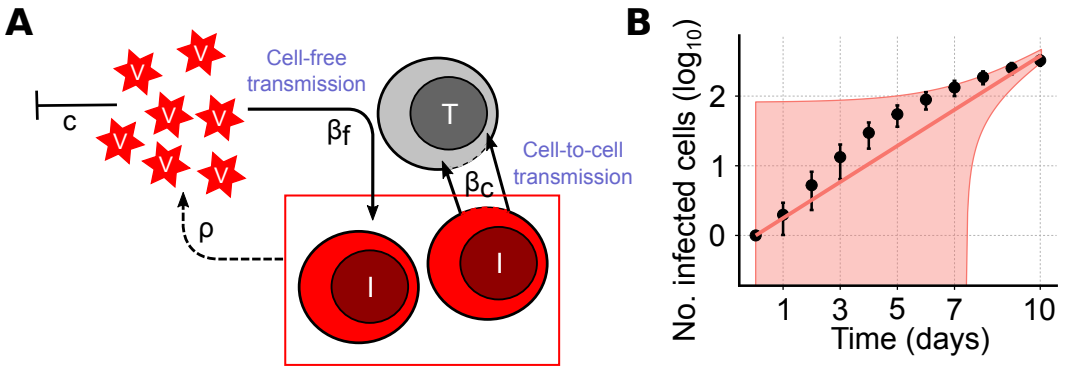

Fig. 5.2. **Simple mass-action kinetics model describing cell-to-cell and cell-free transmission.** **(A)** Sketch of model (5.1) with $\delta_I = \delta_T = 0$. Target cells (T, gray) become infected (I, red) either by cell-to-cell transmission with rate β_c dependent on the concentration of infected cells or by cell-free virus with rate β_f dependent on the viral load, V. Viral particles are produced by infected cells with rate ρ and cleared at rate c. However, viral dynamics are not taken into account when analyzing a situation, where cell-free spread is blocked. For simplicity and elimination of confounding factors, the processes of cell death and proliferation are neglected in the ABM as well as the fitted models. **(B)** Simulated dynamics and model predictions for viral spread only considering CC-transmission ($\beta_f = 0$) among stationary cells starting with a single infected cell in the center of the grid. Black dots indicate the mean and vertical lines represent 95%-confidence intervals of total infected cells averaged over 100 individual ABM-simulations sampled every 24 hours. Thick red line indicates the best fit of the basic model as described in Eq. (5.1) with the red shaded area indicating the 95%-prediction band using the estimated standard deviation (Table 5.1). Figure as published in [12].

infected at rate β_c proportional to the concentration of infected cells [70, 98, 146], where parameter β_c describes the rate of cell-to-cell transmission. In summary, the basic model incorporating both transmission modes (Fig. 5.2A) can be written with the following set of ordinary differential equations

$$\begin{aligned} \frac{dT}{dt} &= -\beta_f VT - \beta_c IT - \delta_T T \\ \frac{dI}{dt} &= \beta_f VT + \beta_c IT - \delta_I I \\ \frac{dV}{dt} &= \rho I - cV \end{aligned} \quad , \tag{5.1}$$

where the terms $\beta_f VT$ and $\beta_c IT$ define the contributions of cell-free and cell-to-cell transmission, respectively, to the newly infected cells. Due to the well-mixed assumption in this model all infected cells contribute to cell-to-cell spread at any given time. However, for viral dissemination among stationary or slowly moving cells, as e.g. cells in solid tissues, this assumption is violated. To test the effect of violating this assumption and the overall ability of the basic model (Eq. 5.1) to describe cell-to-cell transmission among stationary cells, I fitted it to the generated *in silico* data as described in the previous section assuming $\beta_f = 0$. Here, I only considered the simplest form of the infection dynamics by blocking cell-free spread and starting with a single infected cell in the center of the simulated well, thus, providing the infection with virtually unlimited target cell numbers.

Figure 5.2B shows the time course of infected cell counts over ten days sampling every 24 hours, where the mean and 95%-confidence intervals were calculated from 100 individual ABM-simulations. Fitting model (5.1) (with $\beta_f = \delta_I = \delta_T = 0$), which assumed standard mass-action kinetics, to these data, clearly illustrated its inability to describe the infection

dynamics (Fig. 5.2B). As long as target cells were not limiting, this model predicted an exponential increase of infected cells due to its linear relationship between infection of new target cells and the density of already infected cells. Hence, it could not explain the decreasing growth rate of a focus of infected cells over time. Accordingly, this showed the failure of simple mass-action kinetics as previously used [70, 90, 146] to appropriately describe viral spread by cell-to-cell transmission among stationary cells.

5.4 Improved description of cell-to-cell transmission by accounting for spatial effects

By examining the ABM-simulated data with blocked cell-free spread, it became apparent that focus growth of infected cells was not constant. To better understand the dynamics of focus growth as a consequence of cell-to-cell transmission, a thought experiment was conducted. Assume a hypothetical virus is only capable of spreading via cell-to-cell transmission among stationary cells during infection. Then, newly infected cells appear next to already infected cells resulting in large foci of infected cells, which in turn lead to a lower proportion of cells that can contribute to cell-to-cell spread (Fig. 5.3A), affecting and especially decelerating focus growth. Thus, the assumption of model (5.1) that all infected cells partake in cell-to-cell transmission at any given time was could not be true for stationary cells and needed to be adapted.

Accordingly, improvement of the standard model could be achieved by adding a correction function $f_c(I)$ to the cell-to-cell infection term $\beta_c IT$, where $f_c(I)$ describes the decreasing proportion of cells contributing to cell-to-cell transmission during progression of infection. The proportion of cell-to-cell contributors (CC contributors), f_c, in a monolayer of stationary cells can be calculated by the ratio of cells in the perimeter and the total focus size under the assumption that cells with the same distance from the focus-founding cell are always infected simultaneously (Fig. 5.3A), i.e., radial focus growth. Thus, f_c is formulated as follows

$$f_c := \frac{\text{No. cells in perimeter of focus}}{\text{No. cells in focus}},$$

where the number of cells in the perimeter is determined by the number of neighbors, k, and the expansion phase, n (Fig. 5.3A). Independent of k, the focus-founding cell contributes to cell-to-cell spread for $n = 0$, i.e., $f_c = 1$. At the end of the first expansion phase, $n = 1$, the number of neighbors per cell is located in the perimeter. After the second and third expansion phase, the number of cells in the perimeter doubles and triples, respectively, while the total focus size grows slightly faster (Fig. 5.3A). In general, the proportion of cells in a focus contributing to cell-to-cell transmission after completion of expansion phase n and dependent on the assumed number of neighbors, k, can be calculated by

$$f_c(n,k) = \frac{kn}{1 + k\sum_{j=1}^{n} j} = \frac{2kn}{kn^2 + kn + 2} \qquad \text{for } n \geq 1. \tag{5.2}$$

Similarly, the total number of infected cells in a focus is described by

$$I(n,k) = \frac{k}{2}n^2 + \frac{k}{2}n + 1. \tag{5.3}$$

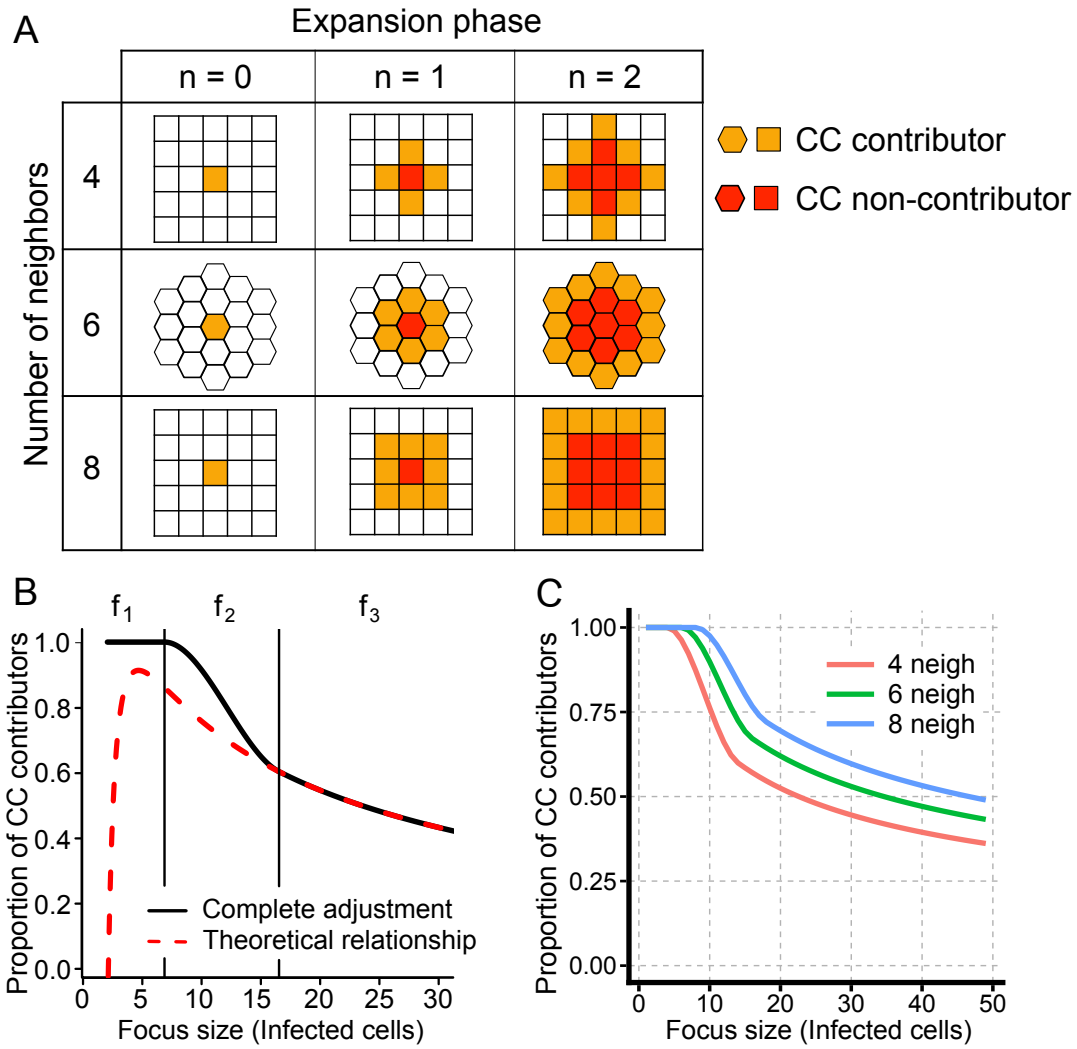

Fig. 5.3. **Varying proportion of cells contributing to cell-to-cell transmission.** **(A)** Sketch of cells contributing to cell-to-cell infection within one focus for different expansion phases and numbers of neighbors per cell while assuming radial focus growth. Whereas cells in the perimeter of the focus (orange) can contribute to CC-transmission, cells without uninfected neighbors (red) cannot. **(B)** Hypothetical proportion of cells contributing to cell-to-cell transmission with respect to the focus size assuming six neighbors per cell ($k = 6$). The theoretically determined relationship (Eq. (5.4), red dashed line) underestimates the true proportion for small focus sizes. The black line indicates the complete adjustment term as described in Eq (5.5)) with $z = 10$. **(C)** Proportion of CC contributors dependent on the focus size assuming different numbers of neighbors per cell, i.e., $k = 4$ (red), 6 (green) or 8 (blue). Again, parameter z was set to 10. Figure as published in [12].

By solving Eq. (5.3) for n and substituting in Eq. (5.2), the proportion of cell-to-cell contributors as a continuous function depends on the number of infected cells in the focus as well as the number of neighbors (Fig. 5.3B, red dashed line) and is determined by

$$f_c(k, I) = \frac{\sqrt{k^2 + 8kI - 8k} - k}{2I}. \tag{5.4}$$

However, Eq. (5.4) only holds true if $I \geq k$. Otherwise, all infected cells in the focus contribute to cell-to-cell transmission because not all neighbors of the founding cell are infected (see Fig. 5.3A). Thus, Eq. (5.4) needs to be adapted to allow a correct approximation of the correction term for small foci sizes. To this end, I set $f_c(I) = f_1 = 1$ for $I \leq k$. To prevent a sudden drop at $I = k$, I introduced a smooth function f_2 in the interval $k < I < k + z$ with $z \in \mathbb{R}^+$ (see Fig. 5.3B and Section C.2 for a detailed derivation of the connection term f_2). This linked the proportion of contributors for small focus sizes, f_1, with the general function for larger focus sizes as obtained in Eq. (5.2). Here, parameter z defines the number of infected cells for which the transition term is used. Combining the above, the final adjustment term $f_c(I)$ for a single focus comprising I infected cells on a grid with k neighbors reads as follows

$$f_c(I) := \begin{cases} 1 & \text{for } I \leq k \\ a\,(I-k)^3 + b\,(I-k)^2 + 1 & \text{for } k < I < k + z \\ \frac{\sqrt{k^2+8kI-8k}-k}{2I} & \text{for } I \geq k + z, \end{cases} \tag{5.5}$$

where $a := a(z, k)$ and $b := b(z, k)$ depend on z and k. These functions ensure smoothness (see Section C.2 for more information) of the complete adjustment term at the limits of the connecting polynomial f_2. In Fig. 5.3C the progression of the cell-to-cell contributor proportion with increasing focus size, I, for different numbers of neighbors per cell is shown. Even though I developed the adjustment term for discrete values of I, it is also valid for continuous I, e.g., when I represents the concentration of infected cells within one focus instead of the absolute number. To approximate the proportion of cells contributing to cell-to-cell transmission in a culture with several foci, I needs to be substituted with I/ϕ, where I defines the total number of infected cells and ϕ the number initial foci.

The derivation of the adjustment term f_c allowed extension of model (5.1) to account for the decreasing proportion of cell-to-cell contributors with progression of infection

$$\begin{aligned} \frac{dT}{dt} &= -\beta_f VT - f_c(I)\beta_c IT - \delta_T T \\ \frac{dI}{dt} &= \beta_f VT + f_c(I)\beta_c IT - \delta_I I \\ \frac{dV}{dt} &= \rho I - cV \end{aligned} \tag{5.6}$$

To limit the number of confounding factors and concentrate solely on the spatial effects of cell-to-cell transmission, cellular turnover was initially not considered, i.e., $\delta_I = \delta_T = 0$. However, when applying this model to previously published data [70], it was adapted to consider cellular turnover and proliferation due to the followed experimental protocol (see Section 5.8).

5.5 Adjusted model improves description of cell-to-cell transmission for individual focus growth

In a next step, the adjusted model was tested to see if it could correctly explain and quantify cell-to-cell transmission in the context of stationary cells. To this end, it was fitted to *in silico* data as described in Section 5.2 with one initially infected cell in the center of the grid (see Section 2.2.2 for more information on the fitting procedure). The adjusted model (aCC-model, Eq. (5.6) with $\beta_f = \delta_T = \delta_I = 0$, see also Table C.2) was able to describe the observed dynamics better than the standard CC-model (Eq. (5.1) with $\beta_f = \delta_I = \delta_T = 0$ and Fig. 5.4A). In contrast to the CC-model, my aCC-model was able to capture the decelerating infection dynamics with increasing focus size (Fig. 5.4A). Additionally, the comparison of the corrected Akaike Information criterion values (see Section 2.2.2 for more details on the calculation of AICc values) of both models to the best fitting model ($\Delta\text{AICc} = 823.1$ and $\Delta\text{AICc} = 29.2$ for the CC- and aCC-model, respectively, showed better performance of the adjusted model.

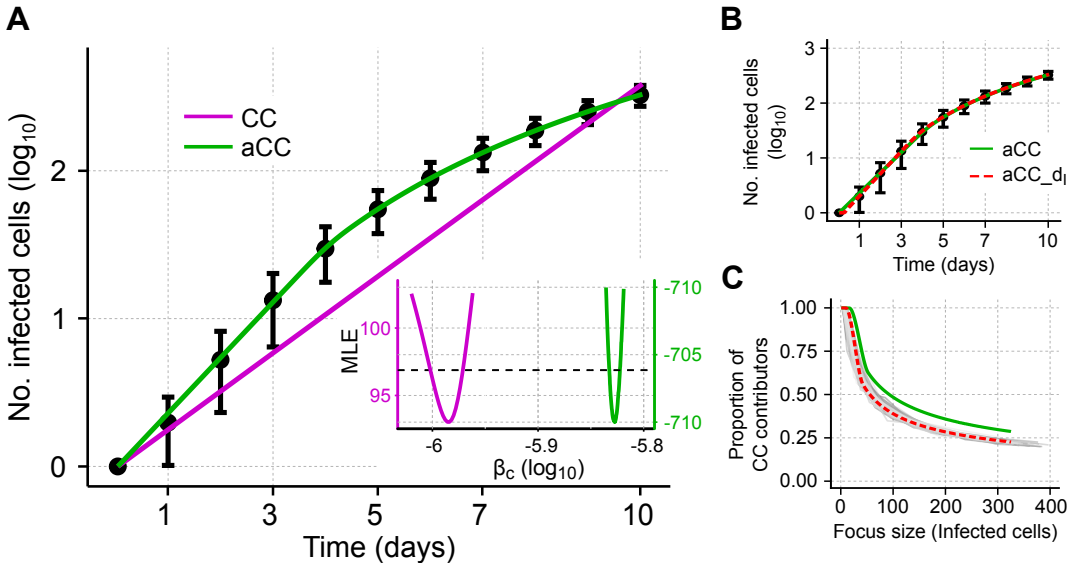

Fig. 5.4. Simulated data and corresponding model predictions describing growth of an individual focus of infected cells. (A+B) Individual focus growth by CC-transmission among stationary cells starting with a single infected cell. The mean and 95%-confidence interval for the total number of infected cells averaged over 100 individual ABM-simulations sampled every 24 hours are indicated with black dots and black lines, respectively. **(A)** Best fits of the CC-model (Eq. (5.1) with $\beta_f = \delta_I = \delta_T = 0$, magenta) and the adjusted model (aCC-model, Eq. (5.6) with $\beta_f = \delta_I = \delta_T = 0$, green) without estimated prediction band for better illustration. Inlay: Profile likelihoods of the estimated cell-to-cell transmission rate, β_c, derived from the CC- (magenta) or aCC- (green) model. **(B)** Model fits were improved when using an extension of model (5.6), which considered a time-delay for cells to become infectious (aCC-d_I,red). **(C)** Proportion of CC contributors as predicted by the aCC-model (green line), and the aCC-d_I-model (red dashed line) in comparison to the proportion observed in the individual ABM-simulations (gray lines). The corresponding parameter estimates are given in Table 5.1. Figure as published in [12].

Neglecting the decreasing proportion of cell-to-cell contributors during progression of infection lead to roughly 1.5-times larger estimates for the transmission rate characterizing cell-to-cell spread in the aCC-model than in the CC-model ($\beta_c = 1.49 \times 10^{-6}\text{cell}^{-1}\text{h}^{-1}$ $[1.47, 1.50]$ aCC-model vs. $\beta_c = 1.04 \times 10^{-6}\text{cell}^{-1}\text{h}^{-1}$ $[1.00, 1.07]$ CC-model, Fig. 5.4(A, insertion) and

Table 5.1). Profile likelihood analysis indicated that all parameters were identifiable based on the given data (Figure C.1).

However, both models did not account for the intracellular RNA dynamics within infected cells in the agent-based model, which followed a sigmoidal growth pattern. This implied a delay in cell-to-cell spread as the majority of this transmission mode would occur only after enough intracellular RNA had been produced. To incorporate this into my adjusted model, I introduced a time-delay accounting for the time that cells need to become infectious in order to participate in cell-to-cell spread. To this end, the term $f_c(I)\beta_c IT$ describing cell-to-cell transmission in the aCC-model was replaced by $f_c(I)\beta_c I(t-\tau)T$, where τ represented the considered time-delay (see Eq. (C.3) in Section C.4 with $\lambda_T = \delta_T = \delta_I = 0$). This defined a new model, namely the aCC-d$_I$-model. It further improved the description of the infection dynamics (Fig. 5.4B and $\Delta\mathrm{AICc} = 29.2$ compared to the aCC-model, Table 5.1).

With my model capturing the overall dynamics of the infected cells in the *in silico* data correctly, I tested if my theoretically derived adjustment term was able to predict the correct proportion of cells contributing to cell-to-cell transmission. To this end, I compared the proportion predicted by f_c with the proportions obtained from the individual ABM-simulations. The aCC-model predicted a slightly higher proportion of cell-to-cell contributors with respect to the focus size than observed in the simulations (Fig. 5.4C, green line). However, this discrepancy dissolved in the aCC-d$_I$-model, which accounted for the time an infected cell needed to accumulate intracellular viral particles, leading to good agreement of the predicted and observed proportions (Fig. 5.4C, red line).

In summary, simple mass-action kinetics fell short when describing individual focus growth among stationary cells. Here, the adjusted model, accounting for the decreasing proportion of cells contributing to cell-to-cell spread provided a more appropriate approach. Additionally, it captured the time course of infected cells participating in cell-to-cell transmission, even though this is a spatial process. The correct prediction of CC contributors allowed a meaningful interpretation of the adjustment term, while still keeping the simple structure of an ODE model.

5.6 Determining cell-to-cell transmission across multiple foci

To apply the adjusted model in the future to data, the *in silico* data should resemble characteristics of experiments more closely. Usually an experiment follows the simultaneous growth of multiple foci, when measuring the viral concentration and density of infected cells on a population level, to reduce experimental variation and ensure reliability of the experiment. The simultaneous growth of multiple foci could impair the ability of the adjustment term f_c to describe the infection dynamics and correctly predict the proportion of cells contributing to cell-to-cell transmission. In this scenario, asynchronous initiation of foci as well as their merging during progression of infection could be confounding factors (Fig. 5.5A).

To investigate the ability of the adjusted model to describe cell-to-cell spread under these conditions, i.e., no cell-free transmission and initiation of several infected cells, the ABM

Tab. 5.1. **Estimated rates for different models fitted to *in silico* data with blocked cell-free spread.** All models were fitted to the concentration of infected cells obtained for the growth of single and multiple foci. Best fitting parameters are given with 95%-confidence intervals shown in brackets. The difference in the corrected AIC values, ΔAICc, was calculated relative to the AICc of the best fitting model ($\Delta\text{AICc} = 0$) for single and multiple focus growth, respectively. Among others the adjustment term depended on the parameter θ, which represents a measurement for irregular focus growth and initiated number of foci (see Section C.2). As infection through cell-to-cell transmission was independent of the extracellular viral concentration, I did not consider viral turnover rates, i.e., c and ρ, in the fitted models when studying the infection dynamics with blocked cell-free transmission.

Model	CC	aCC	aCC $-$ $\mathbf{d_I}$
		Single focus	
β_c ($\times 10^{-6}\text{h}^{-1}\text{cell}^{-1}$)	1.04 [1.00, 1.07]	1.49 [1.47, 1.50]	2.04 [1.82, 2.34]
θ	-	2.7 [2.58, 2.82]	1.62 [1.31, 1.94]
z (cells)	-	13.6 [8.82, 17.9]	20.2 [12.5, 28.6]
τ (hours)			5.71 [3.73, 7.89]
ΔAICc	823.1	29.2	0
		Multiple foci	
β_c ($\times 10^{-6}\text{h}^{-1}\text{cell}^{-1}$)	1.13 [1.07, 1.18]	1.72 [1.70, 1.74]	1.72 [1.70, 1.79]
θ	-	1.78 [1.70, 1.86]	1.78 [1.66, 1.86]
z (cells)	-	2.19 (0, 6.61]	2.09 (0, 6.31]
τ (hours)			1.65×10^{-5} (0, 0.664]
ΔAICc	92.88	0	7.33

was used to generate *in silico* data. Following previous experimental conditions (compare Chapter 4 and [116, 117, 144]), a monolayer of cells, in which infected cells were randomly seeded during a time period of 17 hours after start of the experiment, was simulated with the agent-based model. To resemble realistic experimental intervals between individual measurement, infected cells were sampled every 24 hours. Because the initiation of infected cells could be considered as cell-free spread due to its random distribution, the processes of infection initiation and focus growth arising from new infections needed to be separated. To this end, the initial infection period was neglected and the number of infected cells 17 hours p.i. was considered as initial condition.

Due to averaging effects, a situation in which several infected cells are initiated can be considered closer to the well-mixed assumption than the growth of a single focus. Still, the aCC-model performed better than the CC-model, which assumed a completely mixed system (Fig. 5.5B and Table 5.1, $\Delta\text{AIC}_\text{c} = 92.88$). Even in this scenario, including confounding factors such as heterogeneous initiation of several infected cells and merging of foci, the decelerated infection dynamics could not be explained by a model neglecting the proportion of cell-to-cell contributors. Again, a 1.5-fold increase in the cell-to-cell transmission rates estimated from the two models was observed ($\beta_c = 1.13 \times 10^{-6}\,\text{cell}^{-1}\text{h}^{-1}$ [1.07, 1.18] CC-model, $\beta_c = 1.72{\times}10^{-6}\text{cell}^{-1}\text{h}^{-1}$ [1.70, 1.74] aCC-model, Table 5.1). Introducing a delay in the cell-to-cell infection term (aCC-d_I) did not improve fits leading to an estimated delay of zero. This was to be expected due to the initiation process resulting in a heterogeneous population of infected cells with respect to their time of infection at the start of the fitting procedure 17h p.i. Hence, several infected cells were already infectious 17 hours p.i. Consequently, an

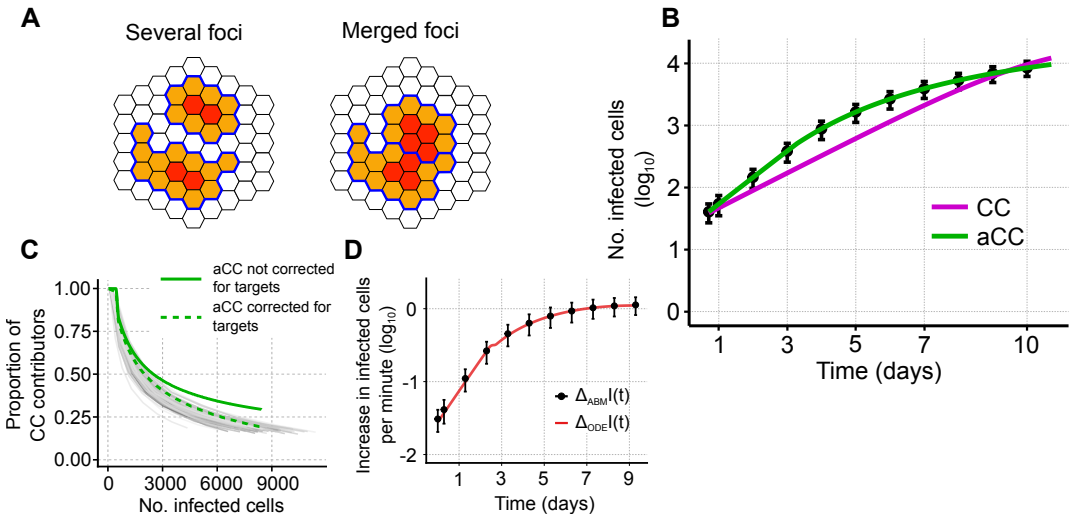

Fig. 5.5. **Cell-to-cell spread in a culture with several foci. (A)** Left and right panel show the same foci, with the smaller focus being lowered in the right panel by one row resulting in fewer CC contributors (orange) in the merged foci compared to the individual foci on the left. Boundaries of the two foci are marked in blue and CC non-contributor in red. **(B)** Simulated data and model predictions for a scenario, where cell-free spread was blocked and several foci were initiated within 17 hours p.i. The mean and 95%-confidence interval for the total number of infected cells averaged over 100 individual ABM-simulations sampled every 24 hours are indicated with black dots and black lines, respectively. Colored lines show the best fit of the CC- (magenta) or aCC-model (green). Corresponding parameter estimates are shown in Table 5.1. For better comparability between models the estimated prediction bands are not shown. In the aCC-d_I-model the time-delay until cells become infectious was estimated to be 0. Thus, this model is not shown here as it is essentially the aCC-model. **(C)** Prediction of the proportion of CC contributors (green solid line) obtained from the adjustment term with the best fitting parameter set compared to the proportions resulting from 100 individual ABM-simulations (gray lines). The corrected adjustment term, which was multiplied with the proportion of target cells relative to the number of target cells at the beginning of the simulation, i.e., $f_c(I(t))T(t)/T_0$, is indicated with a dashed green line. **(D)** Approximate increase of infected cells per minute in the ABM (black dots, mean and 95%-CI based on 100 simulations) as defined by Eq. (5.7). Additionally, this increase was calculated for the ODE model (red line) using Eq. (5.8). Figure as published in [12].

additional time-delay could be neglected and only the aCC-model was considered for this scenario.

As previously, the ability of the adjustment term f_c to correctly predict the proportion of cell-to-cell contributors was tested. To this end, the proportion obtained from running the respective models with the best fitting parameter set was compared to the proportion of the individual agent-based model simulations (Fig. 5.5C, green solid line). In contrast to the prediction with regard to single focus growth, my aCC-model seemingly performed worse in this more complex scenario. Especially for later time points the proportion of cells contributing to cell-to-cell spread was overestimated. However, this discrepancy could be explained, when analyzing CC contributors in the ABM and ODE model in more detail. The average increase of infected cells per time step, $\Delta_{\mathrm{ABM}}I(t) = I(t+1) - I(t)$, in the agent-based model could be approximated with

$$\begin{aligned} \Delta_{\mathrm{ABM}}I(t) &= \tilde{\beta}_c \bar{V}_{cc} \tilde{f}_c(I,T) I(t) \\ \text{with } \bar{V}_{cc} &:= \frac{I(t_{\mathrm{end}}) - I(t_{\mathrm{start}})}{\tilde{\beta}_c \int_{t_{\mathrm{start}}}^{t_{\mathrm{end}}} I(s) \tilde{f}_c(I,T) \mathrm{d}s} \quad . \end{aligned} \tag{5.7}$$

Here, t_{start} and t_{end} stand for the start and end time of the simulation run, respectively. Over the course of the infection, the average viral concentration per infected cell, which contributes to cell-to-cell spread, is denoted with $\bar{V}_{cc}$. Furthermore, $\tilde{\beta}_c := f_{\text{inf}} s_c$ defines the infectivity per intracellular viral particle and $\tilde{f}_c(I,T)$ the proportion of infected cells contributing to cell-to-cell transmission. A requirement for an infected cell to participate in cell-to-cell spread are uninfected neighboring targets.

In the aCC-model (Eq. (5.6) with $\beta_f = \delta_I = \delta_T = 0$) the increase of infected cells was calculated with

$$\Delta_{\text{ODE}} I(t) = \beta_c f_c(I(t))\, I(t) T(t). \tag{5.8}$$

Because the aCC-model captured the infection dynamics observed in the ABM-simulations well, both equations, Eqs. (5.7) and (5.8), should describe the same increase, i.e., $\Delta_{\text{ABM}} I(t) = \Delta_{\text{ODE}} I(t)$. Indeed, this can be seen in Fig. 5.5D, where the small step just before three days p.i. was due to foci growing larger leading to the appearance of the first CC non-contributors described by the adjustment term. Coercing constants and comparing Eq. (5.7) and Eq. (5.8) showed that target cells, $T(t)$, occur in the ODE - but not the agent-based model. Additionally, reconsidering term $\tilde{f}_c(I,T)$ revealed that it implicitly depended on the available target cells at a given time. Thus, the resulting $f_c(I(t))$, obtained from the best fitting parameter set to the *in silico* data, needed to be corrected with the proportion of still available target cells (Fig. 5.5C, dashed green line), i.e., $\tilde{f}_c(I,T) = f_c(I(t))T(t)/T_0$. Here, $T(t)/T_0$ describes the proportion of available target cells at time t with T_0 defining the total number of target cells at the start of the infection dynamics.

In summary, even though initiation of several foci with subsequent heterogeneous focus growth and merging of foci stands in conflict with the assumptions used to derive the adjustment term f_c, it provided a good description of the data, especially capturing the decelerated infection dynamics during progression of infection (Fig. 5.5B). Furthermore, correcting the adjustment term for the proportion of available target cells, resulted in correct predictions of cell-to-cell contributors (Fig. 5.5C). Therefore, the aCC-model provided a better description of the observed infection dynamics than conventional models when analyzing viral spread by cell-to-cell transmission among stationary cells.

5.7 Using population-dynamics models to disentangle combined transmission dynamics

So far, cell-free transmission was neglected in my analyses. However, in experiments studying the spread of viral infections both transmission modes generally occur simultaneously, if the virus is able to exploit cell-free and cell-to-cell transmission. Therefore, it was important to investigate the ability of population-dynamics models (Eq. (5.1) and Eq. (5.6)) to disentangle the contribution of cell-free and cell-to-cell transmission to viral dissemination. To this end, the agent-based model was simulated with both transmission modes occurring simultaneously. As cell-free transmission is dependent on the extracellular viral concentration, the intracellular production of virions as well as their diffusion through the extracellular space upon release was incorporated in the ABM and the extracellular viral load was followed (see Section 4.3).

Tab. 5.2. Estimated transmission rates obtained from fitting models CCF and aCCF to *in silico* data with simultaneous occurrence of both transmission modes. Transmission rates β_f (cell-free) and β_c (cell-to-cell) are given in units $\times 10^{-7}\mathrm{h}^{-1}$ and $\times 10^{-6}\mathrm{h}^{-1}$, respectively. Fitting only the number of infected cells to *in silico* data, where both transmission modes occurred, without separate quantification of cell-free transmission (Fig. 5.6A), no reasonable estimates for β_f could be obtained, i.e., β_f was not identifiable (ni). Confidence intervals were calculated from 2×10^3 (CC/CF) and 10^3 (CC/CF + CF) individual fits using random starting conditions and considering all parameter combinations within 3.84 of the best MLE. The performance of the different models was evaluated with the corrected AIC, $\Delta\mathrm{AICc}$, which was calculated relative to the AICc of the best fitting model for each scenario, i.e., $\Delta\mathrm{AICc} = 0$.

Scenario	**Both transmission modes**		**Both transmission modes + only CF**	
Model	CCF	aCCF	CCF	aCCF
β_c	1.42 (0, 1.45]	1.64 [1.60, 1.80]	0.92 [0.90, 0.93]	0.92 [0.90, 0.98]
β_f	ni	ni	2.58 [2.19, 3.12]	2.58 [2.20, 2.88]
ΔAICc	60	0	0	9.5

Using this *in silico* data, I tested various ODE models in their ability to predict the proportion of cells infected by cell-free transmission (CF proportion) observed in the ABM-simulations.

In line with the previous sections, cellular turnover was neglected in the agent-based and ODE models. Again, to disentangle the initiation and subsequent infection dynamics, the first 17 hours of the *in silico* data were not considered in the fitting procedure, essentially shifting the *in silico* data. In a first step, I assumed viral diffusion to be slow in the extracellular space. Even though the occurrence of cell-free transmission resulted in a better-mixed system than observed from a situation without cell-free transmission (Fig. 5.1C), the adjusted model (aCCF-model, Eq. (5.6) with $\delta_I = \delta_T = 0$) performed significantly better than the standard model (CCF-model, Eq. (5.1) with $\delta_I = \delta_T = 0$) (see Fig. 5.6A and $\Delta_{\mathrm{AICc}} = 60$ in Table 5.2).

Besides the inability of the CCF-model to correctly describe the infected cell dynamics, it also incorrectly predicted the contribution of each transmission mode. Within confidence of the best fit of this model lay all possible proportions, i.e., proportion of cells infected by cell-free transmission varied between 0 and 1, while the individual time courses did not reflect the dynamics observed in the agent-based simulations (Fig. 5.6B, thick magenta line represents the best fit with shaded area showing part of the confidence interval and dashed lines indicating examples of individual fits). The aCCF-model on the contrary predicted an increasing proportion of cells infected by cell-free transmission during progression of infection, with a relatively narrow confidence bound, comparable to the observations in the *in silico* data (Fig. 5.6B, green line). At later time points, however, the proportion of cells infected by cell-free transmission was underestimated. This was not surprising as slow viral diffusion as used in the ABM mimicked cell-to-cell spread. Nonetheless, the adjusted model provided a reasonable approximation, especially compared to the inability of the standard model to infer the proportion of cells infected by cell-free transmission during progression of infection.

The underestimation of cells infected through cell-free transmission observed in the aCCF-model was presumably caused by slow viral diffusion mimicking cell-to-cell spread. Next, I tested, if a standard mass-action kinetics model was able to describe cell-free transmission dynamics obtained from the ABM. To this end, the agent-based model was simulated with slow and fast viral diffusion and without cell-to-cell spread (Fig. 5.6C). Indeed, fitting the

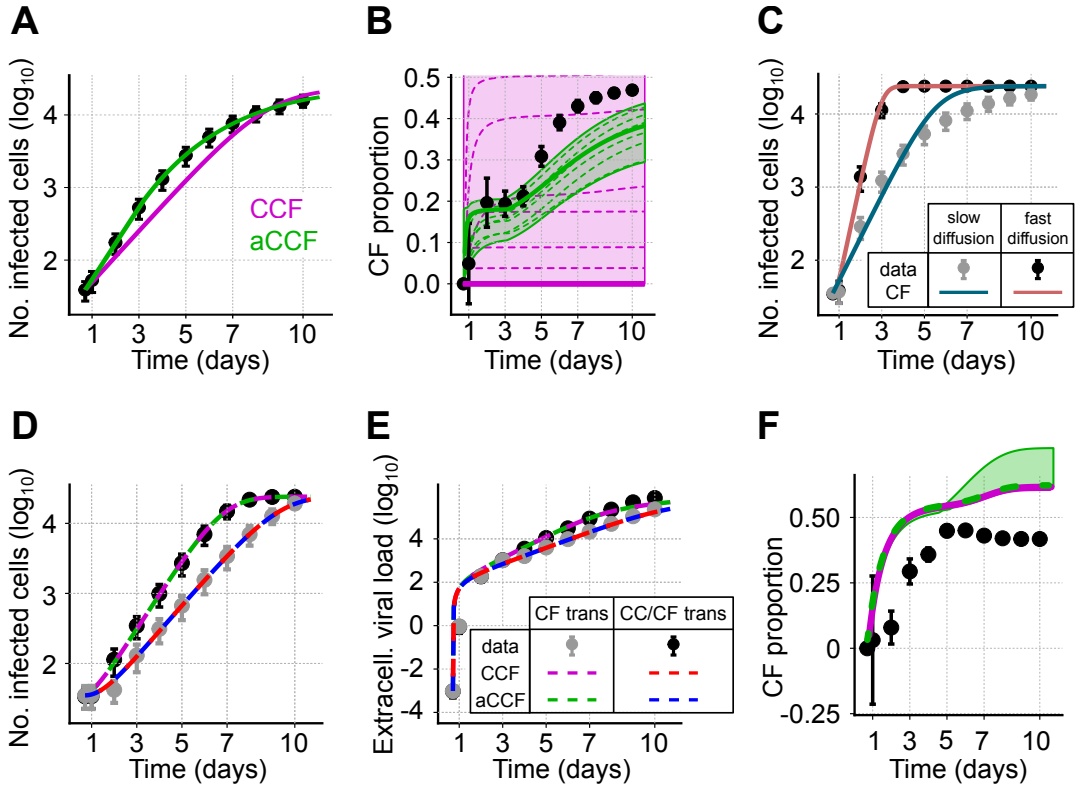

Fig. 5.6. **Disentangling viral transmission modes.** **(A)** Simulated data for a scenario assuming simultaneous occurrence of both transmission modes with slow diffusion of cell-free virus. The mean and 95%-CI for the total number of infected cells averaged over 100 individual ABM-simulations sampled every 24 hours are indicated with black dots and black lines, respectively. Lines show the best fits of a model without (CCF-model, magenta, Eq. (5.1)) or with adjusted cell-to-cell transmission dynamics (aCCF-model, green, Eq. (5.6)) fitted to the number of infected cells. **(B)** The predicted and observed (black dots) proportion of cells infected by CF-transmission. While thick lines indicate the best fit of the respective models, 95%-CI are shown with shaded areas and individual example fits with thin dashed lines. Confidence intervals shown here were calculated from 2×10^3 individual fits using random starting conditions and considering all parameter combinations within 3.84 of the best MLE. Colors correspond to the same models as in **(A)**. Confidence interval for the CCF model stretched to 100% cells infected by cell-free transmission, but was cropped at 50% in this figure for illustration purposes. **(C)** ABM-simulations only allowing CF-transmission to occur with slow (gray) and fast viral diffusion (black). Lines indicate the best fit of the standard model (Eq. (5.1) with $\beta_c = 0$) to the *in silico* data with slow (blue line) and fast viral diffusion (rose-colored line). **(D-F)** ABM-simulations with fast viral diffusion only considering CF-transmission (gray) or simultaneous occurrence of both transmission modes (black). Here, both scenarios were fitted simultaneously to the number of infected cells **(D)** and the dynamics of the extracellular viral load **(E)**. **(F)** The observed (black) and predicted proportions of cells infected through CF-transmission during simultaneous occurrence of both transmission modes. While the 95%-CI of the CCF-model was too narrow to visualize, it is indicated with the shaded green area for the aCCF-model. Corresponding parameter estimates for each of the different models are shown in Table 5.2. Figure adapted from [12].

standard model of virus dynamics (CF-model, Eq. (5.1) with $\beta_c = \delta_I = \delta_T = 0$) showed that infection dynamics with slow viral diffusion could not be captured by this model. This could be linked to occurrence of spatially confined infections rather than a homogeneous distribution of infected cells, which breaches the assumption of a well-mixed system (Fig. 5.6C). However, assuming fast viral diffusion rates (approximately 165 times faster) the agent-based model resembled a well-mixed system, thus, allowing the CF-model to correctly describe the infection dynamics (Fig. 5.6C). Thus, cell-free transmission can only be quantified correctly for fast viral diffusion rates.

In a next step, following a similar approach as taken by Iwami *et al.* [70], I tried to disentangle the contribution of each transmission mode using two distinct *in silico* data sets, i.e., one with the simultaneous occurrence of both transmission modes and one with blocked cell-to-cell spread. Here, the diffusion of virus was assumed to be a fast process. Under these conditions both models, CCF and aCCF, provided a good description of the dynamics for infected cells as well as the extracellular viral load (Fig. 5.6D+E). Fitting this data, the necessity of the adjustment term vanished due to the constant formation of new foci through cell-free spread ($\Delta\mathrm{AICc} = 9.5$, Table 5.2). This lead to small foci sizes and, thus, a high proportion of cell-to-cell contributors, which only decreased due to target cell limitations at late stages of the *in silico* experiment. Therefore, both models lead to similar estimates for the cell-free and cell-to-cell transmission rates, β_f and β_c, respectively (Table 5.2). Surprisingly, despite the correct description of the infection kinetics (Fig. 5.6D+E), both models overestimated the proportion of cells infected by cell-free virus (Fig. 5.6F).

Summarizing, the population-dynamics models presented here provided a rough approximation for the proportion of cells infected by either transmission mode assuming fast viral diffusion and separate quantification of the transmission kinetics. In this scenario, however, no evidence for the application of the adjusted model was found. For slowly diffusing virus, in contrast, the aCCF-model is recommended as it correctly described the data and provided a better approximation of the contribution of each transmission mode to the infection dynamics than the previously published CCF-model.

5.8 Evaluating the transmission dynamics of HIV-1 spread *in vitro*

In Chapter 3, I already showed that the contribution of transmission modes to the infection dynamics of cells cultured in suspension presumably varied between my results and previously published results [70]. To investigate a possible impact of the modeling approach on the obtained contribution of cell-free transmission during infection in the previous study, I re-analyzed their data on the spread of HIV-1 *in vitro* [70]. In this data set Iwami *et al.* either kept their cell culture under static or shaking conditions. In the latter this inhibited cell-cell contacts and, therefore, blocks cell-to-cell spread without influencing cell-free transmission [20, 70].

When applying the adjusted model to this data, one should have in mind that HIV-1 primarily infects motile cells. However, assuming no prior knowledge on T cell migration, e.g., due to limited insight into the motility of T cells in high cell densities as observed in aqueous media,

the adjustment term might prove useful, even though this neglects the fact that cells are not stationary in this context.

In this section, I compared the previous approach by Iwami *et al.*, which was based on mass-action kinetics (CCF-model, Eq. (C.3)), to an adaptation of the aCCF-model (see Table C.2 for more information). To this end, I fitted the data obtained from the static and shaking cell cultures using the mean parameters for viral loss, c, target cell proliferation, λ_T and carrying capacity, T_C, as published in [70]. Following their hypothesis, I assumed complete blocking of cell-to-cell spread in the shaking culture, i.e., $\beta_c = 0$.

In general, introducing a delay on the viral production of infected cells rendered the biggest improvement on model predictions compared to the previously published model [70] (Fig. 5.7A, magenta and blue lines, $\Delta\mathrm{AICc} = 31.7$ of CCF-model vs. CCF-d_p-model, Table C.3). Additionally incorporating the adjustment term, i.e., accounting for decreasing proportions of cell-to-cell contributors, further improved model predictions. In particular, it provided a better description of the kinetics observed in the shaking culture (Fig. 5.7A, blue and green lines, $\Delta\mathrm{AICc} = 4.4$ of aCCF-d_p-model vs. CCF-d_p-model, Table C.3). As observed previously, the estimate of the cell-to-cell transmission rate was slightly higher in the adjusted model with delayed viral production (aCCF-d_p), than in a model neglecting the adjustment term ($\beta_c = 1.59\,[1.26, 2.15] \times 10^{-6}(\mathrm{p24\,day})^{-1}$ in aCCF-d_p vs. $\beta_c = 1.01\,[0.84, 1.18] \times 10^{-6}$ $(\mathrm{p24\,day})^{-1}$ in CCF-d_p) (TableC.3). Accordingly, the cell-free transmission rate was estimated to be lower in the latter model ($\beta_c = 5.58\,[4.88, 6.78] \times 10^{-6}$ $(\mathrm{p24\,day})^{-1}$ in aCCF-d_p vs. $\beta_c = 4.19\,[3.39, 5.30] \times 10^{-6}(\mathrm{p24\,day})^{-1}$ in CCF-d_p). While the value of the introduced delay obtained from the best fit varied between the CCF-d_p- and aCCF-d_p-model, the 95%-confidence intervals overlapped ($\tau = 0.9$ $[0.75, 1.82]$ vs. $\tau = 1.76$ $[1.51, 1.87]$). Thus, in agreement with previous publications [147, 148], an HIV-infected Jurkat cell probably needed between 21 and 44 hours until viral production was initiated in this experiment. Viral production and death of infected cells were comparable between models (Table C.3).

Even though cells used in this experiment were motile T cells, the adjusted model provided a better description of the data than a model assuming a well-mixed system. The improvement in this set-up could stem from locally constrained cellular movement due to high cell densities or the formation of syncytia during the course of infection. While the basic model (CCF-model) as used by Iwami *et al.* [70] predicted a nearly constant proportion of approximately 60% of the infections being due to cell-to-cell transmission, the extended models showed oscillatory behavior of this fraction with values between 25% and 75% (Fig. 5.7B). Thus, the contribution of each transmission mode to HIV spread *in vitro* could be more dynamic than previously suggested. Interestingly, following the analysis from Chapter 3, suspension and loose collagen did not show oscillations with regard to the contribution of transmission modes. However, in dense collagen slight oscillations were observed.

5.9 Discussion

In this chapter, I showed that previously used population-based modeling approaches fall short when trying to explain spatially heterogeneous infection patterns. Those patterns can be observed in stationary or slow-moving cell cultures without cell-free transmission

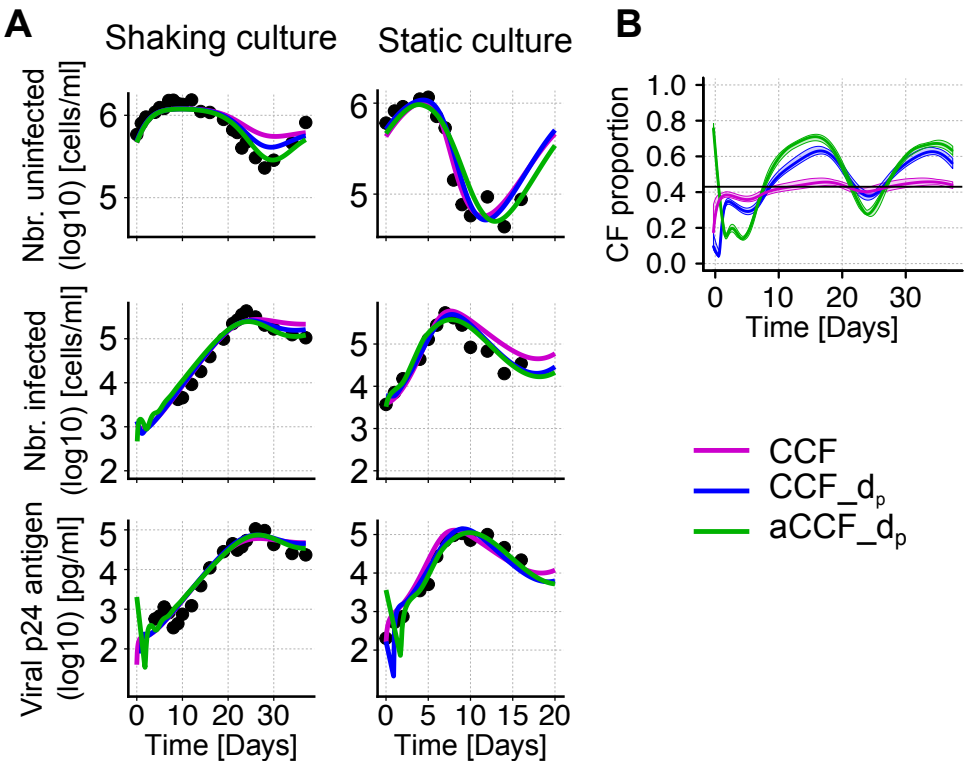

Fig. 5.7. ***In vitro* spread of HIV-1 in shaking and static cell cultures. (A)** Performance of different models in describing the data published in [70]. The measured dynamics of the average densities of uninfected (top) and infected cells (middle), as well as the viral load (bottom) from three independent experiments are indicated with black dots. In comparison to Iwami *et al.* [70], who analyzed each experimental run individually, I performed my analysis on pooled data, i.e., the mean value calculated from the individual experiments per time point. Nonetheless, parameter estimates for the CCF-model were comparable between the two approaches (see Table C.3). Model predictions for the standard model (CCF, magenta), the standard model accounting for a viral eclipse phase (CCF-d_p, blue) and, additionally, considering the adjustment term (aCCF-d_p, green) using the best parameter fits as given in Table C.3 are shown here. **(B)** Predicted CF proportion of total infected cells in the static culture at any given time. Black line indicates the CF proportion published in [70]. Confidence intervals shown here were calculated from 2×10^3 individual fits using random starting conditions and considering all parameter combinations within 3.84 of the best MLE.

(Fig. 5.4A and Fig. 5.5B) or a slowly diffusing virus (Fig. 5.6C). The difficulty mass-action kinetics models encounter when trying describe this kind of infection dynamics is to be expected as they generally assume a well-mixed system and, thus, implicitly that all infected cells contribute to cell-to-cell spread. However, the proportion of contributors decreases with increasing focus sizes as infected cells get surrounded by other infected cells leaving no target cells to infect during progression of infection. A model not accounting for the decrease of cell-to-cell contributor proportions leads to overestimation of infected cells that actually drive the spread of infection. Therefore, such a model cannot explain the decelerated infection dynamics. This shortcoming could be compensated by introducing an adjustment term accounting for the decreasing proportion of cell-to-cell contributors during progression of infection as developed in this chapter (Fig. 5.4B and Fig. 5.5C). The adjusted model was able to explain the decelerated infection dynamics observed for a virus solely spreading through cell-to-cell transmission among stationary cells. Furthermore, it correctly predicted the proportion of cell-to-cell contributors over time. Merging and heterogeneous growth of multiple foci was also captured by the adjustment term (Fig. 5.5).

In general, to disentangle the contribution of cell-free and cell-to-cell transmission, during simultaneous occurrence, is a challenging task for mass-action kinetics models even when accounting for the loss of contributors (Fig. 5.6). Nonetheless, when cell-free virus diffused slowly, the adjusted model provided better approximations of the proportion of cells infected through either transmission mode than previous approaches (Fig. 5.6A+B). However, in this scenario the contribution of cell-free spread to infection was underestimated at late stages of the experiment due to slow viral diffusion leading to locally confined cell-free infections, thus, mimicking cell-to-cell transmission. Analyzing experiments with one transmission mode blocked for separate quantification [70, 117], might be helpful to get better predictions. Unfortunately, cell-free spread needed fast viral diffusion to be reasonably well described by population-dynamics models (CF-model, Fig. 5.6C), which in turn impaired the performance of ODE models as they had difficulties describing the formation of new foci as well as the synergistic effects observed for the simultaneous occurrence of both transmission modes (Fig. 5.6F).

Without assuming prior knowledge on the motility of T cells, I re-analyzed data on the spread of HIV-1 *in vitro* [70] using the newly derived adjusted model. My novel approach described the data best, hinting towards locally confined cellular movements or the formation of syncytia as both explanations would result in the formation of large foci of infected cells. However, incorporating a delay on virus production exhibited the biggest improvement. Both models showed a more dynamic and oscillatory behavior of proportions of cells infected through either transmission mode during the experiment than suggested by Iwami *et al.* [70] with phases of cell-to-cell or cell-free dominated spread (Fig. 5.7B). This oscillatory behavior presumably arose from the interplay between both transmission modes. Limited cell-to-cell transmission due to decreasing proportions of cell-to-cell contributors could be compensated by the formation of new foci by cell-free spread. These dynamics could be observed if cell-to-cell transmission was more efficient or virus diffused slowly leading to large foci of infected cells (see also Chapter 4). For HIV this could in principal be the case as cell-to-cell transmission has been estimated to be 100-18.000 times more effective than cell-free spread [18, 19]. Similar predictions have been reported for other viruses as cell-to-cell transmission shields the virus from host neutralizing antibodies and other viral clearance mechanisms [10, 14]. However, these findings on the efficacy of cell-to-cell spread might be specific to the utilized experimental conditions as pointed out in Chapter 3 and 4.

The adjusted model presented here, can be viewed as a first step towards improved quantification of cell-to-cell transmission among stationary cells using population-based measurements. However, the shortcomings of mass-action kinetics models during the simultaneous occurrence of both transmission modes, showed the necessity of more elaborate models. Individual cell-based approaches, such as agent-based or cellular Potts models presented here (Chapter 4) and elsewhere [106, 109], might be able to allow a more detailed description and analysis of the transmission kinetics. Combining more sophisticated data, which does not solely rely on bulk measurements, with advances in computational methods allowing parameter estimation for stochastic models (see Chapter 4 and [149]), could enhance the possibility to infer the infection kinetics and predict the correct contribution of each transmission mode to viral spread for different pathogens.

Part IV

General discussion

6 General discussion

The way a virus spreads within tissues using cell-free and cell-to-cell transmission strongly influences the infection dynamics and also affects possible targets for drug and vaccine development. While several experimental studies have tried to shed some light on the efficiency of transmission modes [9, 18–20], they were limited in their attempt to disentangle the contribution of transmission modes to the infection dynamics due to experimental limitations. On that account, it is surprising that from a mathematical modeling point of view the disentanglement of transmission modes has been a neglected field of study with only few publications addressing this topic [70, 111, 150]. Interestingly, most studies including mathematical modeling predict higher contributions of cell-free transmission than would be anticipated from studies only relying on experimental data (with the exception of HBV, where both, experiments and modeling, predicted mainly cell-free transmission [111]). To enhance the limited literature on mathematical modeling of cell-to-cell spread, I studied the dissemination of HIV and HCV, viruses capable of infecting cells with both modes of transmission, under different conditions with various modeling approaches.

6.1 Contribution of transmission modes to the infection dynamics is shaped by the environment

From previous studies it has become evident that mathematical modeling in combination with experimental data can give valuable insights not achievable otherwise (e.g. [90, 92]).

To guide drug and vaccine development efficiently, knowledge of the contribution of cell-to-cell transmission in the context of viral infections *in vivo* would be helpful. However, without the ability to measure quantities governing the infection dynamics in-detail, e.g., viral load or number of infected cells in lymph nodes over time, or sufficient possibilities to modify certain within-host aspects, such as cell densities in lymph nodes, disentangling the contribution of transmission modes *in vivo* is not yet within reach, given the available experimental tools. So far, *in vitro* studies have not been designed carefully enough or mathematical models were not sufficiently detailed to obtain *in vitro* results transferable to *in vivo* situations with respect to the utilized transmission modes of particular viruses [21, 70, 99]. In an attempt to resolve the problems of transferability between *in vitro* and *in vivo* situations, I studied the spread of HIV and HCV under varying conditions with different modeling approaches. This revealed that the contribution of the transmission modes to the infection dynamics depended on a variety of factors, such as the amount of externally provided lipids or the density of cells. The latter could be linked to the provided extracellular micro-environment, which could either lead to a dense monolayer of cells in the case of aqueous media or serve as a scaffold for motile cells allowing exploration of all space dimensions in collagen environments. While my analysis gave no clear cut answer for the *in vivo* situation with regard to the predominant mode of

transmission utilized by HIV and HCV, it still provided quantification of the transmission modes in specific conditions. This comes as no surprise, because my analysis showed that the studied viruses were able to adapt to the encountered extracellular environments, therefore impeding statements as to which transmission mode is used mainly *in vivo*, where the virus is confronted with various environments. In contrary to the general opinion that cell-to-cell transmission is orders of magnitude more efficient than cell-free transmission and, thus, plays a dominant role in the infection dynamics [9, 18–21], I found conditions under which cell-free transmission was the main contributor. For example, in a lipid-rich environment HCV spread mainly by cell-free transmission and in the case of HIV this was predicted in aqueous media with its high cell densities.

Using the best fitting parameter set, my studies on HIV predicted approximately 0%, 60%, 80% cell-to-cell infected cells in aqueous media, dense collagen, and loose collagen, respectively, with estimates ranging widely, reaching values of up to 100% in all environments (see Chapter 3). However, irrespective of the exact estimates, viruses in collagen environments exhibited a stronger shift towards cell-to-cell transmission in comparison to aqueous media. The low densities of CD4 T cells observed in collagen environments result in large distances, which need to be covered by the virus until encountering a target cell, presumably causing differences in the contribution of cell-free transmission between aqueous media and collagen. A virus diffusing in the extracellular space is exposed to immune pressure as it may be encountered by patrolling immune cells. Covering large distances therefore increases the risk of being detected by the immune response and, additionally, of loosing infectivity. With this knowledge a shift towards cell-to-cell transmission in the context of low cell densities seems a beneficial or even necessary strategy for HIV. Comparing data obtained from bovine (loose) and rat tail (dense) collagen revealed that infection of T cells was more efficient in dense than loose collagen, which could be linked to differences in the velocity profiles of T cells [69]. This presumably illustrates, why viral spread is predominantly observed in the lymph node, a densely packed 3D structure similar to the dense collagen environment [63]. High target cell densities as observed in lymph nodes lead to an increase of the total number of long contacts between uninfected and infected cells compared to other tissues. Following my analysis, this could promote cell-to-cell spread, therefore cell-to-cell being the predominant transmission mode in the lymph node. Because transfer of drawn conclusions from *in vitro* to *in vivo* situations is desirable and the collagen environment resembles the lymph node more closely, this highlights the importance of 3D cell cultures in the context of HIV infection [63].

In contrast to HIV, a monolayer of cells seems a reasonable set-up to study HCV *in vitro* as hepatocytes *in vivo* also form dense layers of stationary cells. Although *in vivo* hepatocytes occur in a 3D structure, using a 2D system *in vitro* should not affect the results, because the liver is a regular organized organ, where each space dimension can be treated equally. At first glance, the contribution of cell-to-cell transmission to HCV infections of Huh7 cells in a monolayer appeared to vary largely across identical experiments, assuming values between 25% and 75% of cell-free infected cells after an initial phase, during which only cell-to-cell transmission was exploited (see Chapter 4). On a second look, when analyzing the precise experimental setup, it showed that my collaborators had changed the fetal bovine serum (FBS) supplied to the cells between experiments (before change: Exp. 29C and 29D, after change: Exp. 29I and 29J). The discrepancy could therefore be linked to varying compositions of the

FBS, providing uneven amounts of lipids. Referring to the data obtained from the various experiments, proliferation and infected cell counts were higher in experiments performed after change of the FBS, hinting towards a serum richer with lipids. Tying in with these observations, previous publications showed that lipids were necessary for hepatocyte proliferation [151] and viral replication of HCV [141, 142, 144]. This theory was supported when additionally fitting Exp. 29I resulted in similar dynamics of the contributions of cell-free transmission as predicted for Exp. 29J. The missing lipids in the earlier experiments could also result in lower numbers of cell-free infected cells as lipids previously have been associated with viral release [142]. To study HCV spread *in vivo*, several studies made use of single cell laser capture microdissection, which lead to the discovery of focal distributions of infected cells in the liver [101, 152, 153]. While the infection patterns could be linked to cell-to-cell transmission, my results show that in case of slow viral diffusion clustering is also observed for high proportions of cell-free infected cells as seen in Exp. 29J. A strong contribution of cell-free spread in the liver would go hand in hand with high availability of lipids in this organ.

Besides adaptation of the virus to changing environments, my studies also offered valuable clues on why HCV and HIV have evolved and kept two separate modes of transmission. For example, in case of HCV a synergistic effect between transmission modes was predicted in this thesis, which could act as an evolutionary benefit. For a virus to keep both modes of transmission is presumably less energy efficient than entertaining only one of them. Nonetheless, the possibility of adapting to different environments and the synergistic effect between transmission modes seems to provide HCV with an evolutionary advantage counteracting a possibly less energy-efficient strategy when possessing two separate transmission modes. In the context of HIV infections, my results showed strong dependence of the contribution of transmission modes with regard to the encountered extracellular environments. As HIV moves through the body, it encounters various tissues, thus, making both transmission modes indispensable. My analyses showed that HIV and HCV are capable of spreading within different environments exploiting both modes of transmission to adapt to various environments. Unfortunately this means that a drug or vaccine would have to block both transmission modes simultaneously. Otherwise the virus would most likely escape the pressure applied by the drug or vaccine. Effective vaccines or drugs therefore need to attack either early points in the viral life cycle or components involved in both transmission modes.

6.2 Modeling approach influences predicted contribution of transmission modes

The ability to determine the contribution of each transmission mode to viral spread and, thus, to judge their biological importance also depends on the modeling approach. To enhance the knowledge on the effect of different modeling approaches to the contribution of transmission modes during viral infections, I studied viral spread in the context of stationary cells (Chapter 5). Here, a standard mass-action kinetics model missed to capture the infection dynamics even in the simplest form, i.e., one cell, infected with a virus only capable of using cell-to-cell transmission, initially seeded in the middle of a well. Extending this model with an adjustment term, which took the decreasing proportion of cells contributing to cell-to-cell transmission with increasing focus sizes into account, allowed correct description and

quantification of this process. Assuming slow viral diffusion, my adjusted model, in contrast to the standard model, was able to recover the changing proportion of cell-free infected cells during simultaneous occurrence of both transmission modes over the course of the *in silico* experiment. Although faster viral diffusion allowed similar performance of both models, they failed to recover the correct proportion of cell-free infected cells.

To what extent the motility of cells in the context of HIV might circumvent spatial limitations, allowing constant mixing between target and infected cells, still remains to be investigated. An indication towards the need to apply the newly developed adjustment term even for motile target cells could be my results obtained in Section 5.8, where I fitted the adjusted model to a previously published data set [70]. This revealed a varying contribution of cell-free transmission to the infection dynamics, which was not captured by the authors of this study using the standard mass-action kinetics model. However, improvement was just minor with the largest difference stemming from incorporating a delay between infection and start of viral production. The data described in Chapter 3 could give more insights on this topic in the context of motile target cells.

Altogether, my analyses showed that a correct description of cell-to-cell spread is important to obtain reliable results. In motile cells, the contact duration between cells is an essential factor that should be captured by the applied model. When it comes to stationary or slow moving cells, local constraints on the infection exerted by cell-to-cell transmission should also be incorporated into the model used to analyze the infection dynamics. Several possibilities to include a spatial dimension have been studied. For example, Funk *et al.* used a grid-based approach to discretize partial differential equation models describing virus-immune dynamics [134]. This revealed that spatially homogeneous and heterogeneous models behaved considerably different, especially with regard to the infected cell numbers at peak of infection. Other possibilities include agent-based [104, 109] and cellular Potts [105, 106] models. Especially in the case of HIV, the latter seems a necessary choice for future modeling approaches as it is able to account for cell motility, a factor that can influence HIV infections among PBMCs.

6.3 Mathematical modeling of cell-to-cell transmission in other studies

Interestingly, most publications treating cell-to-cell spread mathematically have acknowledged the spatial dimension of this transmission mode and have refrained from simple mass-action kinetics models applying more complex models. Following a similar approach as presented in Chapter 4, Yakimovich *et al.* were able to show that the infection dynamics of Human Adenovirus could be described solely with cell-free transmission [150]. They infected human lung carcinoma cells in a monolayer and overlaid some wells with agarose. This blocked convection and therefore far-range diffusion of cell-free viral particles. However, they neglected cell-to-cell spread completely and the impact thereof was not discussed in their publication. For the duck hepatitis B virus, the experimentally derived hypothesis of cell-free transmission being the main source of infection [154] was validated using an agent-based model [155]. They also hypothesized that the virus under immune pressure might be able to adjust its strategy shifting towards more efficient cell-to-cell transmission [155], which is in line with the

findings presented in this thesis. In a different study considering only cell-to-cell transmission, Miyashita *et al.* estimated the number of viral genomes establishing infection of cells with the tomato mosaic virus [156]. For HCV a study on the efficiency of transmission modes is still lacking. In the context of HIV infections, several publications have tried to disentangle the two transmission modes. The first publication, combining experimental data with mathematical modeling to estimate the efficiency of transmission modes, stated that the efficiency of cell-to-cell was orders of magnitude higher than cell-free transmission [21]. Since they co-cultured uninfected with infected cells or viral inoculum produced by the same number of infected cells, their result was most likely biased as described in the *Introduction*. The first study presenting an estimate for the actual contribution of cell-to-cell transmission to HIV infection dynamics *in vitro* was published by Komarova *et al.* [99], closely followed by a publication of Iwami *et al.* [70]. Both studies predicted between 50% and 60% of infections occurring due to cell-to-cell transmission. While this gave a first rough estimate during steady state, they neglected the dynamics of the predicted contribution and, using a simple-mass action kinetics model, presumably further impaired their predictions (see Chapter 5). Comparing their result to mine is difficult due to their usage of a cancerous cell line. Their estimate of approximately 50% was considerably lower than the best estimate obtained in Chapter 3, with almost exclusive occurrence of cell-free infections in aqueous media. However, the large confidence interval found in my analysis with regard to this estimate could not exclude the possibility of comparable results.

6.4 Outlook

Besides providing us with new insights, proper research always leads to new unknowns that need unraveling. Along those lines, the research presented in this thesis is far from done and gives various possibilities to extend it.

My studies on PBMCs in several environments revealed the necessity of an adaptation phase to describe the data. As this has to my knowledge neither been reported nor studied, the mechanisms governing this process are not yet known and would need more work to be identified. Furthermore, the implications of previous models omitting the adaptation phase with regard to parameter estimates should be analyzed and previously published values adjusted accordingly. Although overfitting the data, a model including pyroptosis, i.e., an inflammatory process describing cells lost by apoptosis during HIV cell-to-cell transmission, allowed better description of the data than a model without pyroptosis. If this process is an artifact of *in vitro* infection of kidney cells or could also be observed in PBMCs is still unresolved. An interesting fact not directly related to cell-to-cell transmission was the enhanced viral production in aqueous media compared to collagen environments. To address this point, intracellular measurements would be most informative.

Concerning my agent-based model, more confidence in the predictions could be gained, if the model would resemble the data more closely, especially with regard to the comparatively high number of small foci in the model. In this thesis, I raised the hypothesis that the lipid content of the used FBS impacted the contribution of the transmission modes largely. To address this point, the lipid content of the respective sera could be measured and compared for differences. Subsequently, spread assays could be performed enriching the lipid-poor FBS with lipids found

in the lipid-rich serum. Another possibility of extending my work would be to study how the assumed delay between time point of infection and detection of 18 hours, which was the lower bound for delays reaching more than 48 hours for some cells, affected my results.

Furthermore, my hypothesis of varying contributions of transmission modes in different environments would benefit largely from experimental validation. As long-term dynamics are not feasible in the presented experimental protocol used for HIV spread due to observed cell death after 21 days in culture, one could imagine an experiment with varying densities of target cells. These data could be used to validate the predictions presented in this thesis. In the case of HCV, a possibility to enhance parameter identifiability would be to add higher anti-E2 concentrations, allowing complete blocking of cell-free transmission over the whole course of the experiment.

From a theoretical point of view, my newly developed adjustment term could be improved by incorporating the formation of new foci. A different possibility would be to analyze the influence of non-productively infected cells on the perimeter of foci and adapt the adjustment term accordingly. An interesting study could be to investigate how movement of cells challenges the necessity of the adjustment term with the help of *in silico* data obtained from a cellular Potts model (CPM), especially as this could confirm the hypothesis of slow moving Jurkat cells predicted for the experimental protocol followed in [70].

Finally, there are many viruses which were not yet or only experimentally studied in the context of exploiting different viral transmission modes [7]. For example, cell-to-cell transmission of the human cytomegalovirus (HCMV) is known to occur through cell-cell fusion [157]. Experimental findings associate cell-to-cell spread mainly with clinical HCMV, whereas cell-free spread is thought to play a dominant role in passaged laboratory strains [158]. For the measles virus experimental data suggested that cell-to-cell transmission is the main contributor to new infection within host and cell-free virions are believed to regulate the inter-host infections [159]. Forming different viral particles vaccinia virus, essential part of the only vaccine that eradicated a disease [160], namely small pox, is able to disseminate via cell-to-cell and probably cell-free transmission [161]. Several other viruses are also able to exploit both modes of viral transmission within hosts [7]. Applying any of the approaches presented in this work could add to the existing knowledge of the studied viruses. Because cell-to-cell transmission is often linked to chronic infections [14–16], its role should be evaluated for more viruses. Studying the evolutionary advantage of viruses with regard to the contribution of transmission modes to the infection dynamics would also be interesting. The question, if there is an optimal cell-free to cell-to-cell ratio and what the influencing factors of such a ratio are, could be addressed with any of the models presented in this thesis.

In summary, I have presented several techniques to quantify cell-to-cell spread and its contribution to the infection dynamics of viruses exploiting both modes of transmission. While mass-action kinetics models feature many advantages over more elaborate models, the latter should be favored, if the data are sufficiently resolved, as complex models, e.g., ABM or CPM, are able to describe the experimental data with more detail. Furthermore, I have highlighted the necessity of carefully choosing experimental protocols as they can have a strong impact on virus dynamics. To allow generalization and translation to *in vivo* situations, structures resembling the environments found in the body should be used to study viruses in a setting close to their natural habitat.

Part V

Appendix

A Additional Material to Chapter 3: Environments shape cell-to-cell spread during HIV infections

A.1 Profile likelihoods for T cell dynamics in different environments

Profile likelihoods for parameters of model (3.1). The adaptation phase was fixed to 2.5 days. For illustration purposes all y-axes were scaled such that $\Delta_{\mathrm{MLE}}(i) := \mathrm{MLE}(i) - \min(\mathrm{MLE})$. The 95%-confidence intervals, i.e., $\Delta_{\mathrm{MLE}} = \chi^2(0.05, 1) \approx 3.84$ (see Section 2.2.2 for more information), are indicated by the dashed black line. Best fitting parameter values with 95%-confidence intervals are shown in Table 3.1.

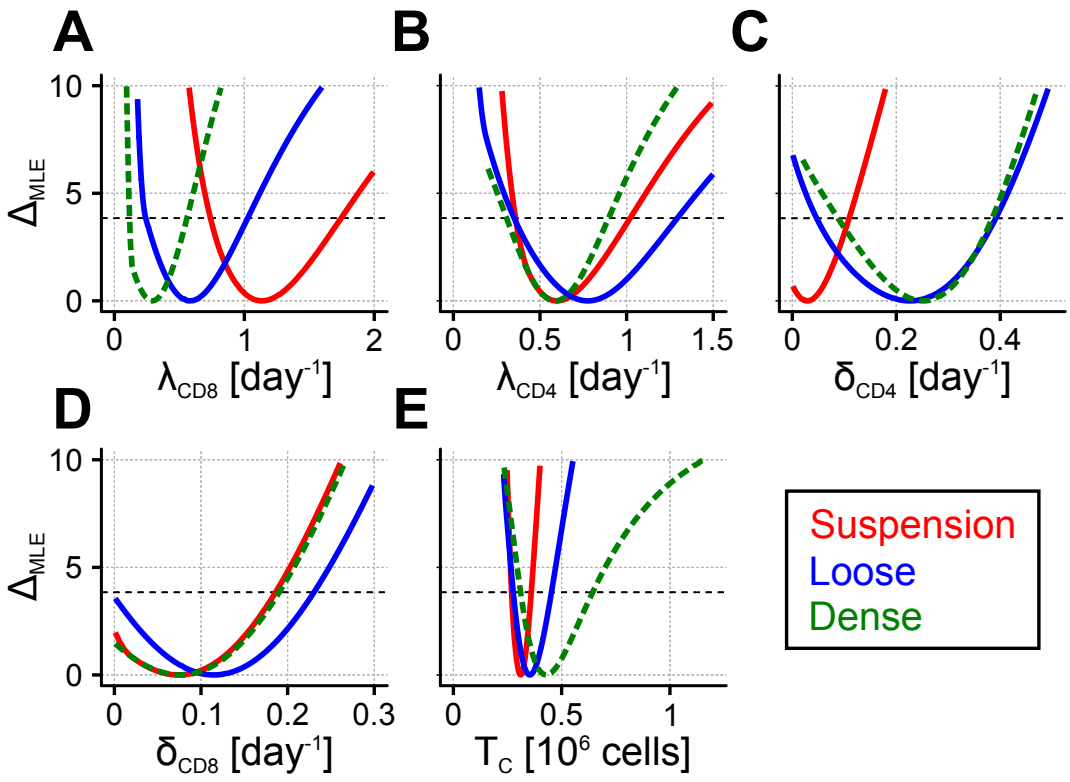

Fig. A.1. Profile likelihoods for parameters governing T cell dynamics. For illustration purposes, y-axes were scaled such that $\Delta_{\mathrm{MLE}}(i) := \mathrm{MLE}(i) - \min(\mathrm{MLE})$. 95%-confidence intervals are indicated by the dashed black line. Shown are the profile likelihoods for proliferation rates of CD8 **(A)**, CD4 **(B)** and death rates for CD8 **(C)** and CD4 **(D)**. Panel **(E)** displays the capacity of T cells per well. The different environments are indicated in solid red (suspension), solid blue (loose) and dashed green (dense) lines.

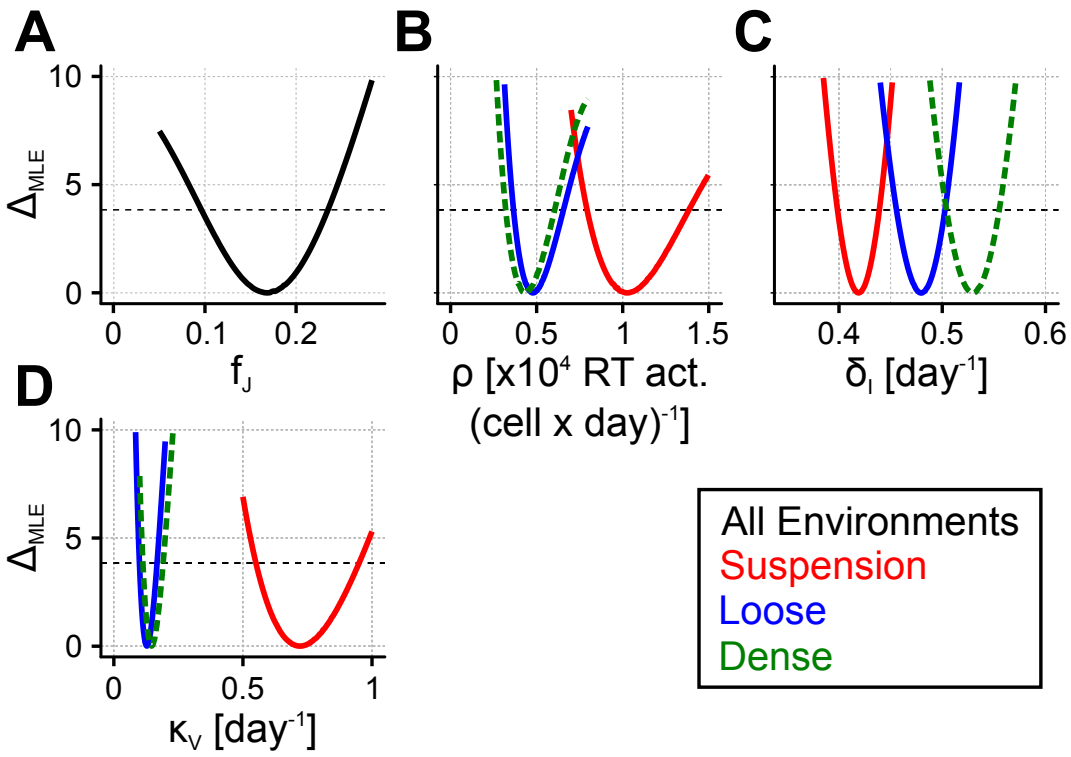

Fig. A.2. **Profile likelihoods for parameters governing infected cell turnover and viral kinetics.** For illustration purposes, y-axes were scaled such that $\Delta_{\mathrm{MLE}}(i) := \mathrm{MLE}(i) - \min(\mathrm{MLE})$. 95%-confidence intervals are indicated by the dashed black line. Black lines representing profile likelihoods imply equal values across environments. **(A)** Profile likelihood of the target cell fraction of initially non-productively infected cells. The profile likelihoods of the viral production rate **(B)**, death rate of infected cells **(C)** and viral diffusion rate **(D)** are also shown. The different environments are indicated in solid red (suspension), solid blue (loose) and dashed green (dense) lines.

A.2 Profile likelihoods for HIV virus dynamics in different environments

Profile likelihoods for parameters of model (3.2). Average eclipse phase for non-productively infected cells, i.e., $1/\kappa_I$, was set to 17.3 hours and half-life of RT activity, c_v, was fixed to 38 hours. As in the previous section, y-axes were scaled such that $\Delta_{\mathrm{MLE}}(i) := \mathrm{MLE}(i) - \min(\mathrm{MLE})$ and the 95%-confidence intervals are indicated by the dashed black line. Best fitting parameter values with 95%-confidence intervals are shown in Table 3.2.

A.3 Profile likelihoods for HIV infection kinetics in different environments

Profile likelihoods for parameters of model (3.3) without death by abortive infections, i.e., the $\mathrm{R_p}$-model. Additionally to the above assumed rates, I fixed the half-life of viral infectivity to 17.9 hours and efficiency of cell-free transmission was decreased in collagen to 14% of its efficacy in suspension, i.e., $\beta_f^{\mathrm{coll}} = 0.14 \times \beta_f^{\mathrm{susp}}$. Again, y-axes were scaled such that

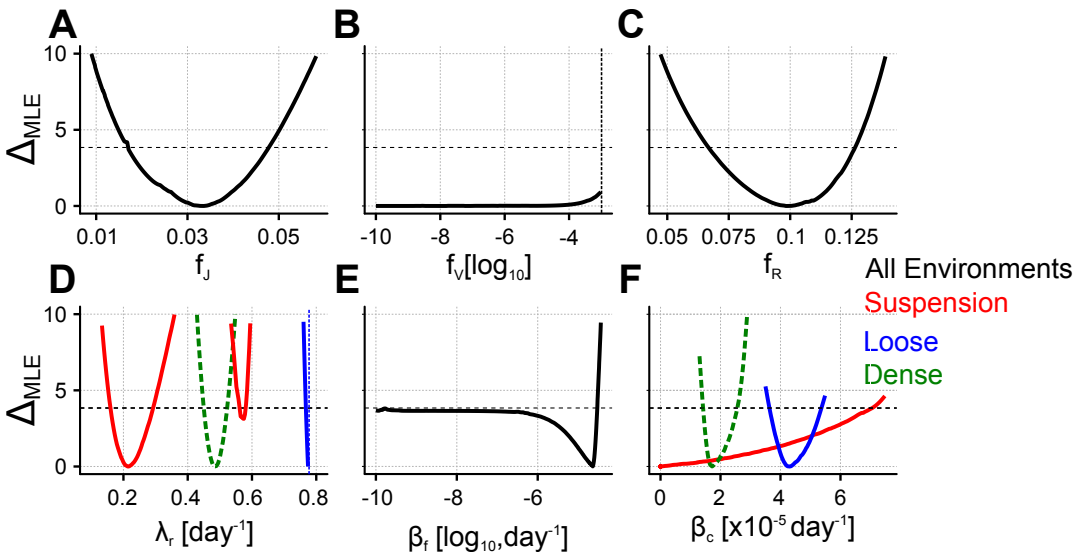

Fig. A.3. **Profile likelihoods for parameters governing the infection dynamics.** For illustration purposes, y-axes were scaled such that $\Delta_{\mathrm{MLE}}(i) := \mathrm{MLE}(i) - \min(\mathrm{MLE})$. 95%-confidence intervals are indicated by the dashed black line. Black lines representing profile likelihoods imply equal values across environments. Vertical dashed lines indicate fixed limits for the respective parameter. Shown are the profile likelihoods of the target cell fraction of initially non-productively infected cells **(A)**, initial target cell fraction of refractory cells **(B)** and infective proportion of total virus in culture **(C)**. In panel **(D)** the proliferation rate of refractory cells is displayed. Finally, panels **(E)** and **(F)** show cell-free and cell-to-cell transmission rates, respectively. The different environments are indicated in solid red (suspension), solid blue (loose) and dashed green (dense) lines.

$\Delta_{\mathrm{MLE}}(i) := \mathrm{MLE}(i) - \min(\mathrm{MLE})$ and the 95%-confidence intervals are indicated by the dashed black line. Best fitting parameter values with 95%-confidence intervals are shown in Table 3.3.

A.4 Adaptation of recently published model describing HIV infection dynamics

To compare my models to an already published approach by Iwami *et al.*, I adapted their model and fitted it in a stepwise approach as described in Chapter 3. The HIV infection kinetics model is termed *Standard* model.

The underlying model describing T cell dynamics for model *Standard* is as follows

$$\begin{aligned} \frac{dT_{\mathrm{CD8}}}{dt} &= \lambda_{\mathrm{CD8}} T_{\mathrm{CD8}} \left(1 - \frac{T_{\mathrm{CD8}} + T_{\mathrm{CD4}}}{T_c}\right) \\ \frac{dT_{\mathrm{CD4}}}{dt} &= \lambda_{\mathrm{CD4}} T_{\mathrm{CD4}} \left(1 - \frac{T_{\mathrm{CD4}} + T_{\mathrm{CD8}}}{T_c}\right) \end{aligned} \tag{A.1}$$

$$\text{with } T_{\mathrm{CD8}}(0) = T_{\mathrm{CD8},0},\ T_{\mathrm{CD4}}(0) = T_{\mathrm{CD4},0}$$

Here, CD8 and CD4 cells proliferate with rates λ_{CD8} and λ_{CD4}, respectively, competing for resources until a capacity T_c is reached. This model is comparable to model (3.1) without

adaptation phase and death of T cell subsets. To follow the approach in [70], I fitted initial conditions for CD8, $T_{\mathrm{CD8},0}$, and CD4 cells, $T_{\mathrm{CD4},0}$.

Description of the T20 experiment was accomplished using model (3.2) without explicitly following non-productively infected cells, which then served as underlying model for the *Standard* model. Additionally, I did not account for the change of media, which lead to the following model

$$\begin{aligned}\frac{dI}{dt} =& -\delta_I I\\ \frac{dV_c}{dt} =& \rho I - c_v V_c - \kappa_v V_c\\ \frac{dV_s}{dt} =& \kappa_v V_c - c_v V_s\\ \text{with } I(0) =& f_I(T_0 + I_0),\ V_c(0) = V_{c,0} \text{ and } V_s(0) = V_{s,0},\end{aligned} \tag{A.2}$$

where I assumed one parameter describing the initial proportion of infected cells across all environments. Furthermore, T_0 and I_0 are target and infected cell counts, respectively, as observed in the experiments.

In a last step, model (3.3) was adapted to resemble the model as described in [70]. To this end, refractory cells, non-productively infected cells and non-infective virus in culture were not followed explicitly. However, to some extent initial conditions were allowed to vary, i.e., I fitted an initial proportion of CD8 cells, $T_{\mathrm{CD8},0}$, within the pool of all T cells, $T_{\mathrm{all},0}$. In addition, an initial proportion, f_I, of target and infected cells as observed in the experiments was fitted across all environments. Besides that I accounted for variability of measurements at the start of the experiment in viral titers by fitting an initial proportion of virus in culture and supernatant, respectively. Furthermore, no adaptation phase, change of media, death through abortive infection or death of uninfected T cells was considered. In summary, the model reads as follows

$$\begin{aligned}\frac{dT_{\mathrm{CD8}}}{dt} &= \lambda_{\mathrm{CD8}} T_{\mathrm{CD8}} \left(1 - \frac{T_{\mathrm{CD8}} + T + I}{T_c}\right)\\ \frac{dT}{dt} &= (\lambda_{\mathrm{CD4}} T \left(1 - \frac{T_{\mathrm{CD8}} + T + I}{T_c}\right) - \beta_f T V_i - \beta_c T I\\ \frac{dI}{dt} &= \beta_f T V_i + \beta_c T I - \delta_I I\\ \frac{dV_i}{dt} &= \rho I - c_i V_i - \kappa_v V_i\\ \frac{dV_s}{dt} &= \kappa_V V_i - c_v V_s,\\ \text{with } T_{\mathrm{CD8}}(0) &= T_{\mathrm{CD8},0},\ T(0) = T_{\mathrm{all},0} - T_{\mathrm{CD8},0},\ I(0) = f_I(T_0 + I_0),\ V_i(0) = V_{i,0},\ V_s(0) = V_{s,0}\end{aligned} \tag{A.3}$$

.

Here, T_0 are the target and I_0 the infected cell counts observed in the experiments.

Fits of model (A.1) and (A.2) are shown in Fig. A.4A and B, respectively. Fits of the infection dynamics model (A.3) can be seen in Fig. A.5.

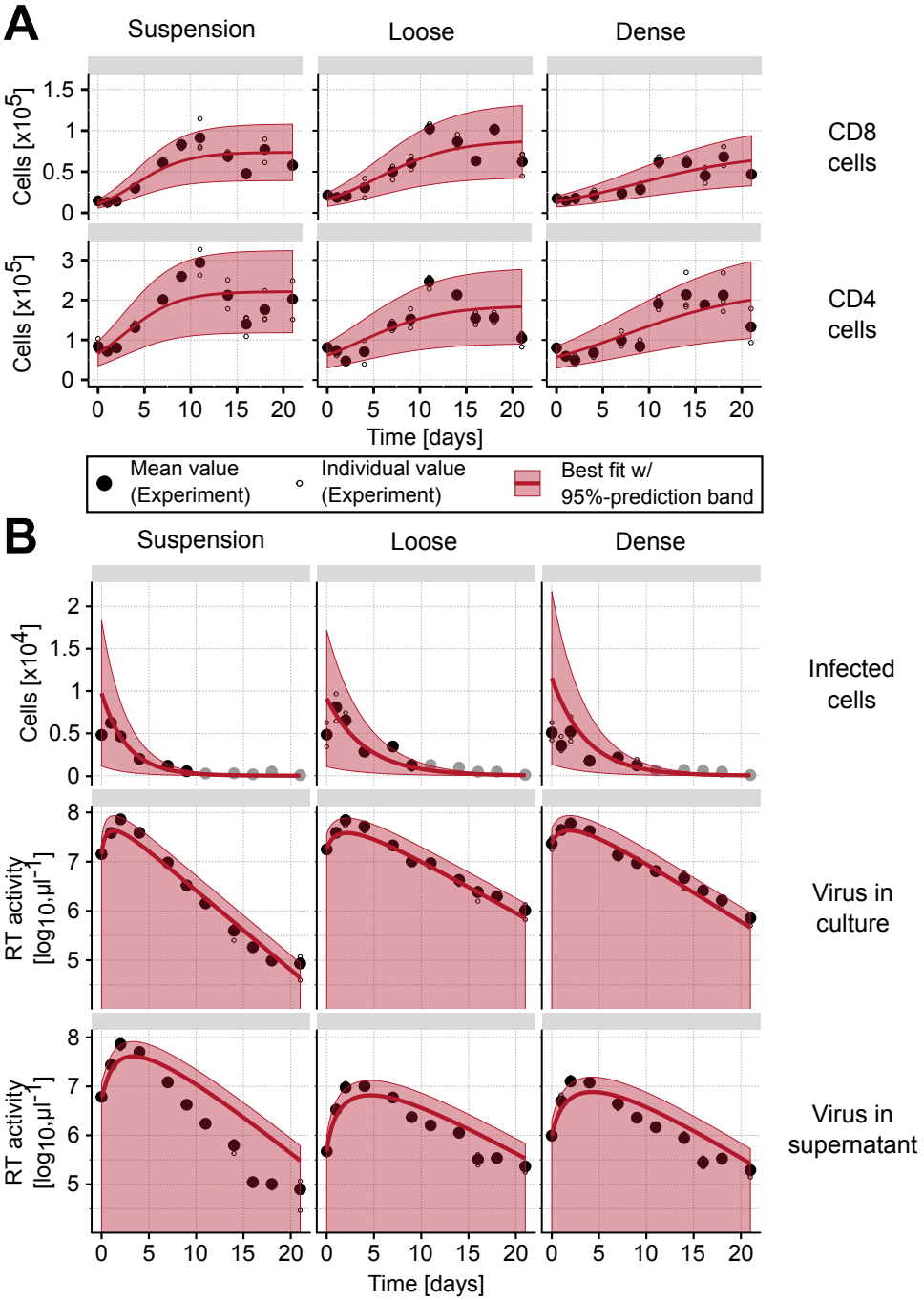

Fig. A.4. **T cell dynamics, infected cell turnover and viral kinetics as predicted by an adapted version of a previously published model.** Shown are mean counts (solid black dots) calculated from three independent experiments (open black dots) of CD8 (A, top row), CD4 (A, bottom row) and infected cells (B, top row), virus in culture (B, center row) and virus in supernatant (B, bottom row) in suspension (left column), loose (middle column), and dense collagen (right column) . **(A)** Best fit of model (A.1) (thick red line) with estimated 95%-prediction band (shaded red area) to MOCK data. Environments were fitted separately. **(B)** Best fit of model (A.2) (thick red line) with estimated 95%-prediction band (shaded red area) to T20 data. Environments were fitted simultaneously with the same initial fraction of measured infected cells. Gray dots were not fitted (see main text for details). Half-life of RT activity, c_v, was fixed to 38 hours.

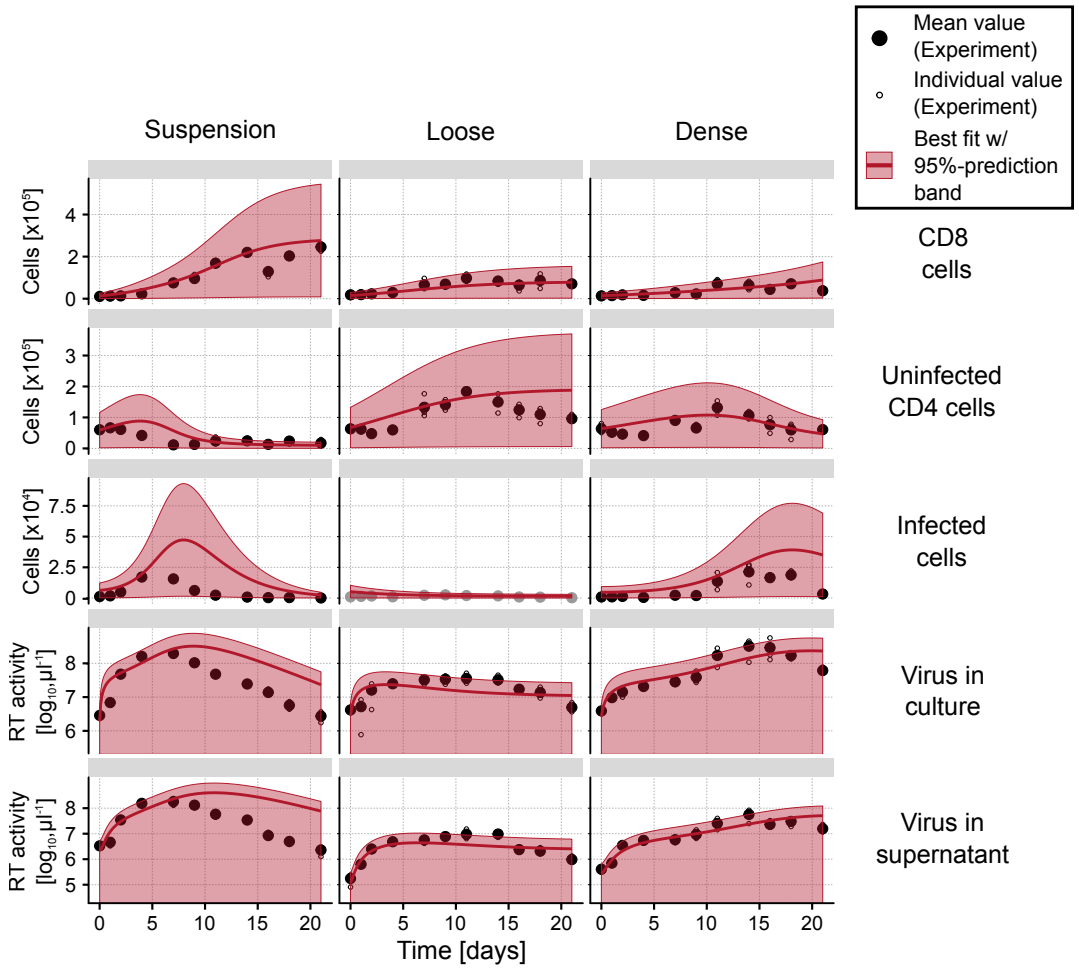

Fig. A.5. **HIV infection dynamics as predicted by an adapted version of a previously published model.** Shown are mean counts (solid black dots) calculated from three independent experiments (open black dots) of CD8 (1^{st} row), uninfected (2^{nd} row) and infected CD4 cell counts (3^{rd} row), virus in culture (4^{th} row) and virus in supernatant (5^{th} row) in suspension (left column), loose (middle column), and dense collagen (right column). Best fit of the *Standard*-model (Eq. (A.3), thick red line) with estimated 95%-prediction band (shaded red area) to WT data. All environments were fitted simultaneously with the same initial fraction of CD8 cells, of virus in culture and of infected cells. Infected cells in loose collagen were not fitted (indicated in gray, see main text for more information). Parameters already estimated or fixed previously were adopted here. Efficacy of cell-free transmission was assumed to decrease in collagen to 14% of its efficacy in suspension, i.e., $\beta_f^{\text{coll}} = 0.14 \times \beta_f^{\text{susp}}$.

A.5 Comparison of estimated proliferation rates for models with and without adaptation

A model neglecting the initial adaptation phase (Eq. (A.1)) estimated lower proliferation rates than one incorporating this phase (Eq. (3.1)). Table A.1 shows the ratio of proliferation rates between model with and without adaptation. As model (A.1) neglected cell death, a net proliferation rate for model (3.1) was also calculated (Table A.1, lower two rows) and compared to the estimated proliferation rate of the model including an adaptation phase (Eq. (3.1)). This ratio revealed that a model neglecting the adaptation phase estimated higher proliferation rates irrespective the environment and cell type than one with adaptation phase.

Tab. A.1. **Proliferation rates for models w/ and w/o adaptation.** Comparison of estimated proliferation rates for model (3.1) (with adaptation) and model (A.1) (without adaptation). Here, the ratio of the estimated proliferation rates between the former and latter model are given for CD8 and CD4 cells in different environments. As model (A.1) has no explicit cell death, I also calculated the ratio with an approximated net proliferation rate, i.e., $\lambda_{\text{adapt}}^{\text{net}} := \lambda_{\text{adapt}} - \mu_{\text{adapt}}$, for model (3.1) in all environments.

	Suspension	**Loose**	**Dense**
	$\lambda_{\text{adapt}}/\lambda_{\text{no\_adapt}}$		
CD8	2.31	1.87	1.71
CD4	1.94	3.90	4.21
	$\lambda_{\text{adapt}}^{\text{net}}/\lambda_{\text{no\_adapt}}$		
CD8	2.16	1.52	1.24
CD4	1.84	2.75	2.79

B Additional Material to Chapter 4: Contribution of cell-to-cell transmission to HCV spread *in vitro*

B.1 Intracellular HCV replication and export

To parameterize intracellular viral replication and export, my collaborators conducted an additional experiment (see Section 2.1.2). A mass-action kinetics model was fitted to the obtained data to estimate the parameters governing intracellular viral replication and export.

B.1.1 *In vitro* data of intracellular HCV replication and export

In this data set the intra- and extracellular RNA counts per cell were measured at frequent intervals (Fig. B.1). After an initial decline due to an excess of viral inoculum, the intracellular RNA counts per cell started to increase after 6 hours p.i. A steady state at approximately 10^5 cells was reached after 50 hours p.i. The extracellular RNA decreased for longer with the first clear signal of newly produced extracellular RNA between 36 and 48 hours.

B.1.2 Profile likelihoods of parameters governing intracellular replication

Profile likelihoods showed identifiability of all parameters governing intracellular viral replication of HCV in Huh7 cells within small bounds (Fig. B.2). The best fitting parameter set was used to parameterize viral dynamics in the agent-based model. The profiles of the initial intra- and extracellular RNA counts, intracellular replication rate, and the capacity of intracellular RNA per infected cell is shown in Fig. B.2. Furthermore, the profiles of the export rate and the loss of extracellular RNA rate are presented in this figure. The 95%-confidence intervals, i.e., $\Delta_{\mathrm{MLE}} = \chi^2(0.05, 1) \approx 3.84$ (see Section 2.2.2 for more information), are indicated by the dashed black line.

B.2 Comparison of different experiments

Several experiments were conducted by my collaborators to measure HCV infection kinetics in a monolayer of hepatocytes. Comparing the experiments showed that cumulative densities of untreated wells could be binned into two groups consisting of Exp. 29C and 29D on the one

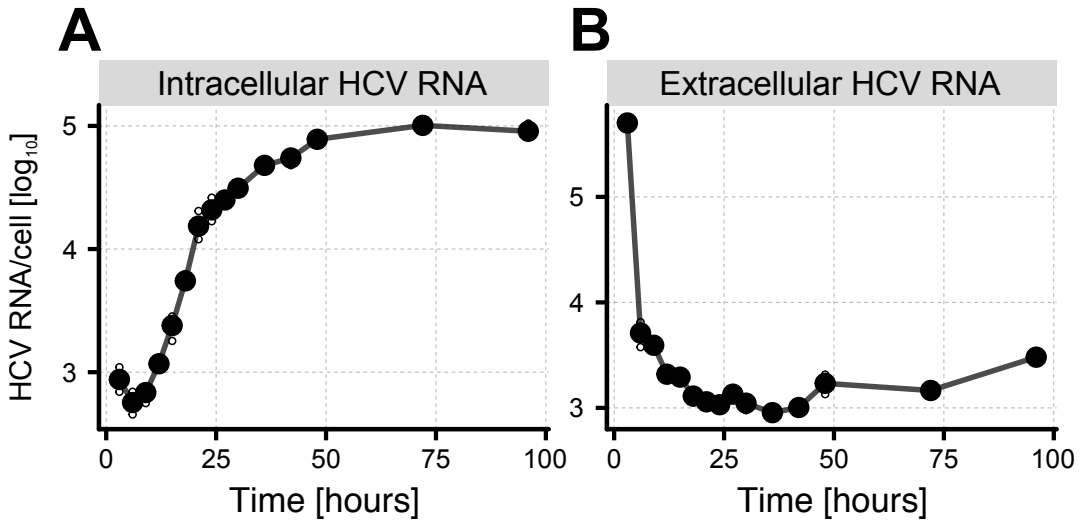

Fig. B.1. **Experimental data of intracellular viral replication and export.** Three hours p.i. viral inoculum is removed from cell cultures. Solid dots represent the mean of three (intracellular RNA) or two (extracellular RNA) individual measurements (open dots). Panel **(A)** shows the intracellular HCV RNA per cell. Residual virus from the inoculum is still detectable three and six hours p.i. **(B)** Extracellular HCV RNA declines until 18 hours p.i. due to residual inoculum remaining after media change reaching a constant level until increasing around 36 hours p.i. Experiment was performed by the Uprichard lab, Department of Microbiology and Immunology, Loyola University Medical Center, Maywood, Illinois, USA.

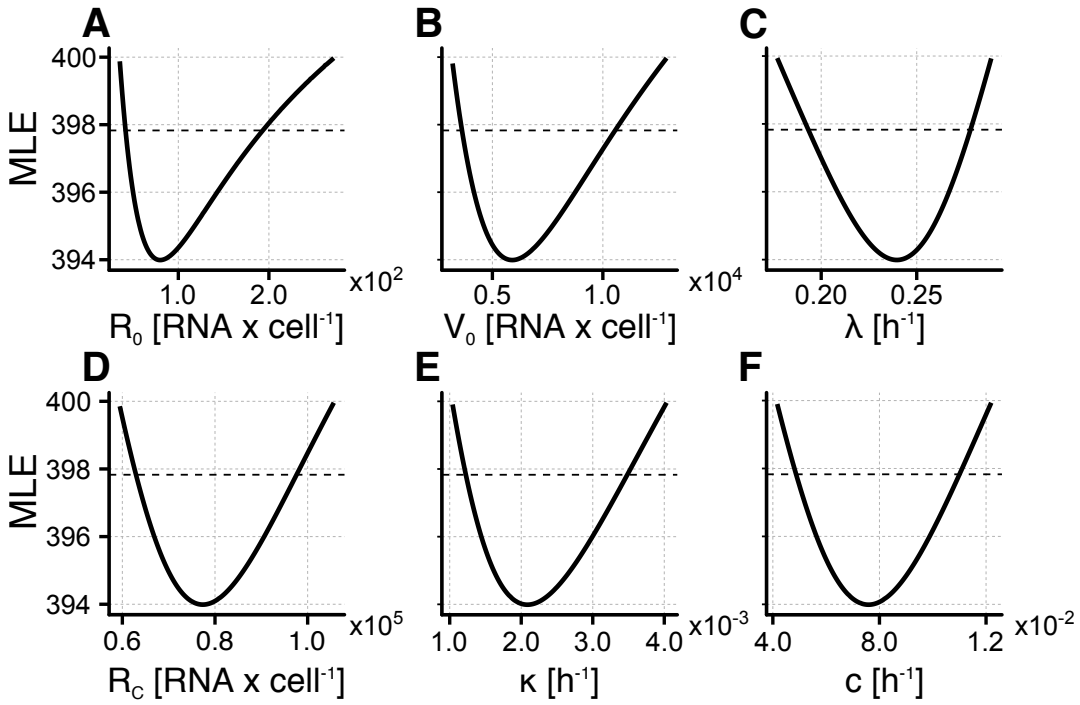

Fig. B.2. **Profile likelihoods for parameters governing intracellular viral replication of HCV in Huh7 cells.** Shown are the profile likelihoods for initial intracellular RNA count after infection **(A)**, initial residual viral inoculum after change of media **(B)**, intracellular replication rate **(C)** and the capacity of intracellular RNA per cell **(D)**. Panel **(E)** and **(F)** display the RNA export rate from infected cells and the loss of extracellular viral infectivity, respectively. 95%-CI are indicated by the dashed black line.

Tab. B.1. **Summary of different pyABC runs fitting *in vitro* HCV spread in stationary cells.** The median distance of each generation, i.e., 100 accepted particles, is denoted with ϵ. Number of simulations used to calculate average cumulative densities and mean number of infected cells is shown in column 3. If not mentioned in the comments all time points were used for fitting, the diffusion rate was fixed and on average 35 cells were infected during the initiation period.

Data	Generations	Simulations per fit	Total Evaluations	ϵ of last generation	Lowest distance	Comments
In silico data	15	1	35078	1.67	1.31	
Exp. 29D	15	1	95826	4.46	3.61	
Exp. 29J	12	1	32143	7.42	6.68	
Exp. 29J	14	1	64584	4.98	4.23	Neglected 96h p.i., diffusion fitted
Exp. 29J	13	5	21013	4.64	3.66	Neglected 96h p.i., diffusion fitted, 25 initially infected cells

side and Exp. 29I and 29J on the other (Fig. B.3A). To some extent this was also visible in the number of infected cells without anti-E2 treatment (Fig. B.3B). While similarities were also visible in the anti-E2-treated wells within groups, more deviation was observed between groups. This could be due to different efficacies or amounts of provided anti-E2.

B.3 Summary of different fitting approaches using pyABC

I used various approaches to fit my model to the different data sets, which describe HCV spread among hepatocytes in a monolayer. A summary is shown in Table B.1. As expected the *in silico* data provided the smallest distance between measurements and predictions. Because I used the same number of time points in Exp. 29D and the last pyABC run of Exp. 29J, they could be compared showing that both experiments were fit equally good with my model as indicated by the same smallest distance.

B.4 Validation of modeling and fitting approach with *in silico* data

I generated *in silico* data by running the ABM five times with and without administration of anti-E2 to evaluate the performance of pyABC with respect to recovery of true parameters and prediction of the correct contribution of cell-free infected cells. The parameters used in the ABM to generate the *in silico* data are summarized in Table B.2 and the data are shown in Fig. B.4. Here, the focus size distributions, the number of foci, infected cells and the average

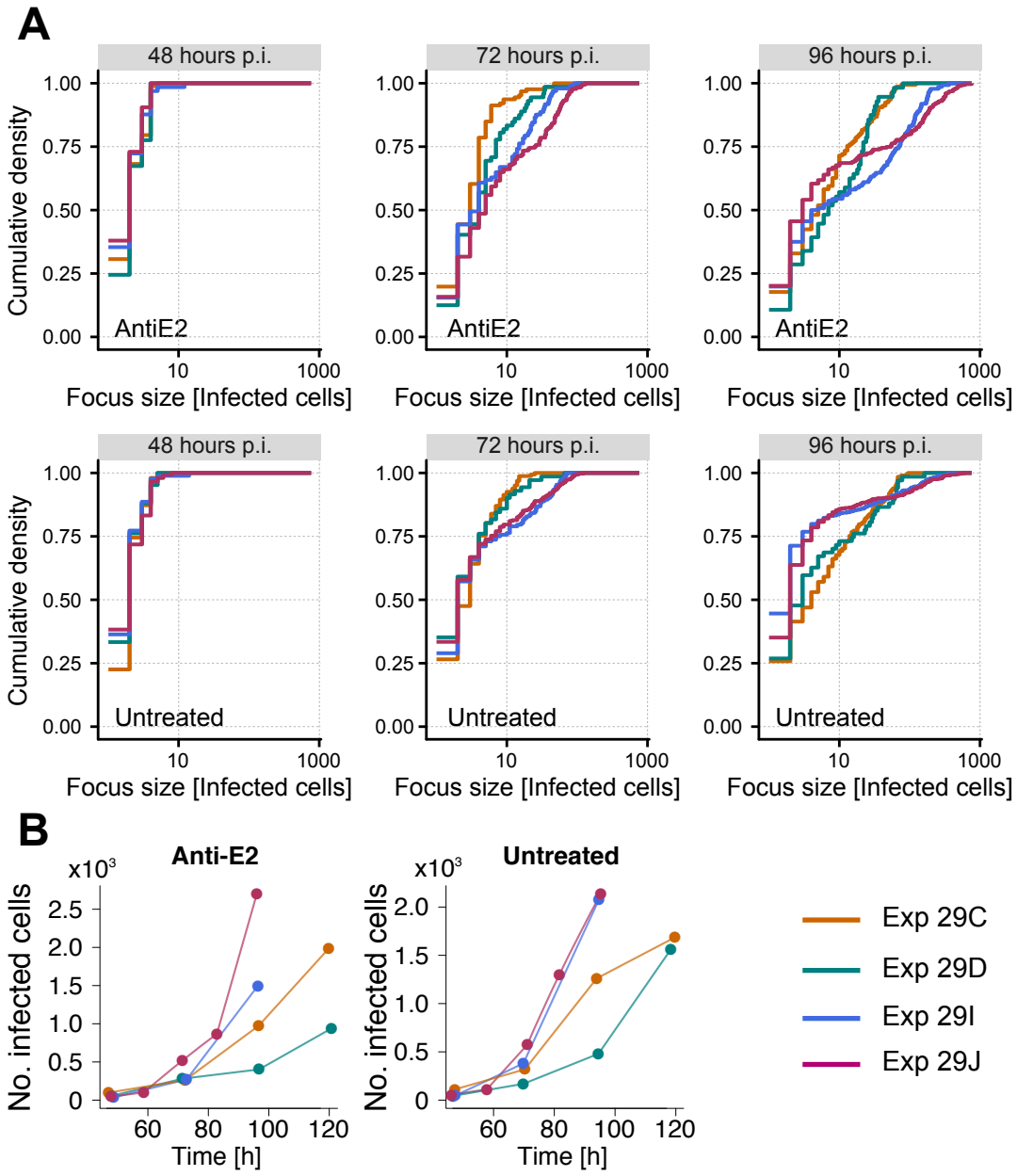

Fig. B.3. **Comparison of different *in vitro* experiments of HCV spread.** The different experiments are indicated in orange (Exp. 29C), blue-green (Exp. 29D), blue (Exp. 29I) and purple (Exp. 29J). **(A)** The average cumulative densities of focus size distributions at 48 (left), 72 (middle) and 96 (right) hours p.i. of anti-E2-treated (top) and untreated (bottom) wells. **(B)** Average numbers of infected cells in anti-E2-treated (left) and untreated (right) wells. Experiments were performed by the Uprichard lab, Department of Microbiology and Immunology, Loyola University Medical Center, Maywood, Illinois, USA.

focus sizes are presented. Additionally, the proportion of cells infected through cell-free transmission obtained from the *in silico* data at various times can be seen (Fig. B.4C).

An example fit to the *in silico* data retrieved from pyABC is shown in Fig. B.5, where panel A and B show the measured (black) and predicted (red) focus size distributions and the number of infected cells, respectively. I included Fig. B.6 to visualize the estimated kernel densities and individual particles of the last generation fitting the ABM to the *in silico* data with pyABC.

Tab. B.2. **Parameters used to generate *in silico* data fitted with pyABC.** In contrast to the model describing the experimental data, cells in re-orientation phase halt their intracellular replication and degradation.

Parameter	Description	Unit	Value
cells	Total cells per well	cells	24031
% empty sites	Percent empty sites at start of simulation	1	0.6
t_{sim}	Simulation time	h	120
t_{init}	Initialization period	h	17
t_{mc}	Time of media change	h	17 and 72
τ	Average re-orientation time after successful cell-to-cell transmission	h	23.0
t_{prolif}	Average doubling time of uninfected hepatocytes	h	32
α_{init}	Infection probability during initialization period	h^{-1}	1.27×10^{-3}
c_{init}	Average number of cells infected during initialization period	cells	35
R_0	Initial positive-strand RNA at infection	RNA	80.07
α	Maximal RNA production rate	h^{-1}	4.00×10^{-3}
ρ	RNA export rate	h^{-1}	3.48×10^{-5}
R_{cap}	Capacity of intracellular RNA per infected cell	RNA	7.74×10^{4}
s_f	Scaling factor for CF transmission probability	$(h \times \text{intra. RNA})^{-1}$	6.00×10^{-4}
s_c	Scaling factor for CC transmission probability	$(h \times \text{extra. RNA})^{-1}$	0.190
m	Coupling between lattice sites for viral diffusion	1	0.117
c	Loss of infectivity of extracellular virus	h^{-1}	1.27×10^{-3}
$E_{2,0}$	Initial anti-E2 concentration, when administered	$a.u.$	1×10^{4}
c_{E2}	Antibodies necessary to neutralize one extracellular RNA	anti-E2 $\times$ extra. RNA^{-1}	1

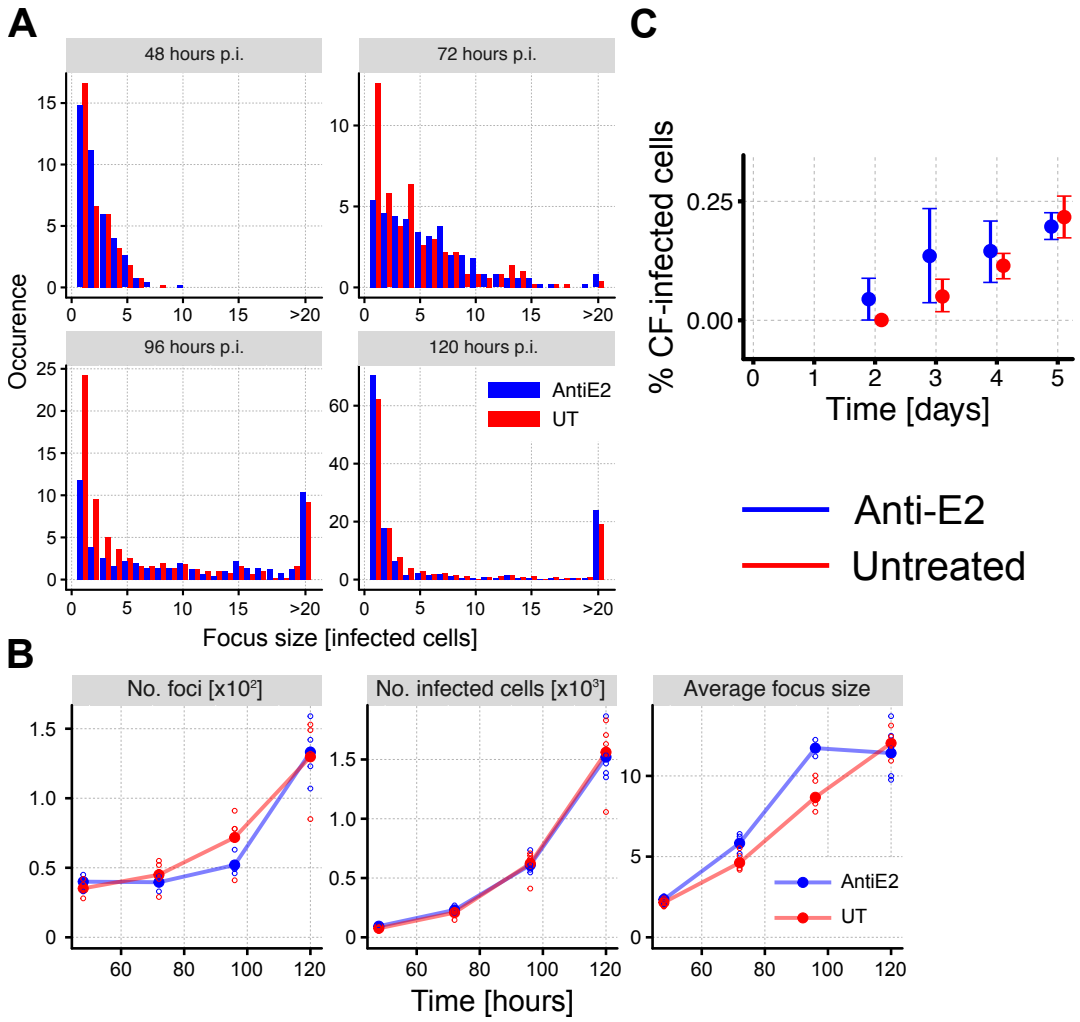

Fig. B.4. ***In silico* data used to evaluate performance of pyABC.** The *in silico* data was generated using the ABM described in Section 4.3 with parameters shown in Table B.2. *In silico* measurements were shifted by 18 hours to model a delay between detection of infected cells and time point of infection mimicking the experiments. **(A)** Mean focus size distributions calculated from 5 individual simulation runs with (blue) and without (red) administration of anti-E2. **(B)** Mean number (solid circles with colored lines) of foci (left), infected cells (center) and average focus sizes (right) at four time points calculated from 5 individual simulation runs (open circles) with (blue) and without (red) administration of anti-E2. (C) Average percentage of cell-free infected cells with 95%-confidence intervals calculated from five individual ABM simulations at 2, 3, 4 and 5 days post infection. The data are shifted slightly for illustration purposes.

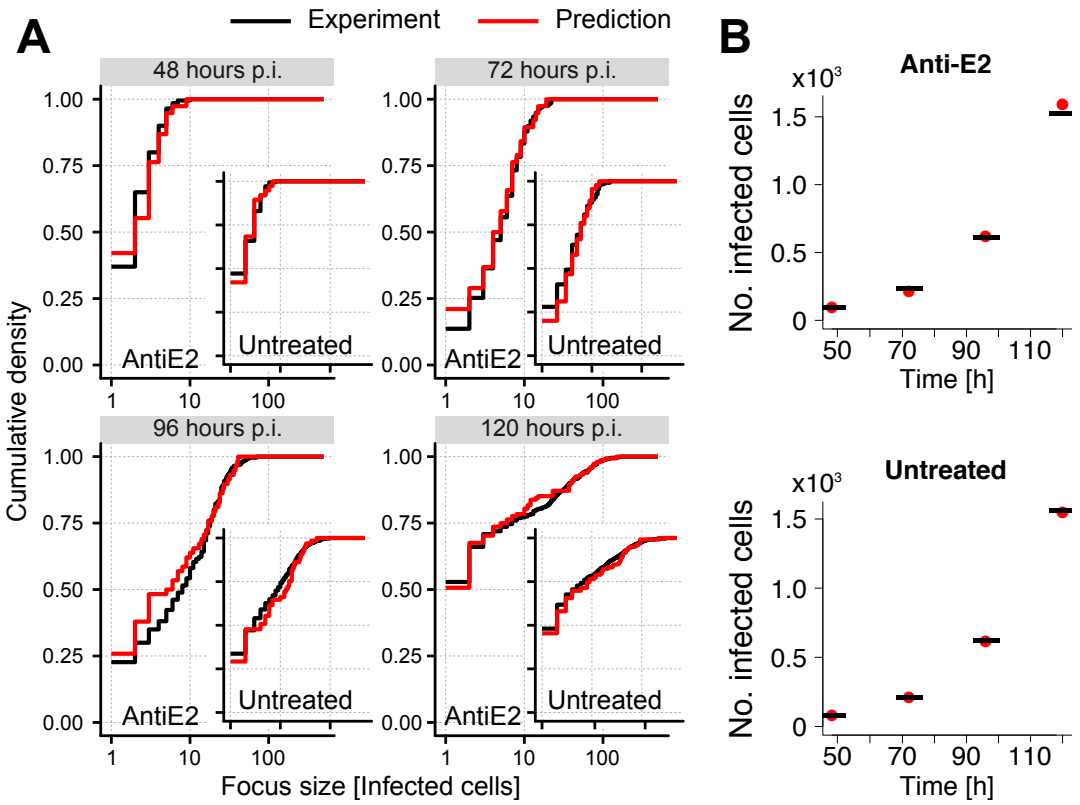

Fig. B.5. **Fit of ABM to *in silico* data simulating HCV spread.** **(A)** Measured (black) and predicted (red) cumulative densities of focus size distributions with (large panels) and without (inlays) administration of anti-E2 after 48 hrs (top left), 72 hrs (top right), 96 hrs (bottom left) and 120 hrs (bottom right). Average measured cumulative densities were calculated from 5-6 replicates. The predicted values stem from the best fitting particle after 15 pyABC generations (termed ID 1 in Fig. 4.7 and B.6). Axis breaks are the same for large figures and the respective inlays. **(B)** Number of infected cells obtained from the *in silico* experiment (black lines) and the prediction (red dots) with (top) and without (bottom) administration of anti-E2.

B.5 Different fitting approaches of Exp. 29J

In an attempt to fit my model to Exp. 29J, I first followed the same approach as in Exp. 29D. However, the surprisingly fast increase of infected cell counts between 83 and 96 hours p.i. in anti-E2-treated wells and a rather slow increase in the untreated wells could not be captured by my model (Fig. B.7). As the last time point had technical issues (personal communication Prof. Susan Uprichard), it was neglected in the following. Additionally, the model predicted too many small foci at any given time. To account for the fact that extracellular virus upon release might preferably infect adjoining cells, leading to a slower diffusion than theoretically calculated, I also fitted the extracellular diffusion rate of the virus. Unfortunately, this could not resolve the overestimation of small foci (Fig. B.8).

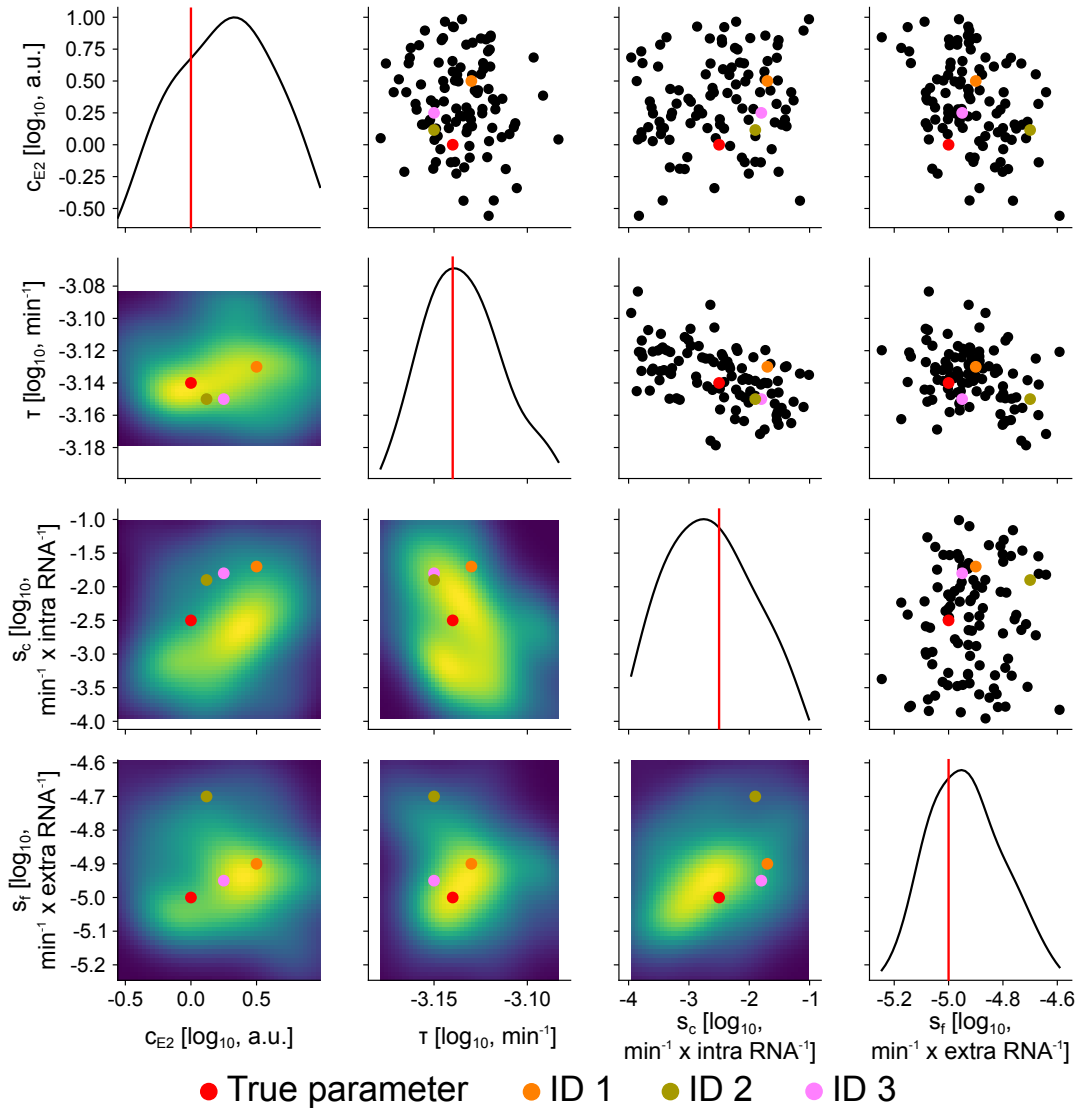

Fig. B.6. **Estimated kernel densities of fitted parameters to *in silico* data after 15 pyABC generations.** 1st row and column show the amount of anti-E2 necessary to neutralize one extracellular RNA in arbitrary units. 2nd row and column display the rate of re-orientation after a successful cell-to-cell transmission per minute. 3rd and 4th row and column show the cell-to-cell and cell-free scaling factor, respectively. Panels above the diagonal present 100 individual parameter combinations (black), which had a distance smaller than 1.67 and below the diagonal the corresponding estimated two-dimensional kernel densities. The kernel density estimates of each parameter are shown on the diagonal. The true parameters are indicated with red and three of the best fitting realizations with orange (ID 1), olive green (ID 2) and rose (ID 3) after 15 generations run with pyABC.

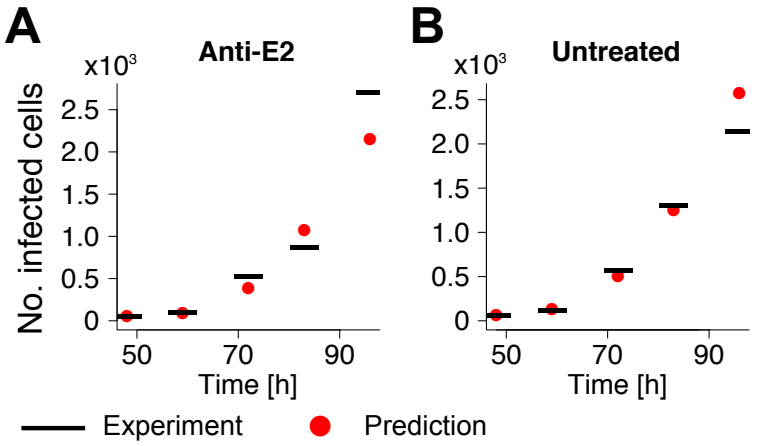

Fig. B.7. **Number of infected cells for Exp. 29J as predicted by pyABC run with individual simulations fitted to data from all measurements.** Predicted (red dots) and measured (black lines) number of infected cells in untreated **(A)** and anti-E2-treated **(B)** wells. Prediction is a result of the best fit obtained by running pyABC for 12 generations with individual simulations fitting the average cumulative densities (not shown) and mean number of infected cells, which were calculated from five to six individual replicates, as obtained from Exp. 29J.

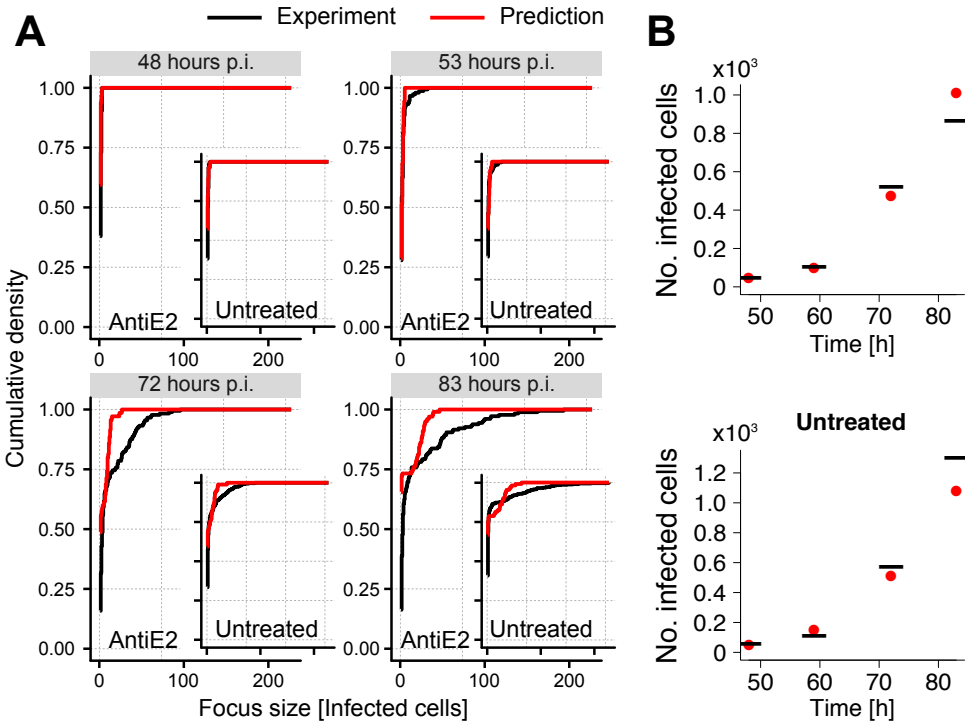

Fig. B.8. **Infection dynamics of Exp. 29J as predicted by pyABC for individual simulations without last time point.** **(A)** Measured (black) and predicted (red) focus size distributions for untreated (inlays) and anti-E2-treated (large panels) wells after 48 hrs (top left), 59 hrs (top right), 72 hrs (bottom left) and 83 hrs p.i. (bottom right). Average measured cumulative densities were calculated from 5-6 replicates. Axis breaks are the same for large panels and the respective inlays. **(B)** Predicted (red dots) and measured (black lines) number of infected cells in untreated (top) and anti-E2-treated (bottom) wells. Predictions stem from the best fit obtained by running pyABC for 14 generations with individual simulations fitting the average cumulative density and mean number of infected cells, which were calculated from five to six individual replicates, as measured in Exp. 29J without the measurement at 96 hours p.i.

C Additional Material to Chapter 5: Quantification of cell-to-cell spread among stationary cells

C.1 Parameters used in agent-based model simulations

Table C.1 shows the parameters used for generation of *in silico* data with the agent-based model described in Section 5.2.

Tab. C.1. Parameters used in generation of *in silico* data for Chapter 5. For simulations shown in Fig. 5.6D,F $s_c = 1 \times 10^{-5}$ (min × intra. RNA)$^{-1}$ and $s_f = 1 \times 10^{-4}$ (min × extra. virus)$^{-1}$.

Parameter	Description	Unit	Value
cells	Total cells per well	cells	24031
t_{sim}	Simulation time	h	240
t_{init}	Initialization period	h	17
α_{init}	Infection probability during initialization period	h^{-1}	6.5×10^{-3}
c_{init}	Average number of cells infected during initialization period	cells	35
R_0	Initial positive-strand RNA at infection	RNA	1
α	Maximal RNA production rate	h^{-1}	0.446
ρ	Export rate for enveloped virus	h^{-1}	2.01×10^{-3}
γ	Degradation rate of intracellular RNA	h^{-1}	0.2
R_{cap}	Capacity of intracellular RNA per infected cell	RNA	2369
s_f	Scaling factor for CF transmission probability	$(h \times \text{intra. RNA})^{-1}$	49.2
s_c	Scaling factor for CC transmission probability	$(h \times \text{extra. virus})^{-1}$	1680
f_{inf}	Fraction of infectious virus per intracellular RNA	1	1×10^{-3}
m	Diffusion parameter (slow)	$\mu m^2 \times h^{-1}$	37.5
m	Diffusion parameter (fast)	$\mu m^2 \times h^{-1}$	6.25×10^3
c	Loss of infectivity of extracellular virus	h^{-1}	6.34×10^{-2}

C.2 Mathematical derivation of a continuous adjustment term for cells contributing to cell-to-cell transmission

Assuming regular growth of infected cells within one focus, the adjustment term, $f_c(k, I)$, can be written as follows

$$f_c(k, I) = \frac{\sqrt{k^2 + 8kI - 8k} - k}{2I}. \tag{C.1}$$

It describes the proportion of cells contributing to cell-to-cell transmission as a continuous function of the assumed number of neighbors per cell, k, and the total number of infected cells in the focus, I.

The general function describing the fraction of cell-to-cell contributors (Eq. (5.4)) is only valid for large focus sizes. It is not suitable for foci smaller than the assumed number of neighbors, $I < k$, as for these focus sizes all cells are able to contribute to cell-to-cell transmission, i.e., $f_1 = 1$. In order to attain a smooth transition between those two parts, I introduced a transition term f_2 connecting f_1 and $f_c(k, I)$. Here, I used a third-order polynomial for f_2 defined by

$$f_2(x) = a(x - k)^3 + b(x - k)^2 + c(x - k) + d, \tag{C.2}$$

where k is the number of assumed neighbors. To obtain a smooth transition from f_1 to f_3, parameters a, b, c and d were chosen such that f_2 satisfied the following conditions:

1. $f_2(k) = f_1(0) = 1$
2. $\frac{df_2}{dI}(k) = \frac{df_1}{dI}(0) = 0$
3. $f_2(k + z) \overset{!}{=} f_3(k + z) =: J_1$
4. $\frac{df_2}{dI}(k + z) \overset{!}{=} \frac{df_3}{dI}(k + z) =: J_2$

Here conditions 1 and 2 ensure a continuous connection between the first, f_1, and second, f_2, part of the adjustment term at position k. Similarly, the last two conditions ensure a continuous connection for the second and third part at $k + z$ cells in the focus with $z \in \mathbb{R}^+$. Thus, parameter z defines the number of infected cells for which the transition term applies. Assuming $f_1 \equiv 1$, and solving Eq. (C.2) and Eq. (5.4), I obtained the following coefficients of the polynomial describing f_2:

$$\begin{aligned} a &= \frac{J_2 z + 2 - 2J_1}{z^3} \\ b &= \frac{3J_1 - J_2 z - 3}{z^2} \\ c &= 0 \\ d &= 1 \end{aligned}$$

Here, J_1 and J_2 define the value of f_2 and f_3 at position $k+z$, respectively. Thus, parameters a and b depend on the number of neighbors as well as the number of infected cells for which the transition term applies. According to Eq. (5.4), J_1 and J_2 can be written as

$$J_1 = \frac{\sqrt{9k^2+8kz-8k}-k}{2(k+z)}$$
$$J_2 = \frac{k\left(\sqrt{9k^2+8kz-8k}-5k-4z+8\right)}{2(k+z)^2\sqrt{9k^2+8kz-8k}}.$$

The combined adjustment term, $f_c(I)$, is a measure for the proportion of cell-to-cell contributors during the growth of an average focus dependent on the number of infected cells located in this focus. The derivation of $f_c(I)$ was based on the assumption that focus growth is circular and synchronous (compare Fig. 5.3A). To account for non-circular and asynchronous focus growth, the number of infected cells needed to be scaled, i.e., $f_c(I/\theta)$, where $\theta = 1$ stands for perfect circular and synchronous focus growth. Larger values correspond to deviations from this assumption. In case simultaneous growth of multiple foci is analyzed, the number of infected cells has to be divided by $\phi := \psi\theta$, as described in Section 5.4, where ψ defines the number of initiated foci. Parameter θ is estimated when fitting the model to data.

C.3 Profile likelihood analysis for parameter estimates considering single and multiple focus growth

Identifiability of parameters was studied performing a profile likelihood analysis (see Section 2.2.2). All parameters were identifiable for single and multiple focus growth (Fig. C.1 and Fig. C.2). The cell-to-cell transmission rate in the standard CC-model was significantly lower compared to the aCC- and aCC-d_I model (Fig. C.1A and Fig. C.2A). For multiple focus growth aCC- and aCC-d_I model performed equally good as the delay was estimated to be approximately 0 hours (Fig. C.2D). Additionally, almost identical profile likelihoods for all other parameters indicated similar performance of the models.

C.4 Model extensions

In Section 5.4 several models were tested. In addition to the models introduced in Eq. (5.1) and Eq. (5.6), an extended model incorporating cellular turnover as well as a time-delay, τ, which accounts for the time an infected cell needs to start viral replication and, thus, to become infectious [84, 147], was also applied. In this case, the model system in Eq. 5.6 changed to

$$\begin{aligned}
\frac{dT}{dt} &= \lambda_T\left(1-\frac{T+I}{T_c}\right) - \beta_f VT - f_c(I)\beta_c I(t-\tau_I)T - \delta_T T \\
\frac{dI}{dt} &= \beta_f VT + f_c(I)\beta_c I(t-\tau_I)T - \delta_I I \\
\frac{dV}{dt} &= \rho I(t-\tau_P) - cV \qquad .
\end{aligned} \tag{C.3}$$

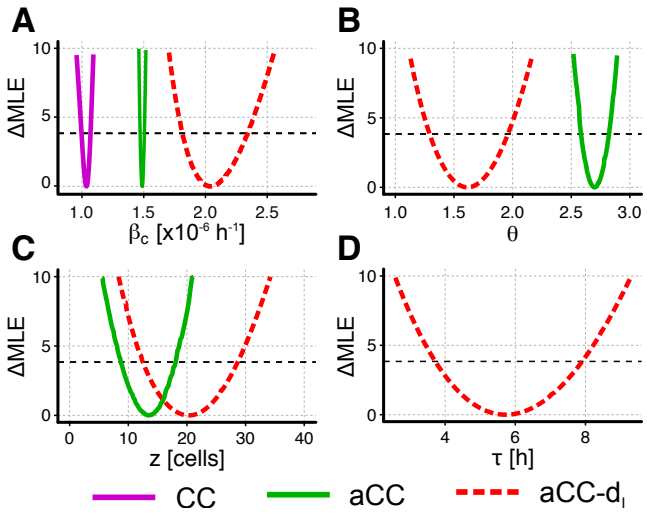

Fig. C.1. **Profile likelihoods for individual focus growth.** All profiles indicate the identifiability of parameters based on the *in silico* data. Standard CC-model, adjusted model with (aCC-d_I) and without (aCC) delay are shown in solid magenta, solid green as well as dashed red lines, respectively. **(A)** Profile likelihood of the cell-to-cell transmission rate β_c. **(B)** Profile likelihood for the parameter $\theta := \phi \cdot \psi$, where ψ defines a measure of non-circular focus shapes and ϕ the number of initially seeded foci (see previous section for more information). **(C)** Profile likelihood for the number of infected cells, z, for which the connection term, f_2, in the adjustment term is applicable. **(D)** Profile likelihood for the duration infected cells need to become infectious.

To evaluate experimental data on HIV infection dynamics as published in [70], proliferation of target cells with rate λ_T up to a capacity of T_c cells had to be taken into account. In this model τ_P and τ_I define the time delay for a cell to start viral production and to participate in cell-to-cell transmission, respectively. Eq. (5.1) can be adapted accordingly. Models additionally accounting for the viral eclipse phase are indicated by $-d_\mathrm{P}$ and $-d_\mathrm{I}$ dependent on the delay considered. An overview of the models used, is shown in Table C.2.

C.5 Parameter estimates obtained from fitting *in vitro* HIV spread data under static and shaking conditions

Table C.3 shows the parameter estimates gained from fitting to *in vitro* HIV spread data under static and shaking conditions. The estimates obtained in a previous study [70] are also shown. The confidence intervals were calculated using a profile likelihood approach (see Section 2.2.2).

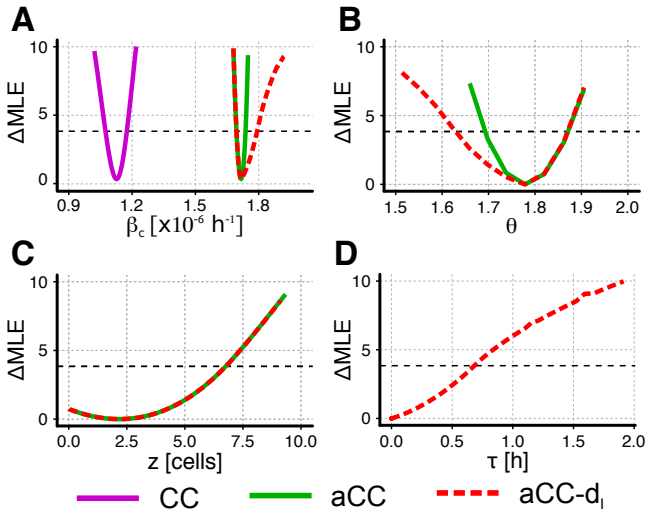

Fig. C.2. **Profile likelihoods for simultaneous growth of multiple foci.** All profiles indicate the identifiability of parameters based on the *in silico* data. Standard CC-model, adjusted model with (aCC-d_I) and without (aCC) delay are shown in solid magenta, solid green as well as dashed red lines, respectively. **(A)** Profile likelihood of the cell-to-cell transmission rate β_c. **(B)** Profile likelihood for the parameter $\theta := \phi \cdot \psi$, where ψ defines a measure of non-circular focus shapes and ϕ the number of initially seeded foci (see previous section for more information). **(C)** Profile likelihood for the number of infected cells, z, for which the connection term, f_2, in the adjustment term is applicable. **(D)** Profile likelihood for the duration infected cells need to become infectious.

Tab. C.2. **Overview of models applied in Chapter 5.** Description of all models considered in Section 5.4 either applied to *in silico* or experimental data.

Name	Description	Equation No.	Assumptions
Applied to ABM-simulated data			
CF	cell-free (CF) transmission model	(5.1)	$\beta_c = \delta_T = \delta_I = 0$
CC	cell-to-cell (CC) transmission model	(5.1)	$\beta_f = \delta_T = \delta_I = 0$
CCF	CF and CC model	(5.1)	$\delta_T = \delta_I = 0$
aCC	adjusted CC model	(5.6)	$\beta_f = \delta_T = \delta_I = 0$
aCC-d_I	adjusted CC model with delay on infected cells	(C.3)	$\lambda_T = \beta_f = \delta_T = \delta_I = \tau_P = 0$
aCCF	CF and adjusted CC model	(5.6)	$\delta_T = \delta_I = 0$
Applied to experimental data [70]			
CCF	CF and CC model	(C.3)	$\tau_I = \tau_P = 0$, $f_c(I) = 1$
CCF-d_P	CF and CC model with delay on viral production	(C.3)	$\tau_I = 0$, $f_c(I) = 1$
aCCF	CF and andjusted CC model	(C.3)	$\tau_I = \tau_P = 0$
aCCF-d_P	CF and adjusted CC model with delay on viral production	(C.3)	$\tau_I = 0$

Tab. C.3. **Parameter estimates for the spread of HIV-1 *in vitro*.** Best parameter estimates and 95%-CI in brackets obtained by re-analyzing experimental data in shaking and non-shaking *in vitro* cultures of HIV-1 as described by Iwami *et al.* [70] are shown here. Previous parameter estimates fitting to individual experiments (Iwami, [70]) and results obtained using pooled data with the same model assumptions (CCF) were comparable. Furthermore, the parameter estimates for models with an additional eclipse phase for viral production with (aCCF-d_P) or without (CCF-d_P) the introduced adjustment term for cell-to-cell transmission are shown. Differences in the corrected AIC values, ΔAICc, were calculated relative to the AICc of the best fitting model (ΔAICc $= 0$ for aCCF-d_p-model). Parameters λ_T, T_c and c described in Eq. C.3 were taken from [70]. Cell-to-cell transmission was assumed to be blocked in the shaking cultures, i.e., $\beta_c = 0$.

Parameter	Unit	Iwami (Mean $\pm$ SE)	CCF	CCF-d_p	aCCF-d_p
β_f	$\times 10^{-6}$ (p24 day)$^{-1}$	4.18 ± 1.41	3.31 [2.59, 4.22]	4.19 [3.39, 5.30]	5.58 [4.63, 6.49]
β_c	$\times 10^{-6}$ (p24 day)$^{-1}$	1.09 ± 0.33	0.92 [0.76, 1.09]	1.01 [0.84, 1.18]	1.59 [1.19, 2.13]
ρ	day^{-1}	0.50 ± 0.16	0.51 [0.38, 0.70]	0.66 [0.52, 0.88]	0.70 [0.57, 0.87]
δ_I	day^{-1}	0.50 ± 0.10	0.46 [0.38, 0.54]	0.63 [0.55, 0.72]	0.75 [0.65, 0.85]
T_0^{stat}	$\times 10^5$cells/ml	3.96 ± 1.83	4.31 [3.33, 5.76]	5.14 [3.89, 7.24]	4.66 [3.60, 6.33]
T_0^{shak}	$\times 10^5$cells/ml	5.85 ± 4.71	4.67 [3.35, 7.42]	4.80 [3.55, 7.38]	4.66 [3.42, 6.97]
I_0^{stat}	$\times 10^3$cells/ml	3.74 ± 2.21	4.0 [2.88, 5.81]	6.05 [2.33, 9.00]	3.27 [2.14, 5.96]
I_0^{shak}	$\times 10^3$cells/ml	0.02 ± 0.02	0.001 (0, 2.0]	0.02 (0, 2.05]	0.00050 (0, 2.93]
V_0^{stat}	p24/ml	304.01 ± 317.04	161.8 [83.8, 632.8]	167.4 [90.6, 737.7]	3530 [2380, 6170]
V_0^{shak}	p24/ml	17.88 ± 23.15	40.05 (0, 2853]	711.5 (0, 2485]	2000 (0, 3210]
τ	day^{-1}	-	-	0.90 [0.75, 1.82]	1.76 [1.51, 1.87]
θ		-	-	-	4.38 [1.86, 11]
z		-	-	-	5.2 [0, 260]
ΔAICc		-	31.7	4.4	0

Bibliography

[1] S. Flint, L. Enquist, V. Racaniello, and A. Skalka. *Principles of Virology*. 2nd edition. ASM Press, 2004, p. 140 (cit. on p. 3).

[2] W. Mothes, N. M. Sherer, J. Jin, and P. Zhong. "Virus cell-to-cell transmission". In: *J. Virol.* 84.17 (Sept. 2010), pp. 8360–8368 (cit. on p. 3).

[3] J. K. Taubenberger and D. M. Morens. "The pathology of influenza virus infections". In: *Annu Rev Pathol* 3 (2008), pp. 499–522 (cit. on p. 3).

[4] L. A. Waggoner-Fountain and L. B. Grossman. "Herpes simplex virus". In: *Pediatr Rev* 25.3 (Mar. 2004), pp. 86–93 (cit. on p. 3).

[5] R. A. Weiss. "How does HIV cause AIDS?" In: *Science* 260.5112 (May 1993), pp. 1273–1279 (cit. on p. 3).

[6] D. G. Bowen and C. M. Walker. "Adaptive immune responses in acute and chronic hepatitis C virus infection". In: *Nature* 436 (Aug. 2005), 946 EP – (cit. on pp. 3, 6).

[7] Q. Sattentau. "Avoiding the void: cell-to-cell spread of human viruses". In: *Nat. Rev. Microbiol.* 6.11 (Nov. 2008), pp. 815–826 (cit. on pp. 3–6, 53, 60, 78, 81, 106).

[8] M. Marsh and A. Helenius. "Virus entry: open sesame". In: *Cell* 124.4 (Feb. 2006), pp. 729–740 (cit. on p. 4).

[9] P. Zhong, L. M. Agosto, J. B. Munro, and W. Mothes. "Cell-to-cell transmission of viruses". In: *Curr Opin Virol* 3.1 (Feb. 2013), pp. 44–50 (cit. on pp. 4, 5, 101, 102).

[10] C. L. Brimacombe, J. Grove, L. W. Meredith, K. Hu, A. J. Syder, M. V. Flores, et al. "Neutralizing antibody-resistant hepatitis C virus cell-to-cell transmission". In: *J. Virol.* 85.1 (Jan. 2011), pp. 596–605 (cit. on pp. 4, 98).

[11] C. R. Bangham. "The immune control and cell-to-cell spread of human T-lymphotropic virus type 1". In: *J. Gen. Virol.* 84.Pt 12 (Dec. 2003), pp. 3177–3189 (cit. on p. 5).

[12] P. Kumberger, K. Durso-Cain, S. L. Uprichard, H. Dahari, and F. Graw. "Accounting for Space-Quantification of Cell-To-Cell Transmission Kinetics Using Virus Dynamics Models". In: *Viruses* 10.4 (2018) (cit. on pp. 5, 81, 83, 84, 86, 88, 91, 94).

[13] P. Gupta, R. Balachandran, M. Ho, A. Enrico, and C. Rinaldo. "Cell-to-cell transmission of human immunodeficiency virus type 1 in the presence of azidothymidine and neutralizing antibody". In: *J. Virol.* 63.5 (May 1989), pp. 2361–2365 (cit. on p. 5).

[14] A. Sigal, J. T. Kim, A. B. Balazs, E. Dekel, A. Mayo, R. Milo, et al. "Cell-to-cell spread of HIV permits ongoing replication despite antiretroviral therapy". In: *Nature* 477.7362 (Sept. 2011), pp. 95–98 (cit. on pp. 5, 98, 106).

[15] I. A. Abela, L. Berlinger, M. Schanz, L. Reynell, H. F. Gunthard, P. Rusert, et al. "Cell-cell transmission enables HIV-1 to evade inhibition by potent CD4bs directed antibodies". In: *PLoS Pathog.* 8.4 (2012), e1002634 (cit. on pp. 5, 106).

[16] J. M. Timpe, Z. Stamataki, A. Jennings, K. Hu, M. J. Farquhar, H. J. Harris, et al. “Hepatitis C virus cell-cell transmission in hepatoma cells in the presence of neutralizing antibodies”. In: *Hepatology* 47.1 (2008), pp. 17–24 (cit. on pp. 5, 6, 9, 67, 106).

[17] B. Schmid, M. Rinas, A. Ruggieri, E. G. Acosta, M. Bartenschlager, A. Reuter, et al. “Live Cell Analysis and Mathematical Modeling Identify Determinants of Attenuation of Dengue Virus 2’-O-Methylation Mutant”. In: *PLoS Pathog* 11.12 (Dec. 2016), pp. 1–36 (cit. on p. 5).

[18] P. Chen, W. Hubner, M. A. Spinelli, and B. K. Chen. “Predominant mode of human immunodeficiency virus transfer between T cells is mediated by sustained Env-dependent neutralization-resistant virological synapses”. In: *J. Virol.* 81.22 (Nov. 2007), pp. 12582–12595 (cit. on pp. 5, 7, 9, 52, 98, 101, 102).

[19] H. Sato, J. Orenstein, D. Dimitrov, and M. Martin. “Cell-to-cell spread of HIV-1 occurs within minutes and may not involve the participation of virus particles”. In: *Virology* 186.2 (Feb. 1992), pp. 712–724 (cit. on pp. 5, 7, 9, 52, 98, 101, 102).

[20] M. Sourisseau, N. Sol-Foulon, F. Porrot, F. Blanchet, and O. Schwartz. “Inefficient human immunodeficiency virus replication in mobile lymphocytes”. In: *J. Virol.* 81.2 (Jan. 2007), pp. 1000–1012 (cit. on pp. 5, 7, 9, 11, 52, 95, 101, 102).

[21] D. S. Dimitrov, R. L. Willey, H. Sato, L. J. Chang, R. Blumenthal, and M. A. Martin. “Quantitation of human immunodeficiency virus type 1 infection kinetics”. In: *J. Virol.* 67.4 (Apr. 1993), pp. 2182–2190 (cit. on pp. 5, 101, 102, 105).

[22] L. M. Agosto, P. D. Uchil, and W. Mothes. “HIV cell-to-cell transmission: effects on pathogenesis and antiretroviral therapy”. In: *Trends Microbiol.* 23.5 (May 2015), pp. 289–295 (cit. on pp. 5, 7, 36).

[23] A. Del Portillo, J. Tripodi, V. Najfeld, D. Wodarz, D. N. Levy, and B. K. Chen. “Multiploid inheritance of HIV-1 during cell-to-cell infection”. In: *J. Virol.* 85.14 (July 2011), pp. 7169–7176 (cit. on p. 5).

[24] L. Bracq, M. Xie, S. Benichou, and J. Bouchet. “Mechanisms for Cell-to-Cell Transmission of HIV-1”. In: *Frontiers in Immunology* 9 (2018), p. 260 (cit. on p. 5).

[25] Q. L. Choo, G. Kuo, A. J. Weiner, L. R. Overby, D. W. Bradley, and M. Houghton. “Isolation of a cDNA clone derived from a blood-borne non-A, non-B viral hepatitis genome”. In: *Science* 244.4902 (Apr. 1989), pp. 359–362 (cit. on p. 5).

[26] G. Kuo, Q. L. Choo, H. J. Alter, G. L. Gitnick, A. G. Redeker, R. H. Purcell, et al. “An assay for circulating antibodies to a major etiologic virus of human non-A, non-B hepatitis”. In: *Science* 244.4902 (Apr. 1989), pp. 362–364 (cit. on p. 5).

[27] J. Bukh, R. H. Miller, and R. H. Purcell. “Genetic heterogeneity of hepatitis C virus: quasispecies and genotypes”. In: *Semin. Liver Dis.* 15.1 (Feb. 1995), pp. 41–63 (cit. on p. 5).

[28] E. Gower, C. Estes, S. Blach, K. Razavi-Shearer, and H. Razavi. “Global epidemiology and genotype distribution of the hepatitis C virus infection”. In: *J. Hepatol.* 61.1 Suppl (Nov. 2014), pp. 45–57 (cit. on p. 5).

[29] G. Dusheiko. “Side effects of alpha interferon in chronic hepatitis C”. In: *Hepatology* 26.3 Suppl 1 (Sept. 1997), 112S–121S (cit. on p. 5).

[30] M. W. Fried, M. L. Shiffman, K. R. Reddy, C. Smith, G. Marinos, F. L. Goncales, et al. “Peginterferon alfa-2a plus ribavirin for chronic hepatitis C virus infection”. In: *N. Engl. J. Med.* 347.13 (Sept. 2002), pp. 975–982 (cit. on p. 5).

[31] T. Asselah, N. Boyer, D. Saadoun, M. Martinot-Peignoux, and P. Marcellin. “Direct-acting antivirals for the treatment of hepatitis C virus infection: optimizing current IFN-free treatment and future perspectives”. In: *Liver Int.* 36 Suppl 1 (Jan. 2016), pp. 47–57 (cit. on pp. 5, 11).

[32] J. Mellor, G. Haydon, C. Blair, W. Livingstone, and P. Simmonds. “Low level or absent in vivo replication of hepatitis C virus and hepatitis G virus/GB virus C in peripheral blood mononuclear cells”. In: *J. Gen. Virol.* 79 (Pt 4) (Apr. 1998), pp. 705–714 (cit. on p. 6).

[33] D. Moradpour, F. Penin, and C. M. Rice. “Replication of hepatitis C virus”. In: *Nat. Rev. Microbiol.* 5.6 (June 2007), pp. 453–463 (cit. on p. 6).

[34] B. D. Lindenbach and C. M. Rice. “The ins and outs of hepatitis C virus entry and assembly”. In: *Nat. Rev. Microbiol.* 11.10 (Oct. 2013), pp. 688–700 (cit. on p. 6).

[35] T. von Hahn, J. C. Yoon, H. Alter, C. M. Rice, B. Rehermann, P. Balfe, et al. “Hepatitis C Virus Continuously Escapes From Neutralizing Antibody and T-Cell Responses During Chronic Infection In Vivo”. In: *Gastroenterology* 132.2 (2007), pp. 667–678 (cit. on p. 6).

[36] R. Bartenschlager, F. Penin, V. Lohmann, and P. André. “Assembly of infectious hepatitis C virus particles”. In: *Trends in Microbiology* 19.2 (2011), pp. 95 –103 (cit. on p. 6).

[37] C. J. Neufeldt, M. A. Joyce, N. Van Buuren, A. Levin, K. Kirkegaard, M. Gale, et al. “The Hepatitis C Virus-Induced Membranous Web and Associated Nuclear Transport Machinery Limit Access of Pattern Recognition Receptors to Viral Replication Sites”. In: *PLoS Pathog.* 12.2 (Feb. 2016), e1005428 (cit. on p. 6).

[38] J. Mankouri, C. Walter, H. Stewart, M. Bentham, W. S. Park, W. D. Heo, et al. “Release of Infectious Hepatitis C Virus from Huh7 Cells Occurs via a trans-Golgi Network-to-Endosome Pathway Independent of Very-Low-Density Lipoprotein Secretion”. In: *J. Virol.* 90.16 (Aug. 2016), pp. 7159–7170 (cit. on p. 6).

[39] J. Witteveldt, M. J. Evans, J. Bitzegeio, G. Koutsoudakis, A. M. Owsianka, A. G. Angus, et al. “CD81 is dispensable for hepatitis C virus cell-to-cell transmission in hepatoma cells”. In: *J. Gen. Virol.* 90.Pt 1 (Jan. 2009), pp. 48–58 (cit. on p. 6).

[40] F. Xiao, I. Fofana, L. Heydmann, H. Barth, E. Soulier, F. Habersetzer, et al. “Hepatitis C Virus Cell-Cell Transmission and Resistance to Direct-Acting Antiviral Agents”. In: *PLoS Pathog* 10.5 (May 2014), pp. 1–15 (cit. on p. 6).

[41] V. Lohmann, F. Korner, J. Koch, U. Herian, L. Theilmann, and R. Bartenschlager. “Replication of subgenomic hepatitis C virus RNAs in a hepatoma cell line”. In: *Science* 285.5424 (July 1999), pp. 110–113 (cit. on pp. 6, 11).

[42] T. Kato, T. Date, M. Miyamoto, A. Furusaka, K. Tokushige, M. Mizokami, et al. “Efficient replication of the genotype 2a hepatitis C virus subgenomic replicon”. In: *Gastroenterology* 125.6 (Dec. 2003), pp. 1808–1817 (cit. on p. 6).

[43] B. D. Lindenbach, M. J. Evans, A. J. Syder, B. Wolk, T. L. Tellinghuisen, C. C. Liu, et al. “Complete replication of hepatitis C virus in cell culture”. In: *Science* 309.5734 (July 2005), pp. 623–626 (cit. on p. 6).

[44] F. Barre-Sinoussi, J. C. Chermann, F. Rey, M. T. Nugeyre, S. Chamaret, J. Gruest, et al. “Isolation of a T-lymphotropic retrovirus from a patient at risk for acquired immune deficiency syndrome (AIDS)”. In: *Science* 220.4599 (May 1983), pp. 868–871 (cit. on p. 6).

[45] K. Murphy, P Travers, and M Walport. *Janeway Immunologie*. 7th ed. Springer Spektrum, 2014 (cit. on p. 6).

[46] N. Samuel, H. Andrea, J. Assan, R.-J. Sarah, F. K. L., and M. D. C. “Comparing HIV-1 and HIV-2 infection: Lessons for viral immunopathogenesis”. In: *Reviews in Medical Virology* 23.4 (), pp. 221–240. eprint: `https://onlinelibrary.wiley.com/doi/pdf/10.1002/rmv.1739` (cit. on p. 6).

[47] UNAIDS. `http://www.unaids.org/en/resources/fact-sheet`. Homepage. June 2018 (cit. on p. 6).

[48] M. T. May, M. Gompels, V. Delpech, K. Porter, C. Orkin, S. Kegg, et al. “Impact on life expectancy of HIV-1 positive individuals of CD4+ cell count and viral load response to antiretroviral therapy”. In: *AIDS* 28.8 (May 2014), pp. 1193–1202 (cit. on p. 6).

[49] M. Pope and A. T. Haase. “Transmission, acute HIV-1 infection and the quest for strategies to prevent infection”. In: *Nat. Med.* 9.7 (July 2003), pp. 847–852 (cit. on p. 7).

[50] R. J. Shattock and J. P. Moore. “Inhibiting sexual transmission of HIV-1 infection”. In: *Nat. Rev. Microbiol.* 1.1 (Oct. 2003), pp. 25–34 (cit. on p. 7).

[51] L. Wu and V. N. KewalRamani. “Dendritic-cell interactions with HIV: infection and viral dissemination”. In: *Nat. Rev. Immunol.* 6.11 (Nov. 2006), pp. 859–868 (cit. on p. 7).

[52] C. J. Miller, Q. Li, K. Abel, E. Y. Kim, Z. M. Ma, S. Wietgrefe, et al. “Propagation and dissemination of infection after vaginal transmission of simian immunodeficiency virus”. In: *J. Virol.* 79.14 (July 2005), pp. 9217–9227 (cit. on p. 7).

[53] A. Biancotto, S. J. Iglehart, C. Vanpouille, C. E. Condack, A. Lisco, E. Ruecker, et al. “HIV-1 induced activation of CD4+ T cells creates new targets for HIV-1 infection in human lymphoid tissue ex vivo”. In: *Blood* 111.2 (Jan. 2008), pp. 699–704 (cit. on p. 7).

[54] Q. Li, J. D. Estes, P. M. Schlievert, L. Duan, A. J. Brosnahan, P. J. Southern, et al. “Glycerol monolaurate prevents mucosal SIV transmission”. In: *Nature* 458.7241 (Apr. 2009), pp. 1034–1038 (cit. on p. 7).

[55] G. Alkhatib. “The biology of CCR5 and CXCR4”. In: *Curr Opin HIV AIDS* 4.2 (Mar. 2009), pp. 96–103 (cit. on p. 7).

[56] S. G. Sarafianos, B. Marchand, K. Das, D. M. Himmel, M. A. Parniak, S. H. Hughes, et al. “Structure and Function of HIV-1 Reverse Transcriptase: Molecular Mechanisms of Polymerization and Inhibition”. In: *Journal of Molecular Biology* 385.3 (2009), pp. 693 –713 (cit. on p. 7).

[57] R. Craigie and F. D. Bushman. “HIV DNA integration”. In: *Cold Spring Harb Perspect Med* 2.7 (July 2012), a006890 (cit. on p. 7).

[58] B. R. Cullen. “Regulation of HIV-1 gene expression”. In: *FASEB J.* 5.10 (July 1991), pp. 2361–2368 (cit. on p. 7).

[59] W. I. Sundquist and H. G. Krausslich. “HIV-1 assembly, budding, and maturation”. In: *Cold Spring Harb Perspect Med* 2.7 (July 2012), a006924 (cit. on p. 7).

[60] G. B. Cohen, R. T. Gandhi, D. M. Davis, O. Mandelboim, B. K. Chen, J. L. Strominger, et al. “The Selective Downregulation of Class I Major Histocompatibility Complex Proteins by HIV-1 Protects HIV-Infected Cells from NK Cells”. In: *Immunity* 10.6 (1999), pp. 661 –671 (cit. on p. 7).

[61] R. F. Siliciano and W. C. Greene. “HIV latency”. In: *Cold Spring Harb Perspect Med* 1.1 (Sept. 2011), a007096 (cit. on p. 7).

[62] S. Saeidnia, A. Manayi, and M. Abdollahi. “From in vitro Experiments to in vivo and Clinical Studies; Pros and Cons”. In: *Curr Drug Discov Technol* 12.4 (2015), pp. 218–224 (cit. on p. 7).

[63] O. T. Fackler, T. T. Murooka, A. Imle, and T. R. Mempel. “Adding new dimensions: towards an integrative understanding of HIV-1 spread”. In: *Nat Rev Micro* 12.8 (Aug. 2014), pp. 563–574 (cit. on pp. 7, 8, 27, 102).

[64] J. C. Grivel and L. Margolis. “Use of human tissue explants to study human infectious agents”. In: *Nat Protoc* 4.2 (2009), pp. 256–269 (cit. on p. 8).

[65] J. A. Pedersen and M. A. Swartz. “Mechanobiology in the Third Dimension”. In: *Annals of Biomedical Engineering* 33.11 (Nov. 2005), pp. 1469–1490 (cit. on p. 8).

[66] P Friedl, P. B. Noble, and K. S. Zänker. “T lymphocyte locomotion in a three-dimensional collagen matrix. Expression and function of cell adhesion molecules.” In: *The Journal of Immunology* 154.10 (1995), pp. 4973–4985. eprint: `http://www.jimmunol.org/content/154/10/4973.full.pdf` (cit. on p. 8).

[67] N. Martin, S. Welsch, C. Jolly, J. A. Briggs, D. Vaux, and Q. J. Sattentau. “Virological synapse-mediated spread of human immunodeficiency virus type 1 between T cells is sensitive to entry inhibition”. In: *J. Virol.* 84.7 (Apr. 2010), pp. 3516–3527 (cit. on pp. 8, 9).

[68] P. Zhong, L. M. Agosto, A. Ilinskaya, B. Dorjbal, R. Truong, D. Derse, et al. “Cell-to-cell transmission can overcome multiple donor and target cell barriers imposed on cell-free HIV”. In: *PLoS ONE* 8.1 (2013), e53138 (cit. on p. 8).

[69] A. Imle, P. Kumberger, N. Schnellbächer, J. Fehr, P. Carillo-Bustamante, J. Alez, et al. “Environmental restrictions determine the mode of HIV-1 spread in tissue-like 3D cultures”. In: *submitted* (2018) (cit. on pp. 8, 19, 30, 34, 35, 37, 102).

[70] S. Iwami, J. S. Takeuchi, S. Nakaoka, F. Mammano, F. Clavel, H. Inaba, et al. “Cell-to-cell infection by HIV contributes over half of virus infection”. In: *Elife* 4 (2015) (cit. on pp. 9, 11, 15, 27, 45, 50, 52, 82, 84, 85, 87, 95–98, 101, 104–106, 112, 130–132).

[71] N. Barretto, B. Sainz, S. Hussain, and S. L. Uprichard. “Determining the involvement and therapeutic implications of host cellular factors in hepatitis C virus cell-to-cell spread”. In: *J. Virol.* 88.9 (May 2014), pp. 5050–5061 (cit. on p. 9).

[72] D. N. Martin and S. L. Uprichard. “Identification of transferrin receptor 1 as a hepatitis C virus entry factor”. In: *Proc. Natl. Acad. Sci. U.S.A.* 110.26 (June 2013), pp. 10777–10782 (cit. on p. 9).

[73] P. Kumberger, F. Frey, U. S. Schwarz, and F. Graw. “Multiscale modeling of virus replication and spread”. In: *FEBS Letters* 590.13 (2016), pp. 1972–1986 (cit. on p. 9).

[74] L. Canini and A. S. Perelson. “Viral kinetic modeling: state of the art”. In: *J Pharmacokinet Pharmacodyn* (June 2014) (cit. on p. 9).

[75] F. Graw and A. S. Perelson. “Modeling Viral Spread”. In: *Annu Rev Virol* 3.1 (Sept. 2016), pp. 555–572 (cit. on p. 9).

[76] C. Zitzmann and L. Kaderali. “Mathematical Analysis of Viral Replication Dynamics and Antiviral Treatment Strategies: From Basic Models to Age-Based Multi-Scale Modeling”. In: *Front Microbiol* 9 (2018), p. 1546 (cit. on p. 9).

[77] W. O. Kermack, A. G. McKendrick, W. O. Kermack, and A. G. McKendrick. “Contributions to the mathematical theory of epidemics–I. 1927”. In: *Bull. Math. Biol.* 53.1-2 (1991), pp. 33–55 (cit. on p. 9).

[78] W. O. Kermack, A. G. McKendrick, W. O. Kermack, and A. G. McKendrick. “Contributions to the mathematical theory of epidemics–II. The problem of endemicity.1932”. In: *Bull. Math. Biol.* 53.1-2 (1991), pp. 57–87 (cit. on p. 9).

[79] W. O. Kermack, A. G. McKendrick, W. O. Kermack, and A. G. McKendrick. “Contributions to the mathematical theory of epidemics–III. Further studies of the problem of endemicity. 1933”. In: *Bull. Math. Biol.* 53.1-2 (1991), pp. 89–118 (cit. on p. 9).

[80] A. S. Perelson, D. E. Kirschner, and R. D. Boer. “Dynamics of HIV infection of CD4+ T cells”. In: *Mathematical Biosciences* 114.1 (1993), pp. 81 –125 (cit. on p. 10).

[81] A. S. Perelson. “Modelling viral and immune system dynamics”. In: *Nat. Rev. Immunol.* 2.1 (Jan. 2002), pp. 28–36 (cit. on pp. 10, 11, 83).

[82] M. Binder, N. Sulaimanov, D. Clausznitzer, M. Schulze, C. M. Huber, S. M. Lenz, et al. “Replication vesicles are load- and choke-points in the hepatitis C virus lifecycle”. In: *PLoS Pathog.* 9.8 (2013), e1003561 (cit. on pp. 10, 11, 77).

[83] A. S. Perelson and P. W. Nelson. “Mathematical Analysis of HIV-1 Dynamics in Vivo”. In: *SIAM Review* 41.1 (1999), pp. 3–44. eprint: https://doi.org/10.1137/S0036144598335107 (cit. on p. 10).

[84] C. L. Althaus, A. S. De Vos, and R. J. De Boer. “Reassessing the human immunodeficiency virus type 1 life cycle through age-structured modeling: life span of infected cells, viral generation time, and basic reproductive number, R0”. In: *J. Virol.* 83.15 (Aug. 2009), pp. 7659–7667 (cit. on pp. 10, 12, 129).

[85] L. Rong, J. Guedj, H. Dahari, D. J. Coffield, M. Levi, P. Smith, et al. “Analysis of hepatitis C virus decline during treatment with the protease inhibitor danoprevir using a multiscale model”. In: *PLoS Comput. Biol.* 9.3 (2013), e1002959 (cit. on pp. 10, 11).

[86] N. M. Dixit and A. S. Perelson. “HIV dynamics with multiple infections of target cells”. In: *Proc. Natl. Acad. Sci. U.S.A.* 102.23 (June 2005), pp. 8198–8203 (cit. on p. 10).

[87] C. L. Althaus and R. J. De Boer. “Impaired immune evasion in HIV through intracellular delays and multiple infection of cells”. In: *Proc. Biol. Sci.* 279.1740 (Aug. 2012), pp. 3003–3010 (cit. on pp. 10, 11).

[88] H. Wu, Y. Huang, C. Dykes, D. Liu, J. Ma, A. S. Perelson, et al. “Modeling and estimation of replication fitness of human immunodeficiency virus type 1 in vitro experiments by using a growth competition assay”. In: *J. Virol.* 80.5 (Mar. 2006), pp. 2380–2389 (cit. on p. 10).

[89] V. V. Ganusov, N. Goonetilleke, M. K. Liu, G. Ferrari, G. M. Shaw, A. J. McMichael, et al. “Fitness costs and diversity of the cytotoxic T lymphocyte (CTL) response determine the rate of CTL escape during acute and chronic phases of HIV infection”. In: *J. Virol.* 85.20 (Oct. 2011), pp. 10518–10528 (cit. on p. 10).

[90] A. S. Perelson, A. U. Neumann, M. Markowitz, J. M. Leonard, and D. D. Ho. “HIV-1 dynamics in vivo: virion clearance rate, infected cell life-span, and viral generation time”. In: *Science* 271.5255 (Mar. 1996), pp. 1582–1586 (cit. on pp. 10, 11, 85, 101).

[91] X. Wei, S. K. Ghosh, M. E. Taylor, V. A. Johnson, E. A. Emini, P. Deutsch, et al. “Viral dynamics in human immunodeficiency virus type 1 infection”. In: *Nature* 373.6510 (Jan. 1995), pp. 117–122 (cit. on pp. 10, 11).

[92] A. U. Neumann, N. P. Lam, H. Dahari, D. R. Gretch, T. E. Wiley, T. J. Layden, et al. “Hepatitis C viral dynamics in vivo and the antiviral efficacy of interferon-alpha therapy”. In: *Science* 282.5386 (Oct. 1998), pp. 103–107 (cit. on pp. 11, 101).

[93] J. Guedj and A. U. Neumann. “Understanding hepatitis C viral dynamics with direct-acting antiviral agents due to the interplay between intracellular replication and cellular infection dynamics”. In: *J. Theor. Biol.* 267.3 (Dec. 2010), pp. 330–340 (cit. on p. 11).

[94] J. Guedj, H. Dahari, L. Rong, N. D. Sansone, R. E. Nettles, S. J. Cotler, et al. “Modeling shows that the NS5A inhibitor daclatasvir has two modes of action and yields a shorter estimate of the hepatitis C virus half-life”. In: *Proc. Natl. Acad. Sci. U.S.A.* 110.10 (Mar. 2013), pp. 3991–3996 (cit. on pp. 11, 78).

[95] B. J. Hammond. “Quantitative study of the control of HIV-1 gene expression”. In: *J. Theor. Biol.* 163.2 (July 1993), pp. 199–221 (cit. on p. 11).

[96] B. Reddy and J. Yin. “Quantitative intracellular kinetics of HIV type 1”. In: *AIDS Res. Hum. Retroviruses* 15.3 (Feb. 1999), pp. 273–283 (cit. on p. 11).

[97] H. Dahari, R. M. Ribeiro, C. M. Rice, and A. S. Perelson. “Mathematical modeling of subgenomic hepatitis C virus replication in Huh-7 cells”. In: *J. Virol.* 81.2 (Jan. 2007), pp. 750–760 (cit. on p. 11).

[98] C. Zhang, S. Zhou, E. Groppelli, P. Pellegrino, I. Williams, P. Borrow, et al. “Hybrid spreading mechanisms and T cell activation shape the dynamics of HIV-1 infection”. In: *PLoS Comput. Biol.* 11.4 (Apr. 2015), e1004179 (cit. on pp. 11, 84).

[99] N. L. Komarova, D. Anghelina, I. Voznesensky, B. Trinité, D. N. Levy, and D. Wodarz. “Relative contribution of free-virus and synaptic transmission to the spread of HIV-1 through target cell populations”. In: *Biology Letters* 9.1 (2012). eprint: http://rsbl.royalsocietypublishing.org/content/9/1/20121049.full.pdf (cit. on pp. 11, 101, 105).

[100] A. J. Kandathil, F. Graw, J. Quinn, H. S. Hwang, M. Torbenson, A. S. Perelson, et al. “Use of laser capture microdissection to map hepatitis C virus-positive hepatocytes in human liver”. In: *Gastroenterology* 145.6 (Dec. 2013), pp. 1404–1413 (cit. on p. 12).

[101] F. Graw, A. Balagopal, A. J. Kandathil, S. C. Ray, D. L. Thomas, R. M. Ribeiro, et al. “Inferring viral dynamics in chronically HCV infected patients from the spatial distribution of infected hepatocytes”. In: *PLoS Comput. Biol.* 10.11 (Nov. 2014), e1003934 (cit. on pp. 12, 56, 58, 103).

[102] M. R. Dowling, D. Milutinovi?, and P. D. Hodgkin. “Modelling cell lifespan and proliferation: is likelihood to die or to divide independent of age?” In: *J R Soc Interface* 2.5 (Dec. 2005), pp. 517–526 (cit. on p. 12).

[103] E. L. Haseltine, J. B. Rawlings, and J. Yin. “Dynamics of viral infections: incorporating both the intracellular and extracellular levels”. In: *Computers & Chemical Engineering* 29.3 (2005). Computational Challenges in Biology, pp. 675 –686 (cit. on p. 12).

[104] M. C. Strain, D. D. Richman, J. K. Wong, and H. Levine. “Spatiotemporal dynamics of HIV propagation”. In: *J. Theor. Biol.* 218.1 (Sept. 2002), pp. 85–96 (cit. on pp. 12, 104).

[105] F. Graner and J. A. Glazier. “Simulation of biological cell sorting using a two-dimensional extended Potts model”. In: *Phys. Rev. Lett.* 69.13 (Sept. 1992), pp. 2013–2016 (cit. on pp. 12, 104).

[106] J. B. Beltman, A. F. Maree, J. N. Lynch, M. J. Miller, and R. J. de Boer. “Lymph node topology dictates T cell migration behavior”. In: *J. Exp. Med.* 204.4 (Apr. 2007), pp. 771–780 (cit. on pp. 12, 98, 104).

[107] S. Wolfram. “Cellular automata as models of complexity”. In: *Nature* 311 (Oct. 1984), 419 EP – (cit. on p. 12).

[108] M. Gardner. “Mathematical Games: The Fantastic Combinations of John Conway’s New Solitaire Game «life»”. In: *Scientific American* 223 (1970), pp. 120–123 (cit. on p. 12).

[109] A. L. Bauer, C. A. Beauchemin, and A. S. Perelson. “Agent-based modeling of host-pathogen systems: The successes and challenges”. In: *Inf Sci (Ny)* 179.10 (Apr. 2009), pp. 1379–1389 (cit. on pp. 12, 98, 104).

[110] C. Beauchemin, J. Samuel, and J. Tuszynski. “A simple cellular automaton model for influenza A viral infections”. In: *J. Theor. Biol.* 232.2 (Jan. 2005), pp. 223–234 (cit. on p. 12).

[111] J. M. Murray and A. Goyal. “In silico single cell dynamics of hepatitis B virus infection and clearance”. In: *J. Theor. Biol.* 366 (Feb. 2015), pp. 91–102 (cit. on pp. 12, 101).

[112] T. Toni, D. Welch, N. Strelkowa, A. Ipsen, and M. P. Stumpf. “Approximate Bayesian computation scheme for parameter inference and model selection in dynamical systems”. In: *Journal of The Royal Society Interface* 6.31 (2009), pp. 187–202. eprint: http://rsif.royalsocietypublishing.org/content/6/31/187.full.pdf (cit. on pp. 13, 24).

[113] E. Klinger, D. Rickert, and J. Hasenauer. “pyABC: distributed, likelihood-free inference”. In: *BioRxiv* (2017) (cit. on pp. 13, 24, 78).

[114] M. Pizzato, O. Erlwein, D. Bonsall, S. Kaye, D. Muir, and M. O. McClure. “A one-step SYBR Green I-based product-enhanced reverse transcriptase assay for the quantitation of retroviruses in cell culture supernatants”. In: *Journal of Virological Methods* 156.1 (2009), pp. 1 –7 (cit. on p. 20).

[115] J. Vermeire, E. Naessens, H. Vanderstraeten, A. Landi, V. Iannucci, A. Van Nuffel, et al. “Quantification of reverse transcriptase activity by real-time PCR as a fast and accurate method for titration of HIV, lenti- and retroviral vectors”. In: *PLoS ONE* 7.12 (2012), e50859 (cit. on p. 20).

[116] N. Barretto and S. L. Uprichard. “Hepatitis C virus Cell-to-cell Spread Assay”. In: *Bio Protoc* 4.24 (Dec. 2014) (cit. on pp. 21, 90).

[117] F. Graw, D. N. Martin, A. S. Perelson, S. L. Uprichard, and H. Dahari. “Quantification of Hepatitis C Virus Cell-to-Cell Spread Using a Stochastic Modeling Approach”. In: *J. Virol.* 89.13 (July 2015), pp. 6551–6561 (cit. on pp. 21, 61, 78, 90, 98).

[118] A. Patel. `https://www.redblobgames.com/grids/hexagons/`. Homepage. Feb. 2018 (cit. on p. 22).

[119] G. Smith. *Numerical Solution of Partial Differential Equations: Finite Difference Methods*. 7th ed. Vol. 3rd Edition. Clarendon Press, Oxford, 2003 (cit. on p. 23).

[120] B. Hamilton and S. Bilbao. “Hexagonal vs. rectilinear grids for explicit finite difference schemes for the two-dimensional wave equation”. In: *Acoustical Society of America Journal* 133 (2013), p. 3532 (cit. on p. 23).

[121] R Core Team. *R: A Language and Environment for Statistical Computing*. R Foundation for Statistical Computing. Vienna, Austria, 2016 (cit. on p. 23).

[122] T. Anderson. *An Introduction to Multivariate Statistical Analysis*. 7th ed. Vol. 3rd Edition. Wiley, 2003 (cit. on p. 23).

[123] A. Raue, C. Kreutz, T. Maiwald, J. Bachmann, M. Schilling, U. Klingmuller, et al. “Structural and practical identifiability analysis of partially observed dynamical models by exploiting the profile likelihood”. In: *Bioinformatics* 25.15 (Aug. 2009), pp. 1923–1929 (cit. on p. 24).

[124] W. Meeker and L. Escobar. “Teaching about Approximate Confidence Regions Based on Maximum Likelihood Estimation”. In: 49 (Feb. 1995), p. 48 (cit. on p. 24).

[125] K. P. Burnham and D. R. Anderson. *Model Selection and Multimodel Inference: A Practical Information-Theoretic Approach*. Springer Science & Business Media, 2003 (cit. on p. 24).

[126] G. Doitsh, M. Cavrois, K. G. Lassen, O. Zepeda, Z. Yang, M. L. Santiago, et al. “Abortive HIV Infection Mediates CD4 T Cell Depletion and Inflammation in Human Lymphoid Tissue”. In: *Cell* 143.5 (2010), pp. 789–801 (cit. on p. 36).

[127] G. Doitsh, N. L. Galloway, X. Geng, Z. Yang, K. M. Monroe, O. Zepeda, et al. “Cell death by pyroptosis drives CD4 T-cell depletion in HIV-1 infection”. In: *Nature* 505.7484 (Jan. 2014), pp. 509–514 (cit. on pp. 36, 51).

[128] S. Iwami, B. P. Holder, C. A. Beauchemin, S. Morita, T. Tada, K. Sato, et al. “Quantification system for the viral dynamics of a highly pathogenic simian/human immunodeficiency virus based on an in vitro experiment and a mathematical model”. In: *Retrovirology* 9 (2012), p. 18 (cit. on pp. 37, 40).

[129] F. R. Santoni de Sio and D. Trono. “APOBEC3G-Depleted Resting CD4+ T Cells Remain Refractory to HIV1 Infection”. In: *PLOS ONE* 4.8 (Aug. 2009), pp. 1–5 (cit. on p. 37).

[130] A. Yates, C. Chan, J. Strid, S. Moon, R. Callard, A. J. George, et al. “Reconstruction of cell population dynamics using CFSE”. In: *BMC Bioinformatics* 8 (June 2007), p. 196 (cit. on pp. 47, 48).

[131] R. J. De Boer and A. S. Perelson. “Quantifying T lymphocyte turnover”. In: *Journal of Theoretical Biology* 327.Supplement C (2013), pp. 45–87 (cit. on pp. 47, 48).

[132] Y. Kakizoe, S. Nakaoka, C. A. Beauchemin, S. Morita, H. Mori, T. Igarashi, et al. “A method to determine the duration of the eclipse phase for in vitro infection with a highly pathogenic SHIV strain”. In: *Sci Rep* 5 (May 2015), p. 10371 (cit. on p. 50).

[133] C. Noecker, K. Schaefer, K. Zaccheo, Y. Yang, J. Day, and V. V. Ganusov. “Simple mathematical models do not accurately predict early SIV dynamics”. In: *Viruses* 7.3 (Mar. 2015), pp. 1189–1217 (cit. on p. 50).

[134] G. A. Funk, V. A. Jansen, S. Bonhoeffer, and T. Killingback. “Spatial models of virus-immune dynamics”. In: *J. Theor. Biol.* 233.2 (Mar. 2005), pp. 221–236 (cit. on pp. 59, 104).

[135] R. Glaser. *Biophysics: An Introduction*. 2012 (cit. on p. 59).

[136] E. Fröhlich, G. Bonstingl, A. Hofler, C. Meindl, G. Leitinger, T. R. Pieber, et al. “Comparison of two in vitro systems to assess cellular effects of nanoparticles-containing aerosols”. In: *Toxicol In Vitro* 27.1 (Feb. 2013), pp. 409–417 (cit. on p. 59).

[137] M. T. Catanese, K. Uryu, M. Kopp, T. J. Edwards, L. Andrus, W. J. Rice, et al. “Ultrastructural analysis of hepatitis C virus particles”. In: *Proc. Natl. Acad. Sci. U.S.A.* 110.23 (June 2013), pp. 9505–9510 (cit. on p. 59).

[138] S. J. Keum, S. M. Park, J. H. Park, J. H. Jung, E. J. Shin, and S. K. Jang. “The specific infectivity of hepatitis C virus changes through its life cycle”. In: *Virology* 433.2 (2012), pp. 462 –470 (cit. on p. 77).

[139] F. Real, A. Sennepin, Y. Ganor, A. Schmitt, and M. Bomsel. “Live Imaging of HIV-1 Transfer across T Cell Virological Synapse to Epithelial Cells that Promotes Stromal Macrophage Infection”. In: *Cell Rep* 23.6 (May 2018), pp. 1794–1805 (cit. on p. 78).

[140] S. Sowinski, C. Jolly, O. Berninghausen, M. A. Purbhoo, A. Chauveau, K. Kohler, et al. “Membrane nanotubes physically connect T cells over long distances presenting a novel route for HIV-1 transmission”. In: *Nat. Cell Biol.* 10.2 (Feb. 2008), pp. 211–219 (cit. on p. 78).

[141] P. Targett-Adams, S. Boulant, M. W. Douglas, and J. McLauchlan. “Lipid metabolism and HCV infection”. In: *Viruses* 2.5 (May 2010), pp. 1195–1217 (cit. on pp. 79, 80, 103).

[142] G. H. Syed, Y. Amako, and A. Siddiqui. “Hepatitis C virus hijacks host lipid metabolism”. In: *Trends Endocrinol. Metab.* 21.1 (Jan. 2010), pp. 33–40 (cit. on pp. 79, 103).

[143] M. E. Burlone and A. Budkowska. “Hepatitis C virus cell entry: role of lipoproteins and cellular receptors”. In: *J. Gen. Virol.* 90.Pt 5 (May 2009), pp. 1055–1070 (cit. on p. 79).

[144] A. Sabahi, K. A. Marsh, H. Dahari, P. Corcoran, J. M. Lamora, X. Yu, et al. “The rate of hepatitis C virus infection initiation in vitro is directly related to particle density”. In: *Virology* 407.1 (Nov. 2010), pp. 110–119 (cit. on pp. 79, 90, 103).

[145] A. J. Pelletier, L. J. van der Laan, P. Hildbrand, M. A. Siani, D. A. Thompson, P. E. Dawson, et al. “Presentation of chemokine SDF-1 alpha by fibronectin mediates directed migration of T cells”. In: *Blood* 96.8 (Oct. 2000), pp. 2682–2690 (cit. on p. 82).

[146] R. V. Culshaw, S. Ruan, and G. Webb. “A mathematical model of cell-to-cell spread of HIV-1 that includes a time delay”. In: *J Math Biol* 46.5 (May 2003), pp. 425–444 (cit. on pp. 84, 85).

[147] N. Dixit, M. Markowitz, D. D Ho, and A. Perelson. “Estimates of intracellular delay and average drug efficacy from viral load data of HIV-infected individuals under antiretroviral therapy”. In: 9 (May 2004), pp. 237–46 (cit. on pp. 96, 129).

[148] R. M. Ribeiro, L. Qin, L. L. Chavez, D. Li, S. G. Self, and A. S. Perelson. “Estimation of the initial viral growth rate and basic reproductive number during acute HIV-1 infection”. In: *J. Virol.* 84.12 (June 2010), pp. 6096–6102 (cit. on p. 96).

[149] N. Jagiella, D. Rickert, F. J. Theis, and J. Hasenauer. “Parallelization and High-Performance Computing Enables Automated Statistical Inference of Multi-scale Models”. In: *Cell Syst* 4.2 (Feb. 2017), pp. 194–206 (cit. on p. 98).

[150] A. Yakimovich, H. Gumpert, C. J. Burckhardt, V. A. Lutschg, A. Jurgeit, I. F. Sbalzarini, et al. “Cell-free transmission of human adenovirus by passive mass transfer in cell culture simulated in a computer model”. In: *J. Virol.* 86.18 (Sept. 2012), pp. 10123–10137 (cit. on pp. 101, 104).

[151] E. Shteyer, Y. Liao, L. J. Muglia, P. W. Hruz, and D. A. Rudnick. “Disruption of hepatic adipogenesis is associated with impaired liver regeneration in mice”. In: *Hepatology* 40.6 (Dec. 2004), pp. 1322–1332 (cit. on p. 103).

[152] J. D. Stiffler, M. Nguyen, J. A. Sohn, C. Liu, D. Kaplan, and C. Seeger. “Focal distribution of hepatitis C virus RNA in infected livers”. In: *PLoS ONE* 4.8 (Aug. 2009), e6661 (cit. on p. 103).

[153] S. Wieland, Z. Makowska, B. Campana, D. Calabrese, M. T. Dill, J. Chung, et al. “Simultaneous detection of hepatitis C virus and interferon stimulated gene expression in infected human liver”. In: *Hepatology* 59.6 (June 2014), pp. 2121–2130 (cit. on p. 103).

[154] A. Funk, H. Hohenberg, M. Mhamdi, H. Will, and H. Sirma. “Spread of hepatitis B viruses in vitro requires extracellular progeny and may be codetermined by polarized egress”. In: *J. Virol.* 78.8 (Apr. 2004), pp. 3977–3983 (cit. on p. 104).

[155] A. Goyal and J. M. Murray. “Modelling the Impact of Cell-To-Cell Transmission in Hepatitis B Virus”. In: *PLoS ONE* 11.8 (Aug. 2016), pp. 1–22 (cit. on p. 104).

[156] S. Miyashita, K. Ishibashi, H. Kishino, and M. Ishikawa. “Viruses roll the dice: the stochastic behavior of viral genome molecules accelerates viral adaptation at the cell and tissue levels”. In: *PLoS Biol.* 13.3 (Mar. 2015), e1002094 (cit. on p. 105).

[157] C. Sweet. “The pathogenicity of cytomegalovirus”. In: *FEMS Microbiol. Rev.* 23.4 (July 1999), pp. 457–482 (cit. on p. 106).

[158] I. Murrell, C. Bedford, K. Ladell, K. L. Miners, D. A. Price, P. Tomasec, et al. “The pentameric complex drives immunologically covert cell-cell transmission of wild-type human cytomegalovirus”. In: *Proc. Natl. Acad. Sci. U.S.A.* 114.23 (June 2017), pp. 6104–6109 (cit. on p. 106).

[159] B. M. Laksono, R. D. de Vries, S. McQuaid, W. P. Duprex, and R. L. de Swart. “Measles Virus Host Invasion and Pathogenesis”. In: *Viruses* 8.8 (July 2016) (cit. on p. 106).

[160] F. Fenner, D. A. Henderson, I. Arita, Z. Jezek, and I. Ladnyi. *Smallpox and its eradication*. World Health Organization, 1987 (cit. on p. 106).

[161] G. L. Smith, B. J. Murphy, and M. Law. “Vaccinia virus motility”. In: *Annu. Rev. Microbiol.* 57 (2003), pp. 323–342 (cit. on p. 106).

List of Abbreviations

ABM	Agent-based model
AICc	corrected Akaike Information Criterion
anti-E2	Human anti-HCV E2 monoclonal antibody MAb AR3A
CC	Cell-to-cell
CC contributor	Cells contributing to CC-transmission
CF	Cell-free
CF proportion	Proportion of cells infected through cell-free transmission
CI	Confidence interval
CPM	Cellular Potts model
DNA	Deoxyribonucleic acid
FACS	Fluorescence-activated cell sorting
FBS	Fetal Bovine Serum
FFU	Focus forming unit
fsd	Focus size distribution
HCV	Hepatitis C virus
HIV	Human Immunodeficiency virus
MLE	Maximum likelihood estimator
MOI	Multiplicity of infection
ODE	Ordinary differential equation
PBMC	Human peripheral blood mononuclear cells
p.i.	Post infection
RNA	Ribonucleic acid
SMV	Standard model of viral dynamics
SVR	Sustained viral response

List of Figures

List of Tables